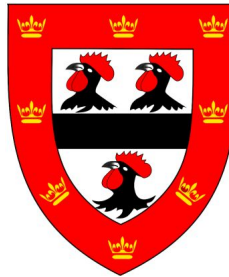


The origin and evolution of warm exozodiacal dust



Jessica Kathryn Rigley

Supervisor: Prof. Mark C. Wyatt

Institute of Astronomy
University of Cambridge

This dissertation is submitted for the degree of
Doctor of Philosophy

Jesus College

April 2022

Declaration

I hereby declare that the contents of this dissertation are original and have not been submitted in whole or in part for consideration for any other degree or qualification in this, or any other university. This dissertation is the result of my own work and contains nothing which is the outcome of work done in collaboration with others, except as declared in the preface and specified in the text. The length of this thesis does not exceed the stated limit of the Degree Committee of Physics and Chemistry of 60,000 words. The following parts of this thesis have already been published in academic journals:

- **Chapter 2** and most of **Chapter 3** were adapted from the published work
Dust size and spatial distributions in debris discs: predictions for exozodiacal dust dragged in from an exo-Kuiper belt
Rigley, J. K. & Wyatt, M. C., 2020, MNRAS, 497, 1143
- **Section 3.4** was adapted from modelling I did as part of the analysis in the published work
The HOSTS Survey: Evidence for an Extended Dust Disk and Constraints on the Presence of Giant Planets in the Habitable Zone of β Leo
Defrère, D., Hinz, P. M., Kennedy, G. M., Stone, J., **Rigley, J.**, et al., AJ, 161, 186
- **Chapter 4** was adapted from the published work
Comet fragmentation as a source of the zodiacal cloud
Rigley, J. K. & Wyatt, M. C., 2022, MNRAS, 510, 834

Jessica Kathryn Rigley
April 2022

The origin and evolution of warm exozodiacal dust

Jessica Kathryn Rigley

Many stars show excess mid-infrared emission which is attributed to warm dust in the habitable zone of the star, known as exozodiacal dust, or exozodi for short. Such dust will be a source of noise and confusion when attempting to detect and characterise Earth-like planets. Therefore, an understanding of exozodiacal dust is crucial to our search for habitable planets and life. In this thesis, I present theoretical models for the origin and evolution of warm exozodiacal dust. Observations find a strong correlation between the presence of warm habitable zone dust and cold belts of planetesimals similar to the Solar System's Kuiper belt. Given this correlation and the short lifetime of dust grains close to the star, it is probable that exozodiacal dust originates further out in the planetary system and is transported inwards.

One possible transport mechanism is Poynting-Robertson (P-R) drag, which causes dust grains to lose angular momentum and spiral in towards the star. Initially, I develop an analytical model for the interplay of P-R drag and catastrophic collisions in a debris disc which predicts the levels of exozodiacal dust dragged into the habitable zone of a star from a cold outer belt. I show that detectable outer belts should produce exozodi levels tens of times higher than our zodiacal cloud via P-R drag, but these levels are insufficient to explain a large fraction of exozodiacal dust detections. In-depth application of the model to the exozodi of β Leo suggests the presence of an additional, warm asteroid belt to explain the radial profile of habitable zone dust.

An alternative mechanism is inward scattering of comets, which spontaneously fragment to produce dust. I then develop a numerical model for the zodiacal dust produced by spontaneous fragmentation of Jupiter-family comets in the Solar System. This is able to produce enough dust to sustain the zodiacal cloud, and give the correct radial and size distribution of dust. I show that cometary input to the zodiacal cloud should be highly stochastic, depending on the sizes and dynamical lifetimes of comets scattered in. The comet fragmentation model is then extended to be applicable to other planetary systems, taking into account the different dynamical effects. This model will show how much dust comets produce and its evolution after being released from a comet to give exozodi radial profiles.

Finally, I summarise the work in this thesis, and discuss the future outlook and my planned projects for furthering our understanding of exozodiacal dust.

Acknowledgements

First, I would like to acknowledge the support of my supervisor Mark Wyatt throughout my PhD. His helpful guidance and feedback have been invaluable to my research. I would also like to thank the postdocs in our group, Seba and Marija, for their advice, especially during job applications.

I would like to thank the Science and Technologies Facilities Council for funding my PhD, and Jesus College for providing additional financial support.

My time at the Institute of Astronomy would not have been the same without my fellow graduate students. I would like to thank my PhD cohort for making the IoA such a fun place to work. Thank you to my office mates past and present from H27 and H28, in particular Jeff, Ryan, Namrah, Chris, Adam, Zofia, Mäns and Connor. Thank you to the boardgamers for all of the fun distractions from work, especially Steve, Stefan, Alex, Andrew, Erik, and Zofia. I am especially grateful to Steve for supporting me through the last few months and making sure I still had fun.

I would also like to thank my housemates Stacey and Serena for making working through lockdown much more bearable with our walks, butterbeer-making and TV marathons. Thank you to the University Powerlifting Club for introducing me to such a fun and empowering sport and providing such a supportive environment to lift heavy things.

Finally, I would like to thank my parents for their endless love and support. Thank you for encouraging my interests in maths and science and always believing in me.

Table of contents

List of figures	xiii
List of tables	xvii
1 Introduction	1
1.1 Planetary systems	2
1.1.1 Planet formation	2
1.1.2 Debris discs	4
1.2 Comets	5
1.2.1 Dynamical evolution	6
1.2.2 Cometary activity	7
1.2.3 Spontaneous fragmentation	8
1.2.4 Exocomets	9
1.3 Debris discs	9
1.3.1 Debris disc properties	10
1.3.2 Gas in debris discs	11
1.3.3 Debris disc forces	12
1.3.4 Numerical modelling of debris discs	15
1.4 The zodiacal cloud	17
1.4.1 Structure	17
1.4.2 Sources of dust	18
1.4.3 Models	20
1.5 Exozodiacal dust	20
1.5.1 Exozodi observations	23
1.5.2 Exozodi models	25
1.6 Thesis structure	28

2	Dust distributions in debris discs	31
2.1	Introduction	31
2.2	Numerical Model	33
2.2.1	Model inputs	35
2.2.2	Optical properties	36
2.2.3	Numerical results	36
2.3	Analytical Model	39
2.3.1	Parent belt size distribution	39
2.3.2	Two-dimensional distribution	43
2.3.3	Application of model	44
2.4	Comparison of numerical and analytical models	45
2.4.1	Disc mass	47
2.4.2	Model fitting	48
2.4.3	Thermal emission	51
2.5	Parameter space	52
2.5.1	Stellar type	52
2.5.2	Belt radius	57
2.5.3	Dispersal threshold of particles	58
2.5.4	Redistribution function	60
2.5.5	Limitations of model	60
2.6	A toy model of the Solar System	61
2.7	Conclusions	64
3	P-R drag model predictions	67
3.1	Introduction	68
3.2	Thermal emission	69
3.3	Application to the HOSTS survey	76
3.4	Modelling the exozodi of β Leo	85
3.4.1	Observational constraints	86
3.4.2	P-R drag model predictions	87
3.4.3	An additional belt?	89
3.5	Conclusions	92
4	Comet fragmentation	95
4.1	Introduction	96
4.2	Comet model	99
4.2.1	N-body data	99

4.2.2	Size distribution	101
4.2.3	Cloning	103
4.2.4	Fragmentation	105
4.2.5	Outcomes of fragmentation	106
4.3	Dust model	113
4.3.1	Input size distribution and dust properties	113
4.3.2	Timescales	116
4.3.3	Collisional evolution	121
4.3.4	Model parameters	122
4.4	Model fitting	123
4.4.1	Observational constraints	123
4.4.2	Fitting	124
4.5	Results	126
4.5.1	Mass input to the zodiacal cloud	126
4.5.2	Dust distribution	128
4.6	Discussion	139
4.6.1	Stochasticity	139
4.6.2	Other free parameters	139
4.6.3	Dominant comet size	140
4.6.4	Historical brightness	141
4.6.5	Model parameters	141
4.6.6	Model limitations	143
4.7	Comparison with other models	148
4.7.1	Accretion rate onto Earth	149
4.7.2	Collisional evolution	149
4.8	Conclusions	151
5	Exocomet model	153
5.1	Introduction	153
5.2	Comet scattering and fragmentation	155
5.2.1	Planetary system	155
5.2.2	Input of comets	158
5.2.3	Fragmentation	160
5.3	Dust evolution	163
5.3.1	Grain properties and size distribution	163
5.3.2	Dust evolution model	165
5.3.3	Interplay between dynamics and drag	169

5.3.4	Kinetic model	173
5.3.5	Dynamical grains	174
5.4	Conclusions	175
6	Conclusions	177
6.1	Summary	177
6.1.1	P-R drag	177
6.1.2	Comet fragmentation	178
6.2	Future prospects	179
	References	183

List of figures

1.1	Diagram showing the locations of small bodies in the Solar System.	4
1.2	Image of Comet C/1995 Hale-Bopp.	6
1.3	Images of the debris disc around Fomalhaut.	11
1.4	Size distribution of bodies in a debris disc.	14
1.5	Vertical profiles of zodiacal dust produced by different sources.	19
1.6	Impact of hot, warm, and cold dust on a star's SED.	21
1.7	Impact of exozodiacal dust on yield of exo-Earth missions.	22
1.8	The exozodi luminosity function.	24
1.9	Diagram of comets being scattered inwards by a planet chain.	28
2.1	Two-dimensional size distributions from the numerical model.	37
2.2	Two-dimensional size distributions predicted by the analytical model.	46
2.3	Radial optical depth profiles.	48
2.4	Ratios used to fit the free parameters of the analytical model, k_0 and γ	49
2.5	SEDs from the numerical and analytical models.	53
2.6	Two-dimensional size distributions for different stellar types.	54
2.7	The ratio of radiation pressure to gravity, β	55
2.8	SED comparison for different stellar types.	56
2.9	Radial profiles for discs with outer belts at different locations.	57
2.10	Effect of collisional strength on the size distribution of particles.	59
2.11	Size distribution in the belt for different redistribution functions.	61
2.12	Size distributions in a toy model of the Solar System.	63
3.1	SED for the toy zodiacal cloud model.	69
3.2	Fractional excesses and luminosities predicted for discs around a Sun-like star.	70
3.3	Detectability of discs at different wavelengths for Sun-like stars.	74
3.4	Detectability of discs at different wavelengths for A-type stars.	75
3.5	Null excess predictions for planetesimal belts of different parameters.	77

3.6	SEDs for discs around A0 and G0 stars.	78
3.7	Null excess predictions for belts with different fractional luminosities.	80
3.8	Null excess predictions for belts using the model of Wyatt (2005).	81
3.9	Radial profiles for β Leo from different P-R drag models.	88
3.10	Parameter space an additional warm belt around β Leo can exist in while satisfying observational constraints.	90
3.11	Best-fit analytical model for β Leo's radial profile.	91
4.1	Histogram of comet N-body data.	100
4.2	Cumulative size distribution of comet nuclei radii.	103
4.3	Cumulative distribution of maximum comet size.	104
4.4	Fraction of comets which survive their dynamical lifetime.	106
4.5	Cumulative distributions of comet lifetimes.	108
4.6	Mean number of perihelion passages survived by comets inside 2.5 au.	109
4.7	Cumulative size distribution of visible comets.	110
4.8	Mass produced by comets of different initial sizes.	111
4.9	Mass lost by comets as a function of pericentre and eccentricity.	113
4.10	The ratio of radiation pressure to gravity, β	116
4.11	Fraction of dust grains dominated by dynamical interactions with Jupiter.	119
4.12	Size distribution of dust input into the dust model.	120
4.13	Total mass input rate into the dust model.	126
4.14	Distribution of mass in pericentre-eccentricity space input into the dust model.	128
4.15	Mass input into the dust model as a function of heliocentric distance.	129
4.16	Mass of dust supplying the zodiacal cloud from comets of different sizes.	130
4.17	Radial profile of dust at different times.	131
4.18	Radial profile of dust for different grain sizes.	132
4.19	Size distribution of dust at different heliocentric distances.	133
4.20	Comparison of the size distribution at 1 au with an empirical model and LDEF measurements.	134
4.21	Evolution of zodiacal cloud observables with time.	135
4.22	Evolution of the zodiacal cloud geometrical optical depth with time.	136
4.23	Evolution of the zodiacal cloud emission seen by a distant observer with time.	137
4.24	Evolution of zodiacal cloud observables during a spike in emission.	138
4.25	Collisional strength of dust grains.	142
4.26	Cumulative size distribution of visible comets with an alternative fragmentation prescription.	145
4.27	The effect of including dynamically "lost" grains on the dust distribution.	147

4.28	The effect of not including collisional fragments on the size distribution. . .	150
5.1	Distribution of comets from N-body simulations with a chain of planets. . .	157
5.2	Size distribution of comets assumed to lie in the outer belt.	159
5.3	Cumulative distribution of the largest comet present each time the size distribution is cloned.	160
5.4	Survival fraction of different sizes of comet.	162
5.5	Histogram of time spent within the critical pericentre for fragmentation. . .	163
5.6	Mass supplied to the exozodi by comets of different sizes.	164
5.7	Region of parameter space which crosses each planet.	168
5.8	Comparison of the analytical P-R drag and diffusion timescales.	170
5.9	Example comparison of semi-analytical predictions and N-body simulations with P-R drag.	172
5.10	Reduced χ^2 used to fit k_{diff} , which is used in diffusion rates.	173

List of tables

2.1	Stellar types.	53
3.1	Comparison of null depths from the analytical model and the HOSTS survey.	82
3.2	Measured null depths for β Leo.	86
4.1	Size distribution of JFC nuclei.	102
4.2	Size distribution of dust grains produced in comet splittings.	114
5.1	Planetary semimajor axes.	158
5.2	Size distribution of exocomets.	159

Chapter 1

Introduction

Over the last couple of decades, the field of exoplanets, studying planets around stars other than our Sun, has grown exponentially. Since the first detection of an exoplanet orbiting a main sequence star, 51 Pegasi b, in 1995 (Mayor and Queloz, 1995), nearly five thousand planets have been detected around other stars, and this number continues to grow rapidly. These have been detected with a variety of techniques, such as the transit method, in which a planet passing in front of a star blocks its light (Borucki et al., 2011; Batalha et al., 2013). When a planet orbits a star, conservation of momentum means that the star also orbits the centre of mass of the planet-star system with an orbit that is smaller than the planet's by the ratio of their masses, known as reflex motion. The radial velocity technique measures the resulting variations in a star's velocity along the line of sight through periodic Doppler shifts of the stellar spectrum (e.g. Pepe et al., 2011; Mayor et al., 2011). A few massive planets further from their stars have been directly imaged, allowing us to watch them orbiting their stars (e.g. Marois et al., 2008, 2010; Lagrange et al., 2010). Other planets are detected by gravitational microlensing, in which a nearby star's gravity bends the path of light from a distant star such that it is imaged as a ring. Planets orbiting the lens star can pass through the line of sight, acting as an additional lens and causing a change in the brightness of the distant star (Beaulieu et al., 2006; Gaudi, 2012; Giannini and Lunine, 2013). More recently, astrometry is allowing us to detect stellar reflex motion in the plane of the sky due to the presence of planets (Kervella et al., 2019; Meunier and Lagrange, 2022). We have discovered a huge diversity of planets, and seen that planetary systems can look very different to our own. However, so far one kind of planet has remained out of reach: a habitable planet just like our Earth.

Today the field has grown to encompass not just detecting other worlds, but unravelling how these planets form, what they are made of, what their atmospheres are like, and even what the planetary system as whole is like. In fact, we can detect the presence of other

things in the planetary system which aren't planets – belts of asteroids and comets similar to our Solar System's asteroid belt and Kuiper belt, and clouds of dust like our zodiacal cloud. These small bodies provide another way to probe the formation and architecture of other planetary systems, inferring the presence of planets and the environment they may be experiencing.

This thesis focuses on one aspect of this field – untangling the origin of warm habitable zone dust. Many stars exhibit high levels of dust in their habitable zones known as exozodiacal clouds, or exozodis. This poses a problem to missions hoping to detect temperate Earth-like planets and eventually life, as such dust obscures the habitable zone, making a challenging detection even more difficult. Thus unravelling the exozodi "problem" is critical to the search for life. Moreover, exozodiacal dust provides a window into what is happening in the habitable zones of other stars. For example, it may be an indicator of the presence of many comets which are bombarding planets, determining their habitability. This could be a key pathway for delivering the constituents needed for the formation of life. Altogether, an understanding of exozodiacal dust is a crucial piece of the puzzle in the search for habitable planets and thus life.

1.1 Planetary systems

1.1.1 Planet formation

When a star forms from a molecular cloud, residual gas and dust forms a circumstellar disc known as a protoplanetary disc, from which a planetary system can form. Residual angular momentum causes the cloud to collapse into a viscous accretion disc, with material at the inner edge falling onto the star. Protoplanetary discs typically have about a hundred times more gas than dust, forming an optically thick disc with high levels of dust ($> 1 M_{\oplus}$). Planets and planetesimals are believed to form early in the lifetime of a star from this material in the protoplanetary disc (Armitage, 2010; Drazkowska et al., 2022).

In order to form planets, micron-sized dust grains must grow by 12 orders of magnitude (e.g. Blum, 2018). Growth to cm-sized pebbles can occur quickly by collisions between grains which lead to coagulation and thus growth (Dominik and Tielens, 1997; Güttler et al., 2010). However, once grains reach cm-size, there are barriers to further growth. Interactions with the surrounding gas determine the evolution of dust grains. The gas is partially supported by an outward pressure gradient, such that it orbits the star at a sub-Keplerian speed. This creates a drag force on dust grains orbiting the star at the Keplerian velocity, causing them to lose angular momentum and drift in towards the star in a process known as radial drift

(Weidenschilling, 1977). Particles larger than a critical size, typically in the mm–m size range, face the radial drift barrier, in which the the timescale for drift onto the star is shorter than the dust growth timescale (Weidenschilling and Cuzzi, 1993). Moreover, as dust grains grow, they become more decoupled from the gas and their relative velocities increase. This leads to what is known as the fragmentation barrier, in which collision velocities are so high that they cause disruption of particles rather than sticking and growth (Brauer et al., 2008; Bukhari Syed et al., 2017). Collisions between grains also pose problems via the bouncing barrier (Zsom et al., 2010) and the erosion barrier (Schräpler et al., 2018). One mechanism which can overcome these growth barriers to form planetesimals, km-sized bodies which may go on to form planets, is a pebble concentration model. Interaction between two fluids, such as the gas and dust in a protoplanetary disc, can lead to a linear instability known as the streaming instability (Youdin and Goodman, 2005), which creates local overdensities of pebbles in filaments. In regions where the local dust-to-gas ratio exceeds a critical level, which is of order unity, planetesimals can then form by gravitational collapse (Johansen et al., 2007). This forms a size distribution of planetesimals up to ~ 100 km in size, with a cumulative mass function exponent of -1.6 (e.g. Simon et al., 2017; Schäfer et al., 2017). However, this mechanism requires high Stokes numbers ($> 10^{-3}$), high dust-to-gas ratios, and high metallicity (e.g. Carrera et al., 2015; Li and Youdin, 2021).

Once particles overcome these growth barriers to form planetesimals, further growth to planets is better understood, and can occur through two mechanisms. Planetesimal accretion is a gravitational process, in which collisions between planetesimals lead to growth. The accretion rate is enhanced by gravitational focussing, and can lead to runaway growth (Ormel et al., 2010). If solids stay in the form of pebbles, they can be accreted by planetesimals or planetary embryos with the help of gas drag, in a process known as pebble accretion (Ormel, 2017; Johansen and Lambrechts, 2017). This leads to much higher planetary growth rates than planetesimal accretion (Lambrechts and Johansen, 2012). Terrestrial planets and planetary cores can form from planetesimals via these accretion mechanisms. Giant planets may form by two mechanisms (Helled et al., 2014). In the core accretion model (Raymond et al., 2009), gas giant planets form from a rocky or icy planet core which is massive enough ($\gtrsim 5 - 10 M_{\oplus}$) to accrete a gas envelope before the protoplanetary disc is dispersed (e.g. Lissauer et al., 2009; Boley, 2009). Alternatively, giant planets may form via gravitational instabilities in protoplanetary discs where surface densities exceed a critical value, which is the favoured mechanism at greater distances from the star (e.g. Boss, 2011).

1.1.2 Debris discs

Within the first 10 Myr (Ercolano and Pascucci, 2017), the gas disc disperses, leaving behind any planets which have formed, and the leftover planetesimals which did not become planets, usually located in a belt of objects. These planetesimals are typically kilometres in size, and if formed beyond the snowline, can be rich in volatile ices. Planetesimal belts undergo collisional cascades, in which destructive collisions between bodies produce progressively smaller and smaller particles. This produces dust grains, which can be seen through their thermal emission at infrared and sub-mm wavelengths, or in scattered light in the visible and near-infrared. Dust grains have short lifetimes in these discs due to destructive collisions and stellar radiation forces, implying the dust must be continually replenished by collisions of larger bodies. Debris discs have much lower levels of dust than in protoplanetary discs ($< 0.1 M_{\oplus}$), making them optically thin. Together, these small bodies and dust form a planetary system's debris disc. This includes everything in a planetary system which is not a planet: asteroids, comets, planetesimals, and the dust and gas they produce.

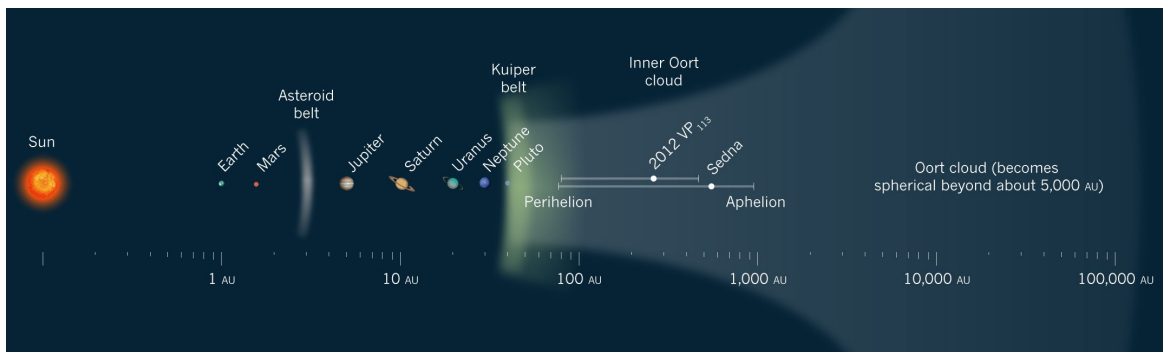


Fig. 1.1 Diagram showing the locations of small body reservoirs in the Solar System (Schwamb, 2014). The asteroid belt sits at 2 – 3.5 au; the Kuiper belt is at $\sim 30 - 50$ au; the Oort Cloud starts at > 1000 au and becomes roughly spherical at $> 10,000$ au from the Sun.

Our own Solar System has a debris disc with several components – three reservoirs of large bodies (see Figure 1.1, Dones et al., 2015) and interplanetary dust (Poppe et al., 2019). The Edgeworth-Kuiper belt is populated by planetesimals and dwarf planets in a relatively thin disc at 30–50 au (Morbidelli and Nesvorný, 2020), with an estimated total mass of $0.02 M_{\oplus}$ (Pitjeva and Pitjev, 2018). Having formed beyond the snowline, these bodies are made of frozen volatiles. Kuiper belt objects (KBOs) can be divided into different dynamical populations which partially overlap (Gladman et al., 2008). The classical Kuiper belt constitutes $\sim 70\%$ of the observed population, and occupies low eccentricity orbits with semimajor axes > 40 au. There are two populations divided according to the inclinations of objects: cold classicals ($i < 5^\circ$) and hot classicals ($i > 5^\circ$). About 20% of KBOs are trapped

in mean-motion resonances with Neptune, which orbits just interior to the Kuiper belt at 30 au. The main resonance which is populated is the 2:3 resonance at 39.4 au, in which Pluto lies, such that this population is known as Plutinos (Jewitt and Luu, 1995). The remaining KBOs lie in the scattered disc, with pericentres in the range 30 – 40 au and high eccentricities $e \sim 0.6$. The population of the scattered disc is likely underestimated due to the further distances from the Sun these bodies orbit at, and may actually be comparable to the classical population (Adams et al., 2014). Nearer to the Sun, the asteroid belt sits at 2–4 au, between the orbits of Mars and Jupiter (Raymond and Nesvorný, 2020). This contains over a million asteroids, rocky bodies which collide together to produce a collisional cascade of fragments, with a total mass of $< 0.001 M_{\oplus}$ (Kuchynka and Folkner, 2013). The distribution of bodies in the asteroid belt is sculpted by planetary resonances. For example, the Kirkwood gaps are created by clearing of Jupiter’s mean motion resonances. Out at $> 10,000$ au from the Sun lies an isotropic reservoir of comets known as the Oort cloud (Oort, 1950; Dones et al., 2004). The Galactic tide and stellar encounters can perturb these bodies, scattering them onto orbits which pass close to the Sun. Interplanetary dust is also present throughout the Solar System (Poppe et al., 2019), though it is concentrated inside the orbit of Jupiter (< 5 au from the Sun). This dust is known as the zodiacal cloud (Sykes et al., 2004; Lasue et al., 2020) and the reflection of sunlight off these particles can be seen close to dawn or dusk as the zodiacal light. The source of interplanetary dust in the Solar System is believed to be a combination of asteroids, comets, and the interstellar medium (Poppe, 2016). Overall, our Solar System’s debris disc contains relatively little mass compared to exoplanetary systems, such that it could not yet be detected around another star (Greaves and Wyatt, 2010; Vitense et al., 2012).

1.2 Comets

Comets are rocky, icy bodies which originate in either the Kuiper belt or the Oort cloud. They are leftover planetesimals after the planet formation phase which are scattered into the inner Solar System by dynamical interactions. Most comets formed far from the Sun, and are rich in volatile ices such as H_2O , CO , CO_2 , and NH_3 , along with refractory grains and organics such as hydrocarbons and aromatic nitriles. As they approach the Sun, volatile ices sublimate and dust is released from the surface of the comet. Images of comets therefore show a coma, comprising the gas lifting off the nucleus, and a tail of dust (Figure 1.2).



Fig. 1.2 Image of Comet C/1995 Hale-Bopp taken in 1997. Two tails can be seen: the dust tail streaks behind the comet in its wake, while the ion tail (blue) points away from the Sun. Credit: ESO/E. Slawik.

1.2.1 Dynamical evolution

Comets can be placed into broad categories depending on the natures of their orbits. Short-period comets (SPCs) have periods < 200 yr, while long-period comets (LPCs) have longer periods, such that they are rarely seen to make a return passage through the inner Solar System. LPCs come from Oort cloud objects with semimajor axes $> 10,000 - 20,000$ au, where Galactic tides are strong enough to decrease the perihelion of a comet from > 30 to ~ 1 au (Duncan et al., 1987). SPCs can be further split into Jupiter-family comets (JFCs), which primarily interact with Jupiter, and have Tisserand parameters (Murray and Dermott, 1999) with respect to Jupiter of $2 \lesssim T_J \lesssim 3$, and Halley-Type comets (HTCs), which have Tisserand parameters $T_J < 2$ (Levison, 1996). In general, JFCs have shorter periods ($P < 20$ yr), whereas HTCs have intermediate periods ($20 < P < 200$ yr). A small number of SPCs are Encke-type comets, with $T_J > 3$ and semimajor axes inside Jupiter. JFCs are thought to originate in the scattered disc (the population of KBOs on eccentric orbits with $a > 50$ au), from which some bodies are scattered inside Neptune's orbit into what

is known as the Centaur region, then again into the inner Solar System (e.g. Levison and Duncan, 1997). The source of HTC is not yet clear. Due to how isotropic it is, the Oort cloud struggles to produce the inclination distribution of HTCs, unless there is an inner Oort cloud with flattened inclinations (Levison et al., 2001). Levison et al. (2006) suggested that bodies from the outer edge of the scattered disc could evolve to much larger semimajor axes ($a > 1000$ au), then have their perihelia scattered inwards by Galactic tides, but this requires the scattered disc to be an order of magnitude more massive. An Oort cloud model which includes comet fading is able to fit the inclination and semimajor axis distribution of HTCs (Wang and Brassier, 2014). More recently, detection of cometary activity from bodies in the asteroid belt has led to the discovery of a new class of bodies called Main Belt comets (Bertini, 2011) which are dynamically asteroid-like. These are also known as active asteroids (Jewitt, 2012), as the observed activity is not necessarily due to sublimation of volatile ices.

1.2.2 Cometary activity

The characteristic tails of comets (Figure 1.2) show they are losing mass via gas and dust, typically at a rate which increases as the comet gets closer to the Sun. It has generally been thought that cometary activity is dominated by the sublimation of water ice (H_2O), which starts at temperatures of ~ 150 K, or around 3 au from the Sun (e.g. Womack et al., 2017). However, a growing body of evidence suggests that comets are active at much greater distances from the Sun (e.g. Hui et al., 2019; Farnham et al., 2021). Cometary volatile ices also comprise species such as CO and CO_2 , which sublime at much lower temperatures than water, corresponding to 120 and 13 au respectively. Other processes, such as crystallisation of amorphous water ice, may also contribute to the activity (e.g. Prialnik and Bar-Nun, 1990). Indeed, LPC C/2017 K2 (K2) was observed to be active at large heliocentric distances, with pre-discovery data suggesting that it was active as far as 23.7 au from the Sun (Jewitt et al., 2017; Hui et al., 2018), which may be due to sublimation of CO ice (Meech et al., 2017; Yang et al., 2021). Jewitt et al. (2021) modelled the development of activity in K2, and suggested that the photometry required the onset of activity to occur at ~ 35 au from the Sun. More recently, a model of their thermal and dynamical evolution suggested that JFCs should be active beyond the orbit of Neptune due to loss of hypervolatile ices such as CO, and comets should lose hypervolatile ices from their surface layers in the Centaur region before they become JFCs (Gkotsinas et al., 2022). Similarly, a dynamical model of their production requires LPCs to fade within five perihelion passages of $\lesssim 12$ au in order to fit the orbital distribution of observed LPCs, suggesting they must be active far from the Sun (Kaib, 2022).

1.2.3 Spontaneous fragmentation

While comet activity is generally attributed to sublimation of volatiles, many are also seen to spontaneously disrupt, which may be the dominant mass loss mechanism from comets (see Boehnhardt, 2004; Fernández, 2009). Splittings are observed more frequently for orbits with smaller perihelia (Fernández, 2005). It is possible that comets may tidally split when in close proximity to planets or the Sun; comet Shoemaker-Levy 9 is thought to have tidally disrupted when it passed within the Roche limit of Jupiter (e.g. Scotti and Melosh, 1993; Asphaug and Benz, 1996). Most fragmentations are spontaneous, requiring other mechanisms, though tidal forces may weaken the structure of comet nuclei. The underlying mechanism of spontaneous fragmentation is difficult to constrain, but several possibilities have been suggested.

Some comets may disrupt via rotational spin-up due to asymmetric outgassing exerting a torque on the comet, to the point where the centrifugal force exceeds self-gravity. In particular, this is likely a size-dependent effect, with sub-km comet nuclei particularly susceptible to rotational disruption (Jewitt, 2021). Jewitt et al. (2016) suggested that rotational instability caused the break-up of fragments of split comet 332P/Ikeya-Murakami, and that the nucleus may have been in an excited rotational state, causing it to disrupt over several orbits.

The eccentricity of cometary orbits produces very large variations in their distances from the Sun, such that they experience a wide range of temperatures. This can exert thermal stress on the nucleus, potentially leading to disruption of the comet. Analytical and numerical solutions of the heat diffusion equation suggest that thermal stresses can exceed tidal stresses by several orders of magnitude for bodies close to the Sun (Shestakova and Tambovtseva, 1997; Tambovtseva and Shestakova, 1999). Thermal splitting is highly efficient within ~ 5 au, but may be important even at tens of au from the Sun. It is likely also dependent on the nucleus size, with sub-km comets fully disrupting in a single event, and larger bodies losing fragments off their surface.

Supervolatile ices such as CO that are trapped under the surface of a comet may sublime when close to the Sun. This creates a build-up of pressure underneath the surface, which may cause part of the comet to break off (Whipple, 1978; Brin and Mendis, 1979; Brin, 1980), or cause total disruption of the nucleus (Samarasinha, 2001). The relation of these fragmentation mechanisms to cometary activity suggests splittings should be more frequent closer to the Sun, though comets have been seen to fragment at heliocentric distances as far as > 100 au (Sekanina and Chodas, 2002). Finally, some comets may disrupt if they are impacted by other small bodies (Beech and Gauer, 2002).

Chen and Jewitt (1994) placed a lower limit on the rate of fragmentation of 0.01 per yr per comet based on CCD images of comets, suggesting this is a frequent phenomenon. Indeed, dynamical simulations of the orbital evolution of JFCs from their origin in the scattered

disc require a physical mechanism, such as fragmentation, to self-consistently limit comet lifetimes in order to match the observed orbital distribution (Di Sisto et al., 2009; Nesvorný et al., 2017).

1.2.4 Exocomets

Since so many comets are seen in our own Solar System, it is likely that many other planetary systems also harbour comets, known as exocomets. Indeed, some observations have hinted at the presence of exocomets orbiting other stars. A growing body of evidence comes from transit observations, typically used to search for planets on highly-inclined orbits. However, several stars have shown asymmetric dips in their light curve, with a sharp ingress followed by an egress which gradually tails off. Studies have suggested this is due to exocomets passing in front of the star, with the sharp edge created by the comet nucleus, and the egress coming from the tail of dust trailing behind the comet on its orbit. Indeed, numerical simulations by Lecavelier Des Etangs (1999) showed transiting exocomets should have this characteristic shape. Strong evidence for exocomets came from Kepler observations of transits around KIC 3542116 and KIC 11084727 (Rappaport et al., 2018). An automated search of Kepler data by Kennedy et al. (2019) found these transits, along with one around HD 182952. KIC 8462852, also known as Boyajian's star, is famous for having many irregularly-shaped dips in its light curve, some of which are very deep (Boyajian et al., 2016). While these are a different shape and depth to typical exocometary transits, models have suggested these dips could be created by circumstellar material on a highly eccentric orbit created by fragmentation of a massive (> 100 km) exocomet (Bodman and Quillen, 2016; Wyatt et al., 2018). K2 observations of EPIC 205718330 and EPIC 235240266 exhibit "little dippers" which have been suggested to be exocomet transits (Ansdell et al., 2019). However, the quintessential exocomet star is β Pic, which has shown evidence for infalling evaporating bodies via variations in its spectral lines for decades (e.g. Beust et al., 1990; Kiefer et al., 2014). Several exocomet transits around β Pic have been detected in data collected by TESS (Zieba et al., 2019; Pavlenko et al., 2022). Gas detected in debris discs (Section 1.3.2) is often attributed to being produced by exocomets orbiting the star.

1.3 Debris discs

Around 20% of main sequence stars show excess far-infrared emission in their spectral energy distribution (SED), which is indicative of cold circumstellar dust orbiting the star at tens or hundreds of au. This suggests the presence of a planetesimal belt undergoing a

collisional cascade which is producing the dust (Matthews et al., 2014). This is known as a debris disc, although it should be noted that the term debris disc encompasses everything in a planetary system which is not a planet, not just a cold planetesimal belt. Surveys have been conducted at $24\ \mu\text{m}$ and $70\ \mu\text{m}$ with Spitzer/MIPS (Rieke et al., 2005; Meyer et al., 2006; Su et al., 2006; Hillenbrand et al., 2008) and $70\text{--}160\ \mu\text{m}$ with Herschel/PACS (Eiroa et al., 2013; Thureau et al., 2014; Sibthorpe et al., 2018) in order to detect cold debris discs. These are seen around stars as young as tens of Myr, and as old as several Gyr. They allow us to probe the architectures of planetary systems, and the outcomes of planet formation.

1.3.1 Debris disc properties

The properties of a debris disc can be estimated from the star's SED (e.g. Wyatt, 2008). Assuming that the dust behaves like a black body, the wavelength where the excess emission peaks gives the dust temperature T , and the distance from the star is then $r = (278.3/T)^2 L_\star^{0.5}$, where L_\star is the stellar luminosity. The amount of dust can be characterised by the disc's fractional luminosity, the ratio of the dust's infrared luminosity to that of the star, $f = L_{\text{dust}}/L_\star$. Debris discs are much less luminous than protoplanetary discs, with fractional luminosities $f < 10^{-2}$ (Lagrange et al., 2000), and far lower amounts of gas.

Resolved imaging at wavelengths from optical to millimetre allows us to better characterise the structure of planetesimal belts and dust properties (Hughes et al., 2018). Resolved images often show asymmetries such as warps, clumps, and offsets, implying the presence of planets perturbing the disc (Wyatt, 2018). Imaging with multiple wavelengths also allows to probe the size distribution of dust grains and constrain grain properties, as larger grains emit more efficiently at longer wavelengths. For example, scattered light images trace the smallest grains, which are most affected by radiation pressure, and blown out in a halo. Scattered light images are typically taken using the Hubble Space Telescope (HST), or the Gemini Planet Imager (e.g. Esposito et al., 2020). Many disc morphologies are seen in scattered light depending on the viewing geometry (Lee and Chiang, 2016), and interpretation of the images requires an understanding of the scattering phase function and albedo of dust grains. In contrast, sub-mm images trace the thermal emission of mm–cm sized dust grains, which are less affected by radiation pressure, and thus show the location of the parent belt producing the dust. In the past sub-mm images were taken using the James Clark Maxwell Telescope (JCMT)/SCUBA-2 (Holland et al., 2017), though more recently images with far superior sensitivity and resolution have been taken with the Atacama Large Millimeter/submillimeter Array (ALMA). For example, Figure 1.3 shows a comparison of two images of the debris disc around nearby A star Fomalhaut. The ALMA image (left) at 1.3 mm shows the largest dust grains and thus the parent belt, whereas the HST image in scattered light (right) shows the

behaviour of the smallest grains, which are blown further from the star. Combining scattered light imaging with thermal emission allows to constrain the dust albedo and composition (e.g. Rodigas et al., 2015).

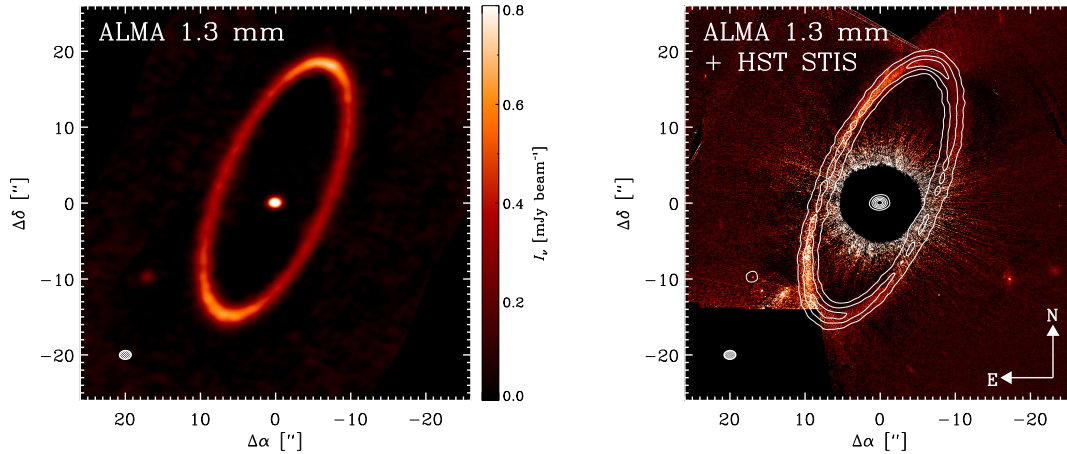


Fig. 1.3 Left: ALMA image at 1.3 mm of the debris disc around nearby young (440 Myr) A star Fomalhaut (MacGregor et al., 2017). The disc is highly inclined to the line of sight (65.6°) and eccentric ($e = 0.12$). Right: the same ALMA image overlaid as white contours on the HST/STIS image of the disc in scattered light (Kalas et al., 2013). Figures from MacGregor et al. (2017).

1.3.2 Gas in debris discs

Although debris discs are gas poor compared to protoplanetary discs, molecular and atomic gas has been detected around several main sequence stars. Most detections are around young A stars (Lieman-Sifry et al., 2016), though gas has also been found around F stars (e.g. Marino et al., 2016) and stars as old as 1 Gyr (Marino et al., 2017). Cold gas further from the star has been detected at far-infrared and mm wavelengths in emission around ~ 20 stars (e.g. Cataldi et al., 2014; Moór et al., 2017; Kral et al., 2020). Circumstellar absorption lines, in particular the Ca II H and K lines and the Na I D line, are used to detect warm gas close to the star. For example, a survey of stars known to host cold gas found 10 of 15 systems also had hot gas (Rebollido et al., 2018), with detections less likely for inclined discs. Another optical survey of 117 stars (Rebollido et al., 2020) detected hot circumstellar gas around 26% of the sample.

It is expected that primordial gas from the protoplanetary disc phase will be dispersed after ~ 10 Myr, either by accretion onto the star or photoevaporation (e.g. Clarke et al., 2001). In some debris discs the gas is not co-located with the dust, suggesting some of the gas

is primordial, as in HD 21997 (Kóspál et al., 2013). However, in general it is likely that debris disc gas is secondary in origin, especially in older systems. Several mechanisms for its production have been suggested, such as release of subsurface volatiles from collisions between comets (Zuckerman and Song, 2012), vaporisation of solids in collisions between dust grains (Czechowski and Mann, 2007), or photodesorption of dust grains (Grigorieva et al., 2007b). In particular, many detections are of carbon monoxide (CO), which should be photodissociated on timescales of ~ 100 yr, implying the gas is being replenished rapidly. To explain the quantities of CO detected, Kral et al. (2019) suggested that neutral carbon released by photodissociation of CO should then shield CO from interstellar UV radiation, allowing it to survive for longer. While CO should be located where it is produced due to its short lifetime, atomic gas with longer lifetimes can viscously spread into an accretion disc (e.g. Kral et al., 2016). Several systems with CO detections have also been found to have high levels of atomic carbon, supporting this "carbon shielding" model (e.g. Higuchi et al., 2019; Cataldi et al., 2020).

Since the origin of the gas is believed to be linked to exocomets if it is secondary, observations of gas in debris discs can constrain the composition of comets in other planetary systems. For example, Matrà et al. (2017) found exocomets around Fomalhaut to have a similar CO + CO₂ ice abundance to Solar System comets. Variable absorption lines in the spectrum of β Pic are thought to be due to exocomets transiting the star (Beust et al., 1990). Kiefer et al. (2014) suggested these are due to two populations of comets, with shallower absorptions produced by old, depleted comets, and deeper lines produced by recent fragmentations. These observations of comets transiting the star can also be used to constrain the orbits of the exocomets (Kennedy, 2018).

1.3.3 Debris disc forces

Particles in debris discs are influenced by many forces (see Krivov, 2007, for a review). The canonical scenario is that large bodies in a planetesimal belt undergo catastrophic and cratering collisions, creating a collisional cascade as planetesimals break up into progressively smaller particles (Dohnanyi, 1969; Tanaka et al., 1996). While collisions can result in catastrophic fragmentation, cratering, or rebounding depending on the impact energy, collision velocities in debris discs are so high that they typically lead to fragmentation, in which the largest fragment has less than half the mass of the original particle. In steady-state, a collisional cascade creates a differential size distribution $n(D) \propto D^{-3.5}$ (Dohnanyi, 1969), where $n(D)dD$ is the number of particles present with diameters $D \rightarrow D + dD$. However, the slope of the size distribution varies with particle size based on the (size-dependent) collisional strength of particles, and the fact that the largest ($>$ km-sized) bodies in a debris disc may not

yet be collisionally active. These collisions deplete the mass in the planetesimal belt, such that the mass, and therefore luminosity, decreases as $1/\text{time}$ (Dominik and Decin, 2003), giving a maximum possible disc mass at a given age which is independent of the initial disc mass (Wyatt et al., 2007a). This is because more massive discs have more frequent collisions, and therefore process their material faster. The size distribution of particles is such that most of the mass is in the largest objects, while the smallest dust grains dominate the cross-sectional area, and therefore the thermal emission. Their small size makes dust grains susceptible to the effects of stellar radiation pressure, in which stellar photons transfer angular momentum to the particles, effectively reducing the stellar gravity they feel. The strength of radiation pressure relative to gravity is characterised by a parameter,

$$\beta = \frac{F_{\text{rad}}}{F_g} = \frac{3L_{\star}Q_{\text{rad}}}{16\pi GM_{\star}c\rho s}, \quad (1.1)$$

where M_{\star} and L_{\star} are the stellar mass and luminosity, Q_{rad} is the radiation pressure coefficient, G is the gravitational constant, and c is the speed of light. The bulk density of particles is ρ and their radius is given by s , such that smaller grains are more susceptible to radiation pressure. Particles below a critical size, s_{bl} , will be put onto hyperbolic orbits and blown out of the system by radiation pressure on short timescales. For particles being released from a circular orbit, this corresponds to $\beta > 0.5$, and grains of radius $\lesssim 1 \mu\text{m}$ for a Sun-like star. A component of radiation pressure, known as Poynting-Robertson (P-R) drag (Wyatt and Whipple, 1950; Burns et al., 1979), acts tangential to a particle's orbit and causes dust grains to lose angular momentum and drift in towards the star. Stellar winds create a drag force which is analogous to P-R drag, and can have a significant effect around late-type stars (Plavchan et al., 2005; Augereau and Beust, 2006; Reidemeister et al., 2011). In our Solar System, the strength of stellar wind drag is about 30% that of P-R drag (Gustafson, 1994; Minato et al., 2006). If significant quantities of gas are present, gas drag due to the difference in velocities between gas and dust particles orbiting the star can oppose the motion of dust grains, causing grains to settle towards the midplane (Olofsson et al., 2022). Once particles are close enough to the star, they may be heated to temperatures such that they begin to sublimate and shrink. Observational limits mean that most observed debris discs are very luminous and massive, implying that P-R drag is insignificant as dust is destroyed on much shorter timescales by mutual collisions (Wyatt, 2005). However, for lower mass debris discs such as the Solar System, P-R drag is the dominant process and collisions between particles are infrequent.

The presence of planets can determine the structure of debris discs, acting as a perturbing force. For example, particles may become trapped in planetary mean motion resonances

(Wyatt, 2003; Mustill and Wyatt, 2011; Shannon et al., 2015). Planets can also sculpt the edges of debris belts, and secularly force them to have an eccentricity (e.g. Pearce and Wyatt, 2014; Shannon et al., 2016). The onset of a collisional cascade requires the belt to be stirred, in which relative velocities between bodies are excited enough that collisions between them become destructive. Some belts may be stirred by the self-gravity of the disc ("self-stirring"), which requires the growth of bodies > 1000 km in size that can excite smaller planetesimals (Kenyon and Bromley, 2004). This requires the disc to be massive enough, and in some cases requires unfeasibly high masses, suggesting something else must stir the debris disc (Pearce et al., 2022). Secular interactions from a planet may cause planetesimal orbits to evolve, and thus stir a debris disc (Mustill and Wyatt, 2009), with more massive planets more effective at stirring. Once the collisional cascade is initiated, destructive collisions produce observable levels of dust. Studies of debris discs therefore constrain the presence of underlying planets, especially those in the outer planetary system, which often would not be detectable with other methods.

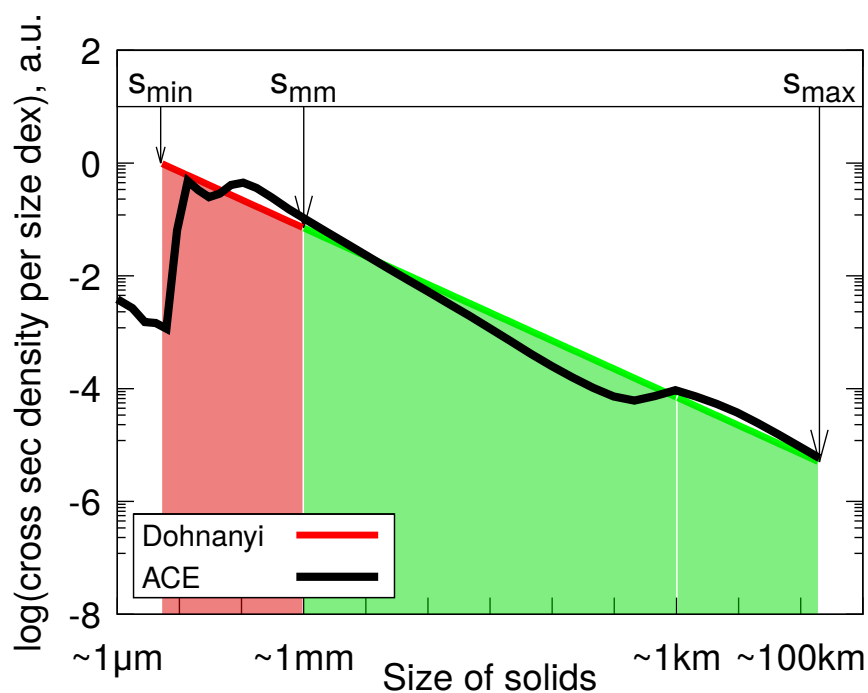


Fig. 1.4 Example of a numerical size distribution of bodies in a debris disc from a collisional evolution code (ACE, Krivov et al., 2006). The slope changes due to the collisional strengths of bodies of different sizes. Large ($> \text{km}$ -sized) bodies have a different slope as they are primordial, and have not yet undergone collisional evolution as their collisional lifetimes are longer than the age of the system. Figure from Krivov and Wyatt (2021).

1.3.4 Numerical modelling of debris discs

Although some properties of debris discs can be derived analytically, numerical modelling is necessary to accurately incorporate the interaction of the different forces acting in debris discs: stellar gravity, dynamical interactions with planets, radiation pressure, drag forces, collisions, and sublimation. This presents numerical challenges due to the large number of particles whose sizes vary over many orders of magnitude. For example, it is not possible to follow the dynamics of each individual particle while also accounting for collisions between particles; each collision produces many smaller particles, causing the number of particles to grow exponentially. Therefore, different numerical methods are used to study different aspects of debris discs, depending on which forces are most relevant to the problem at hand.

N-body simulations such as MERCURY (Chambers, 1999) or REBOUND (Rein and Liu, 2012; Rein and Spiegel, 2015; Rein and Tamayo, 2015, 2016, 2017; Rein et al., 2019) are best for studying the dynamical structures of planetary systems, such as resonance and migrations, and have good spatial resolution (e.g. Krivov et al., 2009; Thébault, 2009). The positions and velocities of individual test particles are followed by integrating their equations of motion to give a steady-state spatial distribution. N-body codes can be modified to handle additional forces, such as P-R drag (e.g. Tamayo et al., 2020). Collisions are neglected, as the production of collisional fragments causes the number of particles whose trajectories must be followed to grow exponentially. These codes cannot handle more than $\sim 10^4$ objects, and are therefore unable to model size distributions. It is possible to include collisions in post-processing with a simplified prescription, either removing objects which come into contact without producing fragments (Lecavelier des Etangs et al., 1996), or producing fragments of equal size (e.g. Wyatt, 2006). This can cause issues when collisional timescales become short, as collisions may become the dominant process, such that the evolution of particles cannot be followed correctly. Therefore, N-body codes are not suitable for finding size distributions, but are useful for studying the dynamical structure of discs created by perturbations from planets or stellar companions, such as the trapping of particles in orbital resonances. They can also be used to follow the dynamical evolution of planetesimals, which are not significantly affected by radiation pressure or drag forces due to their larger size, when collisions are not important. For example, N-body simulations are useful for modelling the inward scattering of comets from a cold outer belt (e.g. Nesvorný et al., 2017; Marino et al., 2018).

The collisional grooming algorithm (Stark and Kuchner, 2009) tries to overcome this limitation by rerunning a code iteratively in order to find the steady state distribution of dust when dynamics and collisions are taken into account. It starts with a seed model which comes from a collisionless simulation, then uses particle positions and velocities from the

seed model to calculate collision rates. This will overestimate particle densities and therefore collision rates, so several iterations are needed to find a steady-state solution. The DyCoSS algorithm (Thébault, 2012; Thebault et al., 2012) uses a similar method to find the steady state distribution with collisions, iteratively running an N-body code. However, these techniques are computationally expensive, requiring the model to be run several times, and ignore any fragments collisions produce. Moreover, they are limited to studying systems in steady state which are only being perturbed by a single body.

Statistical methods instead consider a population of particles in phase space, using ideas based on statistical physics (Boltzmann, 1896; Smoluchowski, 1916). Particles are distributed in a phase space grid, which either considers mass, position, and velocity (such as Thébault et al., 2003; Thébault and Augereau, 2007; Thébault and Wu, 2008; Kenyon and Bromley, 2008, 2010), or mass and orbital elements, as in the Analysis of Collisional Evolution (ACE) code (Krivov et al., 2005, 2006, 2008; Löhne et al., 2008, 2012, 2017) and van Lieshout et al. (2014). The Boltzmann-Smoluchowski equation is solved for the number of particles in each phase space bin at successive time steps, taking into account forces as gain and loss terms from each bin. Collisions are treated as a sink of particles in bins undergoing collisions, and act as a source of smaller particles due to the production of collisional fragments. The particle-in-a-box approach is used to calculate collision rates between particles from different phase space bins. Drag forces such as P-R drag act as diffusion terms, causing particles to migrate between adjacent phase space bins based on the expected rate of change of orbital elements. These methods have the advantage of being able to handle very large numbers of particles and therefore follow the size distribution of particles accurately. However, since individual particles are not considered, these are unable to include dynamical interactions with large perturbing bodies such as planets. Moreover, including more dimensions in the phase space grid vastly increases required computation times, such that typically only two orbital elements are followed. Most codes assume axisymmetry, averaging around the orbits of particles (except for Löhne et al., 2017), and assuming a uniform distribution of inclinations. Therefore, these codes are useful for finding the size distribution of dust grains, but are less useful for studying structure, as they are unable to follow the vertical distribution of particles or account for asymmetries such as dust clumps, and ignore the presence of planets.

Hybrid codes such as LIDT-DD (Kral et al., 2013, 2014) and SMACK (Nesvold et al., 2013; Nesvold and Kuchner, 2015) simultaneously model the dynamical and collisional evolution of particles self-consistently. This is done by representing grains with the same parameters (size, position, velocity) as a single superparticle (SP, Grigorieva et al., 2007a). The motion of these SPs is found using N-body integration, while collisions are calculated

between SPs whose orbits intersect using the particle-in-a-box approach. New SPs are created for the collisional fragments, while similar SPs are merged to reduce the overall number of SPs. This approach is computationally expensive, but can be used to model short-term phenomena such as collisional avalanches (Grigorieva et al., 2007a), break-ups of planetesimals (Kral et al., 2015), and stellar flybys (Nesvold et al., 2017).

1.4 The zodiacal cloud

1.4.1 Structure

The zodiacal cloud consists of a diffuse, interplanetary dust complex which permeates throughout the inner Solar System. Thermal emission and scattered light from this dust is seen as the zodiacal light. The dust is concentrated primarily inside Jupiter’s orbit (< 5.2 au), and extends all the way in to the solar corona ($4R_{\odot}$). It dominates the thermal emission in the sky (Hauser et al., 1984; Kelsall et al., 1998), and has a density which decreases with distance from the Sun (e.g. Leinert et al., 1981; Hanner et al., 1974; Hahn et al., 2002). Several techniques have been used to observe the zodiacal cloud, including in situ measurements of dust particles by spacecraft, measurements of the brightness and polarisation of the zodiacal light, lunar microcraters, and radar and visual observations of meteors (see Grün et al., 2019, for a review). These probe different sizes of particle, which can be amalgamated into empirical models for the distribution of dust (Grün et al., 1985). The infrared emission of zodiacal dust is dominated by small ($1\text{--}100\ \mu\text{m}$) particles.

The zodiacal cloud dominates the thermal emission in the sky, and the first all-sky map of its emission was produced by IRAS (Hauser et al., 1984; Sykes, 1988), which observed in four infrared bands ($12\text{--}100\ \mu\text{m}$). This showed the presence of structure in the zodiacal cloud, such as dust bands (Dermott et al., 1984), populations of dust which are prominent at the same ecliptic latitude (thought to be particles with the same inclination), linked to collisions of specific asteroid families (e.g. Nesvorný et al., 2003, 2006, 2008; Espy Kehoe et al., 2015). Narrow trails of dust were associated with the orbits of comets (Sykes et al., 1986; Sykes and Walker, 1992), believed to be debris ejected from the comet. Thus, both asteroids and comets are believed to supply dust to the zodiacal cloud. The structure of the zodiacal cloud was characterised in more detail by the Cosmic Background Observer (COBE)/DIRBE satellite (Kelsall et al., 1998; Fixsen and Dwek, 2002) at wavelengths $1.25\text{--}240\ \mu\text{m}$ to give the brightness distribution, temperature, and optical depth profiles. A parametric model for the distribution was produced with several components. This included a smooth cloud, with density decreasing with distance from the Sun as $r^{-1.3}$, asteroidal dust

bands, and Earth's circumsolar ring. The zodiacal cloud is not very massive, with a fractional luminosity $\sim 2 \times 10^{-7}$, and a total mass of a few times $10^{-9} M_{\oplus}$ (Nesvorný et al., 2011).

1.4.2 Sources of dust

Many models have been developed to constrain the relative contributions of different sources to the interplanetary dust cloud. Comets are believed to be the dominant source, with asteroids contributing at most 30%. Interstellar dust should make a very minor contribution, and dominate the smallest, submicron, grain sizes (Landgraf et al., 2000; Krüger et al., 2010). Similarly, some dust produced in the Kuiper belt should migrate in, but contributes less than a per cent, as not much dust is able to migrate past Jupiter (Moro-Martín and Malhotra, 2003).

Several models fit to the distribution of $25 \mu\text{m}$ emission seen by IRAS as a function of ecliptic latitude, which essentially follows the vertical distribution of particles, or their inclinations. Zodiacal dust is concentrated in the ecliptic plane, with wings extending to the ecliptic poles. Comets generally have higher inclinations than asteroids, and therefore produce broader latitudinal profiles (Figure 1.5). Liou et al. (1995) required a combination of 1/4 to 1/3 asteroidal dust and 3/4 to 2/3 cometary dust to reproduce the latitudinal profile. On the other hand, Durda and Dermott (1997) modelled the collisional evolution of the main asteroid belt. By using the ratio of emission from the asteroid families to the main belt and the fraction of thermal emission which comes from the dust bands, they concluded that asteroidal dust is responsible for at least 1/3 of the zodiacal cloud. More recent models find comets contribute a much higher fraction of interplanetary dust. For example, the modelling of Nesvorný et al. (2010) (Figure 1.5) found a contribution of $> 90\%$ from comets was required to fit the vertical distribution of thermal emission seen by IRAS. Rowan-Robinson and May (2013) simultaneously modelled the infrared emission from IRAS and COBE empirically, and required contributions of 70, 22, and 7.5%, respectively, from comets, asteroids, and interstellar dust. Another constraint comes from the Earth's resonant ring, in which dust particles are trapped in mean motion resonances with Earth. This exhibits a leading-trailing brightness asymmetry, in which the dust is always brighter behind Earth than ahead of it on its orbit (Dermott et al., 1994). Using infrared observations from AKARI, Ueda et al. (2017) concluded that cometary dust must dominate to fit the leading-trailing brightness asymmetry, with asteroidal dust contributing less than 10% of the infrared emission. Further, comparison of the optical properties of the zodiacal light with those of different minor bodies suggests more than 90% originates from either comets or D-type asteroids (Yang and Ishiguro, 2015).

Meteor data constrains the sporadic meteoroids, giving further information about the types of comets supplying interplanetary dust. Meteoroid streams are trails of particles produced by recent cometary activity and disruption (Jenniskens, 2008). Sporadic meteoroids, on the other

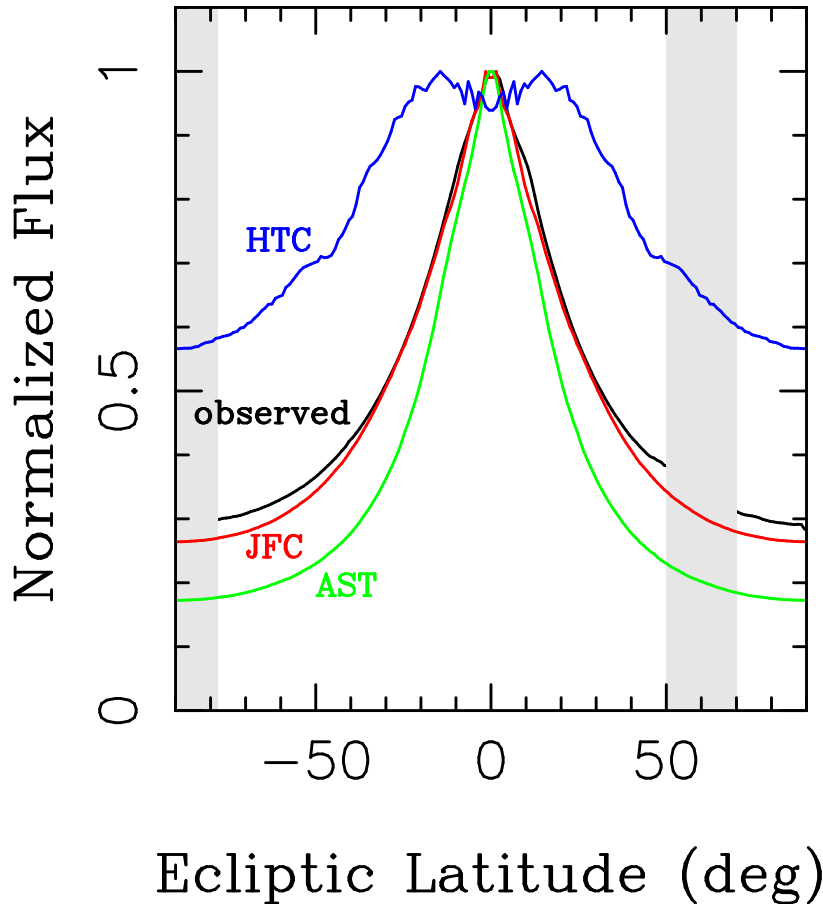


Fig. 1.5 The vertical distributions of zodiacal dust produced by different sources in a numerical model, compared with the IRAS observations at $25\ \mu\text{m}$ (Nesvorný et al., 2010). Halley-type comets (blue) and Jupiter-family comets (red) are compared with asteroids (green).

hand, have evolved so that they are no longer associated with a parent body, and dominate the particles accreted onto Earth (Jones and Brown, 1993). The impact velocities and orbital elements of the sporadic meteoroid complex suggest that SPCs must be the dominant source (Wiegert et al., 2009). Different types of comets are linked to meteoroids in different parts of the sky. For example, the toroidal source is believed to be produced by HTCs (Pokorný et al., 2014). However, the helion and antihelion sources, which contain most of the mass flux, are dominated by particles from JFCs (Nesvorný et al., 2011).

While the structure of the zodiacal cloud is best explained by a cometary source, comet sublimation is insufficient to sustain the quantity of dust presently in the inner Solar System (Nesvorný et al., 2010). However, comets are also seen to spontaneously disrupt, with more splittings observed at lower perihelion distances (Fernández, 2005). Dynamical simulations for the origin of JFCs invoke fragmentation as a mechanism to self-consistently limit the

lifetime of comets in order to match the observed distribution (Di Sisto et al., 2009; Nesvorný et al., 2017). Observations also suggest comets should fragment frequently, with Chen and Jewitt (1994) finding a lower limit for the rate a given comet fragments of 0.01 /yr. Given the likely high frequency of fragmentation events and their ability to cause much greater mass loss than cometary activity, comet fragmentation may dominate the input to the interplanetary dust complex.

1.4.3 Models

Many dynamical models have been developed which aim to replicate either the thermal emission (specifically, the vertical distribution out of the ecliptic plane) of the zodiacal cloud, or the distribution of sporadic meteoroids. Most zodiacal cloud models are dynamical, using N-body simulations to follow the orbital evolution of individual particles due to the influence of the planets, starting them on orbits corresponding to those of different kinds of parent bodies (e.g. Soja et al., 2019; Moorhead et al., 2020). This approach allows the inclusion of forces such as radiation pressure and P-R drag, but neglects or simplifies the effect of mutual collisions.

The greater availability of observational data means that empirical models can be developed for the zodiacal cloud (e.g. Grun et al., 1985; Divine, 1993; Kelsall et al., 1998; Rowan-Robinson and May, 2013). These describe the 3D structure of the zodiacal cloud along with the size distribution of the dust. The parameters describing these distributions may have a basis in the underlying physics, but are ultimately fitted to be able to reproduce certain observations.

1.5 Exozodiacal dust

While far-infrared excesses are produced by thermal emission of cold dust at tens or hundreds of au from a star, many main sequence stars show excess mid- and near-infrared emission, indicating the presence of dust much nearer to the star (see Figure 1.6). These are thought to be analogues of the Solar System’s zodiacal cloud, known as exozodiacal clouds, or exozodis for short (see Kral et al., 2017, for a review).

Hot (> 1000 K) dust produces near-infrared excesses, and must be very close to the star ($\ll 1$ au). It was first detected around Vega (Absil et al., 2006; Defrère et al., 2011), though more recent interferometric surveys have detected these excesses at levels of 1% around many other stars, with a detection rate of 17% in the H band ($1.65 \mu\text{m}$) with VLTI/PIONIER (Ertel et al., 2014; Absil et al., 2021), and 28% in the K band ($2.2 \mu\text{m}$) with CHARA/FLUOR

(Absil et al., 2013). Some of these excesses are seen to be variable on timescales of years (Ertel et al., 2016; Nuñez et al., 2017). Hot dust is typically close to a star's sublimation radius in primarily submicron grains (Kirchschlager et al., 2017) which should rapidly be ejected from the system by radiation pressure, such that its presence is difficult to explain.

Warm (~ 300 K) dust lies close to the habitable zone and produces mid-infrared emission (e.g. Ertel et al., 2020). The origin of dust so close to the star poses problems due to the high collision rates, and thus short dust lifetimes, at these distances. The levels of warm dust are usually measured in units of zodis, where one zodi corresponds to the surface density of the zodiacal cloud at 1 au (Kennedy et al., 2015). Detected warm exozodiacal clouds are orders of magnitude brighter than our Solar System's zodiacal cloud, with levels ranging from 50 to > 1000 zodis. While one might expect a correlation between the presence of hot and warm dust if the hot dust is being transported inwards, surveys suggest they are not connected (Absil et al., 2021). This thesis will focus on understanding the origin of warm, habitable zone dust, which produces mid-infrared thermal emission.

Warm exozodis are of particular interest as their presence in the habitable zone makes them a key source of photon noise in future missions to detect and characterise Earth-like planets. As technology improves, it may be possible to image and take atmospheric spectra

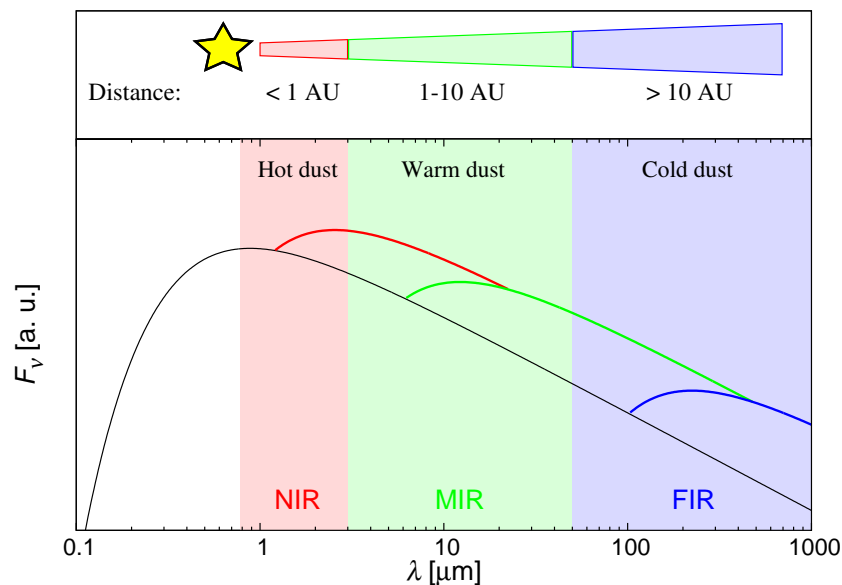


Fig. 1.6 Illustration of how hot, warm, and cold dust contribute to a star's SED as excess emission at different wavelengths, assuming a solar-type star (Kirchschlager et al., 2017).

of potentially habitable Earth-like planets. In reflected light, this requires an extremely high contrast of 10^{-10} , which could be achieved with a > 4 m space telescope operating in the ultraviolet to near-infrared wavelength range with either a coronagraph or starshade to block stellar emission (e.g. The LUVOIR Team, 2019; Gaudi et al., 2020). Alternatively, a space-based mid-infrared nulling interferometer with formation-flying spacecraft would only require a contrast of $\sim 10^{-7} - 10^{-6}$ to image an Earth-like planet in thermal emission, and would provide complementary constraints on biomarkers (Quanz et al., 2021a,b). The levels of exozodiacal dust around other stars will affect the yield of such exo-Earth missions, and influence decisions about the best mission architectures (Figure 1.7). For future direct imaging missions, levels of even ten zodis may hinder exo-Earth imaging (Roberge et al., 2012), while mid-infrared nulling interferometry will be impeded by around 15 zodis (Defrère et al., 2010). This also depends on the inclination of the exozodi: exozodis which are more inclined to the line of sight will be more problematic, as the emission is concentrated on a smaller region of the sky. They will also impede characterisation of Earth-like planets and the search for life, with detection of various biosignatures impacted (Coker et al., 2018). Moreover, if planets lie in the habitable zone, dynamical interactions with the dust will produce asymmetric features such as resonant rings and clumps, which will be a source of confusion for planet searches (Stark and Kuchner, 2008; Defrère et al., 2012). However, these clumps could also act as signposts of unseen planets. An understanding of exozodiacal dust is therefore crucial to the design of future missions to find and characterise Earth-like planets (Stark et al., 2015, 2019).

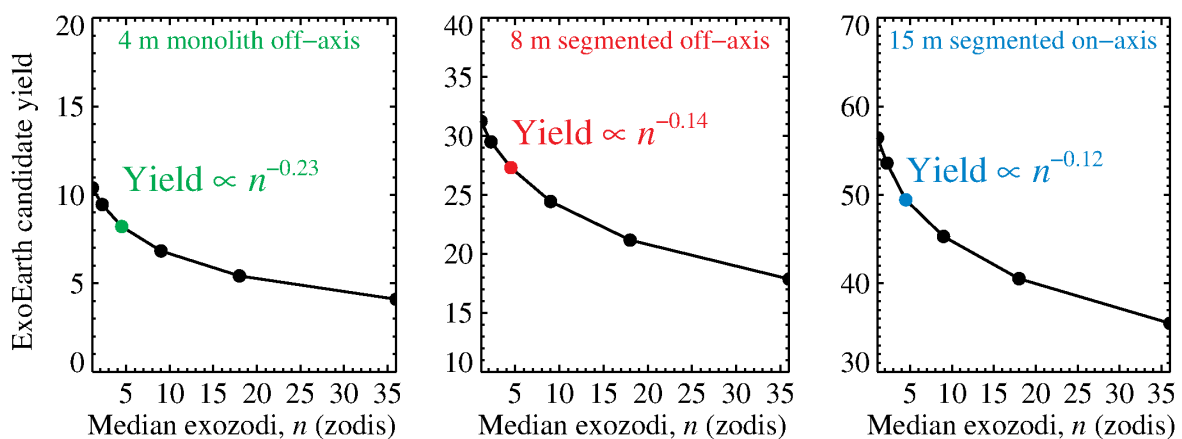


Fig. 1.7 The effect of different levels of exozodiacal dust on the yield of a future exo-Earth imaging mission for several mission architectures (Stark et al., 2019).

Studying exozodis also provides information about the innermost regions of planetary systems, complementary to studying cold planetesimal belts. Knowing the distribution of dust close to the star may allow us to place constraints on the planetary system. For example,

if the dust is being dragged inwards from a cold outer belt, this can rule out the presence of larger intervening planets, which would accrete or eject the dust before it could reach the habitable zone (Bonsor et al., 2018).

Additionally, exozodis can inform us about the habitable zone environment around other stars. For instance, constraints could be placed on the presence and activity of comets in the habitable zone. Such bodies may bombard any planets in the inner planetary system, either delivering volatiles which could lead to the development of life, or depleting their atmospheres (Kral et al., 2018; Wyatt et al., 2020). Indeed, it is thought that volatiles and the ingredients for prebiotic chemistry may have been delivered to Earth by impacts (e.g. Chyba et al., 1990) or accretion of cosmic dust (Ritson et al., 2020). Formation of prebiotic chemicals on Earth may have been catalysed by accretion of carbonaceous chondrite meteorites (Rotelli et al., 2016). It is possible that Earth may have formed dry, with its water delivered by comets and asteroids (Raymond et al., 2009; O'Brien et al., 2014). Understanding cometary bombardment in other planetary systems is thus important to the search for life. Exozodis provide a way to constrain the presence of exocomets, which may determine the habitability of planets in the system.

1.5.1 Observations of exozodiacal dust

Warm exozodiacal dust was first detected around main sequence stars using high-precision photometry in the mid-infrared. Surveys with the Infrared Astronomical Satellite (IRAS, Mannings and Barlow, 1998; Gaidos, 1999; Fajardo-Acosta et al., 2000) at $12\ \mu\text{m}$ and the Infrared Space Observatory (ISO, Laureijs et al., 2002) at $25\ \mu\text{m}$ suggested bright warm discs are relatively rare, with detection rates of 3% and 6% respectively. Using the Infrared Spectrometer (IRS) on the Spitzer Space Telescope, Lawler et al. (2009) did not find excess emission at $8.5\text{--}12\ \mu\text{m}$ around any of a sample of 152 stars, estimating only $1 \pm 0.7\%$ of stars have excess mid-infrared emission at the given sensitivities. The Wide-field Infrared Survey Explorer (WISE) observations at $12\ \mu\text{m}$ were sensitive to excesses of $\gtrsim 15\%$, and detected these around 0.1% of stars (Kennedy and Wyatt, 2013).

The exozodi luminosity function (Figure 1.8) characterises the occurrence rate of different levels of exozodiacal dust around other stars. All detected exozodis are brighter than the zodiacal cloud, which corresponds to an excess of $\sim 5 \times 10^{-3}\%$ (Kennedy et al., 2015). Fainter exozodis are difficult to detect against the stellar photosphere due to uncertainties with calibration and the photospheric models, such that the sensitivity of photometry is limited to 10% of the stellar flux. Interferometry gives much better spatial resolution than photometry, allowing the dust emission to be separated from that of the star such that much fainter excesses can be detected, at levels $\lesssim 1\%$. More recent surveys therefore use

nulling interferometry (Hinz et al., 1998, 2000) to resolve emission close to the star with better sensitivity, a technique which was first proposed by Bracewell (1978); Bracewell and MacPhie (1979). The beams from two telescopes are combined in phase opposition, such that a dark fringe appears along the line of sight, cancelling out the stellar emission. Fringes are produced with spacing λ/B , where B is the baseline length and λ the wavelength of observation. The null depth, given by the ratio of the flux measured in destructive and constructive interference, gives high-angular resolution information of the observed object. This essentially corresponds to a fractional excess, modulated by the transmission pattern of the interferometer. Previously the Keck Interferometer Nuller (KIN, Colavita et al., 2009; Serabyn et al., 2012) studied 47 nearby main sequence stars (Millan-Gabet et al., 2011; Mennesson et al., 2014), and found five had an 8–9 μm excess at a sensitivity of 150 zodis, equivalent to an excess of $\sim 1\%$. Mennesson et al. (2014) also found a higher detection rate of warm dust around stars known to harbour cold dust with far-infrared excesses.

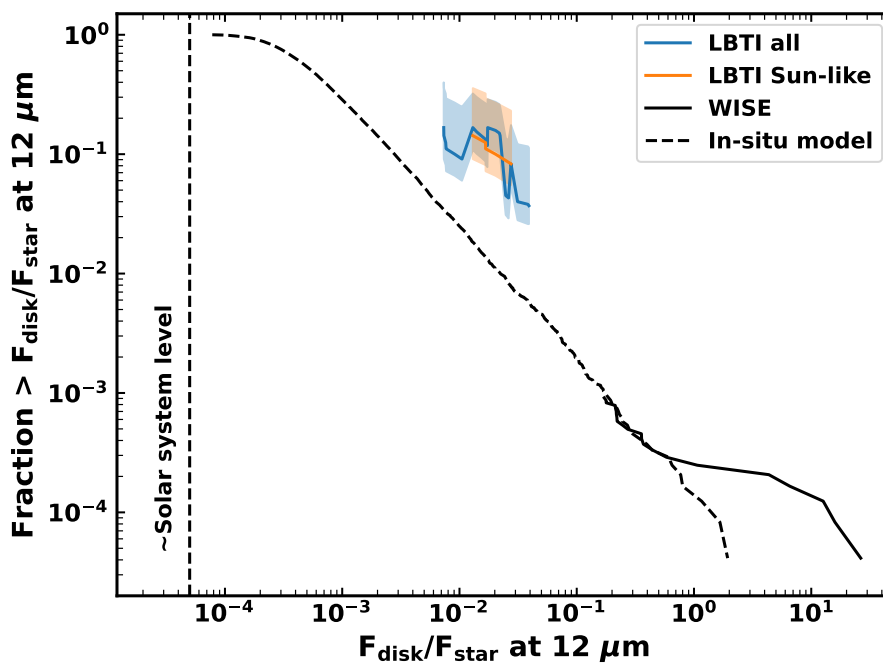


Fig. 1.8 The exozodi luminosity function, which shows the fraction of stars which have a given level of 12 μm excess emission from observations with WISE and LBTI. This is compared to predictions from an in situ model (Kennedy and Wyatt, 2013). Figure adapted from Ertel et al. (2018a).

The most recent data for warm exozodiacal dust come from NASA’s Hunt for Observable Signatures of Terrestrial planetary Systems (HOSTS, Ertel et al., 2018a, 2020) survey, which used nulling interferometry in the N band (11 μm) with the Large Binocular Telescope

Interferometer (LBTI, Hinz et al., 2014; Defrère et al., 2016). LBTI is a nulling interferometer which is sensitive to warm dust down to the level of a few zodis, equivalent to a null excess of $\sim 0.05\%$. Out of 38 nearby main sequence stars, ten (26%) had significant excesses at a sensitivity which decreases from around 50 zodis for Sun-like stars to 20 zodis for early-type stars. The survey aimed to constrain the distribution of warm dust around nearby main sequence stars to ascertain how problematic such dust will be for future missions to detect Earth-like planets. The median level of exozodiacal dust around other stars was constrained to have a best-fit value of 3 zodis, and be < 27 zodis at the 95% limit. Similar to KIN, the HOSTS survey found a strong correlation between the presence of warm and cold dust. Of the nine systems with known outer belts, seven also had exozodiacal emission, suggesting habitable zone dust may be transported inwards from an outer belt. However, it should be noted that warm exozodis can also be detected in systems without known outer belts. For example, three of the detections in the HOSTS survey do not show excess far-infrared emission. Furthermore, HD 69830 (Beichman et al., 2005) has an exozodi level of > 1000 zodis without a detected belt. No correlation was found between warm dust and the presence of hot dust, or the age and spectral type of the star. Even stars with ages of several Gyr can harbour significant levels of warm dust. Of particular note is η Corvi, a 1.4 Gyr old F2V star which has warm dust 2000 times brighter than our zodiacal cloud (Defrère et al., 2015; Lebreton et al., 2016).

1.5.2 Origins of exozodiacal dust

The canonical debris disc model of a planetesimal belt collisionally grinding down to produce dust co-located with the belt is not usually able to explain exozodiacal dust. Belts so close to the star have short collisional timescales due to the higher collision velocities, such that they are depleted too quickly to be seen around stars older than a few tens of Myr (Wyatt et al., 2007a). While some exozodis can be explained by an in situ planetesimal belt (Geiler and Krivov, 2017), particularly for those found in young systems, this is not always the case (see, e.g. Lebreton et al., 2013). A two-component model (Kennedy and Wyatt, 2013), which combines in situ belts with collisions at random times during a star's lifetime, underpredicts the occurrence of exozodiacal dust at fainter levels (Figure 1.8). The presence of exozodiacal dust therefore requires an alternative mechanism which can either supply dust at a high rate, or increase its lifetime close to the star.

Several scenarios have been proposed for the origin of warm exozodiacal dust, and it's possible that different systems fit into different mechanisms. For young (< 120 Myr) stars, the collisional lifetime of an in situ belt can be longer than the age of the star, such that it is possible that the dust is produced in situ by an asteroid belt (Wyatt et al., 2007a).

Alternatively, warm exozodis around very young (< 100 Myr) stars could be signatures of terrestrial planet formation. It is expected that during this period, giant impacts similar to the Moon-forming collision will be frequent (e.g. Kenyon and Bromley, 2006). Such collisions would produce large quantities of dust in the habitable zone, and thus significant mid-infrared emission. For example, Jackson and Wyatt (2012) simulated debris created in the Moon-forming giant impact. Assuming 30% of the debris is mm–cm-sized vapour condensates, and 70% is large planetesimals up to 500 km in size, they find that dust produced by collisions of the planetesimals should be detectable at $24 \mu\text{m}$ for 25 Myr. Kral et al. (2015) model the dynamical and collisional evolution of dust released in a massive collision of two asteroids at several au from a star, showing the resulting distribution of dust is asymmetric, with an overdensity at the impact point, and should be detectable at $24 \mu\text{m}$ with the James Webb Space Telescope (JWST) for several Myr. Genda et al. (2015) showed that giant impacts during terrestrial planet formation should produce $\sim 0.4M_{\oplus}$ of debris in total, and can explain the $24 \mu\text{m}$ excesses for most warm exozodis with ages 10–100 Myr.

Given the correlation between the presence of warm and cold dust, it is possible that dust migrates inwards from a cold outer belt to the habitable zone due to P-R drag. If dust is being produced in a collisional cascade, it is inevitable that the dust will drift inwards by P-R drag unless something else inhibits it. Indeed, $\sim 1\%$ of dust in the zodiacal cloud may migrate in from the Kuiper belt (Moro-Martín and Malhotra, 2003). For example, Kennedy and Piette (2015) used a simple analytical model to show that detectable amounts of dust should be dragged in from known debris discs. Its inevitability means that non-detections of warm exozodis in systems with debris discs may imply the presence of intervening planets which accrete or eject the dust before it reaches the habitable zone (Bonsor et al., 2018). Other mechanisms may be able to extend the lifetime of dust migrating in via P-R drag, enhancing the levels of warm dust. If large enough quantities of gas are present in the inner planetary system, gas drag may oppose inward migration by P-R drag, trapping dust at a certain location close to the star, as proposed for hot dust (Lebreton et al., 2013; Pearce et al., 2020). Particles drifting inwards under P-R drag may get trapped in mean motion resonances (MMRs) with any planets in the system (Shannon et al., 2015), extending their lifetime. In the Solar System, trapping in resonances creates clumps such as Earth’s resonant ring (Dermott et al., 1994; Reach et al., 1995; Reach, 2010) and a ring just outside the orbit of Venus (Leinert and Moster, 2007; Jones et al., 2013).

It is possible that some systems may be observed while they are undergoing a dynamical instability, in which the planetary system goes unstable and scattering between giant planets causes many planetesimals to be scattered into the inner planetary system, similar to the purported Late Heavy Bombardment (LHB) of the Solar System. Booth et al. (2009) modelled

the effect the LHB would have on the Solar System, as seen by a distant observer. They showed that LHB-like events produce an enhancement of dust in the inner regions, which causes significant increases in mid-infrared emission that are detectable for 30 Myr. Bonsor et al. (2013) used a suite of N-body simulations to show that while dynamical instabilities cause high levels of excess emission, the effect is short-lived, lasting only several Myr. Even if every planetary system goes unstable at some point in its lifetime, the effect is too short-lived to explain the occurrence of exozodiacal dust. However, it may be the source for some individual systems with warm dust.

Warm dust could also be fed by inward scattering of planetesimals in a more steady-state scenario. Comets being scattered into the inner planetary system from an outer belt may sublimate or fragment to replenish the exozodiacal dust in situ. This is highly dependent on the planetary system architecture, and several studies have investigated the optimal architecture for a high influx of comets (Bonsor and Wyatt, 2012; Bonsor et al., 2012; Wyatt et al., 2017; Marino et al., 2018). These found that a chain of low-mass ($10s M_{\oplus}$), closely-spaced planets is needed to scatter in enough comets. While this is a plausible scenario, it requires contrived planetary system architectures, and these studies did not consider the production of dust by comets. Marboeuf et al. (2016) developed a thermo-physical model of comets, suggesting comet sublimation may create observable exozodiacal emission. Another question is how to sustain the emission over the lifetime of older (> 100 Myr) stars, which requires comets to be scattered inwards continually. Bonsor et al. (2014) proposed a mechanism in which the outermost planet in a chain migrates outwards into the outer belt due to inward scattering of planetesimals, which then sustains the inward planetesimal scattering rate over Gyr timescales (Figure 1.9). If planets don't migrate, they should deplete the available material too quickly to explain exozodis around Gyr stars. Alternatively, Faramaz et al. (2017) suggested that if there is a moderately eccentric ($e > 0.1$) planet exterior to the belt, it could place planetesimals on highly eccentric orbits if its MMRs overlap with the belt. Planetesimals trapped in inner MMRs of the planet have their eccentricities pumped up by the planet (Beust and Morbidelli, 1996) and get scattered inwards. This only requires a single planet, and delays the scattering by several 100 Myr, providing a potential explanation for excesses around older stars. Inward comet scattering is a promising scenario, but places stringent constraints on the planetary system. Further, the parameter space of possible planetary system architectures is so vast that it is difficult to explore in order to find the optimal architecture for scattering material to the inner regions.

In the future it may be possible to distinguish between these scenarios by accurately measuring the exozodi luminosity function (Figure 1.8) over a wider range of excess levels. However, this will require hundreds of detections, while at present only tens of warm exozodis

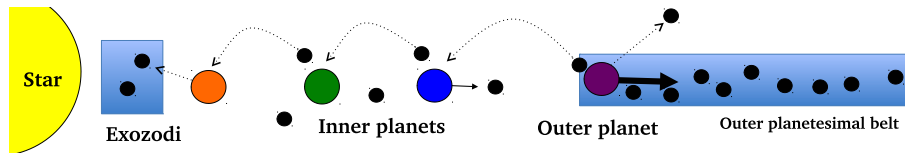


Fig. 1.9 Diagram showing planetesimals being scattered inwards by a chain of planets. Exchange of angular momentum with the planetesimals causes the outermost planet to migrate outwards into the belt, sustaining the influx of planetesimals (Bonsor et al., 2014).

are known due to the sensitivity of current instruments. Models make different predictions for the brightness levels and radial profiles of dust, which can be compared to resolved observations to determine the underlying source for individual systems. It is likely that different systems will fit into different origin scenarios depending on the planetary system's parameters.

1.6 Thesis structure

The focus of this thesis is to model the origin and evolution of warm exozodiacal dust, which resides in the habitable zones of other stars. Application of models to the Solar System is used to calibrate my models, but the focus is on exoplanetary systems. In Chapter 1, I have outlined the relevant background from studies of debris discs around other stars and the Solar System. In Chapter 2, I present an analytical model for the size and spatial distribution of dust grains in debris discs when dust grains are produced by collisions in an outer belt, and migrate inwards due to P-R drag. This is calibrated against numerical debris disc simulations which use a kinetic model. The model provides a method for predicting the levels of dust dragged into the inner planetary system by P-R drag. In Chapter 3, this analytical model is used to make such predictions for real planetary systems. By applying the model across the parameter space of potential planetesimal belts, I show the levels of exozodiacal emission expected from belts with different properties. The model is then applied to the stars from the HOSTS survey with outer belts to determine whether P-R drag can explain observed exozodiacal clouds. Finally, I apply the P-R drag model in more depth to LBTI observations of β Leo, a young A star with significant levels of warm exozodiacal dust. In Chapter 4, I develop a model for the distribution of zodiacal dust produced by spontaneous fragmentation of Jupiter-family comets. This couples a numerical model for the dust produced by comet fragmentation to a kinetic dust model, taking into account the effects of P-R drag, catastrophic collisions, and radiation pressure. I show that comet fragmentation can produce the correct size and spatial distribution of zodiacal dust, supporting theories that comet disruptions are the dominant source of the zodiacal cloud. I also demonstrate that cometary input to the zodiacal cloud

should be stochastic due to variations in the sizes and dynamical lifetimes of comets scattered into the inner Solar System. In Chapter 5, the numerical comet fragmentation model of Chapter 4 is developed further to be applied to exoplanetary systems. This model can be used to predict the distribution of exozodiacal dust which comets should produce in the presence of different planetary system architectures. Finally, in Chapter 6, I summarise the results of the thesis and give my conclusions.

Chapter 2

Dust size and spatial distributions in debris discs

Abstract

In this chapter, I present an analytical model for the size distribution of particles at different radial locations in a debris disc. This assumes the canonical model of a debris disc, in which dust grains are produced by collisions within a planetesimal belt. The grains then migrate inwards due to the effects of P-R drag while undergoing mutual collisions. Results from more accurate but computationally expensive numerical simulations of this process are used to validate the model and fit its free parameters. The model predicts $11\ \mu\text{m}$ excesses for discs with given dust masses and planetesimal belt radii. It improves on previous P-R drag models by finding the two-dimensional size and spatial distribution, allowing realistic grain properties to be used. The model can be applied to mid-infrared observations to predict the levels of exozodiacal dust which should be dragged into the inner planetary system from a planetesimal belt with given parameters, as demonstrated in Chapter 3.

2.1 Introduction

About 20% of main sequence stars show far-infrared excesses, indicating the presence of circumstellar dust orbiting at tens or hundreds of au, known as debris discs. Observations of stars in the mid-infrared show the presence of warm, exozodiacal dust in many systems, at closer proximity to the star than a standard debris disc. Most recently, the HOSTS survey (Ertel et al., 2020) searched 38 nearby main sequence stars for exozodiacal dust using LBTI at $11\ \mu\text{m}$, with a detection rate of 26%.

The origin of warm exozodiacal dust is still not well understood. In the habitable zone, the collisional lifetimes of planetesimal belts are typically too short to survive for the age of the star (Wyatt et al., 2007a). Some exozodis may be explained by transient phenomena, such as a dynamical instability similar to the purported Late Heavy Bombardment (LHB) of the Solar System, which can produce a short-lived enhancement of dust close to the star (Booth et al., 2009; Bonsor et al., 2013). Some bright exozodis may also be explained by recent collisions of large planetesimals similar to the Moon-forming impact (Jackson and Wyatt, 2012; Kral et al., 2015). However, such events cannot explain a phenomenon as common as 26%. Another possibility is that exozodiacal dust is produced in a cold outer planetesimal belt, and transported into the inner regions of the planetary system, either by P-R drag (Kennedy and Piette, 2015) or comet delivery (e.g. Bonsor et al., 2012; Faramaz et al., 2017). The HOSTS survey found a higher occurrence rate of exozodiacal dust around stars with known far-infrared excesses which imply the presence of a cold debris disc (Ertel et al., 2020).

Given the potential correlation of the presence of cold and warm dust, it is important to explore the viability of transport of dust from an outer planetesimal belt as a source of the observed exozodiacal dust. The full distribution of grains created in a planetesimal belt, including all grain sizes and distances to the star, can be studied numerically. For example, ACE (Krivov et al., 2005, 2006, 2008; Reidemeister et al., 2011) finds the distribution of particles in phase space based on the gain and loss of particles to collisions and drag, with simplified dynamics. Similarly, van Lieshout et al. (2014, hereafter V14) produced a numerical model of the evolution of particles in a debris disc, including the effects of collisions, P-R drag, and sublimation. However, numerical methods such as these models are computationally expensive, meaning they are less straightforward to implement than a simple analytical model and are more time-consuming.

A simple analytical prescription for the process of P-R drag transporting dust inward from a planetesimal belt exists, but is only approximate. For example, Mennesson et al. (2014) showed consistency between observations with KIN and the simple analytical prescription of Wyatt (2005) for the interplay of collisions and P-R drag. A modified version of the Wyatt (2005) model was used by Kennedy and Piette (2015) to predict the levels of dust transported inwards from Kuiper belt analogues by P-R drag. They found that LBTI, which probes lower excess levels, should be able to detect this component of dust brought inwards by P-R drag for systems with known Kuiper belt analogues, and that it may detect such dust for some systems with no detectable parent belt. Nevertheless, this model was still inaccurate, and only considered a single grain size, moreover assuming the grains were black bodies.

This provides the motivation for this chapter, which aims to produce an analytical model that considers all particle sizes, rather than only grains just above the blowout size, to give a distribution of dust for a system with an outer planetesimal belt evolving via collisional evolution and P-R drag. The size distribution is described in terms of geometrical optical depth, defined such that $\tau(D, r)dD$ is the cross-sectional area surface density in particles of size $D \rightarrow D + dD$ at radius r . Combining the approach of Wyatt et al. (2011) for the size distribution of a planetesimal belt at a single radial distance with Wyatt (2005) for the radial profile of a given particle size produces a two-dimensional distribution. Results from the analytical model are validated against the numerical model of V14 to show how it can predict two-dimensional distributions in debris discs, and to find the limitations of the analytical model. This gives predictions for the levels of dust transported to the inner regions of a planetary system. Realistic grain properties can be applied to find the corresponding flux, and so the model can be used to assess whether this scenario could explain the observed mid-infrared excesses of exozodis, such as those found by LBTI.

In this chapter, I present the analytical debris disc model which includes collisions and P-R drag. I briefly summarise the numerical model of V14 and my numerical results in Section 2.2, then describe my analytical model in Section 2.3. In Section 2.4 I compare the predictions of my analytical model with results from the numerical model in order to fit the model parameters before exploring the parameter space in Section 2.5. A toy model of the zodiacal cloud using the analytical model is presented in Section 2.6, and my conclusions are given in Section 2.7.

2.2 Numerical Model

The numerical model of V14 considers the evolution of a belt of planetesimals and the debris created when they are destroyed in mutual collisions. It self-consistently takes into account the effects of collisions, P-R drag, and sublimation on these particles. This model uses a statistical method based on that of Krivov et al. (2005, 2006), applying kinetic theory to obtain the spatial and size distribution of particles in a phase space of orbital elements and particle masses. The phase space is over orbital eccentricity e , periastron distance q , and particle mass m ; other orbital elements are averaged over under the assumption that the disc is axisymmetric. It is assumed that there is a uniform distribution of particles over inclination.

The continuity equation is solved numerically to find the number of particles in each phase space bin at successive times. P-R drag and sublimation act as diffusion terms which shift particles to adjacent phase space bins. For these processes orbit-averaged equations are used, assuming that the relevant timescales are longer than an orbital period. Only particles at

< 0.02 au are affected by sublimation around a Sun-like star, and the minimum distance used here is 0.03 au. Sublimation is therefore ignored throughout this chapter, as the focus is on the overall distribution, rather than the innermost edge of the disc. Sublimation would, however, be very important when studying hot exozodiacal dust, which gives rise to near-infrared excesses. My model is only aimed at explaining warm exozodis, for which sublimation is less important.

Collision rates are calculated between pairs of phase-space bins according to analytical equations from Krivov et al. (2006), including the number densities of the particles, their relative velocity, collisional cross-section, and effective volume of interaction. The outcome of collisions is determined by the impact energy per unit mass: if this exceeds the critical specific energy, Q_D^* , the collisions are destructive such that the largest fragment has at most half the mass of the target particle. Cratering collisions, which have specific energy below Q_D^* , are not considered by the model. When two particles collide, their mass is redistributed amongst the bins according to a redistribution function, which is a power law $n_r(D) \propto D^{-\alpha_r}$, where D is particle diameter. Integrating this redistribution function gives the number of particles which go into each bin, up to a maximum mass determined by the specific energy. The orbital elements of collision fragments are determined based on conservation of momentum and the effects of radiation pressure. If a particle has a mass below the lowest mass bin, it is considered lost due to blowout.

The strength of radiation pressure acting on particles of a given size is determined by the ratio of radiation pressure to gravity acting on a particle:

$$\beta = \frac{F_{\text{rad}}}{F_{\text{g}}} = \frac{3L_{\star}Q_{\text{pr}}}{8\pi GM_{\star}cD\rho}, \quad (2.1)$$

where L_{\star} is the stellar luminosity, M_{\star} is stellar mass, ρ is particle density, and c is the speed of light. Q_{pr} is the radiation pressure efficiency averaged over the stellar spectrum, which is a function of particle size; this can be found numerically given assumptions about the dust composition and stellar spectrum (see Section 2.2.2). Grains released from parent bodies on circular orbits will have eccentricities $e = \beta/(1 - \beta)$, and will be blown out of the system on hyperbolic orbits when $\beta \geq 0.5$. From this, I can estimate the smallest particle size which can remain bound, under the assumption of $Q_{\text{pr}} = 1$, such that grains are perfect absorbers, as

$$D_{\text{bl}} = \frac{3L_{\star}}{4\pi GM_{\star}c\rho}. \quad (2.2)$$

It would be computationally expensive to model the entire collisional cascade from km-sized planetesimals down to sub-micron grains, so only particles $0.1 \mu\text{m} < D < 2 \text{ cm}$ are

modelled. The largest bodies will remain confined to the planetesimal belt, with negligible P-R drag, producing dust via collisions. This is taken into account with a source of dust in the belt, which mimics the production of grains by larger bodies, replenishing the dust in the belt each time step with a differential size distribution of slope -3.5. The model is run from an initially empty disc until steady state is reached, such that the distribution changes by less than 1% in a logarithmic time step. For a very massive, collisional disc it takes 10 Gyr to reach steady state due to the time taken by the largest particles to migrate inwards from the belt via P-R drag, as the migration timescale is proportional to particle size. However, the smallest, barely-bound grains will be in steady state after ~ 10 Myr, and dominate the optical depth. The time taken to reach steady state increases as disc mass is decreased, and the least massive disc considered here takes 10^{14} yr to reach steady state at < 1 au. The optical depth of the lowest mass discs is dominated by larger grains, which take longer to evolve inwards. While this is an unrealistically long time, the time taken to reach steady state would likely be shorter with alternative initial conditions. The starting conditions chosen here assume an initially empty disc. It may be more realistic for the disc to start with dust spread throughout the system and so closer to steady state, which would lead to shorter convergence times. In terms of computing time, it takes about a week on a standard desktop. The output of the numerical model is a steady-state distribution of particles in the phase space of orbital elements and particle masses, which can be converted to a distribution over radial distance and particle size via Haug's integral (Haug, 1958).

2.2.1 Model inputs

The inputs to the model include the radius of the parent belt r_0 , stellar mass M_* and luminosity L_* , the semi-opening angle of the disc ϵ , and the slope of the redistribution function α_r . The critical specific energy for catastrophic collisions follows a combination of power laws to represent the strength and gravity regimes as $Q_D^* = Q_a D^{-a} + Q_b D^b$, with the parameters of the power laws being inputs. The overall level of dust in the source belt is set with an input parameter which is the mass supply rate of dust in the belt from collisions of large bodies, \dot{M}_{in} . The mass from the break-up of the largest bodies is distributed according to the redistribution function of collisional fragments $n_r(D)$ across the range of sizes considered, down to the blowout size. The model also takes the grain density ρ , as well as values of β for different particles sizes (see Section 2.2.2).

Typically it is assumed that the slope of the redistribution function is in the range $3 < \alpha_r < 4$, so $\alpha_r = 3.5$ is used. The effect of varying α_r is studied in Section 2.5.4. All particles which are modelled are small enough such that they are in the strength regime of Q_D^* . Laboratory experiments with high-velocity collisions of small particles find a constant

value of $Q_D^* = 10^7 \text{ erg g}^{-1}$ (Flynn and Durda, 2004), which is used for ease of comparison between models. Section 2.5.3 investigates the effect of using a power law for Q_D^* . Most of the simulations are for a Sun-like star, $M_* = M_\odot$, $L_* = L_\odot$, and a disc semi-opening angle (equivalent to the maximum orbital inclination of particles) of $\varepsilon = 8.5^\circ$. Particles initially have a uniform distribution of eccentricities from 0 to 0.1. The fiducial value for the belt radius is $r_0 = 30 \text{ au}$, and for the mass input rate is $\dot{M}_{\text{in}} = 10^{-15} M_\oplus \text{ yr}^{-1}$, though a range of values is considered for each.

A similar phase space grid is used to that of V14. For eccentricity, the grid has ten logarithmically spaced bins for $0 \leq e \leq 1$, for which the lowest bin is at $e = 10^{-4}$, with two linear bins each for hyperbolic orbits ($1 \leq e \leq 2$) and the anomalous hyperbolic orbits of $\beta > 1$ grains ($-2 \leq e \leq -1$). The periastron grid has 60 logarithmic bins from $q = 0.03 \text{ au}$ to $q = 100 \text{ au}$ for the fiducial model, which has a belt at $r_0 = 30 \text{ au}$. The mass grid has logarithmic bins, with higher resolution for the smallest particles. There are 45 high resolution bins from $D = 0.1 \mu\text{m}$ to $D = 20 \mu\text{m}$, with 18 low resolution bins going up to the maximum size $D = 2 \text{ cm}$.

2.2.2 Optical properties

Optical properties of the grains are calculated using the same method as Wyatt and Dent (2002), with compositions from the core-mantle model of Li and Greenberg (1997), first used for interstellar dust, which can also be used for dust in debris discs (Li and Greenberg, 1998; Augereau et al., 1999). This model assumes fluffy aggregates with a silicate core and organic refractory mantle. Grains are nominally assumed to be asteroidal, such that they have volume fractions of 1/3 amorphous silicate and 2/3 organic refractory material with zero porosity, which gives a dust density of $\rho = 2.37 \text{ g cm}^{-3}$. Alternative compositions are considered later in the paper. The radiation pressure efficiency Q_{pr} and absorption efficiencies $Q_{\text{abs}}(\lambda, D)$ are calculated using Mie Theory (Bohren and Huffman, 1983), Rayleigh-Gans theory, or geometric optics, depending on the wavelength (Laor and Draine, 1993). Given Q_{pr} , realistic values of β can be found for use in the numerical model. For the assumed asteroidal composition, the blowout size (i.e. that for which $\beta = 0.5$) is found to be $D_{\text{bl}} \sim 1.5 \mu\text{m}$ around a Sun-like star. Grain temperatures $T(D, r)$ and absorption efficiencies $Q_{\text{abs}}(\lambda, D)$ are used when predicting fluxes from distributions of dust (Section 3.2).

2.2.3 Numerical results

The left column of Figure 2.1 shows the results of simulations for belts with the standard values of Sections 2.2.1 and 2.2.2, but with mass input rates varying from 10^{-18} to

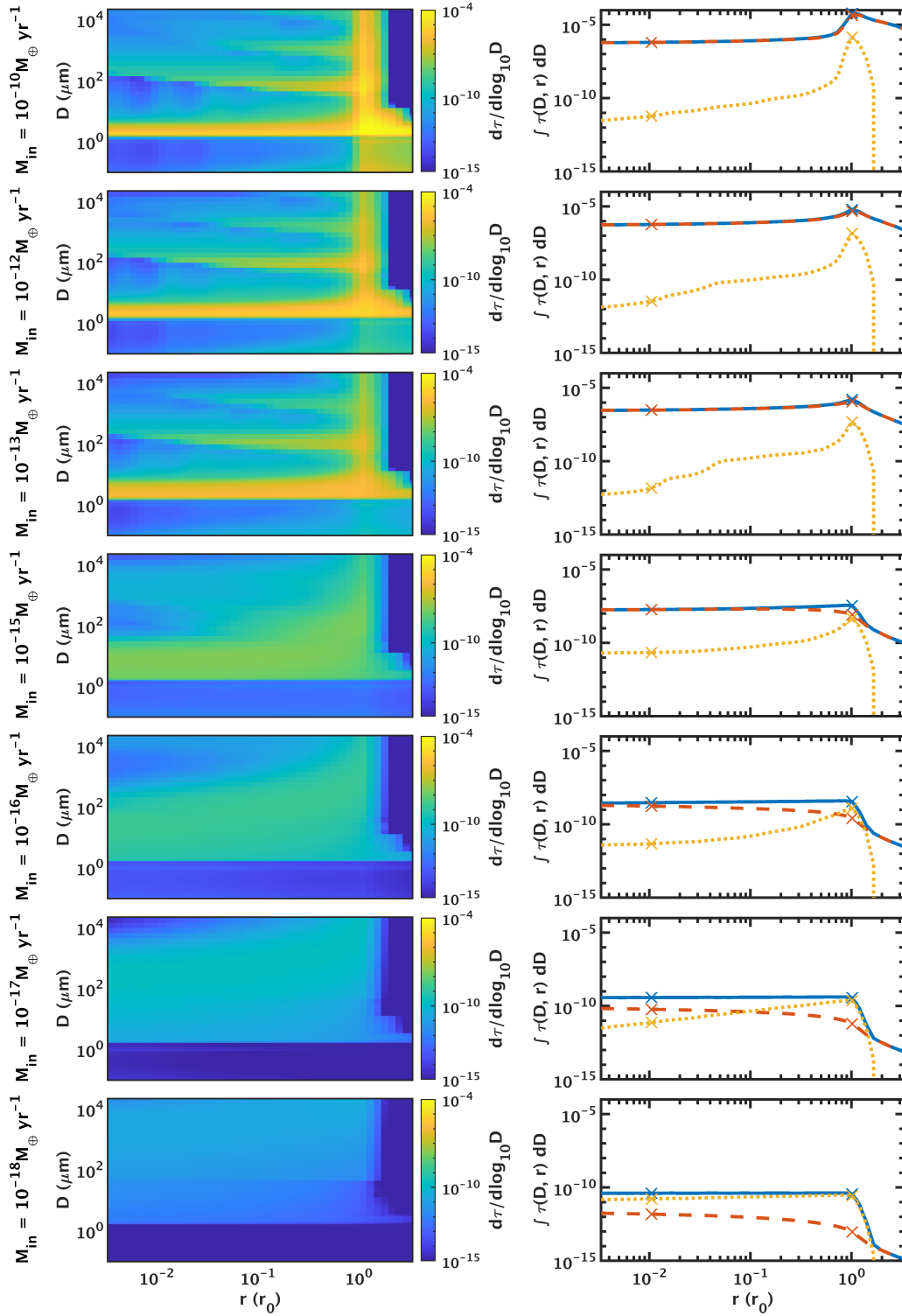


Fig. 2.1 Left: two-dimensional size distribution of particles over size and radial distance from the numerical model of V14 for discs with different dust mass input rates and a belt radius of 30 au. The colour scale gives the optical depth per unit size decade. Right: radial distribution of optical depth integrated over different size ranges: all particles (blue), barely bound grains (orange, dashed), and cm-sized particles (yellow, dotted). Markers show the values close in to the star ($0.01r_0$) and in the belt, which are used later to characterise the behaviour of the model.

$10^{-10} M_{\oplus} \text{ yr}^{-1}$. The colour scale shows the geometrical optical depth per unit size decade, $d\tau/d\log_{10} D$, as a function of both particle size D and radial distance relative to the belt radius r_0 .

Some characteristics are seen at all disc masses, such as a concentration of dust at r_0 with a drop off outside of the belt, while the smallest grains are put onto highly eccentric orbits by radiation pressure, forming a halo at larger radii. Plots are truncated at a radius of $3r_0$, as this study is not focussed on modelling the halo. In all cases grains below the blowout size, $D_{\text{bl}} \sim 1.5\mu\text{m}$, are blown away by radiation pressure such that their contribution is negligible. Grains below the blowout size are present in the belt, where they are produced, and in the halo as they are blown out, with a density which is proportional to the mass input rate. However, these grains do not contribute significantly to the optical depth overall as they are orders of magnitude lower than other grain sizes in the belt. As disc mass is decreased, the discs evolve from being collisional to being dominated by P-R drag, which is reflected by a flattening of the radial distribution.

Where particles are collisional, they are destroyed by collisions before they have a chance to migrate in towards the star, such that their optical depth is heavily depleted inwards of the belt. A characteristic wavy pattern is seen in collisional discs. This is a well-known phenomenon in the size distributions of collisional cascades (see, e.g. Campo Bagatin et al., 1994; Durda and Dermott, 1997; Thébault et al., 2003; Krivov et al., 2006) which is caused by the truncation of the size distribution below D_{bl} , where particles get blown away by stellar radiation. The lack of particles just below D_{bl} means that particles just above the cutoff are not destroyed by collisions due to a lack of impactors, causing an increase in their numbers. This increased number of particles just above D_{bl} then breaks up larger particles faster, causing them to be more depleted than in an infinite cascade, and so on. Within the belt the size distribution follows the standard result for a collisional cascade (Dohnanyi, 1969), such that $n(D) \propto D^{-\alpha}$, with a slope of $\alpha = 3.5$. The wavy pattern is then superposed on this size distribution, and the pattern also extends inwards of the belt since collisions continue to operate on the dust as it is dragged into the inner regions. The barely bound grains just above D_{bl} dominate the optical depth and have a flatter radial profile than larger grains.

For the lowest disc masses, P-R drag is the dominant loss mechanism, and particles migrate inwards while suffering very few collisions. This gives radial profiles which are almost flat, although the largest particles still see a small amount of depletion due to collisions. In these cases, the particle size which dominates the optical depth is the largest particle size which is not significantly depleted by collisions. As expected, the overall number and mass of particles also decreases as mass input rate decreases, leading to lower total cross-section.

The waves seen in the distributions cannot be modelled analytically, so to better compare the numerical and analytical models I also consider the optical depth integrated over decades of particle size to smooth over the waves. The right hand column of Figure 2.1 shows the radial distribution of integrated optical depth. This is shown for three different size ranges: the total optical depth, small grains which are barely bound ($D_{bl} < D < 20\mu\text{m}$), and the largest particles ($2\text{ mm} < D < 2\text{ cm}$). For the most massive discs, the total optical depth is very close to that from the smallest particles, which is due to grains just above the blowout size dominating the cross-section. Larger particles are very depleted, and contribute much less. As disc mass is decreased, the relative contribution of barely bound grains decreases, and the largest particles contribute more. For the least massive disc, most of the cross-section is in the largest grains.

2.3 Analytical Model

Here I present a model which predicts the steady-state size distribution of the disc at different radii by considering the balance between collisional evolution and migration due to P-R drag. First I consider the size distribution expected at the location of the planetesimal belt, then apply a model for how these particles evolve inwards of the belt.

The size distribution within the planetesimal belt can be found using the model of Wyatt et al. (2011), which determines the size distribution in a planetesimal belt at a single radius undergoing catastrophic collisions with loss processes acting. Particles are considered lost from the belt when P-R drag causes them to migrate past the belt's inner edge. To find how the distribution of a given particle size evolves radially I use the model of Wyatt (2005), which found the radial optical depth profile for a population of single-sized particles evolving via destructive collisions and P-R drag. The shape depends on the ratio of the P-R drag timescale to the collision time.

Combining the models of Wyatt et al. (2011) and Wyatt (2005) gives the size distribution of a debris disc at different radial locations, taking into account the collisional evolution of particles and P-R drag.

2.3.1 Parent belt size distribution

Consider a belt of planetesimals at a radius r_0 from the star, collisionally evolving to produce smaller grains. The method of Wyatt et al. (2011) can be used to find the one-dimensional size distribution of particles in the belt, which will extend up to some maximum particle size D_{max} . The lower end of the distribution is determined by the blowout size D_{bl} (equation 2.2). The

size distribution is approximated by a series of broken power laws; the precise power laws depend on the collision timescales, as collisions move material down the collisional cascade. I calculate the collision rate between particles in the disc with the particle-in-a-box approach. The rate of impacts onto a particle of size D from impactors of sizes $D_{\text{im}} \rightarrow D_{\text{im}} + dD_{\text{im}}$ is

$$R_{\text{coll}}(D, D_{\text{im}})dD_{\text{im}} = \frac{n(D_{\text{im}})dD_{\text{im}}}{V} \frac{\pi}{4} (D + D_{\text{im}})^2 v_{\text{rel}}. \quad (2.3)$$

Here V is the disc volume, $n(D_{\text{im}})$ is the number of particles per unit diameter, and v_{rel} is the relative velocity of the collisions. As in the numerical model (Section 2.2), only catastrophic collisions are considered; these are destructive such that the largest fragment has less than half the mass of the target particle, producing fragments according to some redistribution function $n_r(D) \propto D^{-\alpha_r}$. Catastrophic collisions require the impact energy per unit target mass to be above some critical dispersal value Q_{D}^* , so destructive collisions only occur with impactors of a diameter greater than $X_{\text{C}}D$, where

$$X_{\text{C}} = \left(\frac{2Q_{\text{D}}^*}{v_{\text{rel}}^2} \right)^{\frac{1}{3}}. \quad (2.4)$$

The critical specific energy for dispersal in the strength regime is parametrized as $Q_{\text{D}}^* = Q_{\text{a}}D^{-a}$. It is assumed that the velocity of collisions is related to the Keplerian velocity by the maximum inclination, I_{max} , as

$$v_{\text{rel}} = I_{\text{max}}v_{\text{k}} = I_{\text{max}}\sqrt{\frac{GM_{\star}}{r}}, \quad (2.5)$$

where the semi-opening angle of the disc ε in the V14 model would correspond to the maximum inclination. This assumes that the relative velocity of collisions is dominated by the vertical motion perpendicular to the plane of the disc. The volume of a disc of width dr and radius r can be approximated as

$$V = 4\pi r^3 \left(\frac{dr}{r} \right) I_{\text{max}}. \quad (2.6)$$

Within the belt I assume that the number of particles per unit diameter follows a power law

$$n(D) = KD^{-\alpha}, \quad (2.7)$$

such that $n(D)dD$ is the number of particles with diameters $D \rightarrow D + dD$, and the classical power law has $\alpha = 3.5$ when Q_{D}^* is independent of particle size (Dohnanyi, 1969; Tanaka

et al., 1996). Integrating over all possible impactors, I find that the rate of catastrophic collisions for a particle of size D is

$$\begin{aligned} R_{\text{cc}}(D) &= \int_{X_{\text{C}}D}^{D_{\text{max}}} R_{\text{coll}}(D, D_{\text{im}}) dD_{\text{im}} \\ &\approx \frac{\pi}{4(\alpha - 1)} \frac{K v_{\text{rel}}}{V} X_{\text{C}}^{1-\alpha} D^{3-\alpha}, \end{aligned} \quad (2.8)$$

where I assume that $\alpha > 3$ and that $X_{\text{C}} \ll 1$ to find the most relevant term in the collision rate. Therefore, the collision timescale for particles of size D is

$$t_{\text{coll}}(D) \approx \frac{4(\alpha - 1)}{\pi} \frac{V}{K v_{\text{rel}}} X_{\text{C}}^{\alpha-1} D^{\alpha-3}. \quad (2.9)$$

Note that this may have additional size dependence via X_{C} when Q_{D}^* is a power law with size. The normalisation of the size distribution in equation 2.7 can be found by

$$K = \frac{6(4 - \alpha)}{\pi \rho} D_{\text{max}}^{\alpha-4} M_{\text{dust}}, \quad (2.10)$$

where ρ is the density of particles, D_{max} is the maximum particle diameter, and M_{dust} is the total mass of dust particles, under the assumption that $\alpha < 4$ such that the mass distribution is dominated by the largest particles.

The timescale for a particle on a circular orbit to migrate in to the star via P-R drag from a radius r is (Wyatt and Whipple, 1950; Burns et al., 1979)

$$t_{\text{PR}}(r) = \frac{cr^2}{4GM_{\star}\beta}, \quad (2.11)$$

where M_{\star} is the stellar mass, c is the speed of light, and β the ratio of radiation pressure to gravity acting on a particle.

The balance between collisions and P-R drag is described by the ratio of their timescales for particles in the belt,

$$\eta_0(D) = \frac{t_{\text{PR}}(D, r_0)}{t_{\text{coll}}(D, r_0)}. \quad (2.12)$$

Both timescales are dependent on particle size, so the relative strength of collisions and P-R drag is a function of particle size. For low mass discs there is a critical particle diameter D_{pr} such that the P-R drag and collisional timescales are equal,

$$\eta_0(D_{\text{pr}}) = 1, \quad t_{\text{coll}}(D_{\text{pr}}, r_0) = t_{\text{PR}}(D_{\text{pr}}, r_0). \quad (2.13)$$

Wyatt et al. (2011) showed that the size distribution in a planetesimal belt can be approximated by two power laws of different slope, with a transition at the critical particle size D_{pr} . Particles larger than D_{pr} ($\eta_0 > 1$) are dominated by destructive collisions, and they follow the classical size distribution given in equation 2.7, with a slope determined by the power law of Q_{D}^* as

$$\alpha = \frac{7 - a/3}{2 - a/3}. \quad (2.14)$$

However, Wyatt et al. (2011) found a turnover in the slope of the size distribution for particles smaller than D_{pr} such that $\eta_0 < 1$, for which P-R drag is the dominant loss mechanism. The new slope is given by $\alpha_{\text{pr}} = \alpha_r - 1$:

$$n(D) = K_{\text{pr}} D^{1-\alpha_r}, \quad D \leq D_{\text{pr}}, \quad (2.15)$$

where continuity of the size distribution at D_{pr} gives that

$$K_{\text{pr}} = K D_{\text{pr}}^{\alpha_r - \alpha - 1}. \quad (2.16)$$

Once again integrating equation 2.3 over the size distribution of impactors for particles smaller than D_{pr} and assuming that $\alpha > 3$ and $3 < \alpha_r < 4$, for particles such that $D \ll D_{\text{pr}}$ and $X_{\text{C}} \ll 1$, the dominant term in the collision timescale is

$$t_{\text{coll}}(D < D_{\text{pr,eff}}) \approx \frac{4(\alpha_r - 2)}{\pi} \frac{V}{K v_{\text{rel}}} D_{\text{pr}}^{\alpha - \alpha_r + 1} X_{\text{C}}^{\alpha_r - 2} D^{-(4 - \alpha_r)}. \quad (2.17)$$

This is equivalent to replacing α by $\alpha_r - 1$ and K by K_{pr} in equation 2.9. So under the given assumptions, equation 2.9 applies to both regimes of the size distribution, with different parameters α and K .

While the size distribution is continuous, with two regimes which match at D_{pr} , generally t_{coll} and thus η_0 are discontinuous at D_{pr} , motivating the introduction of an effective critical size $D_{\text{pr,eff}}$ at which they are continuous. Then t_{coll} and η_0 have two power laws which join at $D_{\text{pr,eff}}$. It is to be expected that particles slightly bigger than D_{pr} will be affected by the turnover of the size distribution, as it affects the number of impactors that can catastrophically destroy them. The size at which t_{coll} and η_0 are continuous is close to the particle size at

which $X_C D = D_{\text{pr}}$ such that the smallest impactors are of size D_{pr} , so that

$$D_{\text{pr,eff}} = \left(\frac{\alpha_r - 2}{\alpha - 1} \right)^{\frac{1}{1+\alpha-\alpha_r}} X_C^{-1} D_{\text{pr}} \quad (2.18)$$

$$= \left(\frac{\alpha_r - 2}{\alpha - 1} \right)^{\frac{3}{(3-a)(1+\alpha-\alpha_r)}} \left(\frac{v_{\text{rel}}^2}{2Q_a} \right)^{\frac{1}{3-a}} D_{\text{pr}}^{\frac{3}{3-a}}. \quad (2.19)$$

2.3.2 Two-dimensional distribution

Once the size distribution of the parent belt has been found, each particle size is assumed to evolve independently inwards of the belt. The radial profile of a given particle size can be found using the model of Wyatt (2005), which takes into account P-R drag and mutual collisions for a single particle size. The collision timescales from Section 2.3.1 (equations 2.9 and 2.17) and the P-R drag timescales (equation 2.11) are used to calculate the values of η_0 for each size (equation 2.12), which determines the shape of the radial profile. This gives a two-dimensional size distribution over particle size D and radius from the star r . I express the distribution of particles in terms of vertical geometrical optical depth, which is the surface density of cross-sectional area.

For an annulus of particles all of the same size at $r \rightarrow r + dr$, the geometrical optical depth is given by

$$\tau(r) = \frac{\sigma n(r) dr}{2\pi r dr} = \frac{\sigma n(r)}{2\pi r}, \quad (2.20)$$

where $n(r)$ is the number density of particles per unit radius and σ is the cross-section of a particle. Wyatt (2005) solved the continuity equation for $n(r)$ to show that the optical depth due to particles inwards of a belt at radius r_0 is given by

$$\tau(r) = \frac{\tau(r_0)}{1 + 4\eta_0(1 - \sqrt{\frac{r}{r_0}})}. \quad (2.21)$$

The shape of the profile depends on the balance between collisions and P-R drag via the parameter η_0 . For massive debris discs, such as those which are currently detectable, collisions dominate and there is a sharp depletion of particles inwards of the belt, as grains are destroyed before they have a chance to migrate inwards. For less massive discs, however, the dominant process is migration via P-R drag; with negligible collisions the surface density becomes constant throughout the disc.

Now considering a distribution of particle sizes, if $\tau(D)dD$ is the cross-sectional area surface density in particles of size $D \rightarrow D + dD$ at radius r , the optical depth in a belt with

size distribution $n(D)$ is given by

$$\tau_0(D) = \frac{n(D)\pi\frac{D^2}{4}}{2\pi r_0 dr} = \frac{n(D)D^2}{8r_0^2\left(\frac{dr}{r}\right)}. \quad (2.22)$$

As stated above, the model of Wyatt (2005) is applied to each particle size independently. By only considering a single size of particle, this does not take into account the gain of smaller particles due to the fragmentation of larger grains or the overall size distribution. While particles will interact and be destroyed in collisions with particles of different sizes, I assume that the collision rate of grains of a given size scales with the number of similarly sized particles. This approximation will be corrected for in Section 2.3.3. Let $\tau(D,r)dD$ be the cross-sectional area surface density in particles of size $D \rightarrow D + dD$ at radius r , then applying equation 2.21 to each size D , the two-dimensional distribution is

$$\tau(D,r) = \frac{\tau_0(D)}{1 + 4\eta_0(D)\left(1 - \sqrt{\frac{r}{r_0}}\right)}. \quad (2.23)$$

2.3.3 Application of model

The analytical model makes many assumptions, such as that all particles are on circular orbits. It also assumes that inwards of the belt, particles are only destroyed by similarly sized particles, or at a rate which scales with the local density of similarly sized particles. To take into account approximations in the model, I follow Kennedy and Piette (2015) in introducing a factor k which modifies the previously derived collisional timescales, affecting how collisional particles are such that

$$\eta_0(D) = \frac{t_{\text{PR}}(D, r_0)}{kt_{\text{coll}}(D, r_0)}. \quad (2.24)$$

Section 4.4.2 shows that it is necessary for this to be dependent on size, which is implemented as

$$k = k_0 \left(\frac{D}{D_{\text{bl}}}\right)^{-\gamma}, \quad (2.25)$$

for some parameters k_0 and γ which are to be fitted by comparison with the numerical model (Section 2.2), where these approximations were not made.

My model can be used to find the two-dimensional size distribution for a disc, given the belt radius r_0 , the grain density ρ , the stellar mass and luminosity M_\star and L_\star , the maximum inclination I_{max} , the dust mass M_{dust} , and the disc fractional width $\frac{dr}{r}$. These parameters can be input to find the disc volume (equation 2.6), relative velocity (equation 2.5), the critical

impactor sizes (equation 2.4), and the β values (equation 2.1). Then the P-R drag timescale can be found with equation 2.11, and equation 2.9 or 2.17 gives the collisional timescale depending on particle size. The ratio of these timescales gives η_0 , and D_{pr} is the particle size for which $\eta_0 = 1$. Then $D_{\text{pr,eff}}$ can be calculated to find where the two regimes for the collision timescales apply. The k factor should be applied to η_0 after finding D_{pr} . The size distribution within the belt is

$$n(D) = \begin{cases} KD_{\text{pr}}^{\alpha_r - \alpha - 1} D^{1 - \alpha_r}, & D \leq D_{\text{pr}} \\ KD^{-\alpha}, & D \geq D_{\text{pr}}, \end{cases} \quad (2.26)$$

where the normalisation K is given by equation 2.10. This size distribution can be used to find the optical depth in the belt (equation 2.22), which should be applied at radii $r_0 \rightarrow r_0 + dr$ to take into account the finite extent of the belt. Inwards of the belt, the size distribution can be found using equation 2.23. The size distribution is cut off for particles smaller than D_{bl} .

The numerical model uses the rate at which dust mass is introduced to the system by collisions of larger parent bodies, \dot{M}_{in} , as an input. I assume that the disc is in steady state, such that this mass input is balanced by the loss of the largest particles to collisions or P-R drag. Since the largest particles should dominate the mass distribution given the assumption that $\alpha < 4$, the belt mass can be estimated using

$$M_{\text{belt}} \approx \dot{M}_{\text{in}} \min(t_{\text{coll}}(D_{\text{max}}), t_{\text{PR}}(D_{\text{max}})). \quad (2.27)$$

As in the numerical model, the fiducial model has a belt location of $r_0 = 30$ au and a maximum particle inclination of $I_{\text{max}} = 8.5^\circ$. The particles included in the model are in the strength regime, with a maximum size $D_{\text{max}} = 2$ cm, so the critical dispersal threshold is taken to be constant at $Q_{\text{D}}^* = 10^7$ erg g⁻¹. The slope of the size distribution of particles has the standard value when Q_{D}^* is independent of particle size, $\alpha = 3.5$. As for the numerical model, a value of $\alpha_r = 3.5$ is used. The fiducial model considers a Sun-like star with $M_\star = M_\odot$, $L_\star = L_\odot$, and the mass input rate is varied from $\dot{M}_{\text{in}} = 10^{-18}$ to $10^{-12} M_\oplus \text{ yr}^{-1}$.

2.4 Comparison of numerical and analytical models

Comparison of results from the analytical and numerical models was used to find the best fit parametrization of k and test predictions of parameter space trends.

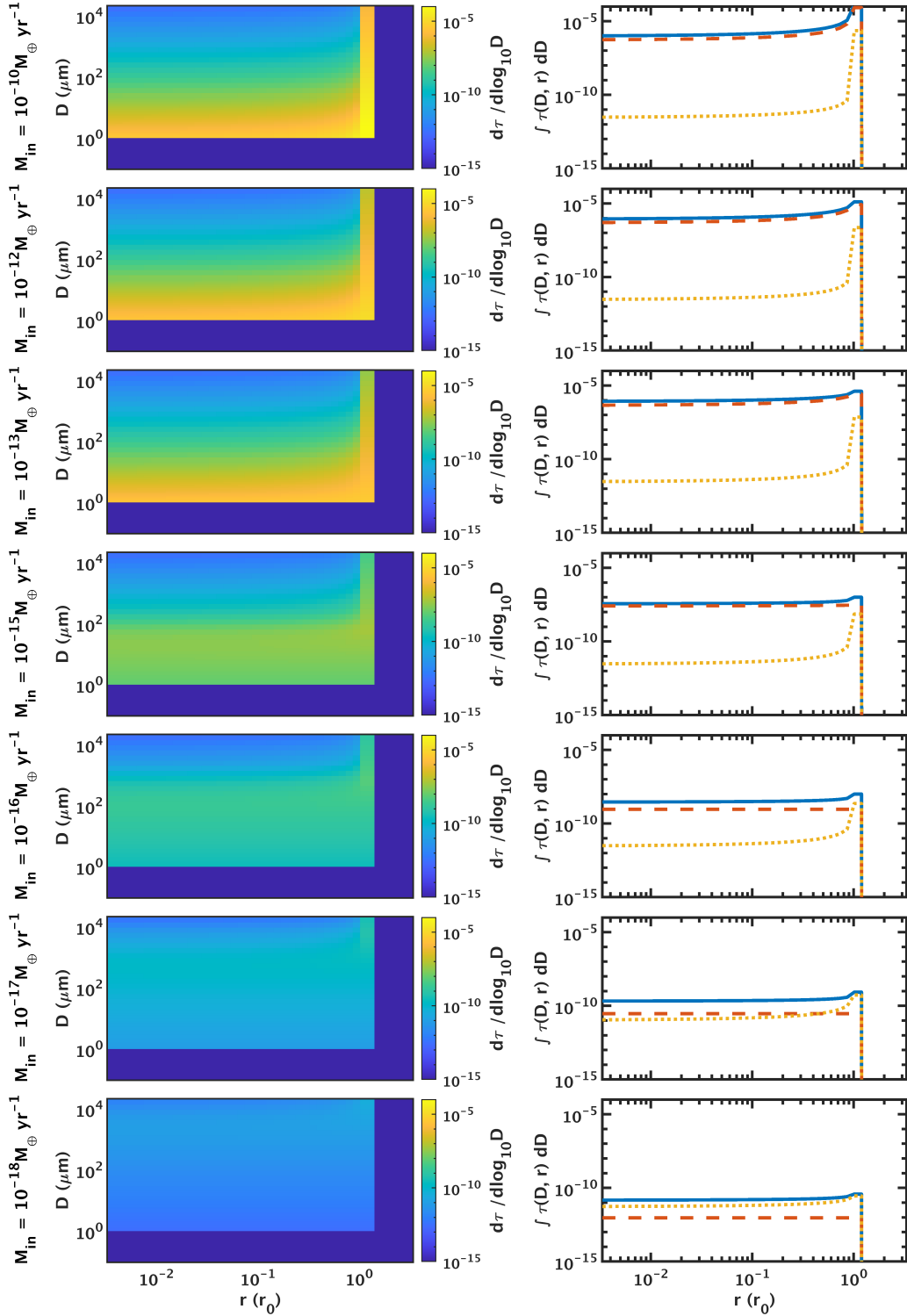


Fig. 2.2 Left: two-dimensional size distribution of particles over size and radial distance for discs with different dust mass input rates and a belt radius $r_0 = 30$ au as predicted by my analytical model, with the best fit of the factor k . The colour scale gives the optical depth per unit size decade. Right: radial distribution of integrated optical depth for all particles (blue), barely bound grains (orange, dashed), and cm-sized particles (yellow, dotted). Markers show values at $0.01 r_0$ and r_0 ; ratios of these integrated optical depths are used to characterise the behaviour of the model.

2.4.1 Disc mass

The left column of Figure 2.2 shows the optical depth per unit size decade $d\tau/d\log_{10}D$ as a two-dimensional distribution in grain size D and radius r for the best fit of k , to be compared with the numerical model in Figure 2.1. In terms of the analytical model, this is equivalent to

$$\frac{d\tau}{d\log_{10}D} = D \log 10 \times \tau(D, r). \quad (2.28)$$

Regardless of the value of k , my model captures the broad trends with disc mass seen in the numerical model, going from particles being collisional to drag-dominated as disc mass is decreased. Low mass discs are in the drag-dominated regime, and the radial profiles are close to flat. The highest mass discs are in the collisional regime, showing a rapid decrease in optical depth inwards of the belt. Intermediate disc masses such as $\dot{M}_{\text{in}} = 10^{-15} M_{\oplus} \text{ yr}^{-1}$ show a transition between being drag-dominated for the smallest particles, while large particles are collisionally depleted. The transition between these two regimes for a given disc mass occurs at a similar particle size in both models. There is an abrupt drop-off in optical depth outside of the belt, as the model has not been constructed to include consideration of the halo, instead focussing on structure within and interior to the belt. There is also a drop-off at particle sizes below D_{bl} , the lower limit of my size distribution, as grains below this size will be blown out by stellar radiation pressure. The analytics (equation 2.2) give a value of $D_{\text{bl}} = 0.98 \mu\text{m}$, slightly smaller than $1.5 \mu\text{m}$ which is found numerically. The main issue is the wavy patterns seen in the most massive discs for the numerical model (Figure 2.1). As noted in Section 2.2.3, to avoid the waves biasing the comparison between models, the behaviour of the models is characterised by integrating the size distribution over particle size.

The right hand column of Figure 2.2 shows the radial distribution of optical depth integrated over particle size to better compare the behaviour of the two models. Radial profiles are given for the total optical depth, the smallest particles ($D_{\text{bl}} < D < 20 \mu\text{m}$), and the largest particles ($2 \text{ mm} < D < 2 \text{ cm}$). Similar trends are seen to the numerical model for the relative contributions of grain sizes. Most of the optical depth for massive discs is in barely bound grains, with the large particles heavily depleted by collisions. As disc mass decreases, the contribution of barely bound grains also decreases. In the lowest mass disc, most of the optical depth comes from the largest particles. The radial profiles of large particles are much flatter in the analytical model, while in the numerical model the profiles are less uniform due to the effect of collisions, and the aforementioned waviness.

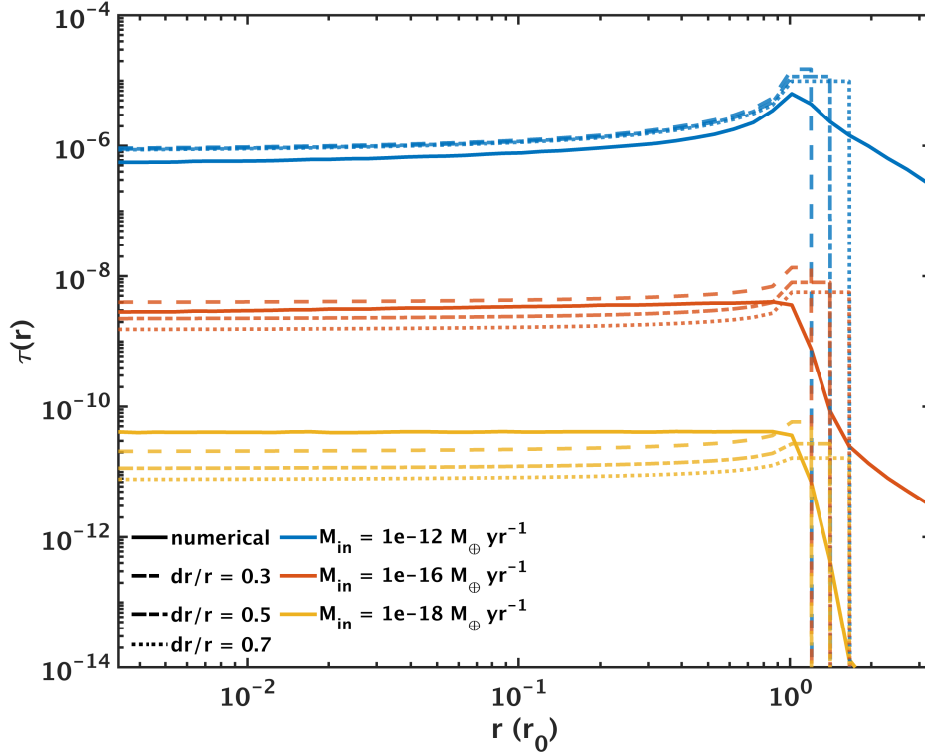


Fig. 2.3 Radial optical depth profiles for discs with mass input rates \dot{M}_{in} of $10^{-12} M_{\oplus} \text{ yr}^{-1}$ (blue), $10^{-16} M_{\oplus} \text{ yr}^{-1}$ (orange), and $10^{-18} M_{\oplus} \text{ yr}^{-1}$ (yellow). Profiles from the numerical model are shown with solid lines, while the analytical model is shown for three values of dr/r : 0.3 (dashed), 0.5 (dash-dotted), and 0.7 (dotted). The analytical model is shown with the values $k_0 = 10$ and $\gamma = 0.7$.

2.4.2 Model fitting

The model has three parameters to fit: the belt width $\frac{dr}{r}$, and the two parameters k_0 and γ which determine the collisional factor k . While $\frac{dr}{r}$ is not a direct input parameter of the numerical model, the belt width can be altered either by changing the eccentricity of the parent bodies in the belt, which mostly affects large grains, or changing the range of initial periastra. This was found to have little effect on the distribution inwards of the belt, only affecting the breadth of the belt. Therefore, the same initial conditions are used throughout for the numerical model. It is assumed in the analytical model that particles are on circular orbits, with no eccentricity inherited from the parent bodies. Varying $\frac{dr}{r}$ in the analytical model affects the breadth of the belt, but also has an effect on the optical depth profile due to the dependence of belt volume and area on its width. The belt width was fitted using the radial optical depth profiles simultaneously along with k_0 and γ , which were fitted using metrics described below.

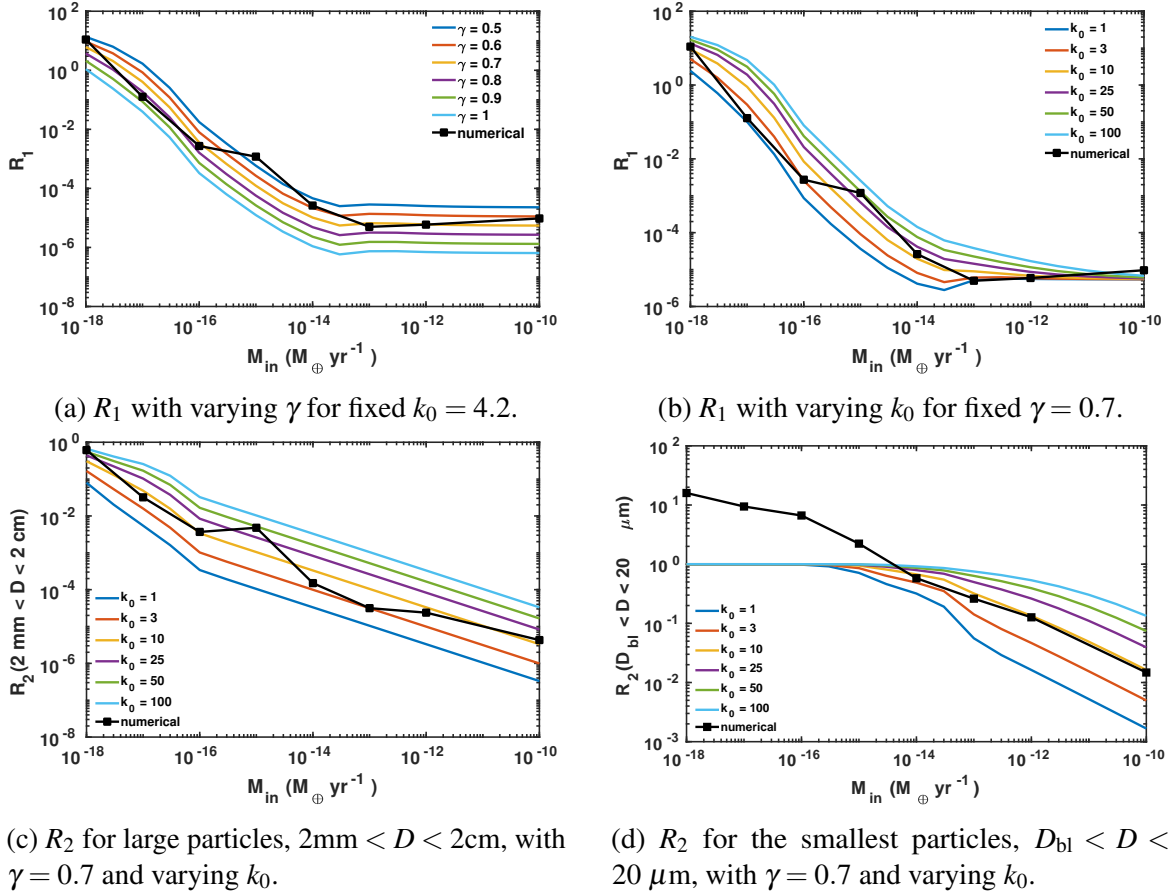


Fig. 2.4 Ratios used to fit the parameters of the factor k (equation 2.25), which matches the analytical model to the numerical one. The top panels show R_1 (equation 2.29), the ratio of integrated optical depth in large particles to small particles when close in to the star at $0.01 r_0$, as a function of mass input rate \dot{M}_{in} , which is related to disc mass. The bottom panels show R_2 (equation 2.32), the ratio of integrated optical depth close in to the star to that in the belt as a function of mass input rate \dot{M}_{in} for two different particle sizes. In all cases the numerical model (black) is compared with the analytical model for various values of the parameters.

Figure 2.3 shows the effect of varying the belt width on the radial optical depth profile. Smaller belt widths cause the optical depth of the belt to be higher (equation 2.22). Similarly, the collision timescale (equation 2.9) is proportional to the disc volume, which depends on the belt width, such that smaller belt widths have shorter collisional timescales, meaning they have profiles which are more depleted. The best fit of $\frac{dr}{r}$ is different for discs with different masses. For example, for the most collisional discs (e.g. $10^{-12} M_{\oplus} \text{ yr}^{-1}$, no value is a very good match as the analytical model overestimates the optical depth. For intermediate mass discs (e.g. $10^{-16} M_{\oplus} \text{ yr}^{-1}$), the best fit is $\frac{dr}{r} = 0.5$. For low mass discs (e.g. $10^{-18} M_{\oplus} \text{ yr}^{-1}$), the optical depth is underestimated, but the best fit would be $\frac{dr}{r} = 0.3$.

The best fit of the factor k was found by considering the model's behaviour in two dimensions, comparing ratios of optical depths for different particle sizes and locations. The right hand columns of Figures 2.1 and 2.2 show markers for which points are compared in the ratios. The first ratio,

$$R_1 = \frac{\int_{2\text{mm}}^{2\text{cm}} \tau(0.01r_0, D) dD}{\int_{D_{\text{bl}}}^{20 \mu\text{m}} \tau(0.01r_0, D) dD}, \quad (2.29)$$

compares the relative contributions of large particles and small particles to the optical depth when close in to the star. In highly collisional discs, $\eta_0 \gg 1$, the optical depth (equation 2.23) close in to the star tends towards a value

$$\tau(D, 0.01r_0) \approx \frac{\tau_0(D)}{3.6\eta_0(D)} \propto \frac{k(D)D^{2-\alpha}}{D^{4-\alpha}} = k(D)D^{-2}. \quad (2.30)$$

This means that the ratio of optical depths in two different sizes just depends on the values of D and k as

$$\frac{\tau(D_1, 0.01r_0)}{\tau(D_2, 0.01r_0)} = \frac{k(D_1)}{k(D_2)} \left(\frac{D_1}{D_2}\right)^{-2} = \left(\frac{D_1}{D_2}\right)^{-2-\gamma}. \quad (2.31)$$

Therefore at large disc masses, R_1 should tend to a constant value depending only on the chosen particles sizes to be compared and γ .

Figure 2.4a shows R_1 plotted as a function of mass input rate, which determines disc mass. As predicted, a plateau is seen at the largest disc masses, where the disc is collisional. When k is a constant with particle size, this plateau cannot be fitted with the analytical model. However, when k becomes a function of particle size, the value of the analytical model can be shifted to match the numerical one. This explains the choice of the prescription of equation 2.25 with k a function of particle size, for which k_0 and γ are parameters to be fitted to the numerical model. Figure 2.4a shows how varying γ shifts the value of the plateau, with a best fit expected to be close to $\gamma = 0.7$.

The effect on R_1 of varying k_0 with fixed $\gamma = 0.7$ is shown in Figure 2.4b. A broad range of values are feasible for k_0 , but the most consistent value is close to $k_0 = 3$ or 10 . The other ratio used to fit k is the ratio of optical depth close in to the star to that in the belt, given by

$$R_2 = \frac{\int_{D_{\text{lower}}}^{D_{\text{upper}}} \tau(0.01r_0, D) dD}{\int_{D_{\text{lower}}}^{D_{\text{upper}}} \tau(r_0, D) dD}. \quad (2.32)$$

This varies for different ranges of particle size D_{lower} to D_{upper} . When considering the largest particles, as in Figure 2.4c, which shows R_2 for $2 \text{ mm} < D < 2 \text{ cm}$, there is some fluctuation, but broadly the best fit is expected to be close to $k_0 = 10$. However, when considering the smallest particles as in Figure 2.4d ($D_{\text{bl}} < D < 20 \mu\text{m}$), my analytical model cannot fit to the drag-dominated regime (low disc masses) for any values of the parameters. The integrated optical depths in Figure 2.1 show that in low mass discs the optical depth of barely bound grains in the numerical model decreases with radius, causing the ratio plotted in Figure 2.4d to exceed 1. By construction, the radial profile of a single particle size in the analytical model must either be flat, or increase with radius, meaning that this ratio cannot exceed 1. In the drag-dominated regime, a flat radial profile is predicted, giving a ratio of 1.

One reason for this discrepancy is the assumption in the analytical model that particles of different sizes evolve independently inwards of the belt. However, the breakup of large particles will act as a source of smaller grains, such that optical depth of small particles actually increases in towards the star, rather than being flat, for the numerical model.

Fitting of the three parameters was done by minimising χ^2 for the logarithms of the ratios R_1 (equation 2.29) and R_2 for large particles (equation 2.32), along with the radial profile of optical depth $\tau(r)$. For example, the χ^2 for R_1 would be given by

$$\chi^2(R_1) = \sum_{M_{\text{in}}} (\log R_{1,\text{analytical}} - \log R_{1,\text{numerical}})^2. \quad (2.33)$$

The ratios R_1 and R_2 have a single point for each mass input rate, while the radial optical depth profile is sampled at n_r different points for each mass input rate. Therefore, the χ^2 for $\tau(r)$ is weighted by $1/n_r$ such that each of these factors contributes equally to the fit. While a range of values for each parameter gives reasonable results, combined minimisation gives the best fit values $\frac{dr}{r} = 0.4$, $\gamma = 0.7$, and $k_0 = 4.2$.

2.4.3 Thermal emission

Thermal emission from dust grains can be seen at infrared wavelengths in the spectral energy distributions (SEDs) of stars as excess flux above the stellar photosphere. This can be

described as a fractional excess, $R_V = F_V \text{ disc}/F_{V\star}$. Once the size and spatial distribution of dust in a disc has been determined using a model, infrared excesses of the disc can be predicted by applying realistic grain properties (Section 2.2.2) for the absorption efficiencies $Q_{\text{abs}}(\lambda, D)$ and temperatures $T(D, r)$ of grains. The disc flux in Jy at a given wavelength can be found from the model by summing the emission from different radii and particle sizes as

$$F_V = 2.35 \times 10^{-11} d^{-2} \iint Q_{\text{abs}}(\lambda, D) B_V[T(D, r)] 2\pi r \tau(D, r) dD dr, \quad (2.34)$$

where d is the distance from the star in pc, radius r is in au, and B_V is the spectral radiance in Jy sr⁻¹ (Wyatt et al., 1999).

As an example, Figure 2.5 shows a comparison of the SEDs resulting from the numerical and analytical models for the discs considered in Sections 2.2.3 and 2.4.1. An inner cut-off at a radius of 0.1 au is used, such that the SEDs will not be fully accurate at wavelengths below $\sim 6 \mu\text{m}$. Only thermal emission has been included, while scattered light will also contribute below $\sim 5 \mu\text{m}$. Realistic optical properties for asteroidal grains are used for both models, so both models include similar features in the SED. A similar pattern is seen as when fitting the optical depth in Figure 2.3. The analytical model fits very well at intermediate disc masses, but slightly overestimates the optical depth for the most massive discs, and slightly underestimates the optical depth of the least massive discs. For the disc with a mass input rate of $10^{-10} M_{\oplus} \text{ yr}^{-1}$, the fractional $11 \mu\text{m}$ excess is overestimated by a factor 2.0, while for the disc with a mass input rate of $10^{-18} M_{\oplus} \text{ yr}^{-1}$, the $11 \mu\text{m}$ flux is underestimated by a factor of 2.5. This shows that while there are differences between the two models, the $11 \mu\text{m}$ excess should not differ by more than a factor ~ 3 for discs of masses similar to those considered here.

2.5 Parameter space

Once the model has been fitted for the fiducial planetesimal belt properties, its ability to predict parameter space trends can be tested by further comparison with the numerical model. The dependence of size distributions on individual input parameters is investigated in the following subsections.

2.5.1 Stellar type

To ascertain the effect of stellar mass and luminosity, the model was applied to stars of different types, whose parameters are given in Table 2.1. The optical properties for dust around different stars were calculated for the numerical model using the method described

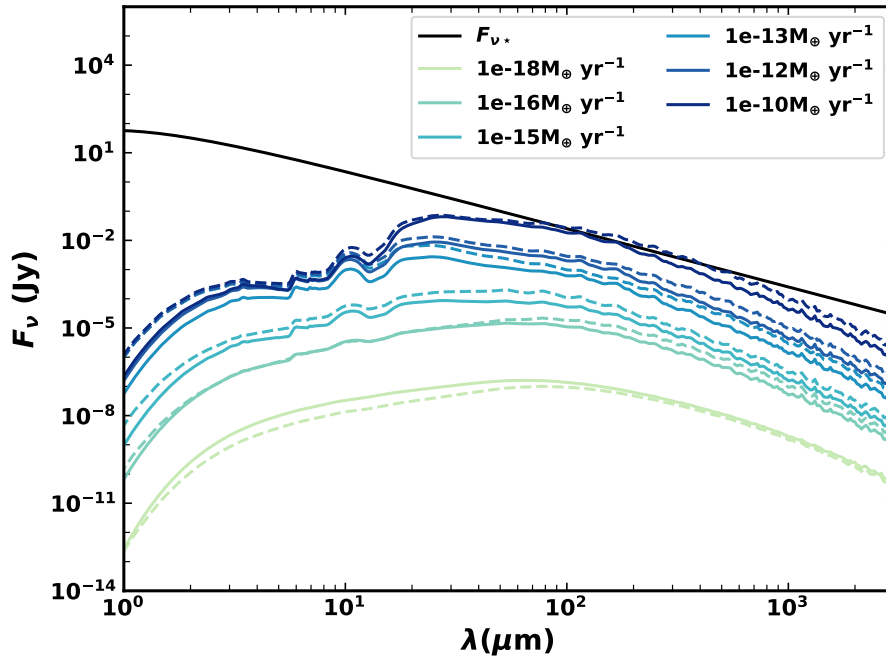


Fig. 2.5 Comparison of SEDs based on the numerical (solid lines) and analytical (dashed lines) models for the discs considered in Sections 2.2.3 and 2.4.1. Realistic optical properties were used, assuming asteroidal grains.

Table 2.1 Stellar types used in comparison of the models (Figure 2.6).

Stellar type	Mass M_{\odot}	Luminosity L_{\odot}	Temperature K
M0	0.5	0.074	3822
K2	0.75	0.31	4958
G2	1.0	1.1	5868
F7	1.25	2.4	6264
A5	2.0	14.0	8204
A0	3.0	61	9722

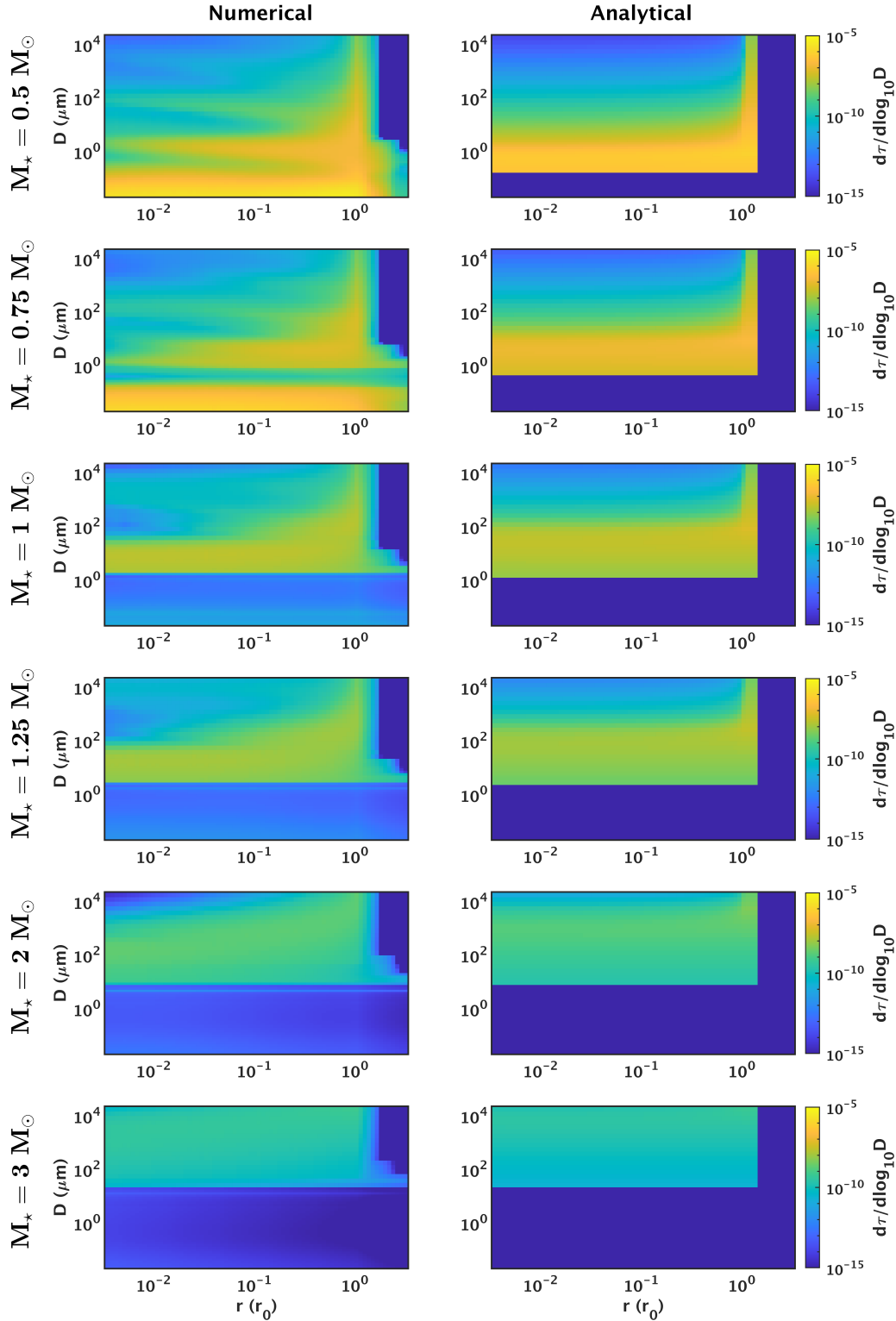


Fig. 2.6 Two-dimensional size distribution of particles over size and radial distance for discs with different stellar types, as produced by the numerical model of V14 (left) and my analytical model (right). The colour scale gives the optical depth per unit size decade. The mass input rate is fixed throughout at $\dot{M}_{\text{in}} = 10^{-15} M_{\oplus} \text{ yr}^{-1}$, and the planetesimal belt has a radius of $r_0 = 30 \text{ au}$.

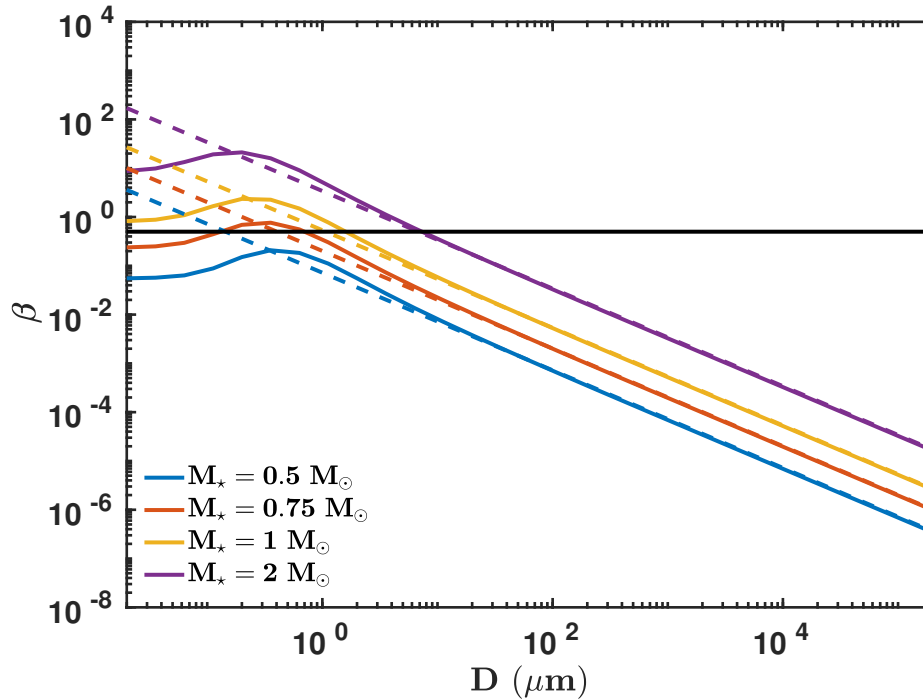


Fig. 2.7 β as a function of particle diameter, D , for grains around stars of different masses. Solid lines show numerical values, while dashed lines show the analytical predictions from equation 2.1, assuming $Q_{\text{pr}} = 1$. The black line shows $\beta = 0.5$, the limit above which particles should be blown out of the system on unbound orbits by stellar radiation pressure.

in Section 2.2.2. Equation 2.1 was used for the analytical model, assuming $Q_{\text{pr}} = 1$. A comparison of the size distributions from the numerical and analytical models is given in Figure 2.6 with fixed mass input rate $\dot{M}_{\text{in}} = 10^{-15} M_{\oplus} \text{ yr}^{-1}$ and a belt of radius $r_0 = 30 \text{ au}$. As stellar mass is increased, the blowout size increases due to higher stellar luminosity and therefore stronger radiation pressure. Both models broadly follow the same trends without having to change the factor k , although for the lowest mass stars sub-micron grains are present in the numerical results, whereas such grains are assumed to be removed by radiation pressure in the analytical model.

The β profiles for grains around stars of different masses are plotted in Figure 2.7, calculated numerically using the approach in Section 2.2.2, and analytically using equation 2.1. The standard shape of the profile of β is that it is inversely proportional to particle size, with a turnover at the smallest particle sizes. Since $\beta \propto L_{\star}/M_{\star}$, low mass stars have lower values of β , such that either when the profile turns over it drops back below 0.5 (as seen for $0.75 M_{\odot}$), or β never actually exceeds 0.5 (as seen for $0.5 M_{\odot}$). Sub-micron grains are therefore present around low mass stars in contradiction to the simple analytical prescription suggesting that they should be blown out on hyperbolic orbits. A limitation of the analytical

model is that it cannot faithfully reproduce the distribution of small grains for late-type stars, for which radiation pressure is weaker, such that it is not always possible to blow particles out (e.g. Sheret et al., 2004). Furthermore, drag forces around late-type stars are significantly enhanced by stellar winds (Plavchan et al., 2005), which have not been considered. It may be possible to incorporate the effects of stellar wind drag by modification of β if the magnitude of the stellar wind is known, as described in V14, but that is beyond the scope of this work.

The effect of stellar type on the SED is shown in Figure 2.8 for discs with a mass input rate of $10^{-15} M_{\oplus} \text{ yr}^{-1}$. Overall the shapes of the SEDs are similar between the two models, with slight differences in the magnitude of the flux. For an A star ($3 M_{\odot}$), the $11 \mu\text{m}$ excess is underestimated by a factor of 1.6, while the Sun-like star ($1 M_{\odot}$) is overestimated by a factor 1.3. For the M dwarf, the analytical model overestimated the $11 \mu\text{m}$ flux by a factor of 7. Therefore the model is most applicable to Sun-like and A stars. As concluded previously from the optical depth, there is a much poorer fit for M stars due to the discrepancy with β . However, how well the model fits will also vary with the mass of the disc.

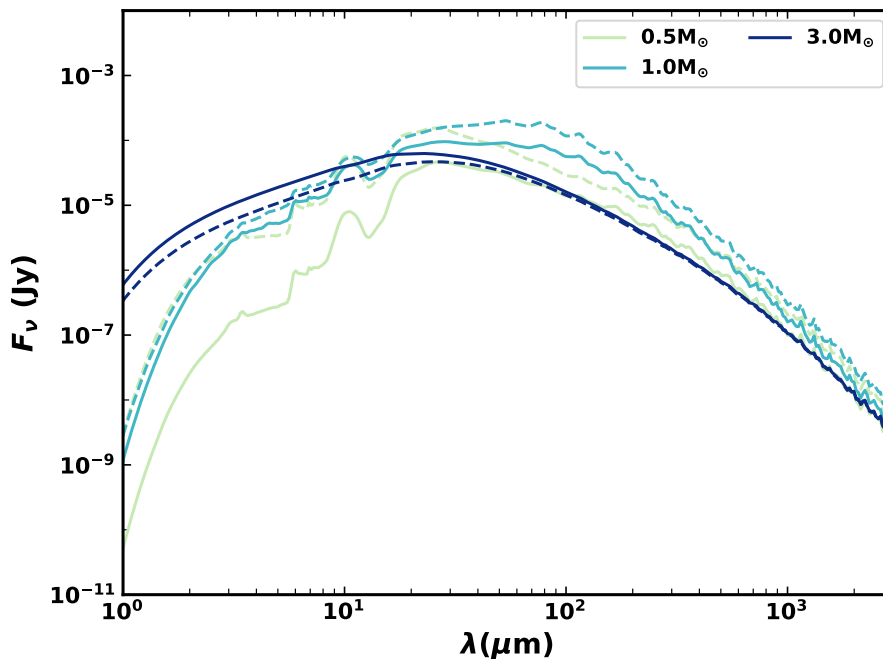


Fig. 2.8 Comparison of SEDs from the numerical (solid lines) and analytical (dashed lines) models for discs with a mass input rate of $10^{-15} M_{\oplus} \text{ yr}^{-1}$ and different stellar masses, assuming asteroidal grains.

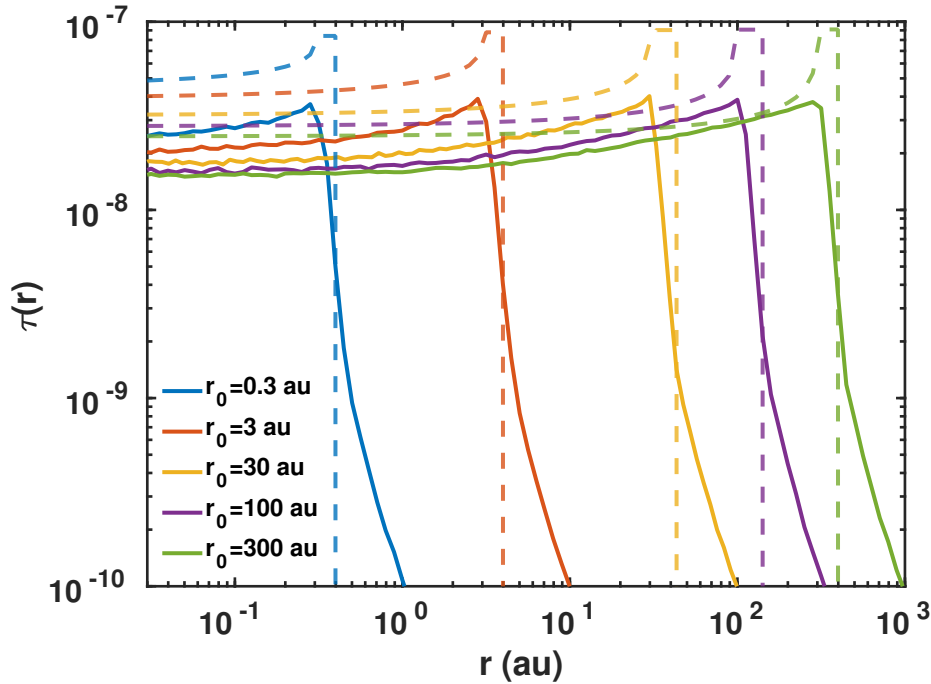


Fig. 2.9 Total geometrical optical depth as a function of radius for discs with parent belts at different radii and a mass input rate of $\dot{M}_{\text{in}} = 10^{-15} M_{\oplus} \text{ yr}^{-1}$. Results from the numerical model are solid lines, while the dashed lines show the analytical model.

2.5.2 Belt radius

Another parameter of the model which can be varied is the distance of the planetesimal belt from the star, r_0 . Simulations were run with belt radii in the range 0.3 – 300 au. Figure 2.9 shows the radial profile of optical depth as r_0 is varied at constant mass input rate. As was seen for the fiducial model in Figure 2.2, the radial profiles predicted analytically are quite flat, with either a sharp drop inwards of the belt before becoming flat for collisional particles, or a completely flat profile for drag-dominated particles. The numerical radial profiles are moderately flat, but less so than the analytical ones. In the analytical model, the optical depth in the belt has a weak dependence on belt radius for fixed mass input rate, so varying the radius over a few orders of magnitude causes little variation. The numerical results also show similar optical depth levels in the belt regardless of r_0 . As the belt location moves outwards there is a slight decrease in the level the optical depth flattens out to in the inner regions of the disc. Comparison of the radial profiles shows that both models follow similar trends with radius, but the analytical profiles overestimate the optical depth by a factor of ~ 2 . However, this offset does not significantly affect the predicted size distribution, and is expected due to the compromise needed when choosing $\frac{dr}{r}$ to fit the model over a large range of \dot{M}_{in} (see Figure 2.3).

2.5.3 Dispersal threshold of particles

So far the critical dispersal energy, Q_D^* , has been taken to be independent of particle size. However, this is not necessarily a realistic prescription, and many attempts have been made to characterise its dependence on particle size. For example, Benz and Asphaug (1999) used SPH to simulate collisions, while Housen and Holsapple (1999) used laboratory experiments to measure the outcomes of collisions between small particles. Durda and Dermott (1997) and Durda et al. (1998) ran numerical collisional evolution models, and fit these to observations of the main belt asteroid size distribution to find the best fit of Q_D^* . In general, it is assumed that Q_D^* can be approximated by a sum of two power laws, representing the strength and gravity regimes. All particles considered in this chapter are small enough that material strength determines their critical dispersal threshold, which can be described by a single power law, $Q_D^* = Q_a D^{-a}$. Holsapple (1994) found a dependence in the strength regime of $Q_D^* \propto D^{-0.33}$, while Housen and Holsapple (1990) found $Q_D^* \propto D^{-0.24}$. Benz and Asphaug (1999) considered both basalt and ice, and found that depending on the material and impact velocity, the dependence varied between $a = 0.36 - 0.45$. However, it should be noted that none of these prescriptions for Q_D^* consider particles smaller than cm-sized, and thus may not be applicable for micron-sized grains (e.g. Thebault and Kral, 2019). Here I choose to use the same values as Löhne et al. (2008), which in my notation gives $Q_a = 2.45 \times 10^7 \text{ erg g}^{-1}$ and $a = 0.3$, with D given in cm.

As shown in Figure 2.10, using a power law prescription for Q_D^* only had a minor effect on the size distribution of particles in the belt. For the numerical model, particles are assumed to be within the parent belt if they are between radii $30 \leq r_0 \leq 45 \text{ au}$. The most significant effect is that for collisional discs, such as $\dot{M}_{\text{in}} = 10^{-12} M_{\oplus} \text{ yr}^{-1}$, using a power law for Q_D^* dampens the collisional waves which are due to truncation of the distribution at the blowout size. For the chosen values, Q_D^* also has a greater value when a power law is used, so this may be an effect of using a greater Q_D^* value. The slope of the size distribution in the collisional regime should also be affected. Wyatt et al. (2011) derived that the slope of the steady state size distribution depends on the power law of Q_D^* as in equation 2.14, which gives a slope of -3.63 for the chosen prescription. Comparison of the distributions for $\dot{M}_{\text{in}} = 10^{-12} M_{\oplus} \text{ yr}^{-1}$ shows that with a power law, the slope of the distribution becomes steeper, going from -3.52 to -3.57. The increased Q_D^* for the power law prescription also causes the collisional waves in size distributions to move closer together, due to particles being destroyed by other particles which are a larger fraction of their own size (as shown by equation 2.4). This change in spacing of the waves is most evident in the inner regions of the disc, where the waves are more significant.

The discs with $\dot{M}_{\text{in}} = 10^{-15} M_{\oplus} \text{ yr}^{-1}$ show a transition between regimes, with large particles being collisional, while smaller particles are drag-dominated, with a shallower slope. The analytical model predicts that the location of the turnover, D_{pr} , should be smaller with constant Q_{D}^* due to its lower value. The numerical model similarly has a change in slope of the size distribution at a larger particle size for the power law Q_{D}^* . Low mass discs, such as $\dot{M}_{\text{in}} = 10^{-18} M_{\oplus} \text{ yr}^{-1}$, are drag-dominated, such that the slope of their size distribution depends only on the redistribution function. Therefore, no difference is seen in the size distribution when Q_{D}^* is changed, with a slope of -2.5 in both cases agreeing with the analytical prediction of $1 - \alpha_{\text{r}}$. A minor difference is seen in the analytic model due to the different values of D_{pr} obtained with the different Q_{D}^* values. The normalisation of the size distribution of the drag-dominated regime, K_{pr} , depends on D_{pr} as in equation 2.15.

Collision timescales increase with Q_{D}^* (equation 2.9), so the analytical model predicts that discs will be less collisional with the power law prescription. This will cause the radial optical depth profiles to become flatter. However, very minimal differences are seen in the radial profiles of the numerical model, as they are dominated by barely bound grains, which are mostly flat. Thus these profiles are not shown. The grains which are most affected by Q_{D}^* are cm-sized, but these grains contribute less to the overall optical depth profile of the disc.

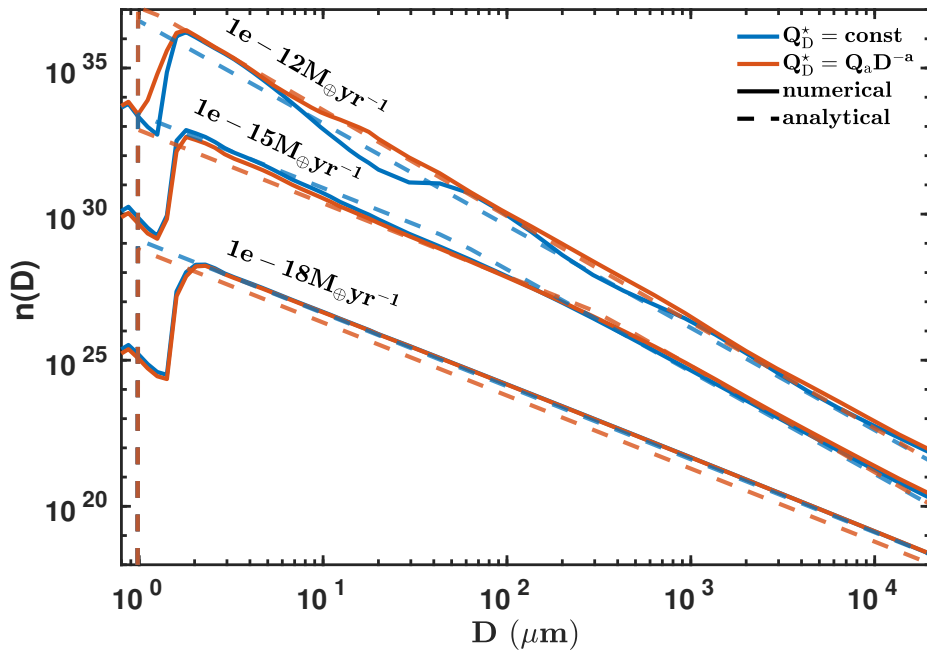


Fig. 2.10 The size distribution $n(D)$ of particles within the belt for discs of different mass input rates, both with $Q_{\text{D}}^* = \text{const}$, and $Q_{\text{D}}^* = Q_{\text{a}} D^{-a}$. Results from the numerical model are shown with solid lines, and the analytical predictions are shown with dashed lines.

2.5.4 Redistribution function

As derived in Wyatt et al. (2011), the redistribution function of collisions should determine the slope of the size distribution for particles which are dominated by P-R drag, such that their size distribution has a slope $1 - \alpha_r$. It is expected that the size distribution should change slope at the critical particle size D_{pr} . Figure 2.11 compares the size distribution of particles in the belt from the numerical and analytical models as α_r is varied. These distributions show the expected decrease in steepness of the slope as α_r is decreased.

Figure 2.11 shows the size distribution for a disc with $\dot{M}_{in} = 10^{-15} M_{\oplus} \text{ yr}^{-1}$. This is a disc for which the largest particles are collisional, while the smaller particles are drag-dominated. For the larger, collisional particles, the slope is the same for all redistribution functions and agrees with the analytical model. Below $100 \mu\text{m}$ there is a change in slope as predicted, though the slope does not perfectly match the analytical prediction. One possible explanation for the numerical model having a steeper slope is the inclusion of small particles which are put onto eccentric orbits by radiation pressure, forming the halo.

The size distribution of a lower mass disc is given at the bottom of Figure 2.11, which shows a drag-dominated disc with $\dot{M}_{in} = 10^{-18} M_{\oplus} \text{ yr}^{-1}$. Since this disc is more fully in a P-R drag dominated regime, the slopes in the numerical model match better with the analytical predictions, and once more a slope change is seen when varying α_r . The slope of the numerical model varies between -2.7 for $\alpha_r = 3.75$ and -2.02 for $\alpha_r = 3$, while the analytical predictions of the slope are -2.75 and -2 respectively.

2.5.5 Limitations of model

The model has been fitted over a large range of mass input rates, with the highest mass input rate, $10^{-10} M_{\oplus} \text{ yr}^{-1}$, corresponding to a dust mass of $3 \times 10^{-4} M_{\oplus}$ for a belt with a radius of 30 au, while the lowest disc mass the model was fitted to is $3 \times 10^{-8} M_{\oplus}$. Some of the discs this model is applied to may have higher dust masses, such that they are outside the range the model has been fitted to. Further, the model was fitted for a Sun-like star, and may slightly underestimate the flux for A stars (see Section 2.5.1). It is advised not to apply the model to M dwarfs, where the β profile differs significantly from the analytical prediction, and stellar winds need to be considered. It would be possible to include stellar winds by adjusting β for a specific system, if the magnitude of the stellar wind were known.

Further, real debris discs can either be very broad or very narrow, while my model assumes discs to have a width $dr/r = 0.4$, and does not predict the correct dependence when varying disc width. Therefore it is difficult to apply the analytical model to discs which are very broad, such as τ Ceti, which has inner and outer radii of 6 and 52 au respectively. While

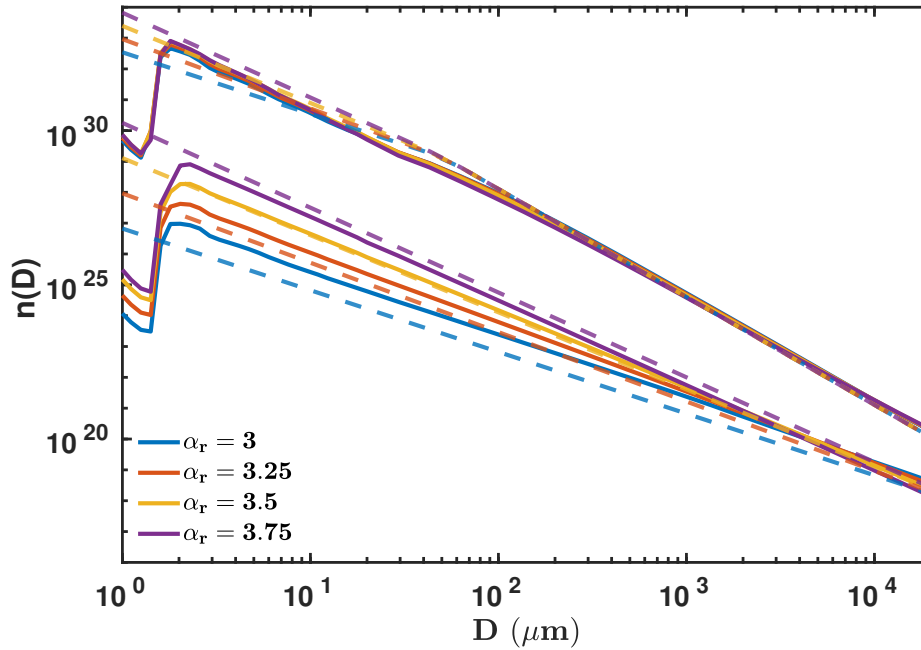


Fig. 2.11 The size distribution $n(D)$ of particles in the belt for a disc with mass input rate $\dot{M}_{\text{in}} = 10^{-15} M_{\oplus} \text{ yr}^{-1}$ (top) and $10^{-18} M_{\oplus} \text{ yr}^{-1}$ (bottom). The slope of the redistribution function, α_r , is varied between 3 and 3.75 in both the numerical model (solid lines) and the analytical model (dashed lines) to show the corresponding change in slope of the size distribution for drag-dominated particles.

the model has been fitted to a range of disc masses, it is difficult to constrain the best value of k , and a range of parameters can produce acceptable results. For a different stellar type or belt radius, it may be that slightly different values of k_0 and γ fit better than those chosen here. Overall for the discs considered in this chapter, the model should fit to within a factor ~ 3 , except for M stars.

2.6 A toy model of the Solar System

The model can be used as a simple way to predict the distribution of particles within the inner Solar System. As a toy model, I assume a belt with a radius of $r_0 = 3$ au, and vary its mass to best fit the optical depth of the zodiacal cloud at 1 au. This is not meant to provide a more accurate description of the zodiacal cloud than currently available models. Rather it is used to serve as a quick illustration of the model in a situation where there are observational constraints on its predictions before it is applied to systems with fewer constraints. The source of dust at 3 au could either be from collisions of asteroids, or delivery of material from comets. For a face-on optical depth at 1 au of $\tau(1 \text{ au}) = 7.12 \times 10^{-8}$

(Kelsall et al., 1998), fitting the radial optical depth profile to this value gives a dust mass of $M_{\text{dust}} = 6.62 \times 10^{-9} M_{\oplus}$, including all particle sizes up to $D = 2$ cm. This agrees with the predicted mass of the inner zodiacal cloud from Nesvorný et al. (2011), who predicted a mass of $\sim 6.6 \times 10^{-9} M_{\oplus}$ within the inner 5 au, assuming a single grain size of $D = 100 \mu\text{m}$ and grain density $\rho = 2 \text{ g cm}^{-3}$, though this estimate is dependent upon the model parameters and chosen grain size. This low value of the dust mass means that P-R drag is significant, such that the toy model predicts only a modest drop (factor of ~ 2) in optical depth inwards of the source region due to collisions, giving a relatively flat radial profile.

The predicted size distribution at different radii from the Sun is given in Figure 2.12 (top) in terms of the differential number density of particles. Number density is used to better compare with observations; the number density at a given radius can be found from optical depth as

$$n_v(D) = \frac{\tau(D, r)}{h\sigma}, \quad (2.35)$$

where $h = 2r \sin \epsilon$ is the height of the disc, and $\sigma = \pi D^2/4$ is the cross-sectional area of a grain with a given size. At 3 au the size distribution is as described in Section 2.3.1, with a turnover to a shallower slope below $D_{\text{pr}} = 27.5 \mu\text{m}$. Small grains have a flat radial optical depth profile, and converting number per cross-sectional area to number density requires dividing by r , such that closer to the star the number density of small grains increases. Particles larger than D_{pr} are depleted by collisions inwards of the source belt, causing the slope of the size distribution to be steeper inwards of 3 au. The model predicts a steep slope of -4.7 for large particles inwards of 3 au, with a shallower slope for small grains.

Also shown in Figure 2.12 (bottom) is a comparison of the model with two empirical models for the size distribution of dust at 1 au in the Solar System which were obtained by fitting to measurements of interplanetary dust particles (IDPs). Grun et al. (1985) developed an empirical model for the interplanetary meteoroid flux at 1 au based on data from the lunar crater size distribution for large meteoroids ($m \gtrsim 10^{-6} \text{ g}$, or $D \gtrsim 91 \mu\text{m}$), and in situ measurements from micrometeoroid detectors on board the Highly Eccentric Orbit Satellite 2 (HEOS-2) and the Pegasus satellite for small meteoroids ($m \lesssim 10^{-9} \text{ g}$, or $D \lesssim 9.1 \mu\text{m}$). Love and Brownlee (1993) determined the mass flux distribution of meteoroids in the mass range $10^{-9} \leq m \leq 10^{-4} \text{ g}$ accreted onto Earth using hypervelocity impact craters on the Long Duration Exposure Facility (LDEF) satellite. This is equivalent to a size range of $9.1 \leq D \leq 424 \mu\text{m}$. The size distribution shown for LDEF has taken into account the effect of gravitational focussing, as the Earth's gravity will increase the flux of particles onto the Earth. Fluxes were converted to number densities using equation 3 from Grun et al. (1985), assuming an isotropic flux.

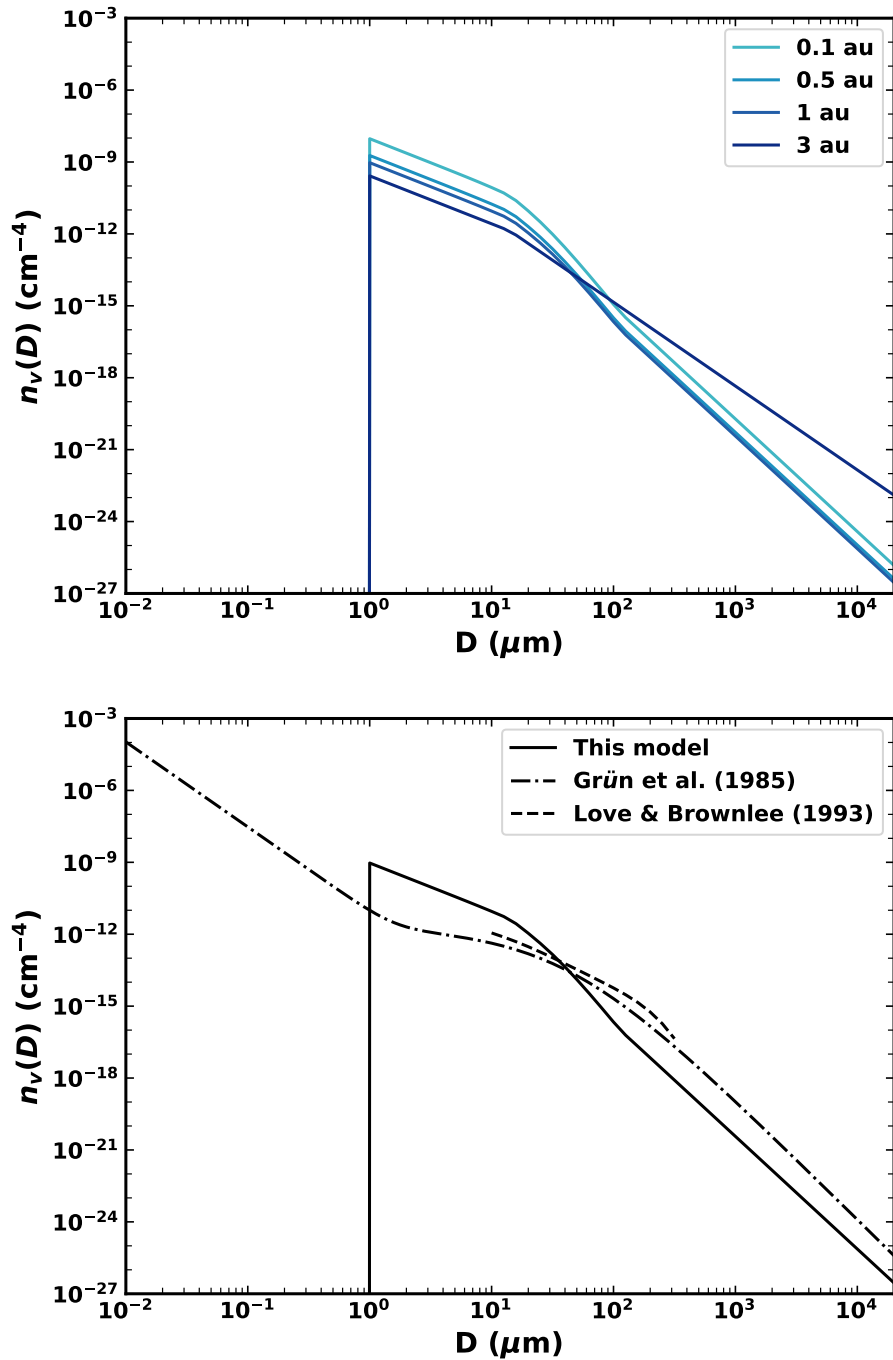


Fig. 2.12 Size distribution, shown as differential number density, for a belt with radius 3 au fitted to the optical depth of the inner Solar System at 1 au as a toy model for the zodiacal cloud. Top: the size distribution at different radii in the disc. Bottom: the size distribution at 1 au for the model (solid), and the empirical models of Grun et al. (1985) (dash-dotted) and Love and Brownlee (1993) (dashed).

For large particle sizes, which will be the most collisional, the slope of the model from Grun et al. (1985) is -4.9, in good agreement with the analytical model. For collisional particles, the analytical size distribution close in will be $\propto n_0(D)/\eta_0(D)$, such that the size dependence of the factor k affects the slope of the size distribution inside of the belt. Without the size dependence of k , the slope of the size distribution would be shallower, and have a poorer fit to that of the Grun et al. (1985) model, providing further justification for the size dependence of k .

Despite the good agreement for large particles, there are some differences between the analytical and empirical models at small sizes. While all the models include a turnover to a shallower slope at smaller particle sizes, the turnover is smoother in the empirical models, whereas the simpler analytical prescription necessitates a sharper change. The analytical model turns over at a value of $D_{\text{pr}} = 27.5 \mu\text{m}$, however the empirical models suggest that this should be slightly larger, perhaps closer to $D_{\text{pr}} = 100 \mu\text{m}$. Wyatt et al. (2011) showed that the size distribution of drag-dominated particles can be indicative of the redistribution function. Generally the redistribution function power law is assumed to lie in the range $3 \leq \alpha_r \leq 4$. The empirical size distributions have shallower slopes than the analytical model at small particle sizes, so a value of $\alpha_r = 3$ is chosen to better match the empirical models. This fits the slope of the LDEF model, and is the smallest value that would typically be expected for α_r . In order to best fit the Grun et al. (1985) model, a value of $\alpha_r \sim 2$ would be needed. Another discrepancy between the models is that Grun et al. (1985) suggests there is a high density of submicron grains. However, such small grains are not included in this chapter as it is expected that they will be blown out by stellar radiation pressure. Despite these discrepancies, the analytical model captures most of the main features of the empirical models, which are also not completely accurate, and is good for a rough approximation of the size distribution at 1 au. This provides confidence that my model gives reasonable predictions for the exozodi properties in other systems, which are described in the following chapter.

2.7 Conclusions

In this chapter I have presented an analytical model which can predict two-dimensional size distributions in debris discs for particle size and radial distance, taking into account the effects of both collisional evolution and P-R drag. This builds on previous, simpler analytical models which only considered a single dimension. My model provides a reasonable approximation to results from detailed numerical models whilst being much faster, allowing it to be used to explore the parameter space of outer belts. Finding a two-dimensional size distribution means it can be used with realistic grain properties to predict the thermal emission resulting

from dust produced by planetesimal belts of different parameters around stars of different spectral types. The model predicts the distribution of dust in the inner planetary system, and can therefore be used to predict the distribution of exozodiacal dust resulting from P-R drag migration from an outer belt. The model can be applied to stars where exozodiacal dust has been detected to determine whether their exozodis originate from dust being dragged inwards from an outer planetesimal belt while undergoing collisions, or whether an alternative scenario is needed. In Chapter 3 this model will be applied to observations of mid-infrared emission around nearby stars.

Chapter 3

Predictions for exozodiacal dust dragged in from an exo-Kuiper belt

Abstract

In this chapter I apply the analytical debris disc model of Chapter 2 to predict the levels of dust dragged into the habitable zones of other stars from an outer belt, seen as an excess of 11 μm emission (R_{11}). I show that P-R drag should produce exozodiacal dust levels detectable with the Large Binocular Telescope Interferometer (LBTI, $R_{11} > 0.1\%$) in systems with known outer belts. Therefore, non-detections in such systems may indicate removal of dust by an intervening planet. I also find that LBTI could detect exozodiacal dust dragged in from a belt too faint to detect at far-infrared wavelengths, with fractional luminosity $f \sim 10^{-7}$ and radius $\sim 10 - 80$ au. Application to systems observed with LBTI shows that P-R drag can likely explain most (5/9) of the exozodiacal dust detections in systems with known outer belts. Two systems (β Uma and η Corvi) have exozodis which are too bright, and may be due to exocomets. I suggest that the three systems in the HOSTS survey with exozodiacal dust detections but no known belt may have cold planetesimal belts too faint to be detectable in the far-infrared which dust is dragged in from. Even systems without outer belt detections could have exozodiacal dust levels $R_{11} > 0.04\%$ due to P-R drag which are problematic for exo-Earth imaging. In-depth application of the model to LBTI observations of β Leo shows that when the observational geometry is taken into account, P-R drag from its outer belt is insufficient to explain the habitable zone dust seen. However, superposition of a second, warm asteroid belt at ~ 5 au gives a distribution of dust which fits the radial profile of habitable zone dust and the star's SED simultaneously.

3.1 Introduction

Warm exozodiacal dust is seen around $\sim 20\%$ of stars at the levels which are currently detectable. The HOSTS survey (Ertel et al., 2018a, 2020) searched 38 nearby main sequence stars for warm exozodiacal dust using nulling interferometry at $11 \mu\text{m}$ with the Large Binocular Telescope Interferometer (LBTI). Warm dust was detected around 10 stars, giving a detection rate of 26%. In addition, a very strong correlation was found between the presence of warm exozodiacal dust and cold dust detected in the far-infrared. Of the nine stars in the survey known to host cold debris discs, seven had detected exozodis (78%). While many scenarios have been proposed for the origin of exozodis, this correlation suggests an origin related to inward transport of material from an outer planetesimal belt. Dust produced in the collisional cascade of an outer belt will inevitably migrate inwards by P-R drag, unless it is removed by other mechanisms such as intervening planets (Bonsor et al., 2018). Consequently, it is important to consider P-R drag from an outer belt as a source of exozodiacal dust, and determine whether this mechanism can produce the correct level and distribution of dust to explain the observations.

In Chapter 2, I presented an analytical model for the distribution of dust grains in terms of their sizes and radial distribution when considering the interplay of collisions and P-R drag. Since this includes the radial distribution inwards towards the star, this can predict the distribution of dust in the habitable zone of a star which is dragged inwards from an outer belt. Thus, the model can predict the mid-infrared emission and levels of exozodiacal dust created by P-R drag from an cold planetesimal belt.

In this chapter, I apply the analytical model of Chapter 2 (Rigley and Wyatt, 2020) to mid-infrared observations of warm exozodis to ascertain whether they can be explained by a P-R drag origin. In Section 3.2 I use the model to make general predictions about the excess emission at different wavelengths for outer belts of different masses and radii, and thus the detectability of habitable zone dust produced by P-R drag. I then apply the model to the stars observed by the HOSTS survey which have outer debris discs, and predict whether their $11 \mu\text{m}$ emission could be from P-R drag in Section 3.3. In Section 3.4 I apply the model to one system from the HOSTS survey, β Leo, in more depth, to ascertain whether its radial profile of habitable zone dust fits a P-R drag model and constrain the underlying planetary system. Finally, I give my conclusions in Section 3.5

3.2 Thermal emission

As discussed in Section 2.4.3, SEDs can be found from the model of Chapter 2 for a given distribution by finding realistic grain temperatures and absorption efficiencies, and integrating the optical depth over grain size and radius.

For example, Figure 3.1 shows the resulting SED for the disc used in the toy model of the zodiacal cloud in Section 2.6, as well as the contributions from different radii. This disc produces small excesses at all wavelengths relative to the stellar flux. The fractional excess at $11 \mu\text{m}$ is 7.6×10^{-5} , and the emission peaks at $19 \mu\text{m}$, where the fractional excess is 2.9×10^{-4} . As would be expected, at the shortest wavelengths the emission is dominated by the warmest dust, which is close to the star. Habitable zone dust dominates the mid-infrared, and the colder dust further out dominates far-infrared emission.

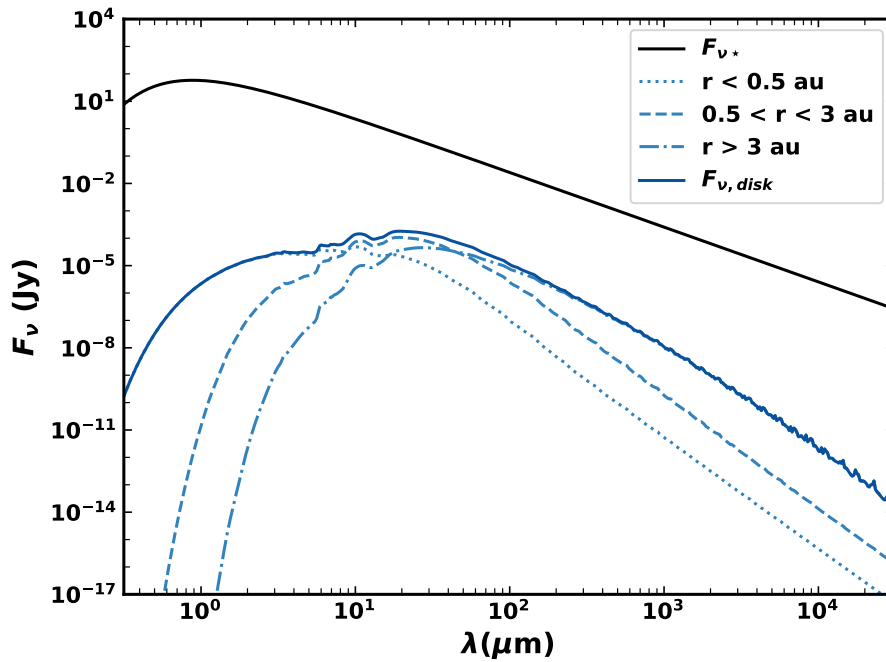


Fig. 3.1 SED for the toy model for the zodiacal cloud from Section 2.6, showing the contributions from different radii ranges, as well as the total disc emission and that of the Sun, as observed at a distance of 10 pc.

Figure 3.2 shows predictions of fractional excesses and fractional luminosity from the model for discs across the broader parameter space of dust mass and belt radius for a Sun-like star, where the dust mass is defined to be the mass in grains up to $D_{\text{max}} = 2 \text{ cm}$ in the belt. Figures 3.2a, 3.2b, and 3.2c show the predicted excesses at $11 \mu\text{m}$, $24 \mu\text{m}$, and $70 \mu\text{m}$ respectively for various discs. The highest excesses are seen for discs with small radii and

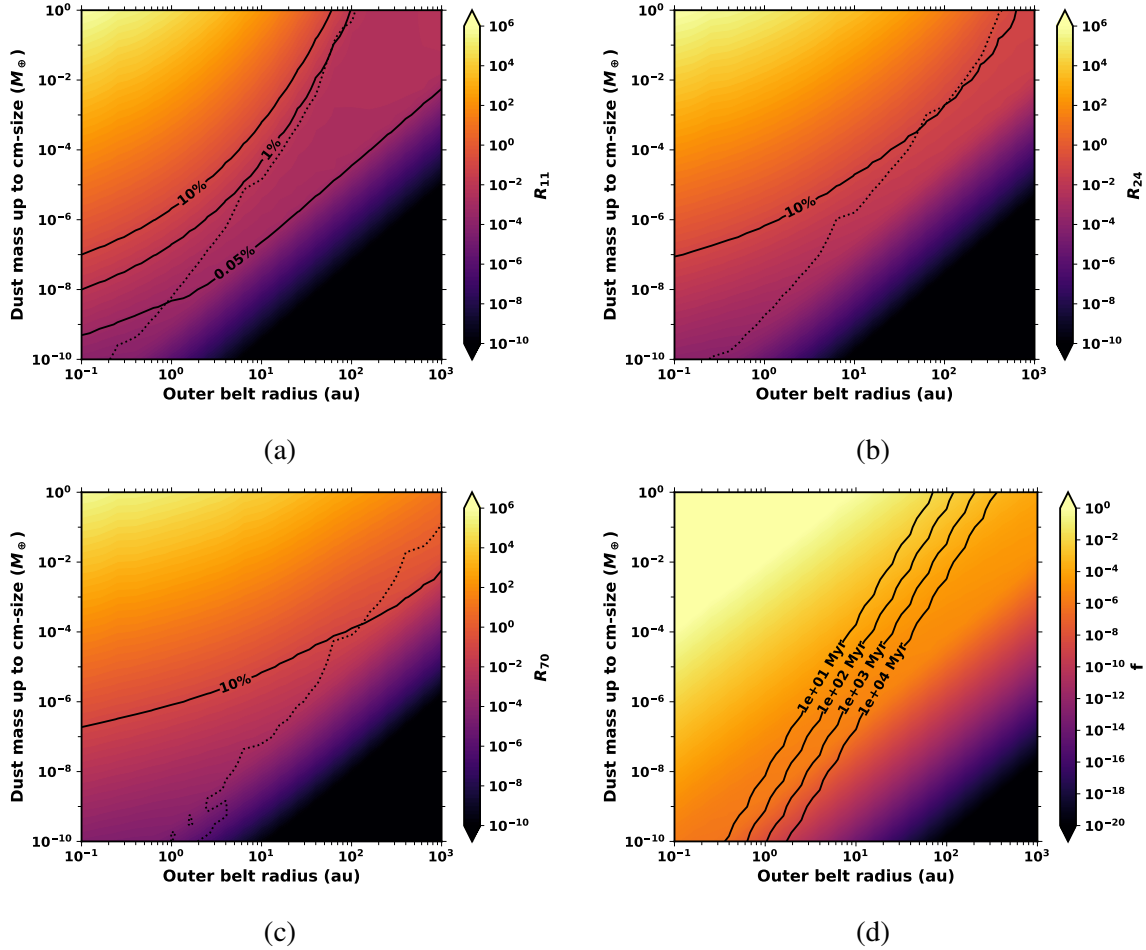


Fig. 3.2 Fractional excesses and luminosities for discs of various dust masses M_{dust} and belt radii r_0 around a Sun-like star, as predicted by my analytical model for realistic asteroidal grains. Dotted contours show where 50% of dust emission comes from the planetesimal belt, with the other half from dust interior to that belt, such that the thermal emission of discs to the left of these contours is dominated by the parent belt. (a) Fractional excess at $11 \mu\text{m}$, R_{11} . Contours show excesses of 10%, 1%, and 0.05%, which correspond to the approximate sensitivities of WISE, KIN, and LBTI. (b) Fractional excess at $24 \mu\text{m}$, R_{24} . The sensitivity of Spitzer/MIPS photometry, $\sim 10\%$, is indicated by a contour. (c) Fractional excess at $70 \mu\text{m}$, R_{70} . The sensitivity of Spitzer/MIPS or Herschel/PACS photometry, $\sim 10\%$, is indicated by a contour. (d) Fractional luminosity f of discs, as obtained by integrating the disc flux over the whole spectrum. Contours show upper limits on dust mass for discs around a Sun-like star at different ages, based on the model of Wyatt et al. (2007a), using the parameters from Sibthorpe et al. (2018).

high dust masses, but these will have short lifetimes, as they would rapidly grind down by collisions to a lower mass (Wyatt et al., 2007a). While a large range of belt radii are considered, most planetesimal belts would be expected to lie between ~ 1 au and a few hundred au. Discs which are detectable with a given instrument should lie above a given excess level, which corresponds to the instrument sensitivity. The solid lines in Figures 3.2a, 3.2b, and 3.2c give an indication of the regions of parameter space for which the discs would be detectable. For example, it is estimated that LBTI can detect mid-infrared ($11 \mu\text{m}$) null excesses down to 0.05% (Hinze et al., 2016), and KIN had a sensitivity of $\sim 1\%$. Thus Figure 3.2a shows how the improved detection capabilities of LBTI mean that the exozodis are detectable for a much larger range of outer belt properties than with previous instruments. Photometry, which is used at all wavelengths considered here, has a detection limit $\sim 10\%$. For example, Spitzer/MIPS (e.g. Su et al., 2006; Meyer et al., 2006) and Herschel/PACS (e.g. Eiroa et al., 2013; Sibthorpe et al., 2018) have been used to detect debris discs at $24 \mu\text{m}$ and $70 \mu\text{m}$. WISE (Wright et al., 2010) has been used at $12 \mu\text{m}$ to observe bright exozodis (Kennedy and Wyatt, 2013).

The dotted contours on the excess plots show the line where 50% of the disc emission comes from the planetesimal belt. Discs to the left of this contour have most of their emission originating from dust in the parent belt, while discs to the right have emission which is dominated by dust in the inner regions of the system. At $24 \mu\text{m}$ and $70 \mu\text{m}$, this means that the emission from most discs that can be detected must originate in the planetesimal belt, rather than closer in. However, at $11 \mu\text{m}$, for parent belts which are not very close to the star ($r_0 \gtrsim 10$ au), emission will be dominated by the warm dust which is dragged in to the inner regions. The fractional luminosity, f , of the discs is shown in Figure 3.2d, as found by integrating the disc flux and stellar spectrum then finding the ratio. As expected, the fractional luminosity correlates with the fractional excesses.

As mentioned previously, in situ belts at small radii will rapidly grind down by collisions such that their mass is depleted. Wyatt et al. (2007a) showed that the mass of a planetesimal belt will decrease with time once the largest planetesimals in the belt are broken up by collisions, giving a time dependence of

$$M_{\text{tot}}(t) = M_{\text{tot}}(0)/(1 + t/t_c(0)), \quad (3.1)$$

where M_{tot} is the mass of the planetesimal belt, and $t_c(0)$ is the collision timescale of the largest planetesimals at the initial time. Since the collision timescale depends on the total mass, at late times the mass of the belt will be independent of its initial mass. Based on

equation 19 of Wyatt et al. (2007a), the maximum dust mass at a given age, t_{age} , is

$$M_{\text{dust,max}} = \frac{2.3 \times 10^{-15} \rho r_{\text{BB}}^{13/3} (dr/r) A}{M_{\star}^{4/3} t_{\text{age}}} \quad (3.2)$$

in M_{\oplus} , where ρ is in kg m^{-3} , r_{BB} is the radius which would be inferred from the dust temperature assuming black body emission in au, A in $\text{km}^{0.5} \text{J}^{5/6} \text{kg}^{-5/6}$ is a parameter which can be found by fitting to observations, M_{\star} is in M_{\odot} , and t_{age} is in Myr. It has been assumed that the mean eccentricities and inclinations of planetesimals are equal.

The Wyatt et al. (2007a) model gives the total planetesimal belt mass, which has been converted to mass in dust up to 2 cm in diameter by scaling with a factor $M_{\text{dust,max}} = \sqrt{\frac{2 \times 10^{-5}}{D_c}} M_{\text{max}}$, where D_c is the maximum planetesimal size in km. This assumes that the size distribution of bodies up to the largest planetesimals has a slope of -3.5. Sibthorpe et al. (2018) fitted the model to observations of Sun-like stars from the Herschel DEBRIS survey. The model was chosen to have the parameters $\rho = 2700 \text{ kg m}^{-3}$ and $dr/r = 1/2$. The best fitting model also had $A = D_c^{0.5} Q_D^{\star 5/6} e^{-5/3} = 5.5 \times 10^5 \text{ km}^{0.5} \text{J}^{5/6} \text{kg}^{-5/6}$. The model uses the black body radius of a planetesimal belt, while the resolved radius is typically 1–2.5× larger due to inefficient emission of dust grains (Booth et al., 2013; Pawellek et al., 2014). Therefore, to compare with my model I assume that the disc radius plotted in Figure 3.2 is $r_0 = 2r_{\text{BB}}$ as an approximation. The upper limits on dust mass up to cm-size grains from this model for a Sun-like star at different ages are shown in Figure 3.2d. The Wyatt et al. (2007a) model shows that the brightest belts, which have very small radii and high dust masses, would not be in steady state even around very young stars of a few hundred Myr. Therefore, the region of parameter space I would expect to observe systems in is at lower dust masses and larger radii.

A direct comparison of the mid-infrared excesses which can be detected by LBTI with the 10% limits at 24 μm and 70 μm is shown in Figure 3.3. The model predicts that stars which have excesses detected at longer wavelengths with photometry should have exozodiacal dust levels due to P-R drag from the outer belt which are detectable by LBTI. Therefore, non-detections around stars with known cold dust could imply other mechanisms are depleting habitable zone dust. For example, planets could deplete exozodi levels by accreting dust or ejecting it from the planetary system, such that this could be a way to infer the presence of planets (see Bonsor et al., 2018).

The shading in Figure 3.3 highlights the region of parameter space for which it may be possible to detect warm exozodiacal dust that has been dragged inwards from an outer belt which is not currently detectable in far-infrared photometry. However, the limits on

dust mass based on the model of Sibthorpe et al. (2018) shown in Figure 3.2d rule out a lot of this shaded region around stars older than ~ 100 Myr. For example, for a Gyr Sun-like star, it remains possible for LBTI to detect warm dust dragged in from planetesimal belts without a far-infrared detection, however the region of parameter space in which such a disc might be present is smaller than the shaded region shown in Figure 3.3, e.g. requiring a planetesimal belt $\gtrsim 3$ au in radius for asteroidal grains. Consequently, it may be the case that LBTI detections without far-infrared excesses are the result of dust being dragged inwards from a planetesimal belt which is too faint to detect at longer wavelengths, but there are limits on the possible disc radius and dust mass of such systems, depending on the age of the star. There were three such detections in the HOSTS survey (Ertel et al., 2020). Also of note in Figure 3.3 is the dotted contour, which shows where half of the $11 \mu\text{m}$ emission comes from the planetesimal belt. Discs for which emission is dominated by the belt will lie to the left of this line, but comparison with the age limits shows that such discs will typically collisionally deplete on a ~ 10 Myr timescale. Therefore if warm dust is detected by LBTI in a system without a far-infrared detection, it would not be dust in the planetesimal belt that is being detected, but rather the dust dragged into the inner region.

Throughout this study grains have been assumed to be asteroidal, with no porosity, and a core-mantle model with $1/3$ silicates and $2/3$ organic material. Grain composition may differ from that assumed in Section 2.2.2, so the effect of using cometary grains was investigated. These grains came from the core-mantle model of Li and Greenberg (1998), with a porosity $p = 0.95$; half of the vacuum is filled with water ice. The matrix remains $1/3$ silicates and $2/3$ organic material, as for the asteroidal composition. This gives grains with a much lower density of $\rho = 0.688 \text{ g cm}^{-3}$. Overall there is no qualitative change to the conclusions with this alternative composition, but there are relatively minor quantitative changes. The excess plots shown in Figure 3.2 were not significantly affected, with the same overall trends, but a slight change in contour shape. Figure 3.3 shows how a cometary composition affects the region of parameter space for which dust is detectable. The parameter space for which LBTI can detect exozodiacal dust dragged inwards from an undetected planetesimal belt decreases slightly with a cometary composition. Only belts which are relatively close to the star, $r_0 \lesssim 5$ au, can be detected uniquely by LBTI, and the relevant region of parameter space is greatly reduced by collisional evolution. Stars known to host cold debris belts should still be detectable by LBTI in the mid-infrared.

The detectability of discs around A stars is demonstrated in Figure 3.4, which shows the detection thresholds for realistic asteroidal and cometary grains. Again the model predicts that stars with excesses detectable at longer wavelengths should have detectable levels of

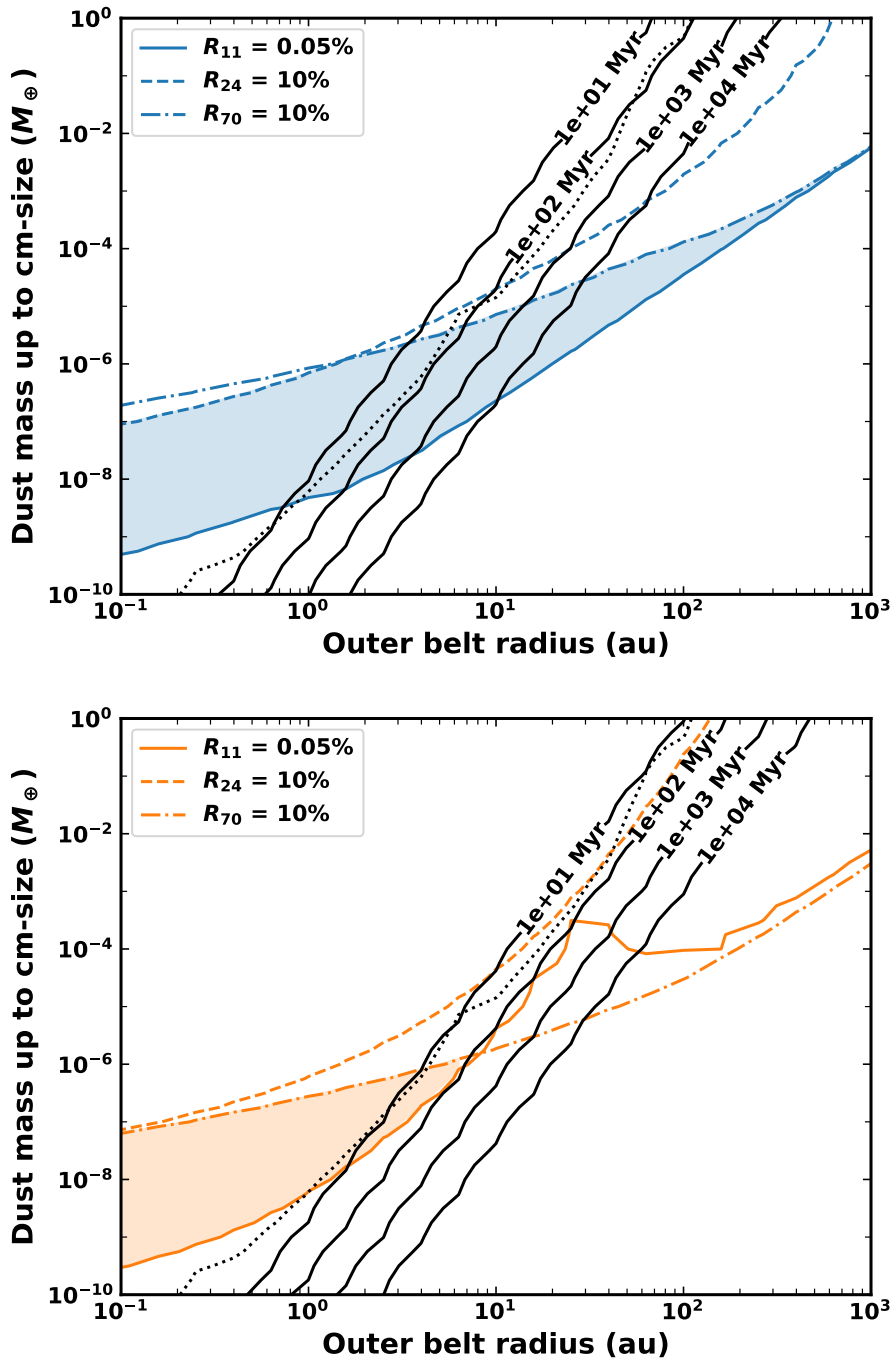


Fig. 3.3 Detectability thresholds for different wavelengths for asteroidal grains (top) and cometary grains (bottom). The solid contours show $R_{11} = 0.05\%$, the level above which LBTI should be able to detect discs. Dashed and dashed-dotted contours show where a disc would have a 10% excess at $24\ \mu\text{m}$ and $70\ \mu\text{m}$ around a Sun-like star, such that the parent belt is detectable in far-infrared photometry. The shaded region is the region of parameter space for which I predict that LBTI would be able to detect warm dust dragged in from a cold outer belt that has not been detected in the far-infrared. Solid lines show the upper limits on dust mass at given ages based on the model of Wyatt et al. (2007a), as fitted to Sun-like stars in Sibthorpe et al. (2018). Dotted contours show where 50% of $11\ \mu\text{m}$ dust emission comes from the planetesimal belt, with the other half from dust interior to the belt, such that the thermal emission of discs to the left of these contours is dominated by the parent belt.

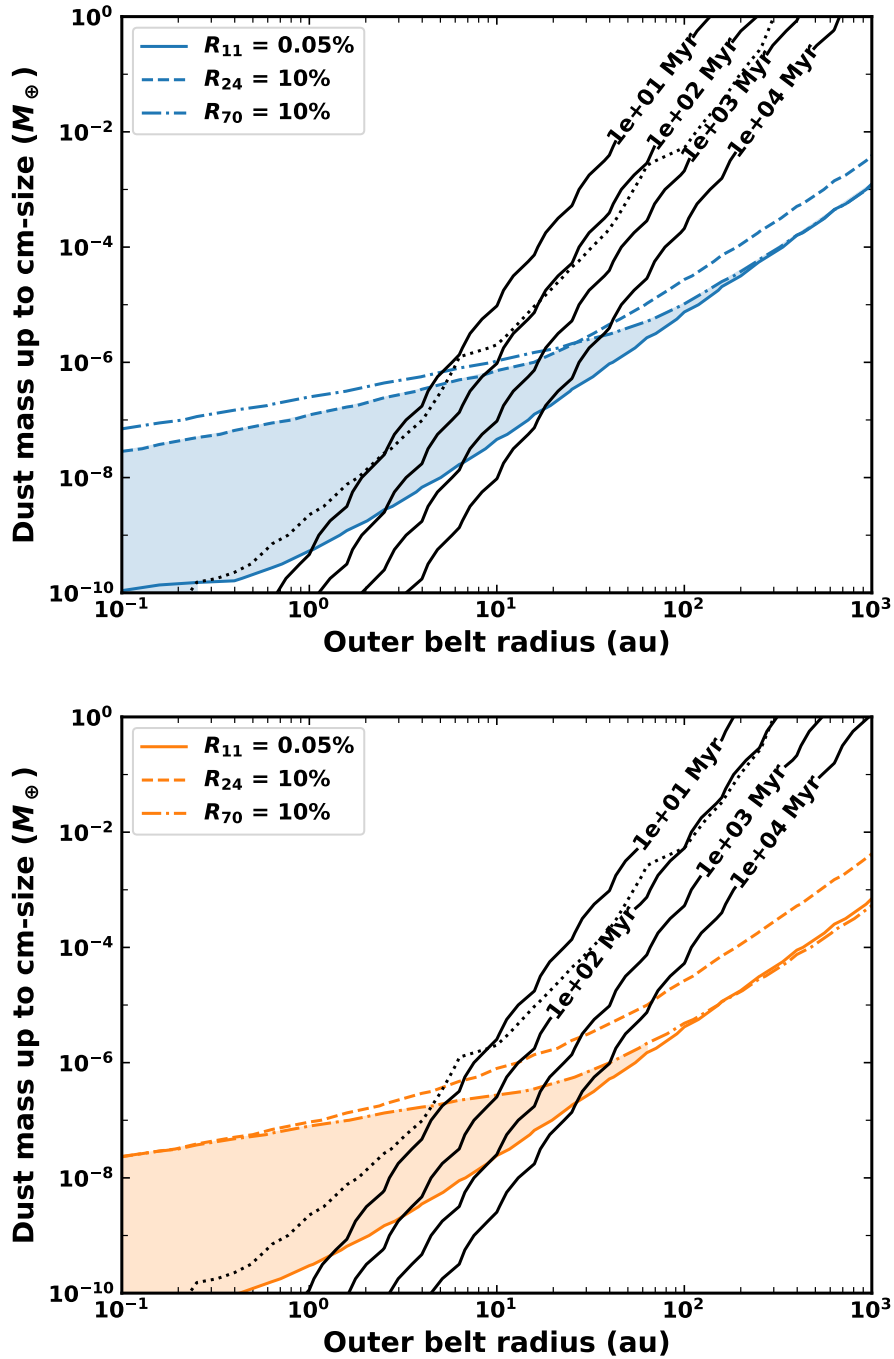


Fig. 3.4 The same as Figure 3.3, but for A-type stars. Solid lines show the upper limits on dust mass at given ages based on the model of Wyatt et al. (2007b).

exozodiacal dust. Overall the conclusions are similar to those for Sun-like stars, though LBTI could detect slightly lower dust masses around an A star.

3.3 Application to the HOSTS survey

The HOSTS survey (Ertel et al., 2018b, 2020), searched for exozodiacal dust around 38 nearby main sequence stars, of which 9 have previously detected cold outer debris belts. LBTI uses nulling interferometry to subtract the stellar emission, resulting in a measurement of null depth. Predictions can be made using the analytical model presented in Chapter 2 for the excess around a certain star given the radius of the planetesimal belt and the mass of millimetre to centimetre-sized grains. To take into account the fact that total flux (which is that reported in Figure 3.2) will be attenuated by the LBTI transmission pattern, my predicted fluxes are divided by a factor of 2 to better correspond to null depths. This is a very rough approximation, as the transmission pattern is highly dependent on the distance to the star and disc orientation. It is likely that the observed null depth will be less than half of the fractional excess, but the precise factor relating fractional excesses to null depths will depend on the geometry and vary between systems, such that individual systems need to be modelled (see Kennedy et al., 2015).

Predictions are presented in Figure 3.5 (top) for null depths around stars of different spectral types for discs of certain dust masses and planetesimal belt radii, assuming asteroidal grains. Also shown are results from HOSTS survey stars with known debris discs. While the sensitivity of LBTI is around 0.1%, predictions are shown down to $10^{-3}\%$, i.e. just below the null depth corresponding to 1 zodi. While the exact null depth corresponding to 1 zodi will vary between systems, in Section 2.6 I found a fractional excess of $7.6 \times 10^{-3}\%$ for my toy model of the zodiacal cloud, giving a null depth in good agreement with the value of $\sim 2 \times 10^{-3}\%$ found by Kennedy et al. (2015) for the null depth around a Sun-like star corresponding to 1 zodi. Predictions down to this level are important because detection of Earth-like planets would be hampered by dust at the level of 10–20 zodis (Beichman et al., 2006; Defrère et al., 2010; Defrère et al., 2012; Roberge et al., 2012) for both visible coronagraphs and nulling interferometers.

When dust mass is kept fixed, Figure 3.5 shows that the predicted null as a function of planetesimal belt radius shows the same behaviour for all disc masses and spectral types. The null starts off high for the smallest radii, and drops sharply as radius is increased, before reaching a plateau for intermediate radii, then drops off rapidly again at the largest radii. The first transition (i.e. the beginning of the plateau) occurs when the $11 \mu\text{m}$ emission changes from being dominated by dust in the planetesimal belt for smaller radii, to being dominated

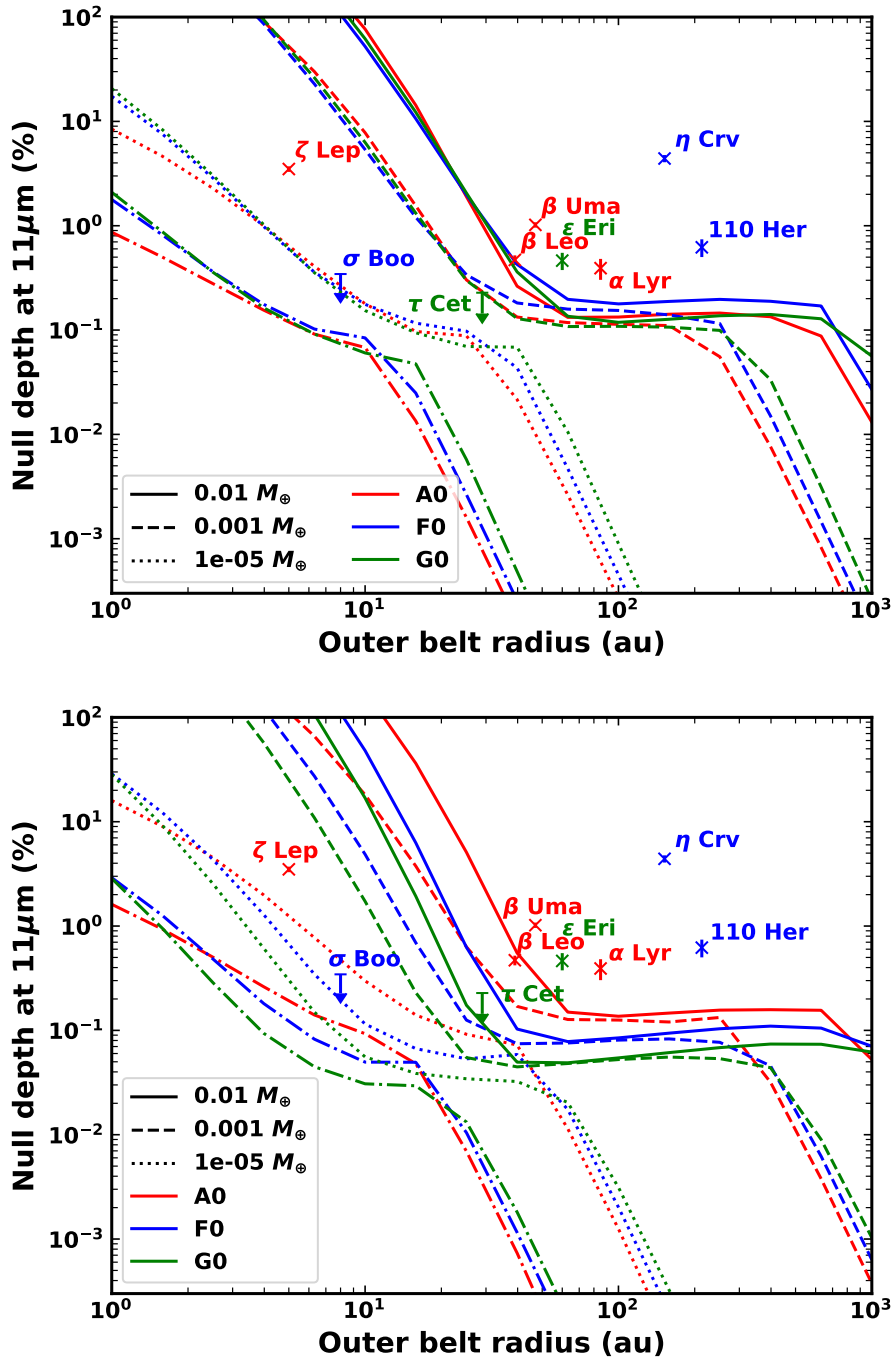


Fig. 3.5 Null excess predictions at 11 μm for planetesimal belts of different radii, dust masses and stellar spectral types with asteroidal grains (top) and cometary grains (bottom). The HOSTS results for the nine stars with detected debris discs are also shown. Arrows show 3σ upper limits for stars which had no detection.

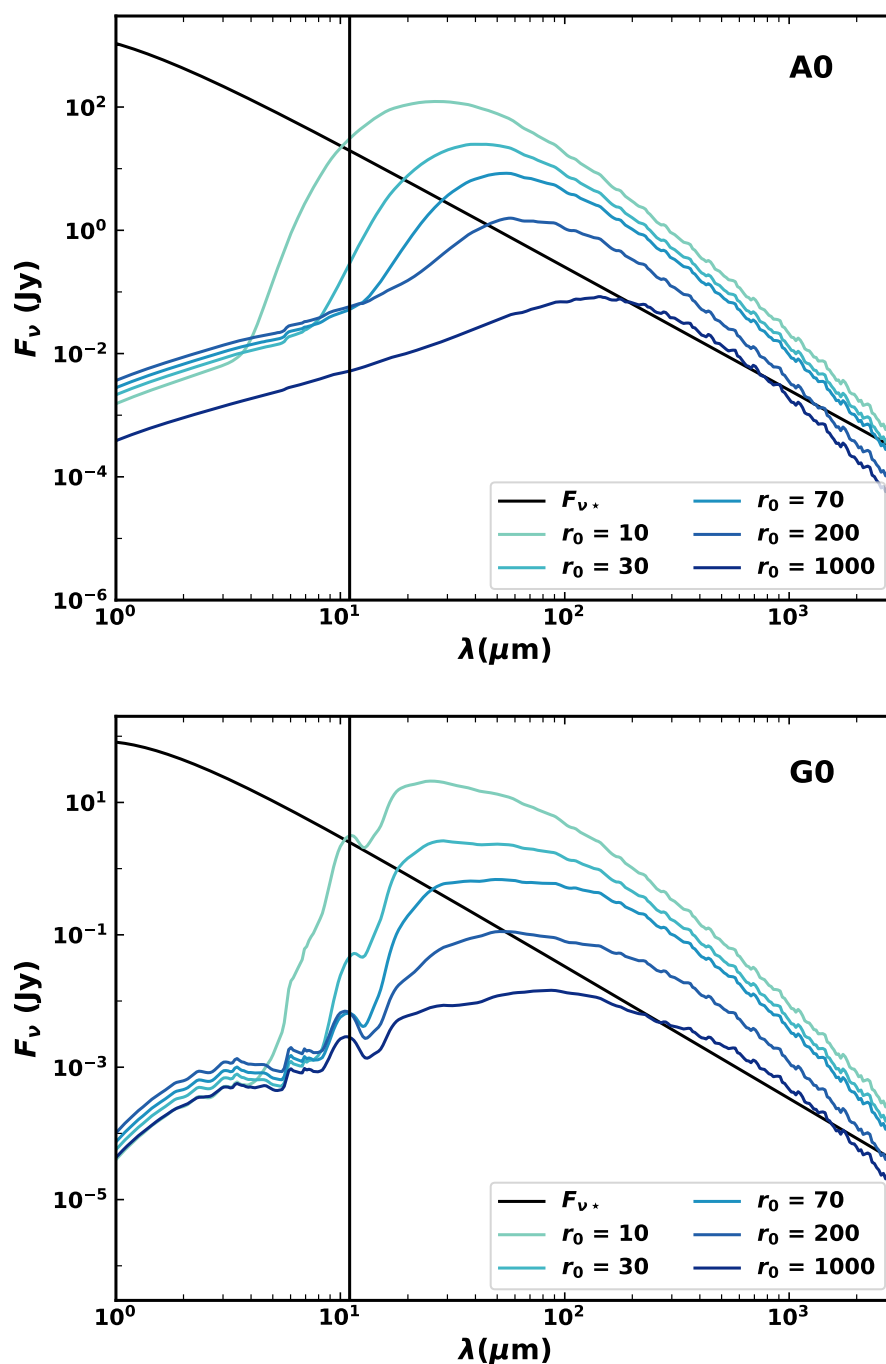


Fig. 3.6 SEDs for discs of mass $M_{\text{dust}} = 0.01 M_{\oplus}$ around stars of spectral type A0 (top) and G0 (bottom), with planetesimal belts of different radii. In each case the stellar spectrum is shown in black. The vertical line highlights 11 μm , the wavelength at which LBTI measurements are made. It is assumed that the systems are at a distance of 10 pc from the Sun.

by warm dust interior to the belt. For example, for a disc with mass 0.01, half of the flux comes from the planetesimal belt for $r_0 \sim 50$ au (see dotted line in Figure 3.2a), and the plateau begins at around 50 au. The origin of the plateau is evident from Figure 2.9, which showed that at fixed dust mass there is little change in the levels of dust dragged into the innermost regions when varying the belt radius. Thus the null does not vary significantly with planetesimal belt radius when emission is due to dust interior to the belt. However, at the largest belt radii there is a sharp decrease in null with belt radius once more. This is due to the discs becoming drag-dominated, such that increasing radius decreases the density, reducing the levels of warm dust. Less of a plateau is seen for lower mass discs, as they become drag-dominated at much smaller radii. Many of the observed HOSTS stars appear to cluster around the region where the high dust mass curves plateau.

It should be noted that the field of view of LBTI is 2.3" in diameter, such that emission from a planetesimal belt at tens of au would be outside the aperture used to observe stars in the HOSTS survey. The radii from which emission can be detected will be dependent upon distance to the star, and depend on other factors such as the disc orientation, which will affect the LBTI transmission pattern. For example, if a star is very far away, all of the dust emission could be within the first null of the LBTI transmission pattern such that no emission is seen. A more detailed discussion of modelling the transmission pattern can be found in Kennedy et al. (2015), and it would be necessary to consider the specific parameters of individual systems to fully understand the effect. Discs with outer belts at more than ~ 40 au will have their $11 \mu\text{m}$ emission dominated by warm dust in the inner regions, however the limitations of the field of view will still reduce the observed null depth from my predictions here.

Interestingly, stellar spectral type does not significantly affect the predicted nulls (for fixed dust mass). To investigate this further, SEDs are shown in Figure 3.6 for discs around both A (top) and G (bottom) stars, with a dust mass of $0.01 M_{\oplus}$. The main effect of stellar spectral type is the SED shape: SEDs are mostly smooth for discs around A stars, while some features are seen at shorter wavelengths around F and G stars. This is because the larger blowout size for higher-mass stars (equation 2.2) prevents the appearance of the silicate feature. The $11 \mu\text{m}$ silicate feature will impact the null depth predictions with asteroidal grains. These SEDs also show how as radius is increased, the $11 \mu\text{m}$ flux decreases, then reaches a point where it becomes constant, before decreasing again. The peak of the SED moves to larger wavelengths as the planetesimal belt becomes colder.

Grain composition plays an important role, as the optical properties of grains impose a lot of structure on the SED. The null depths for grains which are cometary are presented in Figure 3.5 (bottom). Broadly the shape of the null curves is the same for a cometary composition, with plateaus which occur at a similar level to the asteroidal case. Asteroidal

grains exhibit a feature at $11\ \mu\text{m}$ due to the presence of silicates, which impacts predictions of mid-infrared excesses. SEDs for cometary grains lack the $11\ \mu\text{m}$ feature, but have other features at different wavelengths. Changing the composition therefore means that different stellar spectral types no longer give the same null for a disc of certain parameters, however the difference between spectral types is small, and generally less than a factor ~ 2 .

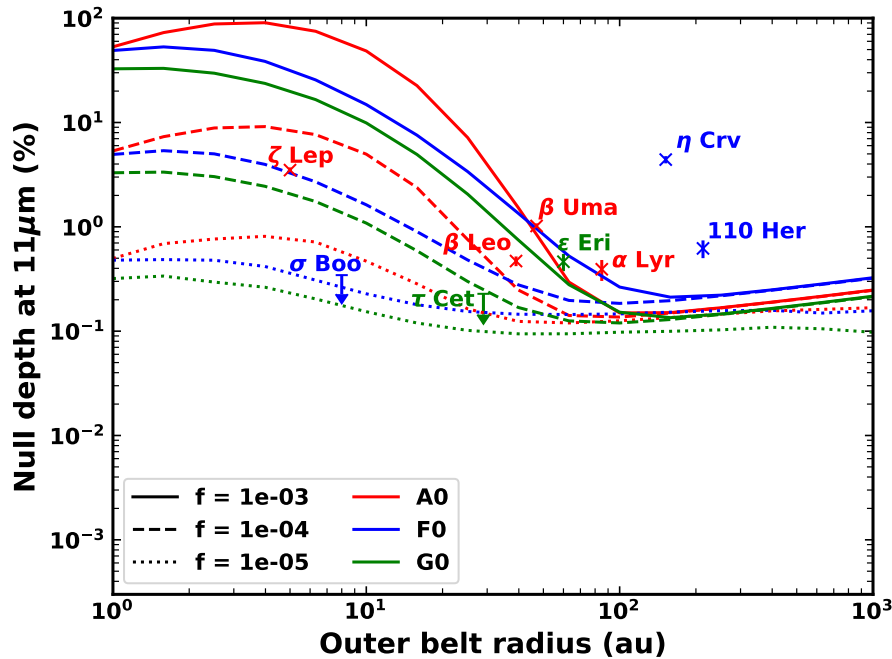


Fig. 3.7 Null excess predictions at $11\ \mu\text{m}$ for planetesimal belts of different radii, fractional luminosities and stellar spectral types with asteroidal grains. The HOSTS results for the nine stars with detected debris discs are also shown. Arrows show 3σ upper limits for stars which had no detection.

Whereas Figure 3.5 showed null predictions for discs when dust mass was kept constant, Figure 3.7 shows the same prediction, but keeping the disc's fractional luminosity constant. The shape of the curves in Figure 3.7 are similar to those for fixed dust mass. However, at fixed fractional luminosity, the disc mass increases with belt radius (Figure 3.2d). Therefore, rather than flattening out the way the constant dust mass curves do, there is an upturn at larger belt radius due to increasing dust mass causing an increased null. Which of Figures 3.5 and 3.7 is appropriate depends on what is known about the disc it is being applied to. If the disc has been observed at sub-mm wavelengths, the dust mass can be derived, whereas if the disc has been observed at far-infrared wavelengths, its fractional luminosity may be known. In either case, the disc should ideally be resolved, such that its radius is known, rather than having to infer this from the spectrum, given the uncertainties in such an inference (Booth

et al., 2013; Pawellek et al., 2014). In general, the reader should bear in mind that implicit with the $11\ \mu\text{m}$ null predictions is the full SED at all wavelengths (Figure 3.6).

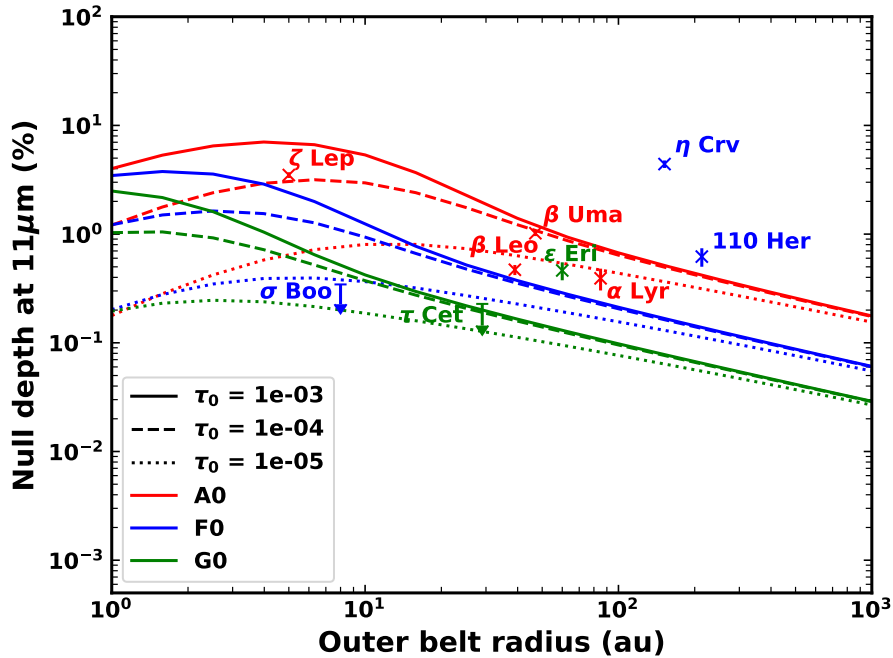


Fig. 3.8 Null excess predictions at $11\ \mu\text{m}$ for planetesimal belts of different radii and stellar spectral types using the model of Wyatt (2005), for different values of the belt optical depth τ_0 . The HOSTS results for the nine stars with detected debris discs are also shown. Arrows show 3σ upper limits for stars which had no detection.

Figure 3.8 shows the null excesses which are predicted using the simpler analytical model of Wyatt (2005), assuming a single grain size of $\beta = 0.5$ and black body grains, for different values of belt optical depth τ_0 . More variation is seen between the spectral types, due to the black body assumption. At fixed optical depth τ_0 there is also a weaker dependence on the belt radius than for fixed dust mass (Figure 3.5) or fractional luminosity (Figure 3.7). While this model gives broad trends, and can be used for an order of magnitude estimate (e.g. Mennesson et al., 2014), the conclusions are significantly different to the more accurate model of Chapter 2. Therefore, the two-dimensional model of Chapter 2 is necessary for more detailed analysis of exozodis.

Table 3.1 Comparison of predictions for null depths from the model based on dust mass M_d and fractional luminosity f with measurements from the HOSTS survey for stars with cold dust, assuming asteroidal grains.

Star	M_{dust} M_{\oplus}	f 10^{-5}	r_0 au	Observed Null %	Predicted Null (M_d) %	Predicted Null (f) %
τ Cet ^a	2.3×10^{-4}	1.2 ^c	29 ^h	< 0.228	0.095	0.073
ϵ Eri	2.2×10^{-3}	8 ^c	60 ⁱ	0.463	0.080	0.079
ζ Lep		8.9 ^d	5 ^j	3.50		5.74
β Uma	$< 6.4 \times 10^{-3}$	1.4 ^d	47 ^k	1.02	< 0.157	0.119
β Leo	$< 1.3 \times 10^{-3}$	2.2 ^d	39 ^k	0.470	< 0.152	0.148
η Crv	0.038	18.6 ^e	152 ^l	4.41	0.133	0.135
σ Boo ^a	$< 5.1 \times 10^{-4}$	1.4 ^f	8 ^{b,m}	< 0.344	< 0.388	0.139
α Lyr	0.013	1.9 ^d	85 ⁿ	0.392	0.164	0.159
110 Her		0.07 ^g	213 ^{b,o}	0.621		0.0056

^a Stars with non-detections have 3σ upper limits given. ^b For discs which have not been resolved, the black body radius is used, corrected by a factor from Pawellek and Krivov (2015) to convert to real radius. ^c Di Folco et al. (2004) ^d Thureau et al. (2014) ^e Lebreton et al. (2016) ^f Sibthorpe et al. (2018) ^g Eiroa et al. (2013) ^h Mean of R_{in} and R_{out} from MacGregor et al. (2016). ⁱ Greaves et al. (1998) ^j Mean of inner and outer radii from Moerchen et al. (2007). ^k Matthews et al. (2010) ^l Marino et al. (2017) ^m Sibthorpe et al. (2018) ⁿ Sibthorpe et al. (2010) ^o Eiroa et al. (2013).

In Table 3.1 my model is applied to the HOSTS stars with far-infrared excesses, based on observed dust masses M_{dust} and fractional luminosities f . While detailed analysis of the SEDs of individual systems is necessary to make precise predictions, this application of the model gives a first approximation. Where given, dust masses are derived from sub-mm observations of SCUBA-2 (Holland et al., 2017), using equation 5 of Wyatt (2008), assuming an absorption opacity of $\kappa_{\nu} = 45 \text{ au}^2 M_{\oplus}^{-1} = 1.7 \text{ cm}^2 \text{ g}^{-1}$. The emission for σ Boo had a large offset from the star, such that it was likely from a background source, and a 3σ upper limit $F_{850} < 2.7 \text{ mJy}$ is used. Two systems, σ Boo and 110 Her, have not been resolved, so instead their black body radii are used. To convert to real radius, I use the power law from Pawellek and Krivov (2015), assuming a composition of 50% astrosilicate and 50% ice, such that $\Gamma = r_0/r_{\text{BB}} = 5.42(L_{\star}/L_{\odot})^{-0.35}$. I can categorise the HOSTS detections as follows:

- Despite large uncertainties, for example given the breadth of the τ Ceti disc (6 – 52 au) and the fact that the σ Boo disc does not have a resolved radius, my model predicts levels for the two systems with non-detections, τ Ceti and σ Boo, which are consistent with their 3σ upper limits. My model suggests that they have exozodi, but these are below the detection limits (unless there is something preventing dust from reaching the inner system).
- 3/7 detections could potentially be explained by my P-R drag model: Vega (α Lyr), β Leo, and ζ Lep, taking into account that I have assumed the null depth to be half of the fractional excess, but this will depend on the geometry of the system. Two of these systems are believed to have additional, warm planetesimal belts closer to the star, which could provide an additional source of exozodiacal dust. Modelling of β Leo suggests the presence of warm dust which is inside the outer belt but outside of the habitable zone (Stock et al., 2010; Churcher et al., 2011), and Vega is thought to have a warm belt close to the star (Su et al., 2013). While not considered by my model, an additional inner belt (and the dust dragged inwards from it) would provide another contribution to the null depth. Thus this strengthens the conclusion that these LBTI detections can be explained by dust dragged in from known planetesimal belts, though if the warm emission contributed by dust dragged in from these inner belts is already large enough to explain the observations then additional processes may be needed to prevent too much dust from reaching the inner regions. ζ Lep has not been observed in the sub-mm, such that there is no reliable estimate of its dust mass, and has only been resolved in the mid-infrared. However, based on its fractional luminosity and the mid-infrared resolved size, it is plausible that the P-R drag scenario explains the observed null.

- 3/7 detections are much higher than expected: η Corvi, β Uma, and ε Eri. η Corvi has a null depth which is a factor ~ 10 higher than predicted, but Marino et al. (2018) showed that its exozodi could be explained by inward scattering of exocomets from its cold planetesimal belt. β Uma may also be explained by the exocomet scenario, though it cannot be ruled out that more accurate SED fitting would allow the observed null depth to be explained by dust dragged in from the outer belt by P-R drag. Mid-infrared observations with Spitzer of ε Eri imply two warm inner belts at 3 au and 20 au (Backman et al., 2009), such that there could be another contribution to its exozodi from a second belt. Indeed, Su et al. (2017) already suggested that the 35 μm SOFIA/FORCAST detection towards ε Eri is incompatible with all of its warm dust originating in the outer belt. More detailed modelling of this system than that presented here would be needed to assess this, as well as to consider the role of stellar winds on the amount of dust dragged in (e.g. Reidemeister et al., 2011).
- 110 Her has an observed null depth much higher than its predicted excess based on fractional luminosity. However, this system has only marginal excesses from Spitzer at 70 μm (Trilling et al., 2008) and Herschel at 70 and 100 μm (Eiroa et al., 2013; Marshall et al., 2013), and is poorly constrained both in terms of its fractional luminosity and its radius. As such I cannot make strong statements about the consistency of the observed null with P-R drag from the known outer belt. However, my model could be used to provide further constraints on the properties of the outer belt on the assumption that the null arises from dust dragged inwards from that belt (e.g. using Figure 3.2a).
- There are three stars in the HOSTS survey (δ Uma, θ Boo, and 72 Her) which had detections of exozodiacal dust, but no known cold planetesimal belt. Based on my model, I suggest that they may have planetesimal belts that lie in the shaded region of Figure 3.3, such that they have cold planetesimal belts which are too faint to be detected at longer wavelengths, but produce observable levels of exozodiacal dust via P-R drag (see Section 3.2).

While more comprehensive modelling of individual systems is needed, overall the model provides a good explanation for the majority of systems observed by HOSTS with known planetesimal belts. The levels of dust dragged in from the planetesimal belts is expected to result in exozodiacal dust levels similar to those observed, or compatible with the upper limits. The exceptions to this are two systems which may have an additional contribution from exocomets, one system which may have an additional, warmer belt, and one system for which the outer belt is poorly constrained by observations.

If the three HOSTS detections with no far-infrared excesses are due to P-R drag from planetesimal belts not yet detected in the far-infrared, this suggests that the outer belt population continues to lower far-infrared flux levels. Based on my model (Figure 3.2), discs which are just below the far-infrared detection threshold would have $11\ \mu\text{m}$ excesses of $0.1 - 1\%$. While the planetesimal belts of the 80% of stars without far-infrared detections are not yet known, these three HOSTS detections suggest the existence of belts below the detection threshold, with 3/38 stars potentially having faint far-infrared planetesimal belts that result in mid-infrared excesses of $0.2 - 0.7\%$. It is reasonable to assume that the distribution of outer belts continues to even lower far-infrared flux levels, and so that mid-infrared excesses can be expected to be present at levels below 0.1% for some stars. This means they could have exozodis at levels above the limit tolerable by exo-Earth imaging of 10–20 zodis (e.g. Defrère et al., 2010; Roberge et al., 2012), which would be equivalent to a null depth of $\sim 0.02 - 0.04\%$. Therefore, even systems where no planetesimal belt is detected may have exozodi levels which are problematic for exo-Earth characterisation.

3.4 Modelling the exozodi of β Leo

One star of particular interest from the HOSTS survey is β Leo, a nearby (11 pc, van Leeuwen, 2007) young A star with a bright exozodi. Its age is believed to lie in the range from 50 Myr, based on membership of the Argus moving group (e.g. Zuckerman, 2019), to 400 Myr, based on isochrones assuming it is a field star (Stone et al., 2018). It is also known to host cold, warm, and hot dust components in its debris disc (Matthews et al., 2010; Stock et al., 2010; Churcher et al., 2011). As part of the HOSTS survey, the profile of its warm dust was observed with LBTI at $11\ \mu\text{m}$, finding a $0.47 \pm 0.05\%$ excess within 1.5 au, equivalent to approximately 50 times the zodiacal cloud.

In Section 3.3, I suggested that the null excess seen around this star could be explained by P-R drag from its outer belt, especially if an additional belt were present to contribute additional dust. However, the modelling in Section 3.3 was very simplified, assuming half of the total disc flux is transmitted. In reality, the LBTI only has a field of view of diameter 2.3", such that emission from the outer belt will likely be truncated, and the interferometric transmission pattern depends on the geometry of the observation (Kennedy et al., 2015). In this section, I apply the P-R drag model of Chapter 2 to model the radial profile of dust seen by LBTI in the inner planetary system of β Leo. This is done in more depth than the general application of Section 3.3 to the whole HOSTS survey, using the disc orientation to take into account the transmission pattern of LBTI. A self-consistent model is developed which fits both the distribution of exozodiacal dust and the stellar SED.

3.4.1 Observational constraints

The star is known to have an outer belt which is relatively close to the star compared to typically observed debris discs. It was first resolved by Herschel/PACS at 100 and 160 μm (Matthews et al., 2010), and found to have a radius of 39 au, making it comparable to the Kuiper belt. Interferometric observations at 2 μm with CHARA/FLUOR detected hot dust close to the sublimation radius (0.12 au, corresponding to 1600 K). Churcher et al. (2011) self-consistently modelled observations at wavelengths ranging from scattered light to sub-mm and proposed three models for the disc, comprising either one, two, or three components. The stellar SED could be fit with a two-component model which has a hot component at 2 au and a cold outer belt from 15–70 au. In the three-component model, there is hot dust at 2 au, a warm belt at 9 au, and the outer belt extends from 30–70 au. The ambiguity in the inner edge of the cold belt comes from the fact that it has not been resolved by Herschel within 30 au. The third, least likely scenario was that there is a single belt with high eccentricity, and a pericentre of 2 au and apocentre at 65 au.

Table 3.2 Null depth measurements for LBTI observations of β Leo with different aperture radii, taken from Defrère et al. (2021).

Aperture radius (mas)	Source null (%)
35.7	0.36 ± 0.230
71.4	0.39 ± 0.150
143	0.47 ± 0.050
179	0.42 ± 0.054
285	0.54 ± 0.100
429	0.81 ± 0.270
571	1.16 ± 0.333

The LBTI observations of β Leo’s habitable zone dust are described in Defrère et al. (2021). The nulling mode of LBTI in the N’ band (11 μm) was used to measure the null depth, the ratio of emission transmitted when the beams are combined in phase opposition relative to the stellar emission. This should effectively be a fractional excess, multiplied by the transmission pattern of LBTI. As a nearby, luminous star, using apertures of different sizes allows to measure the radial profile of dust in the habitable zone. Apertures of radii 36–571 mas were used to measure the distribution of warm dust in the system (Table 3.2). The standard HOSTS disc model (Kennedy et al., 2015) was used to convert the null depth to a level of dust relative to the zodiacal cloud in units of zodis. Considering a range of orientations for the disc, the null was found to correspond to a zodi level of 50 ± 10 zodis, making β Leo’s habitable zone far dustier than our zodiacal cloud.

3.4.2 P-R drag model predictions

Given the presence of an outer belt in the system and the inevitability of dust produced in this belt trying to migrate in, I modelled the distribution of P-R drag dust for comparison with the observations. Previously, when KIN was used to observe warm dust, Mennesson et al. (2014) suggested that the observations, including β Leo, were consistent with the simple analytical P-R drag model of Wyatt (2005). This is a model which solves the continuity equation for dust grains, assuming grains of a single size at the blowout limit and blackbody grains. This model was then updated by Kennedy and Piette (2015) with an additional free parameter, k , to better fit the radial profile found by numerical simulations. It was found that a value of $k = 1/7$ is required for agreement between numerical and analytical models. However, this still assumes a single grain size. Assuming that the inner edge of the disc is at 30 au (Churcher et al., 2011) and that the optical depth of the belt is 1.35×10^{-5} , I used these models to find the radial profile of surface brightness resulting from dust dragged inwards. I used a stellar mass of $2.1 M_{\odot}$ and luminosity of $14 L_{\odot}$. To model the observations, this radial profile must be multiplied by the LBTI transmission pattern, which is a \sin^2 function with distance from the star as described in Kennedy et al. (2015). The profile is then convolved with a Gaussian PSF of FWHM 393 mas to match that of LBTI. For the disc orientation I used a position angle of 125° and an inclination of 57° as found by Churcher et al. (2011). Then the emission within an aperture of a given radius can be found and used to calculate a null depth, using an N' band stellar flux density of 5.4 Jy. The resulting profiles of emission are shown in Figure 3.9 along with the profile observed by LBTI. The improved single-size model (Kennedy and Piette, 2015) significantly decreases the levels of dust in the habitable zone.

However, these simple models do not consider the size distribution of dust, assuming a single grain size. I therefore used my analytical model from Chapter 2 to include a realistic size distribution which varies with distance from the star. With a two-dimensional size distribution of dust, it is also possible to use realistic optical properties of the grains to better predict the resulting thermal emission. This is important, as dust grains should not behave like blackbodies, and optical properties have a significant effect on the predicted flux.

I calculated the optical properties of dust grains using the method of Wyatt and Dent (2002), which uses compositions from the core-mantle model of Li and Greenberg (1997). This assumes that particles have a silicate (amorphous olivine) core and an organic refractory mantle, with three free parameters. A range of compositions were considered, with silicate volume fractions varying from 0 to 1, porosities from 0 to 0.95, and a volume fraction of water ice in the gaps of 0 to 1. Based on the modelling of Churcher et al. (2011), I assumed that the outer belt has an inner edge of $r_0 = 30$ au. Sub-mm observations of β Leo have

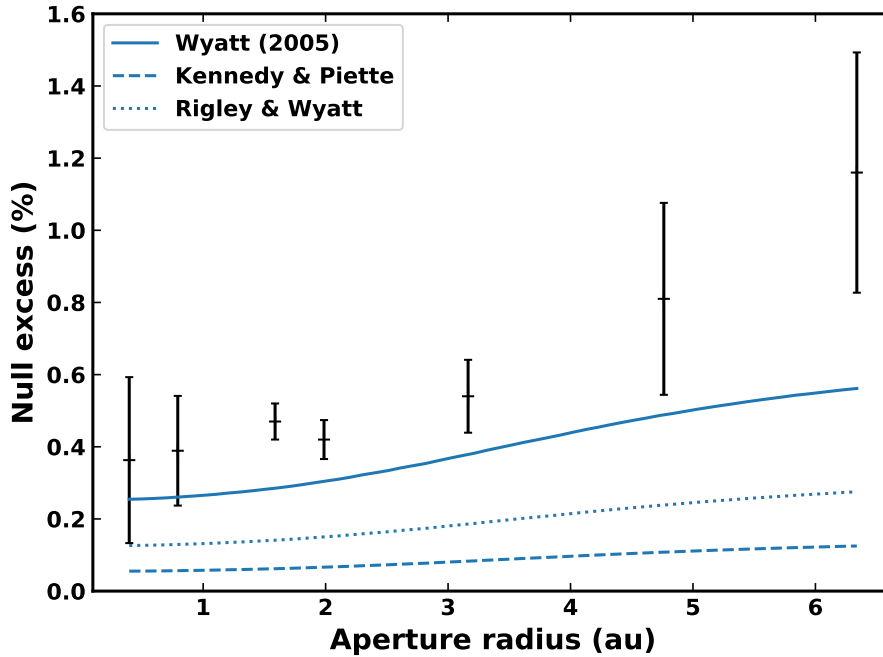


Fig. 3.9 Null excess vs. aperture size for three different analytical P-R drag models: single-sized blackbody grains (Wyatt, 2005, solid), the same model with an empirical factor $k = 1/7$ to correct the model (Kennedy and Piette, 2015, dashed), and a more realistic model using a size distribution and realistic optical properties (Chapter 2, dotted).

only placed upper limits on its emission, so I used the disc flux at $100 \mu\text{m}$ of 0.416 Jy (Churcher et al., 2011) to fit the mass of dust in the outer belt. I found the best-fit composition for the dust grains by minimising chi-squared across a grid of compositions. This was a combined chi-squared which fit to both the observed exozodi profile (Table 3.2), and photometry data. The photometry is similar to the data listed in Churcher et al. (2011), but also includes measurements from WISE (Wright et al., 2010), AKARA IRC (Ishihara et al., 2010), and SCUBA2 (Holland et al., 2017). The SED of the star was fit using the method of Yelverton et al. (2019, 2020), which can be subtracted from the photometry to obtain the disc flux at each wavelength. The best-fit composition had grains which were 75% silicate and 25% organic by volume, with no porosity. The best-fit dust mass of the outer belt was $7.9 \times 10^{-4} M_{\oplus}$.

The resulting radial profile from the Rigley and Wyatt (2020) model is also shown in Figure 3.9. The emission is higher than the improved blackbody model, and the difference between the three models highlights the importance of modelling the size distribution and optical properties of dust grains when predicting the emission. However, this also shows

that with a realistic P-R drag model, the flux is too low to explain the observed exozodi by a factor of a few, and the shape of the radial profile is too flat.

3.4.3 An additional belt?

Previous modelling of the system by Churcher et al. (2011) suggested that there may be an additional intermediate, warm belt in the system, which would not have been resolved by Herschel or Spitzer. Their three-component model has a hot component at 2 au, warm dust at 9 au, and cold dust from 30 to 70 au. As a toy model, I superposed the emission of dust dragged in from the known outer belt with a second belt interior to it, assuming dust in both belts has the same composition. The outer belt should dominate the far-infrared emission, so its mass can still be found from the 100 μm flux. To determine the parameters of the inner belt, I used the approach of Figure 3.3 to find what parameters satisfy the observational constraints. These constraints are the observed 24 μm excess of 37%, an excess at 70 μm of 40%, and a null depth of 0.7% within the largest (571 mas) aperture at 11 μm . This is the additional null depth required in the largest aperture which cannot be produced by P-R drag from the outer belt. These three constraints are plotted in Figure 3.10 as a solid line for the LBTI constraint, and dashed lines for Spitzer photometry. The constraints converge on a belt with an inner radius of a few au and a mass of $\sim 10^{-5} M_{\oplus}$. These parameters along with the dust composition and the outer belt mass were refined using a combined chi-squared fit to the SED and null depth data with the two-belt model. The best-fit composition was unchanged, as the chi-squared is dominated by the contribution from the SED. The best parameters for the inner belt were a radius of 5.5 au and a mass of $1.5 \times 10^{-5} M_{\oplus}$, and are primarily determined by the mid-infrared emission. The belt location must be optimised to produce enough flux at 11 μm , yet it is difficult to avoid producing too much 24 μm flux with an additional warm belt. This means that it is challenging to get a perfect fit to the radial profile of warm dust given other observational constraints.

Figure 3.11 shows the predicted radial profile of dust and the resulting SED for the best-fit model with two belts. Combining the emission of the two belts agrees well with the null measurements for larger-aperture radii, while fitting the SED. It should be noted that this is not a comprehensive model for the system. For example, it treats dust created in the outer and inner belts separately, and so ignores collisions between these populations, and still underpredicts the null depth for small apertures. However, this shows how in principle the observations are consistent with the observed null depth having its origin, at least partially, in an inner belt. If the observed exozodiacal dust is being produced by P-R drag, the outer belt alone cannot produce enough dust, and an unseen warm belt could resolve this.

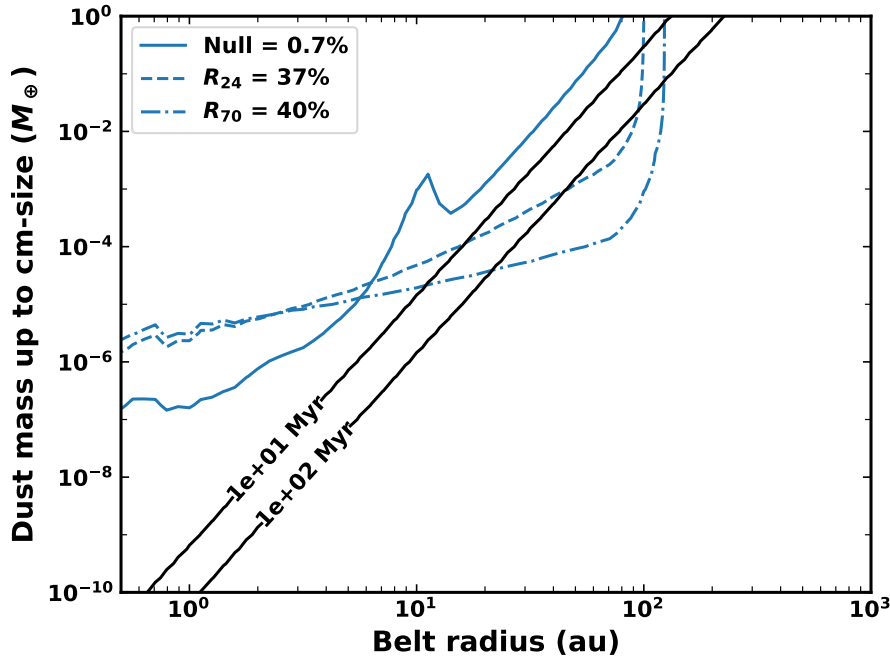


Fig. 3.10 The parameter space of dust mass vs. belt radius used to find the parameters of an additional, warm asteroid belt which is added to the analytical model. Constraints come from the $24 \mu\text{m}$ and $70 \mu\text{m}$ photometry along with the LBTI null and the stellar age.

If some of the dust is indeed dragged inwards from the outer belt, this implies that planets of more than a few Saturn masses do not lie between the outer belt and habitable zone, as these would remove dust migrating inwards by either accretion or ejection (Bonsor et al., 2018). However, a question remains about whether an inner belt at 5.5 au could survive for so long without collisionally depleting. I therefore used the model of Wyatt et al. (2007b) to find the maximum dust mass a belt could have and be in steady state at a given age. This is shown in Figure 3.10 with black solid lines for ages of 10 and 100 Myr. The proposed belt parameters of 5.5 au and $1.5 \times 10^{-5} M_{\oplus}$ lie above the maximum dust mass for both ages, suggesting that the proposed belt is too massive to be in steady state. One potential explanation is that the belt is a relatively recent phenomenon, created in the recent break-up of a very large asteroid. Alternatively, the belt could be continually replenished by inward scattering of comets from the outer belt. This would require the presence of low-mass planets which scatter planetesimals onto eccentric orbits (e.g. Bonsor and Wyatt, 2012; Marino et al., 2018). More observations are needed to further constrain the disc geometry and search for asymmetric disc structures.

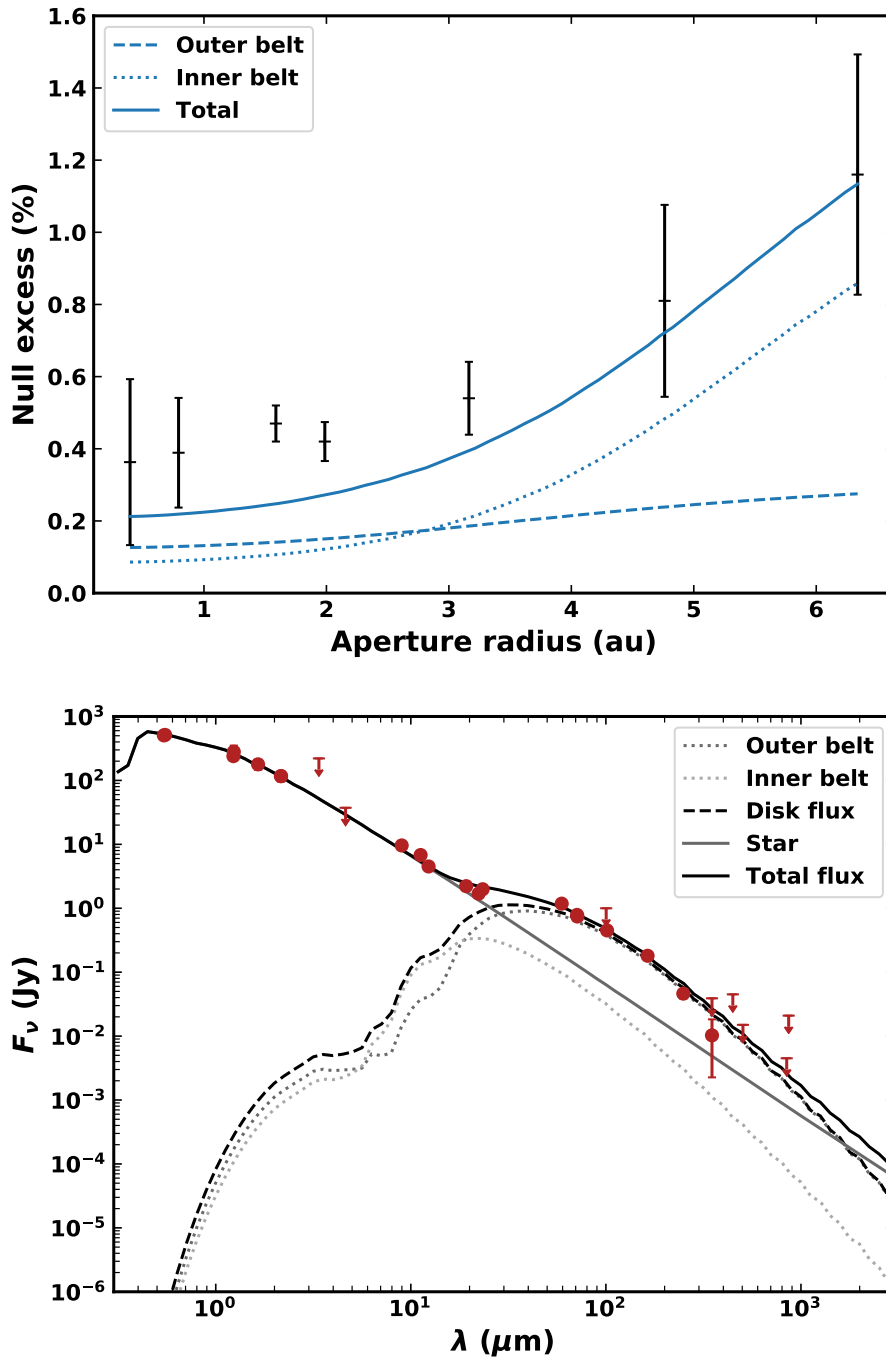


Fig. 3.11 The best-fit P-R drag model for β Leo. Top: the radial profile of null excess vs aperture size. The analytical model of Chapter 2 is used to find the dust dragged in from the outer belt seen at 30 au (dashed), and a suggested additional, warm belt at 5.5 au (dotted). These are superposed to give the total emission (solid). Bottom: the SED of β Leo, compared with the two-belt model.

3.5 Conclusions

In this chapter I have applied the analytical model of Chapter 2 to predict the levels of habitable zone dust dragged inwards from outer belts with different parameters and the resulting mid-infrared thermal emission. I have shown that the effect of P-R drag transporting dust inwards from an outer belt means that systems with known planetesimal belts should have sufficient levels of exozodiacal dust to be detectable at $11\ \mu\text{m}$ with LBTI. Non-detections in these systems could therefore imply the presence of unseen planets which are accreting or ejecting dust before it reaches the habitable zone. Further, I have shown that LBTI may be able to detect exozodiacal dust which has been dragged inwards from outer belts which are too faint to detect in the far-infrared, particularly for belts with lower dust masses and small radii. Grain composition has only a minor effect on the results, such that my conclusions remain unchanged.

Application of my model to systems observed by the HOSTS survey shows that my model can provide a good explanation for the majority of the warm exozodiacal dust detections, with the exception of two systems which are particularly bright, potentially due to exocomets, one system which is believed to have a warm inner belt, and one system which is poorly constrained. This means that the scenario of P-R drag transporting dust inward from an outer belt may be a viable source of exozodiacal dust. Further, for the three exozodi detections in the HOSTS survey with no known planetesimal belt in the system, I suggest that the source of the exozodiacal dust could be a faint outer belt which is not yet detectable in the far-infrared. In the future it may be possible to use models such as the one presented in Chapter 2 to determine whether a particular exozodi originates from P-R drag or an alternative scenario, by considering the level and radial distribution of dust.

Future attempts to detect and characterise exo-Earths will be impeded by levels of exozodiacal dust even ten times that of the Solar System's zodiacal cloud. I have shown that even planetesimal belts much less massive than the bright Kuiper belt analogues which have already been detected around other stars could produce mid-infrared excesses a few times greater than the zodiacal cloud. While systems with previously detected belts are expected to have warm exozodiacal dust, even those where no belt has been detected could potentially be problematic for exo-Earth imaging and characterisation. Understanding the occurrence of exozodiacal dust will therefore be crucial to the design of exo-Earth detection and characterisation missions.

The nature of nulling interferometric measurements means that the measured level of emission is not simply the excess emission produced by the dust, but depends on the geometry of the observation. I applied my P-R drag model in more depth to the observations of β Leo, taking into account its orientation and thus the fraction of flux transmitted. This showed

that P-R drag from the outer belt detected in the system is unable to produce enough dust to fit the exozodiacal emission. Moreover, a P-R drag model produces a radial profile of dust which is too flat compared to the observations. By simultaneously fitting the SED and the mid-infrared null depth, I showed that inclusion of a warm asteroid belt at ~ 5 au provided a better fit to the dust profile while agreeing with the star's SED. However, such a belt should not be in steady state given the age of β Leo, and may need to have been created recently. Either the exozodiacal dust is coming from a combination of dust dragged inwards from the outer belt at 30 au and a second, currently undetected warm belt, or another source is required.

Chapter 4

Comet fragmentation as a source of zodiacal dust

Abstract

Models of the zodiacal cloud's thermal emission and sporadic meteoroids suggest Jupiter-family comets (JFCs) as the dominant source of interplanetary dust. However, comet sublimation is insufficient to sustain the quantity of dust presently in the inner Solar System, suggesting that spontaneous disruption of JFCs may supply the zodiacal cloud. In this chapter I present a model for the dust produced in comet fragmentation and its evolution. Using results from dynamical simulations, the model follows individual comets drawn from a size distribution as they evolve and undergo recurrent splitting events. The resulting dust is followed with a kinetic model which accounts for the effects of collisional evolution, Poynting-Robertson drag, and radiation pressure. This allows to model the evolution of both the size distribution and radial profile of dust, and I demonstrate the importance of including collisions (both as a source and sink of dust) in zodiacal cloud models. With physically motivated free parameters, this model provides a good fit to zodiacal cloud observables, supporting comet fragmentation as the plausibly dominant dust source. The model implies that dust in the present zodiacal cloud likely originated primarily from disruptions of ~ 50 -km comets, since larger comets are ejected before losing all their mass. Thus much of the dust seen today was likely deposited as larger grains ~ 0.1 Myr in the past. The model also finds the dust level to vary stochastically; for example, every ~ 50 Myr large (> 100 km) comets with long dynamical lifetimes inside Jupiter cause dust spikes with order of magnitude increases in zodiacal light brightness lasting ~ 1 Myr. If exozodiacal dust is cometary in origin, my model suggests it should be similarly variable.

4.1 Introduction

The zodiacal cloud is a diffuse complex of dust in the Solar System which is concentrated inside Jupiter's orbit (< 5.2 au). It dominates the thermal emission in the sky (e.g. Hauser et al., 1984), and is believed to originate primarily from a combination of asteroids and comets. Many studies have constrained the relative contributions of various sources of zodiacal dust. The most recent models suggest that comets overwhelmingly dominate, supplying $> 90\%$ of the dust (Nesvorný et al., 2010; Yang and Ishiguro, 2015; Ueda et al., 2017). Dynamical modelling of the sporadic meteoroid complex suggests particles from JFCs to dominate the helion and antihelion sources, which contain most of the mass (Nesvorný et al., 2011). However, while comets best reproduce the structure of the zodiacal cloud, comet sublimation is insufficient to sustain the quantity of dust presently in the inner Solar System. Comets are also seen to spontaneously fragment frequently, which may be able to cause much greater mass-loss than cometary activity alone. It has therefore been suggested that comet fragmentation may dominate the input to the zodiacal cloud.

Numerical models of the dust in the zodiacal cloud can be classified into two types: empirical and dynamical. Empirical models describe the 3D structure of the zodiacal cloud along with the size distributions of the dust. The parameters describing these distributions may have a basis in the underlying physics, but are ultimately fitted to be able to reproduce certain observations. Some empirical models of the zodiacal cloud are Grun et al. (1985); Divine (1993); Kelsall et al. (1998); Rowan-Robinson and May (2013).

Dynamical models of the zodiacal cloud use N-body integrators to follow the orbital evolution of individual dust particles from their source to their ultimate loss (e.g. Liou et al., 1995; Wiegert et al., 2009; Nesvorný et al., 2010, 2011; Pokorný et al., 2014; Ueda et al., 2017; Soja et al., 2019; Moorhead et al., 2020). Some of these consider dust from comets, while others compare dust of different cometary types with asteroidal dust. In all cases, the initial orbits of particles are determined by those of their parent bodies. A dynamical approach is useful for following dynamical interactions with planets, and allows inclusion of the effects of radiation pressure, solar wind and Poynting-Robertson (P-R) drag. However, since individual particles are followed, only a simplified collisional prescription can be used. Either particles are removed after their collisional lifetime has elapsed, or a stochastic prescription based on collisional lifetimes determines when to remove particles. The production of smaller grains in collisions is neglected, such that dynamical models are limited in their ability to model the size or radial distribution of dust consistently. The production of collisional fragments (and subsequent disruption of these fragments) supplies smaller grain sizes, and is important in order to follow the size distribution of particles. When modelling meteoroids, only including collisions as a loss mechanism may be a valid

approximation, as for larger ($\gtrsim 1$ mm) dust particles this will be the net effect of collisions. However, when considering smaller particles which contribute to the zodiacal light and thermal emission, it is important to include the supply of smaller particles from disruption of larger grains.

I propose to use a different approach in using a kinetic model, which follows the evolution of a population of particles in a phase space of mass and orbital elements. Such models have found much use in the study of extrasolar debris discs (e.g. Krivov et al., 2005, 2006; van Lieshout et al., 2014), but I am only aware of one use in the context of the zodiacal cloud (Napier, 2001). Kinetic models incorporate the effects of radiation pressure, P-R drag, and solar wind, along with collisional evolution. While such models allow the size distribution to be modelled self-consistently, using a statistical approach requires a simplified prescription of the effect of dynamical interactions with planets. Napier (2001) modelled dust produced by comets on Encke-like orbits and followed the distribution of dust with semimajor axis, eccentricity, and particle mass. I improve on this model by using a more realistic size distribution of comets, N-body simulations of cometary dynamics and a more physical prescription for mass loss from comets by spontaneous fragmentation. Further, in Napier (2001) collisions were only included as removal mechanism; here I include the full effects of collisional evolution, including the production of smaller grains, when modelling interplanetary dust. This allows me to produce a self consistent model for the size distribution, whereas dynamical models must either approximate that a single size dominates, or make assumptions about that distribution (e.g. by using a power law with parameters that are fit to observations).

A further limitation of some models is that given our much better knowledge of interplanetary dust near Earth, most models focus on the dust at 1 au. The radial distribution is typically only included empirically (e.g. Rowan-Robinson and May, 2013), although ESA's IMEM2 (Soja et al., 2019) and NASA's MEM 3 (Moorhead et al., 2020) are dynamical models which consider the radial distribution. My use of a kinetic model allows me to study the radial distribution of dust, taking into account the effect of collisions on the distribution.

Using a kinetic model not only allows me to model the size and spatial distribution of the dust self-consistently, but also addresses issues such as the stochasticity of dust production in the zodiacal cloud. Asteroidal input should be stochastic due to collisional evolution (Durda and Dermott, 1997; Dermott et al., 2001). As far as I am aware, only Napier (2001) has previously studied the stochasticity of a cometary input to the zodiacal cloud. While most comets seen today are smaller than ~ 15 km, bodies in the Kuiper belt, the source of JFCs, can be as large as hundreds of km, though they are far fewer. Thus, it is possible that occasionally in the history of the Solar System, large bodies could be scattered inwards

and deposit large amounts of dust in the interplanetary dust complex. For example, it is hypothesised that the Taurid complex, a collection of asteroids and comets with similar orbits (Ferrín and Orofino, 2021), originated from a series of fragmentations of a large progenitor comet $\gtrsim 100$ km in size tens of thousands of yr ago (e.g. Clube and Napier, 1984; Napier, 2019). Any cometary contribution to interplanetary dust will be highly variable over long timescales depending on the sizes of comets which are scattered in. Studying the potentially stochastic nature of a cometary source is therefore important for understanding the history of the zodiacal cloud.

The final way I aim to improve on previous models is by using a physically-motivated mechanism for the production of dust. I apply a physical prescription for individual comet fragmentations, rather than placing dust on cometary orbits randomly. Marboeuf et al. (2016) modelled the thermo-physical evolution of comets in the context of (exo-)zodiacal dust produced by comet sublimation, but as discussed earlier that is not thought to be the dominant mass loss mechanism from comets. Nesvorný et al. (2010, 2011) model the production of zodiacal dust via comet fragmentation, but simply release dust grains from comets once they reach a critical pericentre, as opposed to modelling individual, recurrent events. I use a more physical model of comet fragmentation which has been fitted to observations of JFCs such that I can model the evolution of individual comets as they fragment repeatedly. The model will also be able to follow the stochasticity of that fragmentation.

To summarise, in this chapter I develop a model for mass input to the zodiacal cloud from comet fragmentation based on realistic cometary dynamics, with a self-consistent model for the evolution of the dust produced by comets as a result of mutual collisions and P-R drag. Dynamical effects are included with a simplified prescription. I aim to show whether comet fragmentation can produce a viable model of the zodiacal cloud in terms of the spatial and size distribution of dust. I also investigate the variability of any cometary source of the zodiacal cloud due to stochasticity relating to inward scattering of comets and its implications for the zodiacal cloud's history.

This chapter is structured as follows: my model of comet fragmentation is given in Section 4.2, and the model of the dust produced by these comets is presented in Section 4.3. Fitting of the model parameters to observational constraints is discussed in Section 4.4. My results are given in Section 4.5 and discussed in Section 4.6. Section 4.7 compares my model to previous zodiacal cloud models. Finally, I give my conclusions in Section 4.8.

4.2 Comet model

To determine the potential contribution of comet fragmentation to the zodiacal cloud, I model the mass input from fragmentation events within a population of comets. That population is created by starting with N-body simulations of the dynamical evolution of Solar System comets over 100 Myr. I clone particles from the N-body simulations in time (to simulate the continual injection of comets), with each cloned particle representing a size distribution of comets. Then each particle in the size distribution is followed as it bounces around the inner Solar System, randomly undergoing fragmentation events which produce dust and reduce the particle's size.

4.2.1 N-body data

JFCs are comets with short orbital periods and relatively low inclinations. Here I define JFCs to have periods $P < 20$ yr and a Tisserand parameter with respect to Jupiter of $2 < T_J < 3$, as in Nesvorný et al. (2017). They are believed to originate in the scattered trans-Neptunian disc, from which some bodies are randomly scattered inside Neptune's orbit, then into the inner Solar System (e.g. Duncan and Levison, 1997).

I apply a fragmentation model to JFCs as they evolve with trajectories from the CASE2 simulation of Nesvorný et al. (2017). Nesvorný et al. followed the evolution of objects from the trans-Neptunian region to the inner planetary system over 1 Gyr to model the origin and evolution of JFCs. Interactions with the giant planets are included, but terrestrial planets are not. Their data give the orbital elements of comets with pericentre distances $q < 5.2$ au at 100 yr intervals. The number of particles in the N-body simulations is relatively low (21,548), and spread over 1 Gyr. I therefore assume that each N-body particle is representative of a size distribution of comets, which is described in Section 4.2.2. Additionally, I assume the time a particle is scattered in is unimportant, and clone each N-body particle in time so that the same particle is introduced every 12,000 yr (see Section 4.2.3).

The orbital elements of the N-body data points in pericentre-eccentricity space are shown in Figure 4.1 as the density of comets in each pericentre-eccentricity bin, averaged over the full time span. The orbital elements are only recorded once the bodies reach $q < 5.2$ au, so generally bodies start at 5.2 au and move inwards. The density is therefore highest at pericentres closest to 5.2 au, as some comets may be scattered outside Jupiter again before reaching very low pericentres. Note that comets may fully disrupt before reaching the innermost regions, such that the distribution of mass deposited by fragmentation, and indeed the distribution of comets, may not match that of the parent N-body particles. The peak in the density of points at $q \sim 3.2$ au and $e \sim 0.15$ is due to one particular body which spends a long

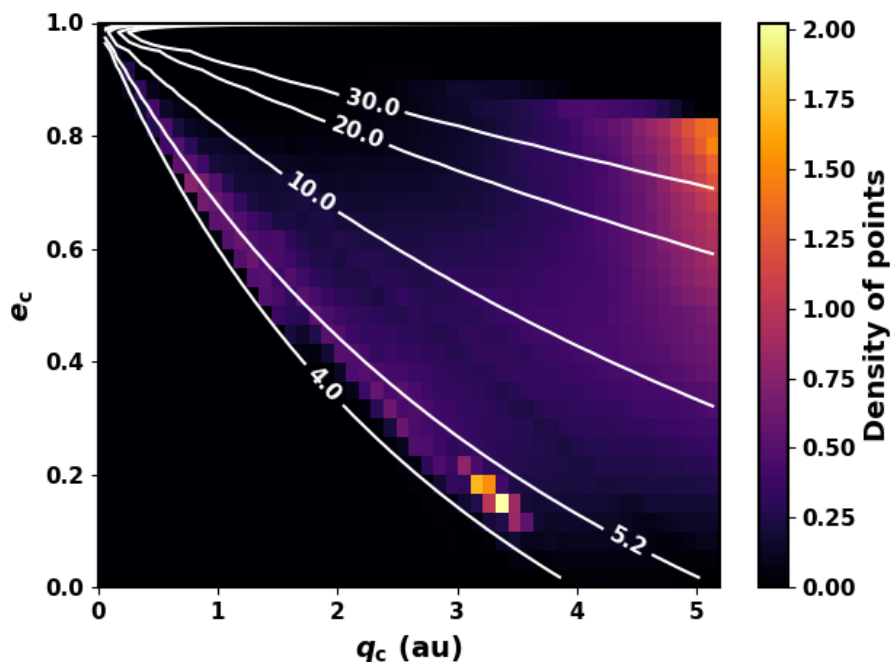


Fig. 4.1 Histogram showing the locations of N-body data points in pericentre-eccentricity space, from the simulations of Nesvorný et al. (2017), averaged over all times. Contours show lines of constant apocentre in au.

time (~ 40 Myr) in the inner system without being scattered by Jupiter. This illustrates how individual comets can have a significant effect on the distribution through rare but long-lived dynamical pathways. The simulations do not include the terrestrial planets, and so the only way comets can reach the inner regions is by scattering off the outer planets, which means their apocentre must be close to or beyond the giant planets. Therefore a dearth of JFCs with apocentres $\lesssim 4$ au is seen.

Comets will bounce around the phase space (Figure 4.1) as they evolve, with the amount of dust produced at each location determined randomly depending on the likelihood of fragmentation events. The mass produced also depends on the initial size of the comet: larger comets have more mass to lose, whereas smaller comets are likely to deplete all of their mass before their dynamical lifetime has elapsed. It is therefore important to follow the evolution of individual comets of different sizes and the fragmentations they undergo to determine the mass input into the zodiacal cloud.

4.2.2 Size distribution

Each cloned particle is representative of a size distribution of comets which could be scattered in from the Kuiper belt. I consider comets of radii ranging from 0.1 to 1000 km, placing them into 40 logarithmic size bins. Each time an N-body particle is cloned, these size bins are filled by choosing random numbers from a Poisson distribution, with the mean values in each bin given by the size distribution described in this section and Table 4.1.

Many attempts have been made to characterise the size distribution of JFCs by converting observed absolute nuclear magnitudes H_N to nuclear radii R_N . Most observations cover the range of radii $1 \lesssim R_N \lesssim 10$ km. For a cumulative size distribution (CSD), defined as $N_R(> R_N) \propto R_N^{-\gamma}$, a range of slopes have been found, $1.6 \leq \gamma \leq 2.7$ (Weissman and Lowry, 2003; Lamy et al., 2004; Tancredi et al., 2006; Snodgrass et al., 2011; Fernández et al., 2013; Belton, 2014). Here I choose to use a slope $\gamma = 2.0$ in this size range, which is also in agreement with observations of Jupiter Trojans, thought to have the same source as JFCs. For example, Yoshida and Terai (2017) found a cumulative slope of 1.84 ± 0.05 for Jupiter Trojans in the size range $1 \lesssim R \lesssim 10$ km.

For small comets with $R_N \lesssim 1$ km, the size distribution is seen to turn over to a shallower slope, measured by Fernández and Morbidelli (2006) to be $\gamma = 1.25$. It is difficult to pinpoint the exact size this turnover occurs at. It has been shown by both Meech et al. (2004) and Samarasinha (2007) that this is not purely an observational effect due to smaller comets being more difficult to observe, but a result either of the inherent parent distribution or the evolution of comets as they are scattered inwards from the Kuiper belt – perhaps smaller comets are more susceptible to erosion by physical effects such as sublimation and fragmentation. In their recent analysis of cratering on Charon and Arrokoth, Morbidelli et al. (2021) found that bodies $\lesssim 1$ km in the Kuiper belt have a slope of $\gamma = 1.2$, which could suggest that the shallow slope for small JFCs may be a result of the primordial distribution of their source in the scattered disc.

For JFCs larger than ~ 10 km, observations are very few, so instead I turn to the size distribution of their parent population. Using the size distribution of the primordial trans-Neptunian disc from Figure 14 of Nesvorný et al. (2017), I assume a slope of $\gamma = 5.0$ for the range $50 \leq R \leq 150$ km and $\gamma = 2.5$ for $150 \leq R \leq R_{\max}$ km. This is based upon Nesvorný and Vokrouhlický (2016), including their requirement for 1000–4000 Pluto-sized objects in the primordial planetesimal disc. My model has an upper limit of $R_{\max} = 1000$ km.

An overview of the differential size distribution slopes, α , used for the comets input when a particle is cloned is given in Table 4.1. These are defined such that the differential

Table 4.1 Slopes of the differential size distribution of JFC nuclei used in my model as input to the inner Solar System.

Size range (km)	Slope, α
$0.1 \leq R \leq 1$	2.25
$1 \leq R \leq 50$	3.0
$50 \leq R \leq 150$	6.0
$150 \leq R \leq 1000$	3.5

size distribution of comets at a given size scales as

$$N(R) = dN/dR \propto R^{-\alpha}, \quad (4.1)$$

meaning that $\alpha = \gamma + 1$ in terms of the slope of the cumulative size distributions given in the literature.

Densities of comets have large uncertainties, as the mass can only be measured indirectly. I assume the comet nuclei to have a bulk density of 0.6 g cm^{-3} , in agreement with the most likely value suggested by Weissman and Lowry (2008).

I normalise the mean size distribution of comets when cloning a particle using the mass in comets of radii $1 \leq R \leq 10 \text{ km}$. Note that each particle may receive more or less than the mean due to the way the population of each size bin is assigned stochastically based on this distribution. This mass input is a free parameter which is fitted to the number of active visible comets in the given size range. The most complete catalogue of JFCs is Tancredi et al. (2000, 2006), who have estimated radii for 58 JFCs in the given size range. This is a lower limit on the number of active visible comets in this range with pericentres $< 2.5 \text{ au}$, as many observed comets do not have estimated radii. In my model, I consider comets to be 'active' for the first 12,000 yr inside 2.5 au based on Levison and Duncan (1997). I tuned the mass input to fit on average 58 active visible comets inside 2.5 au, which gave a mass input of $8.08 \times 10^{19} \text{ g}$ of comets in the range $1 \leq R \leq 10 \text{ km}$ every 12,000 yr.

The final input size distribution of comets which is used every time particles are cloned is shown in Figure 4.2 as the cumulative size distribution. The slopes of the cumulative distribution in each region are given above the line.

The steepness of the size distribution means that it is rare for bodies $R \gtrsim 100 \text{ km}$ to be scattered into the inner Solar System. Figure 4.3 shows the distribution of the largest comet size which is present amongst all 21,548 of the N-body particles each time cloning is done (every 12,000 yr). The largest comet seen in the whole simulation is 501 km, with a total of 34 out of 8334 cloning steps (0.4 per cent) containing a comet with $R \geq 125 \text{ km}$. Most commonly, the largest comet present will be in the range $\sim 30\text{--}60 \text{ km}$. The size distribution

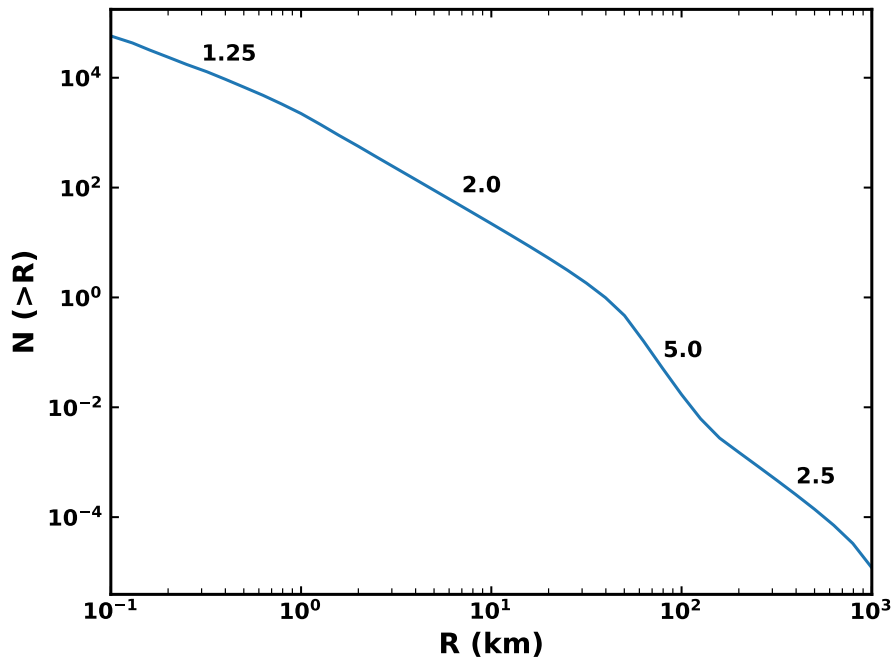


Fig. 4.2 Cumulative size distribution of comet nuclei radii which is input into my simulations each time the N-body particles are cloned. The cumulative slope of the size distribution in each region is labelled above the curve, related to the differential slope (Table 4.1) as $\alpha - 1$. This size distribution has been normalised to have a mass of 8.08×10^{19} g in comets of sizes $1 \leq R \leq 10$ km, and is shared between all N-body particles each time cloning is done.

will always contain many comets a few km in size. The largest comet present in a given cloning step ranges from 16 to 501 km. Given the steep dependence of mass on radius, in the rare cases very large (>100 km) comets are present, they may dominate the mass distribution if they lose a significant fraction of their mass, and it is therefore important to study the effects of such events.

4.2.3 Cloning

I simulate the fragmentation of comets for a total of 100 Myr. This total run time is limited due to computational issues, though is sufficient time for the dust distribution to come to a quasi-steady state. Due to the low number of N-body particles, they are cloned every 12,000 yr, assuming that the time a body is scattered inwards is unimportant. Ideally cloning would happen more frequently if it were feasible computationally, but the time resolution of the output is also limited due to computational resources. The exact frequency of cloning is not too important, so long as it is frequent enough to give good statistics. Given the canonical

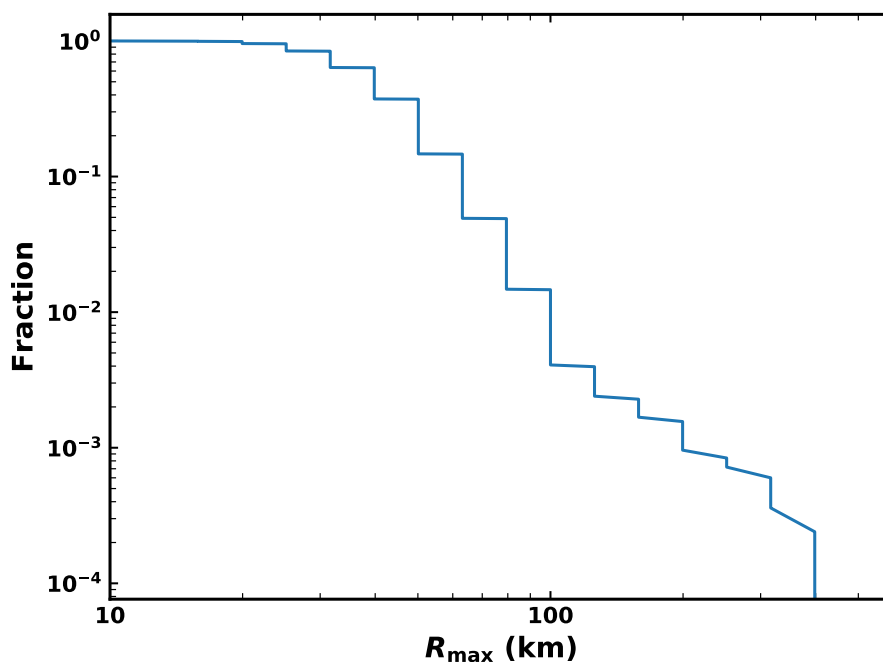


Fig. 4.3 Fraction of cloning time steps for which the largest comet present amongst the randomly drawn size distributions of all N-body particles is larger than R_{\max} .

lifetime of JFCs of 12,000 yr, this should be frequent enough to study the variation in the zodiacal cloud.

Each cloned N-body particle is assumed to represent a size distribution of comets. Every time a particle is cloned, the number of comets in each size bin is randomly drawn from a Poisson distribution, with a mean given by the size distribution of Section 4.2.2. Each individual comet in this distribution is followed as it evolves, calculating the probability that a fragmentation event occurs each orbit, as described in Section 4.2.4. Once all comets have been followed, this gives a mass input into the zodiacal cloud as a function of time, pericentre, and eccentricity.

Observations of comet splittings show that often mass goes to fragments which are tens or hundreds of metres in size (see e.g. Fernández, 2009, for a review). However, fragments are often seen to disappear on relatively short timescales, varying from days to months or a few yr. I assume that a fraction of the mass a comet loses as it fragments is inputted into the interplanetary region as dust grains with a range of sizes, with the rest of the mass lost going into larger fragments that are assumed to follow the same dynamical evolution as the parent comet. The fraction of mass which goes to dust is a free parameter of my model, ϵ . Dust grains are placed onto the relevant orbits depending on their size, taking into account

radiation pressure (see Section 4.3.1). The evolution of this dust is followed with a kinetic code that follows the evolution of particles due to collisions and drag (Section 4.3).

4.2.4 Fragmentation

Since little is known about the exact mechanism of comet fragmentation (for a review see Boehnhardt, 2004), I make no assumptions about which of the possibilities is best, and just apply the prescription given below for the mass loss and occurrence rate.

I use the model of Di Sisto et al. (2009) to simulate the splitting of comets. This is a dynamical-physical model which is fitted to the distributions of orbital elements of observed JFCs in order to determine the frequency and mass loss of fragmentation events.

The probability in the model that a comet fragments in a given orbit is given by

$$f = f_0(q/q_0)^{-\beta}, \quad (4.2)$$

where $q_0 = 0.5$ au, and f_0 and β are free parameters of the model. When a comet does split, its mass loss is some fraction s of its original mass,

$$\Delta M = sM, \quad (4.3)$$

where the fraction $s(R)$ of mass lost is,

$$s(R) = \frac{s_0}{R/R_0}, \quad (4.4)$$

where R is the comet radius in km, $R_0 = 10$ km and s_0 is a free parameter of the model. Di Sisto et al. (2009) fit the free parameters of their splitting model to the orbital distributions of observed JFCs, and give four best fit models. Here I choose to use their model 2, which has $\beta = 1$, $f_0 = 1/3$, and $s_0 = 0.007$. The general trend is that the best fit models have a mass loss per event (and therefore s_0) that is lower when the frequency of splitting (f_0) is higher, which is why they produce comparably good fits to the observed comet population.

Each individual comet is followed as it evolves along its dynamical path. For each 100 yr timestep, the number of orbits with the given orbital elements is found. For each orbit, a random number in the range $[0,1)$ is chosen, and compared to the fragmentation probability, f , (equation 4.2). If f is higher than the random number, a fragmentation event is assumed to occur. Otherwise nothing happens.

If a fragmentation event does occur, the fraction of mass lost, s , is calculated using equation 4.4. The mass which is lost, sM , is then deposited in the corresponding pericentre-

eccentricity bin, and distributed in dust grains as described in Section 4.3. The mass of the comet is reduced by a factor $(1 - s)$ such that the radius will shrink by a factor $(1 - s)^{\frac{1}{3}}$, and the comet's size decreases after each fragmentation. Eventually the comet mass may reach zero; when this happens the comet is assumed to have fully disrupted, and the evolution of the comet is stopped. There are thus two possible end states for a comet: either the comet is lost dynamically (which almost always means it is scattered outwards) after its dynamical lifetime ends with a nonzero mass, or all of its mass is lost in fragmentation events.

4.2.5 Outcomes of fragmentation

Models fitted to observations of JFCs (Di Sisto et al., 2009; Nesvorný et al., 2017) have suggested the need for shorter active lifetimes of comets than the canonical 12,000 yr found by Levison and Duncan (1997), with a potential increase of lifetime with size. As highlighted by Di Sisto et al. (2009), this is a natural outcome of spontaneous fragmentation. Whether a comet survives its dynamical lifetime without fully disrupting depends on two things. First, the initial size of the comet: larger comets have more mass and therefore can survive more splitting events. It also depends on what dynamical path the comet is on. For example, some of the bodies in the simulations of Nesvorný et al. (2017) only spend a few hundred yr inside

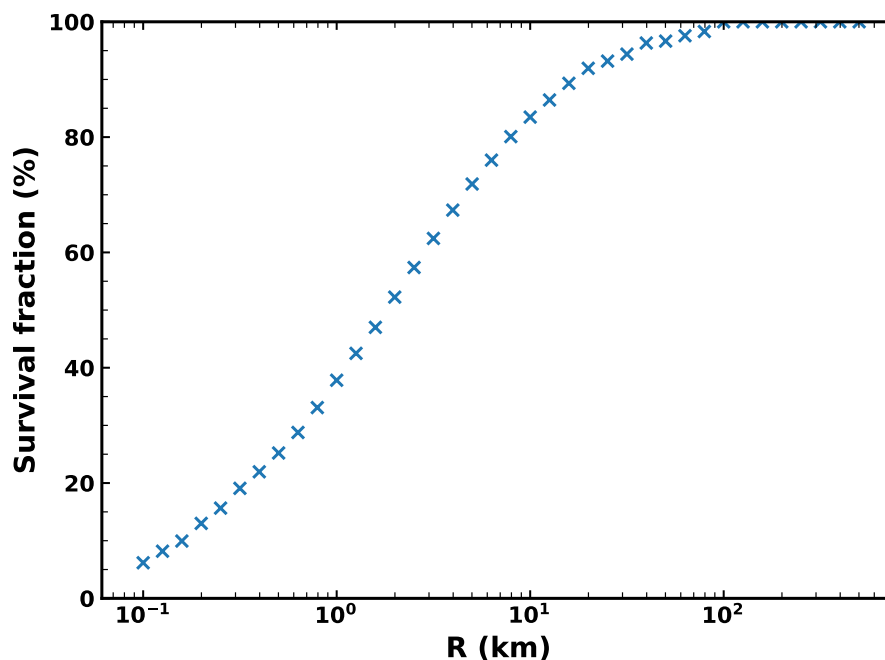


Fig. 4.4 Fraction of comets which survive their dynamical lifetime without fully disrupting as a function of initial comet radius, R .

Jupiter's orbit before being scattered outwards again, such that they may not have sufficient time to disrupt. The fraction of comets of each size which survive their dynamical lifetime, rather than fully disrupting, are shown in Figure 4.4. As expected, the general trend is higher survival fractions for larger comet nuclei, saturating at $R \sim 100$ km. Small comets disrupt much more rapidly, such that generally all of their mass will be input into the zodiacal cloud. Conversely, larger comets do not lose all of their mass, and therefore may not necessarily dominate the input to the zodiacal cloud. Overall, I found that 13 per cent of comets survived, while 87 per cent fully disrupted.

Figure 4.5 (top) shows the distribution of lifetimes individual comets have inside Jupiter's orbit in different size ranges. As expected, larger comets have longer lifetimes, with sub-km comets in particular having far shorter lifetimes than other sizes. Comets with radii > 10 km tend to survive their dynamical lifetime, such that the distributions for comets > 10 km in size generally match the distribution of dynamical lifetimes in the N-body data, although there is some fluctuation for $R > 100$ km comets due to the small number of dynamical paths they sample. Figure 4.5 also suggests that some comets survive for much longer than expected, with a non-negligible fraction of the large comets surviving for over 100,000 yr. The median dynamical lifetime of bodies from the N-body data is 40,200 yr, with a range of 100 yr to 57 Myr.

The canonical result is that the active lifetime of a comet is 12,000 yr (Levison and Duncan, 1997). This applies to comets which are 'visible', defined as those with pericentres < 2.5 au. I find that 18 per cent of the comets reach $q < 2.5$ au. Not all comets will reach small pericentres because they either fully disrupt or get scattered outwards before this point: 63 per cent of the N-body particles reach < 2.5 au at some point, suggesting that the main factor is that small comets fully disrupt before reaching small pericentres. Only 6 per cent of these comets survive their dynamical lifetime – they will fragment more frequently due to the lower pericentre (see equation 4.2). I show the lifetimes with $q < 2.5$ au in Figure 4.5 (bottom). Once more larger comets have longer lifetimes than km-sized and sub-km comets. This plot makes it appear that 10–50 km comets are longer-lived than ≥ 100 km comets inside 2.5 au. However, the distributions of these largest comets are likely affected by small number statistics, with only 123 comets larger than 100 km. Out of the comets with $R \geq 100$ km, 12 per cent are on dynamical paths with a single timestep (i.e. 100 yr) with $q < 2.5$ au. I find that 0.2 per cent of comets that reach inside 2.5 au survive there for longer than 12,000 yr. This is because the size distribution is dominated by sub-km comets, which lose all of their mass rapidly, whereas comets larger than ~ 10 km are able to survive for longer than 12,000 yr. Therefore, it is reasonable that some larger comets survive to continue fragmenting past the 'active' lifetime. It may be that they stop sublimating after this time as they run out of

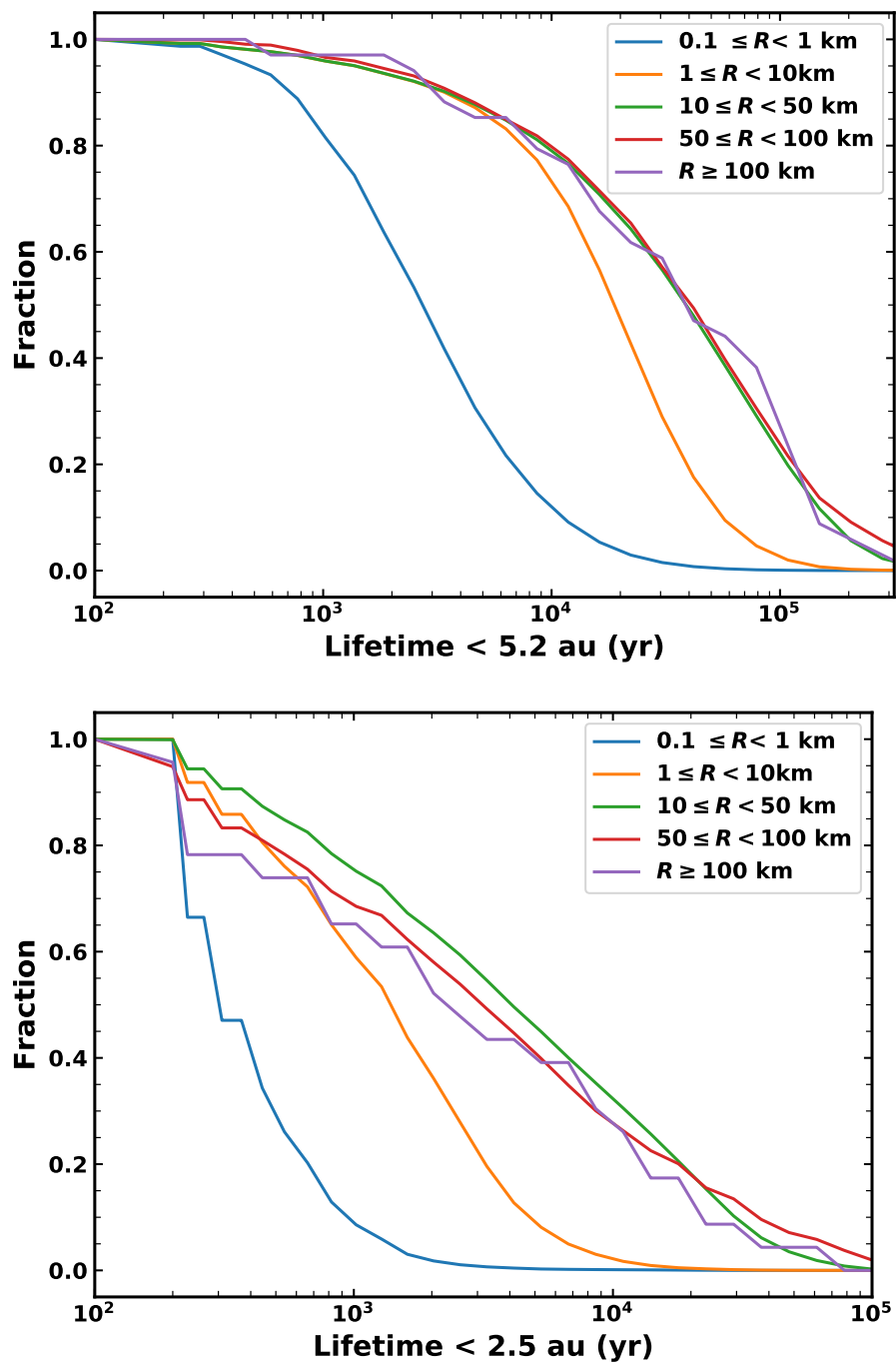


Fig. 4.5 Cumulative distributions of the lifetime each individual comet survives with $q < 5.2$ au (top) and $q < 2.5$ au (bottom) as a function of initial comet radius.

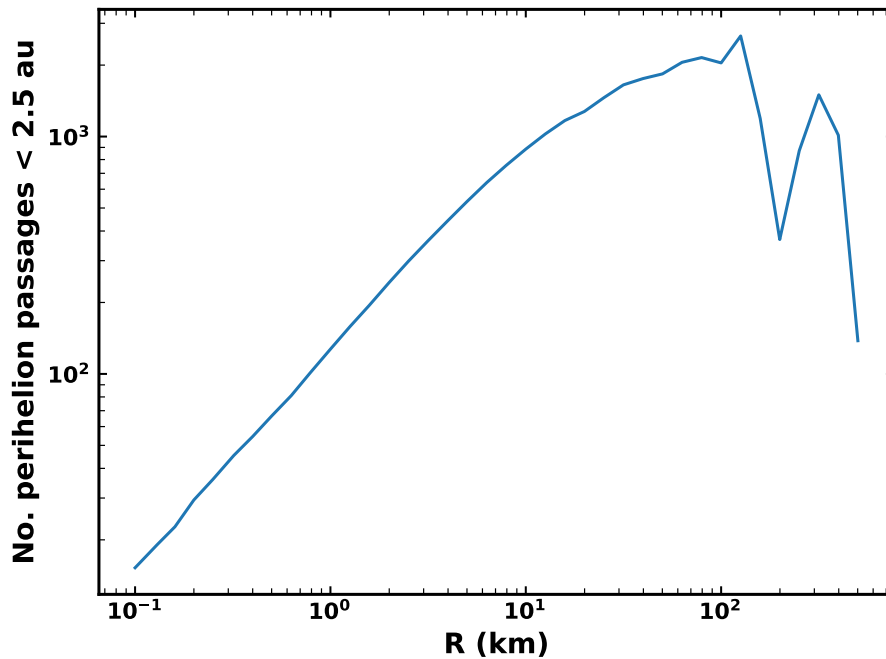


Fig. 4.6 The mean number of perihelion passages comets survive for with $q < 2.5$ au, as a function of the initial comet radius.

volatiles, or due to the build-up of a surface layer, but can continue to fragment spontaneously while dormant.

Previous JFC models have considered the lifetime of comets in terms of the number of times they pass perihelion with $q < 2.5$ au. In Figure 4.6 I therefore show the mean number of times comets of a given size pass pericentre at < 2.5 au. This has a strong size dependence, as larger comets have more mass to lose and therefore survive for longer. However, it starts to turn over at ~ 70 km as comets no longer lose all of their mass in fragmentations, such that the limiting factor becomes the dynamical lifetime of comets at < 2.5 au. In particular, a dip is seen at > 100 km due to the small numbers of comets sampled at these sizes, such that individual dynamical paths become important. I find that 1–10 km JFCs should survive hundreds of perihelion passages, while > 10 km comets should survive > 1000 passages. This is broadly consistent with the model of Nesvorný et al. (2017), which found that ~ 500 perihelion passages is needed to fit the inclination distribution of JFCs, which are mostly a few km in size, but ~ 3000 passages are needed to fit the number of > 10 km comets.

I also compared the rate of comet splitting in my model with observations. The mean rate of comet splitting for visible comets ($q < 2.5$ au) was 0.01 yr^{-1} per comet, which is consistent with the lower limit of 0.01 yr^{-1} per comet found by Chen and Jewitt (1994).

However, including all comets, the average rate decreases due to the drop in fragmentation probability with pericentre (equation 4.2).

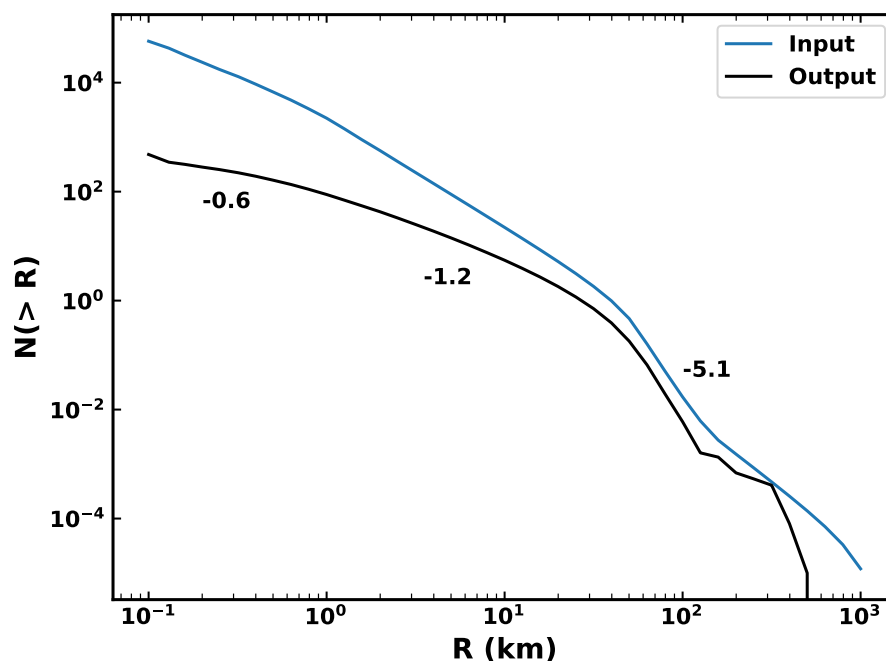


Fig. 4.7 Cumulative size distribution (CSD) of visible comets ($q < 2.5$ au) which is present on average in a 100 yr period (black) compared with the initial distribution of comets which is input (blue). The slopes of the CSD of visible comets in each region are labelled by the curve.

As comets undergo fragmentations their radii shrink, such that the size distribution of comets changes from the input distribution (Figure 4.2). The average cumulative size distribution of visible comets ($q < 2.5$ au) in a 100 yr period is shown in Figure 4.7, taking into account the change in comet size as mass is lost through fragmentation. The shorter lifetimes of comets due to fragmentation causes the slopes of the size distribution to become shallower than the input size distribution. For sub-km comets, the CSD slope found by fitting a power law to this size range goes from -1.25 to -0.6. For $1 \leq R \leq 10$ km comets, the slope goes from -2.0 to -1.2. The slope of $50 \leq R \leq 200$ km comets is relatively unchanged, however, going from -5.0 to -5.1. This change in slope may suggest that if fragmentation is the significant mass loss mechanism for JFCs, the slope of the size distribution of Kuiper belt objects from which they originate should be steeper than the observed distribution of JFCs at smaller sizes. Estimates of the Kuiper belt size distribution suggest that its slope is similar to the observed JFC distribution at these smaller sizes (Section 4.2.2), although the uncertainties in these size distributions can be quite large. For example, the slope in the

sub-km Kuiper belt size distribution was measured to be in the range -1.0 to -1.2 (Morbidelli et al., 2021), and the sub-km JFCs were measured as -1.25 ± 0.3 (Fernández and Morbidelli, 2006). One possible resolution, if these size distributions are in fact identical, is that the prescription for the size dependence of fragmentation used in my model should be changed. Di Sisto et al. (2009) assumed that the fraction of mass lost in a splitting event is proportional to $1/R$ (equation 4.4) based on the escape velocity from the comet nucleus being proportional to its radius. This means that sub-km comets will only survive one or two events, while larger comets almost never fully disrupt. A weaker size dependence would cause the size distribution of comets produced by the model to be closer to their input distribution. The size dependence of mass lost in fragmentations is therefore potentially another free parameter of the fragmentation model which should be explored.

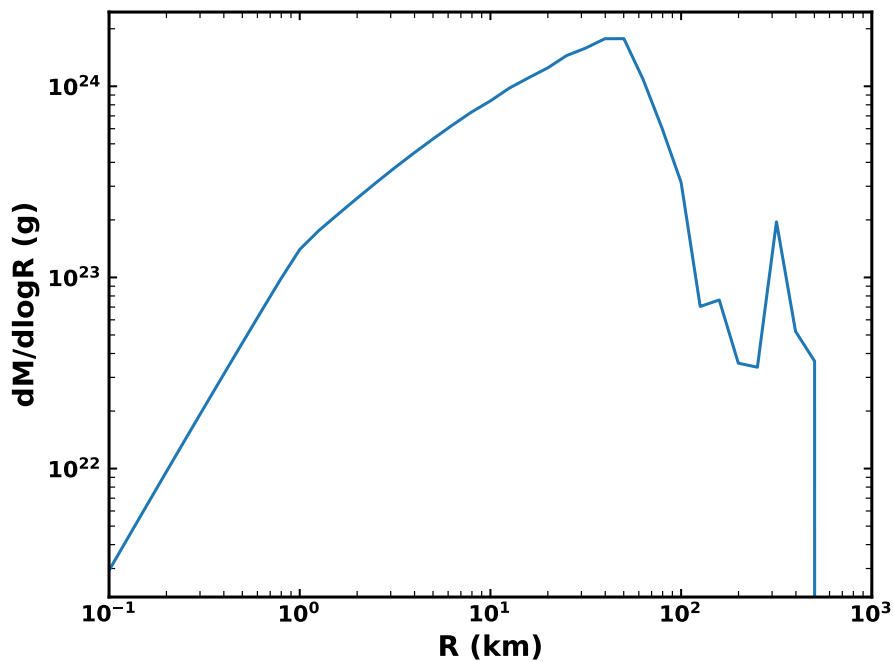


Fig. 4.8 Distribution of mass produced by fragmentation of comets with different initial sizes over the whole 100 Myr simulation. This mass will be distributed over a range of sizes, from dust up to m-size fragments, such that a fraction of this will supply the zodiacal cloud.

To investigate what sizes of comet should dominate the mass input to the zodiacal cloud, Figure 4.8 shows the total mass lost by comets due to fragmentation over 100 Myr vs. the initial size of the comet which produced the mass. It should be noted that this is the mass lost by comets in fragmentations, but only a fraction of this will supply the zodiacal cloud. I assume that only a fraction of the mass lost in a fragmentation becomes dust (see Section 4.3.4), and larger dust grains may be dominated by dynamical interactions and follow

an evolution that sticks with the parent comet (Section 4.3.2). Figure 4.8 shows that the total mass input is dominated by comets around 50 km in size. This is likely due to a balance between larger comets having more mass to potentially lose, and larger comets not losing all of their mass before being scattered out of the inner Solar System. The fraction of mass lost by a comet in a splitting is inversely proportional to its size (equation 4.4), such that a very small comet could lose all of its mass in a single event, while larger comets require many splittings to lose their mass. Further, the nature of my input size distribution of comets (Table 4.1) means that very few > 100 km comets are scattered in throughout the simulation, whereas ~ 50 km comets are present half the time. In terms of the mass in comets, the steep negative slope for 50–150 km means that the second break in the size distribution at 50 km is where the mass in comets peaks. Since most > 10 km comets survive their dynamical lifetime (Figure 4.4), the comet size which dominates the input to the zodiacal cloud is determined by what fraction of their mass large comets lose before the end of their dynamical lifetime. The size distribution is such that the larger fractional mass loss for ~ 10 km comets compared to 50 km comets is not sufficient to overcome the lower mass in such comets, which is why the mass input is dominated by ~ 50 km comets. The smallest comets (< 1 km) do not contribute much mass because, although there are many of them and they will fully disrupt, losing all of their mass, the size distribution is such that most of the mass is in larger comets.

Given that comets have finite mass, and their fragmentation probability depends on pericentre, the distribution of mass produced by comet fragmentations will not match their distribution in pericentre-eccentricity space (Figure 4.1). Figure 4.9 shows the mass lost by comets as a function of pericentre and eccentricity. Comets bounce around in the phase space, though not all will reach < 2.5 au. Conversely, the likelihood of fragmentation increases as pericentre decreases. Therefore, the production of dust peaks at the lowest pericentres, where comets fragment frequently and lose a lot of mass if they reach such low pericentres. The distribution of mass lost (Figure 4.9) looks similar to the distribution of N-body data points (Figure 4.1), weighted towards smaller pericentres due to the fragmentation probability decreasing with pericentre. It should be noted that the orbits of dust grains are affected by radiation pressure, and some grains will be removed dynamically, so the distribution of dust input into the zodiacal cloud will differ from Figure 4.9. In particular, smaller grains will be put onto higher eccentricity orbits.

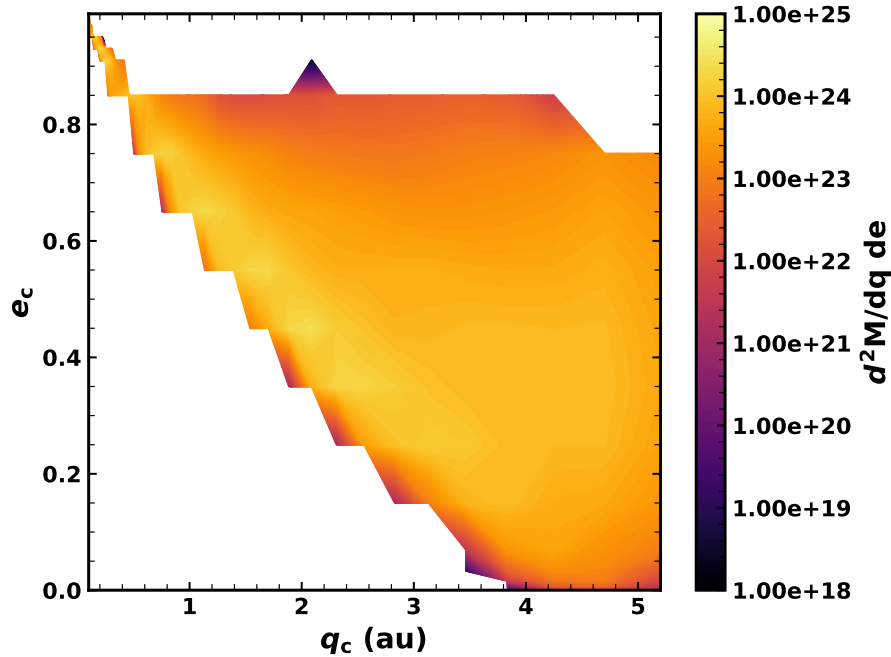


Fig. 4.9 Total mass lost by comets in fragmentation events as a function of pericentre and eccentricity, summed over 100 Myr. A fraction of this will go to dust grains, which will be put on different orbits due to radiation pressure.

4.3 Dust model

4.3.1 Input size distribution and dust properties

I assume that some fraction of the mass lost in the comet splittings of my fragmentation model (Section 4.2) becomes dust. This mass is distributed into particles with a range of sizes via a piece-wise power law size distribution.

The size distribution of dust produced in the comae of comets has been measured by several spacecraft flybys, finding various slopes over different size ranges (e.g. McDonnell et al., 1993; Hörz et al., 2006; Economou et al., 2013). Flybys of comet 1P/Halley showed that the slope varies with both particle mass and time (McDonnell et al., 1993).

More recently, various instruments on the Rosetta mission observed the coma of comet 67P/Churyumov-Gerasimenko. Rotundi et al. (2015) found the dust had a differential slope $\alpha \sim -2$ for $< \text{mm}$ -sized grains, and a slope of $\alpha = -4$ for grains larger than mm -sized. Fulle et al. (2016b) found the size distribution of smaller ($< 1 \text{ mm}$) grains varied with time: before perihelion the slope was -2 , while after perihelion it was -3.7 . However, Moreno et al. (2016) used ground-based images from the VLT to show that a slope of -3 is needed to fit the dust tail, disagreeing with in situ measurements. Further, Soja et al. (2015) found a slope of

Table 4.2 Slopes of the differential size distribution of dust grains produced in comet splittings in my model.

Size range	Slope, α
$D_{\text{bl}} \leq D \leq 100 \mu\text{m}$	3.25
$100 \leq D \leq 500 \mu\text{m}$	1.0
$500 \mu\text{m} \leq D \leq 2 \text{ cm}$	3.25

-3.7 for large ($> 100 \mu\text{m}$) particles from Spitzer observations of the dust trail of 67P. This suggests that the size distribution varies with time and particle size, and may differ between the coma and the tail.

Dust measured in comae by flybys likely originates from sublimation. Since I am concerned with the products of comet fragmentation, I instead choose to focus on the debris trails, which may be linked to the break-up of comets rather than just sublimation. Indeed, some of the dust seen near a comet is placed on unbound orbits, and so does not remain in the system. Reach et al. (2007) observed the debris trails of 27 JFCs with Spitzer, and found three populations of particles with different size distribution slopes. The breaks in the size distribution occurred at D of $100 \mu\text{m}$ and $500 \mu\text{m}$. The differential size distribution slopes resulting from the mass distribution of Reach et al. (2007) are given in Table 4.2. Notice that for this distribution, the mass will be dominated by the largest grains, while the cross-sectional area will be dominated by grains near the second break in the distribution, at $D \sim 0.5 \text{ mm}$. Assuming the dust in comet trails is linked to comet fragmentation, I therefore choose this distribution for the mass produced in my model. The lower limit of the size distribution is set by the fact that the smallest grains will be blown out on hyperbolic orbits by radiation pressure. For grains released from circular orbits, $D_{\text{bl}} \sim 1.2 \mu\text{m}$, but the blowout limit depends on the eccentricity of the parent body, the assumed composition of dust grains, and where around the orbit grains are released, as discussed later in this subsection. Submicron interplanetary dust grains are believed to be primarily of interstellar origin (e.g. Landgraf et al., 2000), and I therefore do not try to model such grains. The maximum grain size is chosen to be $D_{\text{max}} = 2 \text{ cm}$; the effects of this parameter are discussed in Section 4.6.2.

Cometary dust is typically thought to be composed of fluffy, porous grains containing ices, though they are often approximated to be compact and spherical. Measurements from the Grain Impact Analyzer and Dust Accumulator (GIADA) of the Rosetta mission found a bulk density range of $1.9 \pm 1.1 \text{ g cm}^{-3}$ for spherical grains in the size range $50 \mu\text{m} \lesssim D \lesssim 0.5 \text{ mm}$ (Rotundi et al., 2015). Fulle et al. (2016a) derived a density of $0.795_{-0.065}^{+0.84} \text{ g cm}^{-3}$ for compact $\sim\text{mm}$ -sized particles of porous icy dust also from GIADA. Here I assume cometary fragments to have a bulk density of 1.9 g cm^{-3} based on Rotundi et al. (2015).

Radiation pressure means that the orbits of dust created in the break-up of a comet on an orbit with a given pericentre and eccentricity depend on where around the orbit the break-up occurs. Thus the model needs to make an assumption about where around the orbit mass is lost in order to determine the orbits grains are placed on. For instance, most mass loss from sublimation occurs close to perihelion. Comet splittings have been observed even at large distances from the Sun. For example, splitting beyond 100 au was suggested for Comet C/1970 K1 by Sekanina and Chodas (2002), and the progenitor of the Kreutz sungrazer system is believed to have fragmented near aphelion (Sekanina, 2021). There is evidence that splitting should occur all around the orbit (e.g. Sekanina, 1982, 1997, 1999), although it could be argued that some mechanisms may cause fragmentation to be more likely closer to perihelion due to their temperature dependence.

I assume that each comet splitting occurs at a random location around the orbit, choosing a random mean anomaly for each event. The true anomaly f and heliocentric distance r at which a fragmentation takes place can then be found using Kepler's equation. The orbits of dust released by a comet depend on the ratio of radiation pressure to gravity acting on the particle, which is given by

$$\beta = \frac{3L_{\star}Q_{\text{pr}}}{8\pi GM_{\star}cD\rho}, \quad (4.5)$$

where D is the particle diameter, L_{\star} is the stellar luminosity, M_{\star} is stellar mass, ρ is the bulk density of the particle, and c is the speed of light. Q_{pr} is the radiation pressure efficiency averaged over the stellar spectrum. Then the orbital elements q_{d} and e_{d} of particles released from a comet with semimajor axis a_{c} and eccentricity e_{c} are determined from β as follows:

$$e_{\text{d}}^2 = \frac{e_{\text{c}}^2 + \beta^2 + 2e_{\text{c}}\beta \cos f}{(1 - \beta)^2} \quad (4.6)$$

and

$$q_{\text{d}} = \frac{a_{\text{c}}(1 - \beta)(1 - e_{\text{d}})}{(1 - 2\beta a_{\text{c}}/r)}, \quad (4.7)$$

where f is the true anomaly of the parent comet at the time of fragmentation, and r is the heliocentric distance its fragmentation occurs at. For my purposes I assume zero ejection velocity of particles from the comet when it fragments. The ratio of radiation pressure to gravity, β , is plotted in Figure 4.10. I calculated the optical properties of dust grains using the method of Wyatt and Dent (2002), which is based on the core-mantle model of Li and Greenberg (1997). In order to fit the density of 1.9 g cm^{-3} used in my model, grains were assumed to have a volume fraction of 1/3 silicate to 2/3 organic refractory material, with a porosity of 20 per cent. The smallest grains will be put onto hyperbolic orbits ($e_{\text{d}} > 1$) by radiation pressure, and are therefore rapidly ejected from the Solar System. For grains

released at pericentre ($f = 0$), this is given by $\beta > \frac{1}{2}(1 - e_c)$, while for grains released at apocentre ($f = \pi$), this is given by $\beta > \frac{1}{2}(1 + e_c)$. The mean value of e_c is 0.45.

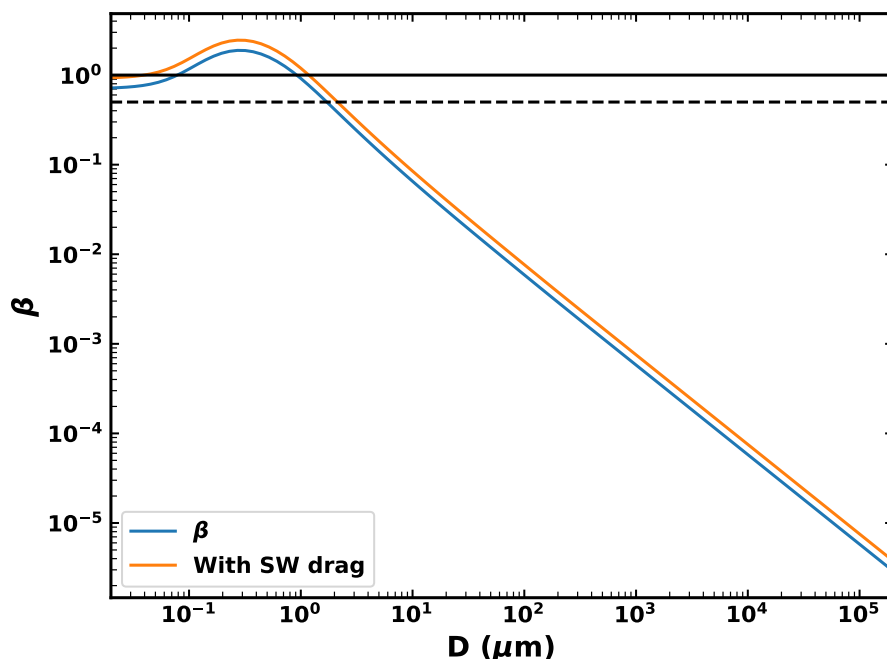


Fig. 4.10 The ratio of radiation pressure to gravity, β , for grains of different sizes (blue) with a composition which is 1/3 silicate to 2/3 organic material with a porosity of 20 per cent. The orange line shows β after being multiplied by a factor 1.3 to include the solar wind drag. The dashed and solid horizontal lines show $\beta = 0.5$ and 1 respectively. Grains released from circular orbits will be put onto hyperbolic orbits for $\beta > 0.5$, while any grains with $\beta > 1$ will be blown out of the system.

4.3.2 Timescales

Dust grains in the inner Solar System will be subject to radiation pressure, mutual collisions, P-R drag, and dynamical interactions with the planetary system. However, it is not possible to fully model all of these effects simultaneously. I therefore find the dominant physical process acting on a given debris particle by comparing the timescales for dynamical interactions, P-R drag, and collisions. Where the P-R drag or collision timescales are shortest the dust is put into a code which follows the evolution of debris in a kinetic model that accounts for drag and collisions. If the dynamical lifetime is shortest, the dust is assumed to stick with its parent comet and be lost on the dynamical timescale.

One limitation of this approach is that the model ignores the possibility of dynamical interactions with the planets during the drag and collision-dominated phase. This is a

necessary approximation, and for example does not allow for the possibility that dust becomes trapped in mean-motion resonances with planets (such as the Earth's resonant ring), or migrates into a region where the scattering timescales once more become dominant. The secular resonances at 2 au may also be important, increasing particle eccentricities and inclinations, which would influence their accretion onto Earth. Smaller particles will migrate through resonances faster than larger particles, such that larger particles would be affected more significantly. However, I expect this approximation to allow the model to reproduce the broad structure of the zodiacal cloud, but not detailed structures such as the resonant ring.

Dynamics

JFCs and grains released from them are subject to close encounters and dynamical interactions with Jupiter. Dynamical interactions will dominate the motion of the largest fragments, which are less affected by radiation pressure and P-R drag. When a particle is released from a comet, I define its dynamical lifetime to be the remaining time the parent comet has left with $q < 5.2$ au.

Poynting-Robertson Drag

The tangential component of radiation pressure, known as P-R drag, circularises the orbits of bodies and causes them to spiral in towards the star as they lose angular momentum (see, e.g. Wyatt and Whipple, 1950; Burns et al., 1979). The strength of effect P-R drag has on a body depends on the ratio of radiation pressure to gravity, β (equation 4.5). The inverse dependence of β on particle size means that P-R drag is strongest for the smallest particles. I define the P-R drag timescale to be the time for drag to reduce the aphelion of the particle to below 4 au, such that the particle is effectively dynamically decoupled from Jupiter. Given that the combination of orbital elements

$$C_0 = Q(1 - e)e^{-4/5}, \quad (4.8)$$

where Q is the aphelion and e is the eccentricity, is constant throughout evolution due to P-R drag, I can find the corresponding eccentricity for an aphelion of 4 au based on the initial orbital elements. Since P-R drag decreases both the eccentricity and aphelion monotonically, I can then find the time taken for the particle to reach an aphelion of 4 au by finding the time to reach the corresponding eccentricity, using an equation for de/dt in terms of only e and constants, as in the method of Wyatt and Whipple (1950).

In order to take into account the effect of solar wind drag, I assume it has a strength 30 per cent that of P-R drag (e.g. Gustafson, 1994; Minato et al., 2006). I therefore multiply the

values of β by a factor 1.3 to incorporate the solar wind into my model, effectively reducing P-R timescales (see Figure 4.10).

Mutual collisions

I calculate the mean time between mutual destructive collisions using the method of van Lieshout et al. (2014), further discussed in Section 4.3.3. This involves binning the particles in terms of their size, pericentre, and eccentricity, and taking into account the overlap of different orbits in order to calculate the rate of collisions between grains of different sizes/orbits. Collision rates are scaled based on the population of each bin. Summing over all sizes of impactors which can destroy target particles of a given size gives the rate of catastrophic collisions; its inverse is the mean collisional lifetime.

Effect on size distribution

Every time a splitting event occurs, the lost mass is distributed in a size distribution as described in Section 4.3.1. Grains for which the dynamical timescale is shorter than the collisional and P-R drag timescales are assumed to be dominated by their interaction with the planets (mostly Jupiter), such that I do not further include them in my calculations. Ideally I would continue to follow these grains for their dynamical lifetime, however this proved too computationally expensive. Hence the approximation that dynamically-dominated grains are lost is made, although such particles will likely contribute to the zodiacal light in part before they are scattered outwards by Jupiter. The effect of these 'lost' grains is discussed further in Section 4.6.6.

The fraction of different-sized grains which are dominated by dynamics as a function of pericentre and eccentricity is shown in Figure 4.11. The dynamical lifetime will depend on which comet dust is released from, and the collision lifetimes vary with time based on how much dust is present. Therefore, this is an average over all times and all comets. This also shows where in $q - e$ space particles of different sizes are produced, which differs from the distribution of comets (Figure 4.1) due to radiation pressure (see equations 4.6 and 4.7). Smaller grains are put onto higher eccentricity orbits by radiation pressure, while mm-cm size grains follow the same orbits as their parent comets. Collisions sometimes dominate for the largest grains which are very close in, or at times when the density of dust is high, but in general P-R drag dominates for the smallest dust grains and those closer to the Sun, while dynamical interactions dominate the largest grains and those which are further out. The fractions of the total cross-sectional area of dust dominated by drag, collisions, and dynamics are 10.2, 0.5, and 89 per cent respectively. It should be noted that while collisions

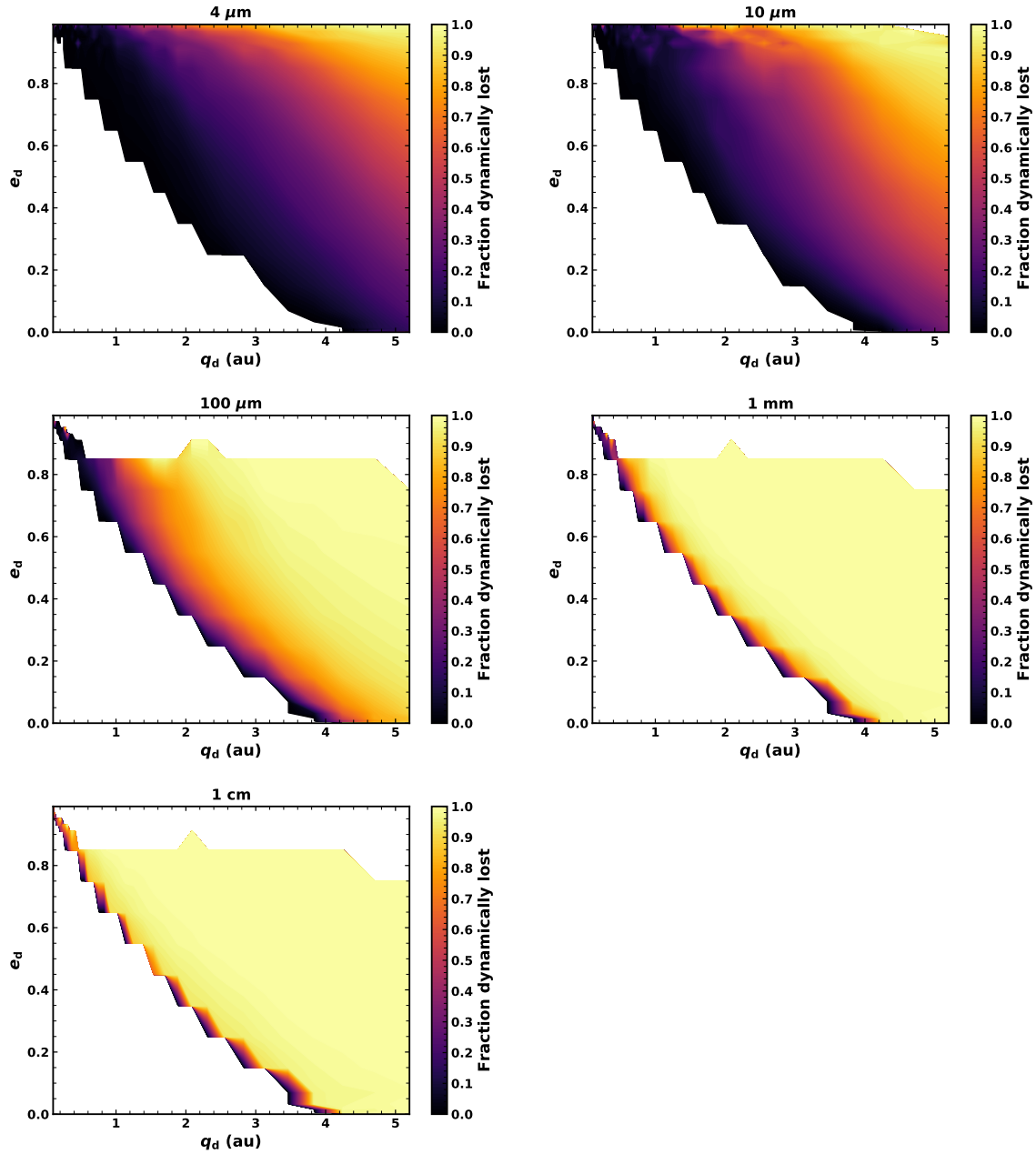


Fig. 4.11 Fraction of grains of diameter $4 \mu\text{m}$, $10 \mu\text{m}$, $100 \mu\text{m}$, 1 mm , and 1 cm which are dominated by dynamical interactions with Jupiter, as a function of pericentre q_d and eccentricity e_d . Grains for which the dynamical timescale is shorter than those of collisions and P-R drag are assumed to be lost on the dynamical timescale, and are therefore not followed by the kinetic model.

are not usually dominant when a grain is released from a comet, this does not mean that collisions will not become important later in the evolution. For example, as dust migrates inwards, collisions become more destructive due to increased velocities. While I remove the dynamically-dominated grains, their effect is discussed further in Section 4.6.6.

The dependence of the drag and collision timescales on grain size affects the size distribution input into my dust model. Figure 4.12 shows this as the distribution of cross-sectional area of grains per size decade input into the model, once 'dynamical' grains have been removed, summed over all time. The distribution of cross-sectional area produced by comets is also shown with arbitrary scaling, to highlight the effect of removing dynamically-dominated grains on the shape of the distribution. Due to the fact that larger grains are very weakly affected by radiation forces, and therefore preferentially removed from the model due to dynamics dominating their evolution, my original input size distribution is shifted towards smaller grain sizes. In particular this effect is more prominent at larger pericentre distances, where P-R drag timescales are longer, such that most large grains are removed dynamically. Hence the input size distribution is close to the distribution I assume is produced by comets

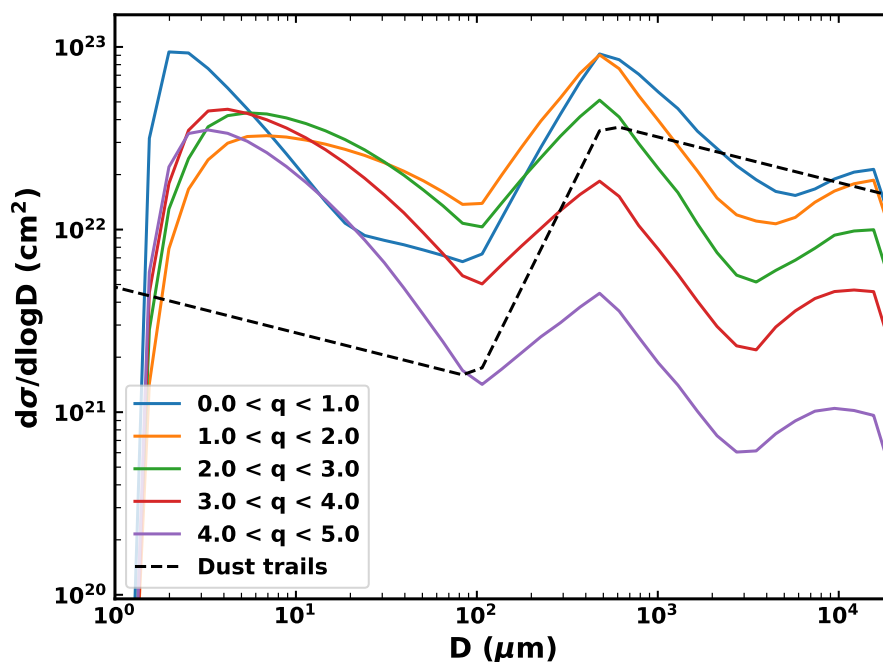


Fig. 4.12 The distribution of cross-sectional area per decade of grain size input into the dust model (Section 4.3.3) within different ranges of pericentres, summed over the whole 100 Myr. Also shown is the size distribution produced by comets based on dust trails (Reach et al., 2007, dashed black) with arbitrary scaling. The size distribution input to the dust model is modified by removal of grains which are believed to be dominated by dynamical interactions.

(Table 4.2) for grains which are close in ($q \lesssim 1$ au), whereas the size distribution of grains further out is much more dominated by the smaller grains. In all cases two peaks are seen in the cross-sectional area distribution due to the three-slope nature of the original power law: one at the smallest grain sizes, and another around where the second break in the size distribution is at $D \sim 0.5$ mm. These are unchanged by the physical processes, but the relative magnitude of the peak at 0.5 mm decreases for input at larger pericentres due to the loss of large grains.

4.3.3 Collisional evolution

After using the relevant timescales to determine which particles are lost to dynamics and which evolve due to collisions and drag, I input the drag- and collision-dominated particles into the numerical model of van Lieshout et al. (2014). This is a kinetic model which follows the distribution of particles in the phase space described by orbital elements and particle size. This includes the effects of mutual collisions and P-R drag on a population of particles, using a statistical method based on Krivov et al. (2005, 2006) to find the spatial and size distribution of particles. Particles are distributed in phase space bins in terms of their pericentre q , eccentricity e , and mass m ; other orbital elements are averaged over under the assumption that the disc is axisymmetric. A uniform distribution of inclinations is assumed. The population of each bin changes with time according to the rates of collisions and migration due to P-R drag. Starting from no mass being present, dust is added as it is produced in my comet model (Section 4.2). I follow the evolution of the mass produced by comet fragmentations over 100 Myr to find the radial profile and size distribution of the zodiacal cloud which would result from the outcome of comet fragmentation.

Only catastrophic collisions are considered by the model. The outcome of a collision is determined by the specific energy Q relative to the critical specific energy, Q_D^* , of the target. This is defined as the energy per unit mass of a collision for which the largest fragment has half the mass of the target. When two particles collide destructively, their mass is redistributed amongst smaller size fragments according to a redistribution function, which is a power law $n_r(D) \propto D^{-\alpha_r}$, where D is particle diameter. The maximum fragment mass scales with the specific energy of the collision as -1.24. These fragments are placed onto orbits determined by radiation pressure in a similar manner to equations 4.6 and 4.7, but including radiation pressure on the disrupted particles too.

4.3.4 Model parameters

For the phase space grid I use 30 logarithmic bins of pericentre from 0.1 to 5.2 au. Grain sizes are distributed into 30 logarithmic bins from diameters of 0.1 μm to 2 cm. For eccentricity, 9 logarithmic bins from 2×10^{-4} to 0.1 are used for low eccentricity grains. For higher eccentricity, there are 8 linear bins from 0.1 to 0.9, then 5 more linear bins up to $e = 1$ for the highest eccentricities.

As discussed in Section 4.3.1, I assume the dust to be porous with a density of 1.9 g cm^{-3} . For small ($< 100 \text{ m}$ -size) bodies, collisional strength Q_D^* is dominated by the material strength, and decreases with particle size. For dust grains self-gravity will be negligible. The strength of grains can therefore be parametrized by a single power law, $Q_D^* = Q_0 (\frac{s}{\text{cm}})^{-a}$, in this regime. While the collisional strength of various materials has been studied in the literature, most laboratory experiments are performed with particles $\gtrsim 10 \text{ cm}$ in size, and simulations focus mostly on larger sizes. Therefore the collisional strength for dust ($< \text{cm}$ -size) is poorly constrained, and I must extrapolate from simulations of $\geq \text{cm}$ -size objects. Benz and Asphaug (1999) used SPH simulations, and found basalt should have a slope ~ -0.37 , while ice should have a slope ~ -0.4 and lower strength overall. Jutzi et al. (2010) simulated collisional destruction of both porous and non-porous bodies, and found that in the strength regime porous bodies (such as pumice) are stronger than non-porous bodies (such as basalt), with similar dependencies on grain size to Benz and Asphaug (1999). Cometary material is believed to be porous, so as a starting point I used the prescription of Jutzi et al. (2010) for porous materials, with $Q_0 = 7.0 \times 10^7 \text{ erg g}^{-1}$ and $a = 0.43$, but both Q_0 and a are considered as free parameters.

The numerical model assumes a uniform distribution of inclinations. In principle, inclination could be added as another dimension of the phase space grid, but this would increase computational time, which is already a limiting factor. Based on the fact that > 95 per cent of JFCs should lie within this range (see Figure 8 of Nesvorný et al., 2017), I use a maximum inclination of 30° to approximate the inclination distribution. P-R drag does not affect the inclinations of particles, and collisions should not have a major effect either. However, it should be noted that Nesvorný et al. (2010) showed from their dynamical model that the inclinations of JFC particles will be increased by interactions with Jupiter after their release from comets.

Another free parameter of the model is the slope of the size distribution of fragments produced in collisions, α_r . The canonical value for this is $\alpha_r = 3.5$, based on the slope of a collisional cascade with constant collisional strength (Dohnanyi, 1969). Laboratory experiments of catastrophic impacts suggest a range of $2.5 \lesssim \alpha_r \lesssim 4.0$ (Fujiwara, 1986).

For values of $\alpha_r > 4$, the total mass will be dominated by the smallest particles, whereas for $\alpha_r < 3$, the cross-sectional area will be dominated by the largest grains.

The final free parameter of my model is ϵ , the fraction of mass lost by a comet in a fragmentation event which goes to dust, i.e. the efficiency of fragmentations. This is fitted in Section 4.4 to match the absolute value of geometrical optical depth to the present-day zodiacal cloud.

4.4 Model fitting

I compare my model with observables of the zodiacal cloud in order to fit four free parameters: the size distribution of collisional fragments, α_r ; the normalisation Q_0 and slope a of the collisional strength, Q_D^* ; and the fraction of mass lost in fragmentations which becomes dust, ϵ . These are chosen based on finding a model which can best fit the present-day zodiacal cloud at some point in time.

4.4.1 Observational constraints

I aimed to fit both the radial profile of geometrical optical depth, equivalent to the surface density of cross-sectional area, and the size distribution of interplanetary dust. The structure of the zodiacal cloud has been characterised in a lot of depth using COBE/DIRBE (Kelsall et al., 1998). The DIRBE model has different parametrizations for various components of the zodiacal cloud, but the dominant structure is the smooth cloud, which has a fan-like structure, with a density which decreases with heliocentric distance. Integration of the density of the smooth cloud vertically gives an optical depth of the zodiacal cloud at 1 au of 7.12×10^{-8} .

Kelsall et al. (1998) measure a radial power law slope of -1.34 ± 0.022 with DIRBE for the volume density of cross-sectional area. This is in agreement with other measurements of the radial structure of the zodiacal cloud. Photometry on Helios 1 and 2 found the spatial density of zodiacal light particles to vary with a slope -1.3 in the range $0.3 \leq r \leq 1$ au (Leinert et al., 1981). Meanwhile, Hanner et al. (1976) fit a power law to Pioneer 10 observations of the zodiacal light at > 1 au, and found the best fit was either a single power law with a slope ~ -1 , or a power law with a slope of -1.5 with additional enhancement in the asteroid belt. Both models had a cut off at 3.3 au, outside which the zodiacal light is no longer visible over the background. I use these measurements to fit both the absolute value of the geometrical optical depth and its radial slope. Since geometrical optical depth is the volume density of cross-sectional area integrated vertically, if the number density has a radial dependence $n(r) \propto r^{-\nu}$, the geometrical optical depth should have a radial dependence $\tau(r) \propto r^{1-\nu}$

(for my assumption about the inclination distribution, which means that the scale height is proportional to r). Therefore, I want to fit to a radial slope for the geometrical optical depth of ~ -0.34 between 1 and 3 au.

Finally, I consider the size distribution of zodiacal dust, focussing on the grain size which dominates the cross-sectional area and therefore the zodiacal light emission. At present, the size distribution of particles in the interplanetary dust cloud is best known at 1 au. The most comprehensive model of the size distribution is that of Grun et al. (1985), which combined measurements of different particle sizes based on in situ measurements from Pioneer 8 and 9, Pegasus, and HEOS-2 along with lunar microcraters to produce an empirical model for the size distribution of interplanetary dust particles (IDPs) near Earth. The model of Grun et al. (1985) has a peak in the cross-sectional area distribution $d\sigma/d\log D$ at $D \approx 60 \mu\text{m}$. Love and Brownlee (1993) measured the flux of particles onto a plate on the LDEF satellite near Earth. Converting their flux to a distribution of cross-sectional area gives a peak at $D \approx 140 \mu\text{m}$. I therefore want my distribution of cross-sectional area at 1 au to peak at particle sizes of $\gtrsim 60 \mu\text{m}$.

4.4.2 Fitting

The free parameters of my model are fitted to three observables: the absolute value of geometrical optical depth at 1 au, $\tau(1 \text{ au})$, the slope of that optical depth between 1 and 3 au, and the grain size which dominates the cross-sectional area. It is part of the stochastic nature of my model that these variables will vary over time depending on what comets are scattered in and how much they fragment. Therefore, my aim in fitting this model to the zodiacal cloud is simply to find for what parameters can it pass through the correct values of all three observables simultaneously at some time. While a range of parameters can give reasonable results, here I try to find the best combination. This is not to say that I have developed a comprehensive model for the zodiacal cloud: I have made some important approximations about the inclinations of particles and the effects of dynamical interactions with Jupiter. Further, other sources (other types of comets and asteroids) should contribute a small amount to our current zodiacal cloud. Here I am simply trying to show the feasibility of a physical comet fragmentation model.

As expected, since ε determines the total mass input into my dust model, the primary effect of increasing ε is an increase in the absolute value of the geometrical optical depth. However, increasing the overall number of particles will also increase collision rates, which are proportional to the number density of particles. This shifts the size distribution to smaller grain sizes, as increased collision rates cause the destruction of larger grains and increased production of smaller fragments. The relationship between ε and $\tau(1 \text{ au})$ is not linear, but it

is monotonic, and so I can simply adjust the efficiency to match the absolute optical depth $\tau(1 \text{ au})$.

Dust migrating inwards due to P-R drag is expected to have a flat radial profile. Collisions will be more destructive closer in due to higher collision velocities, which would give a positive radial slope. However, the fact that my source is extended, with comets fragmenting at a range of heliocentric distances, produces a negative radial slope as seen for the zodiacal cloud (see Leinert et al., 1983). With the canonical values of my free parameters described in Section 4.3.4, the slope is too steep at all times, with a maximum value of -0.45. Therefore, α_r and Q_D^* must be altered to improve this slope.

The redistribution function α_r describes the distribution of mass produced in disruptive collisions. The range of potential values is $2.5 < \alpha_r < 4$, with my initial value $\alpha_r = 3.5$. Decreasing α_r shifts the mass produced in collisions to larger sizes, which also shifts the overall size distribution to larger particles. It also causes an increase in the overall optical depth and a decrease in the radial slope.

The collisional strength Q_D^* has two parameters which can be varied: the absolute value Q_0 , and the dependence on particle size a . Increasing the absolute value Q_0 makes particles of all sizes more difficult to disrupt via collisions, increasing their collision timescales. The peak in cross-sectional area should occur at a grain size for which the collision and P-R drag timescales are the same. Therefore, increasing Q_0 and thus the collision timescales means this occurs at a larger grain size, such that the cross-sectional area peaks for larger grains. Increasing Q_0 also causes a slight decrease in the radial slope.

The other free parameter is a , the slope of the power law of Q_D^* . Increasing a increases the collisional strength of all grains $< \text{cm}$ -size, with a stronger effect for smaller grain sizes. Similar to an increase in Q_0 , this can increase the grain size which dominates the cross-sectional area by increasing the collision timescales of small grains. Again, the reduced collision rates cause a slight decrease in the radial slope.

The main difficulty in fitting the zodiacal cloud was the radial slope. With my canonical model, the maximum slope was -0.45, which was too steep to fit the observed slope of -0.34. In order to increase the radial slope, I increased α_r to 3.75. However, this shifts the size distribution to smaller grain sizes such that the fit for the dominant grain size was poor. I therefore had to increase a to 0.9 to shift the peak of the cross-sectional area distribution to $60 \mu\text{m}$ grains. Finally, I decreased Q_0 to $2 \times 10^7 \text{ erg g}^{-1}$. Fitting to the absolute optical depth, I found an efficiency ε for fragmentations of 5 per cent. In one representative run, this gave me a best fit of a slope of -0.34, optical depth at 1 au of 7.1×10^{-8} , and a peak of cross-sectional area at $60 \mu\text{m}$ at 66.7 Myr, with another good fit of -0.34, 7.3×10^{-8} and

57 μm at 37.4 Myr. While the model matches the observed values on two occasions during this run, the observables are highly variable due to stochasticity, as discussed in Section 4.6.1.

The model has several free parameters, and it could be argued that there are alternative ways the model could be parametrized while fitting the observables. However, while I do not claim to have a unique model, it does allow to link the zodiacal cloud to its origin in the dynamical and physical evolution of comets, using a physically plausible model.

4.5 Results

4.5.1 Mass input to the zodiacal cloud

Given the stochastic nature of what comets scatter in as part of my model (and what path they take), the amount of mass being produced by comet splittings is stochastic and highly variable. Figure 4.13 shows the total mass input rate to my dust model as a function of time. This takes into account the 'loss' of grains dominated by dynamical interactions and an efficiency parameter of 5 per cent. The mass input to the zodiacal cloud then ranges from 18 to $5.1 \times 10^5 \text{ kg s}^{-1}$, with a mean value of 990 kg s^{-1} and a median of 300 kg s^{-1} . At the two

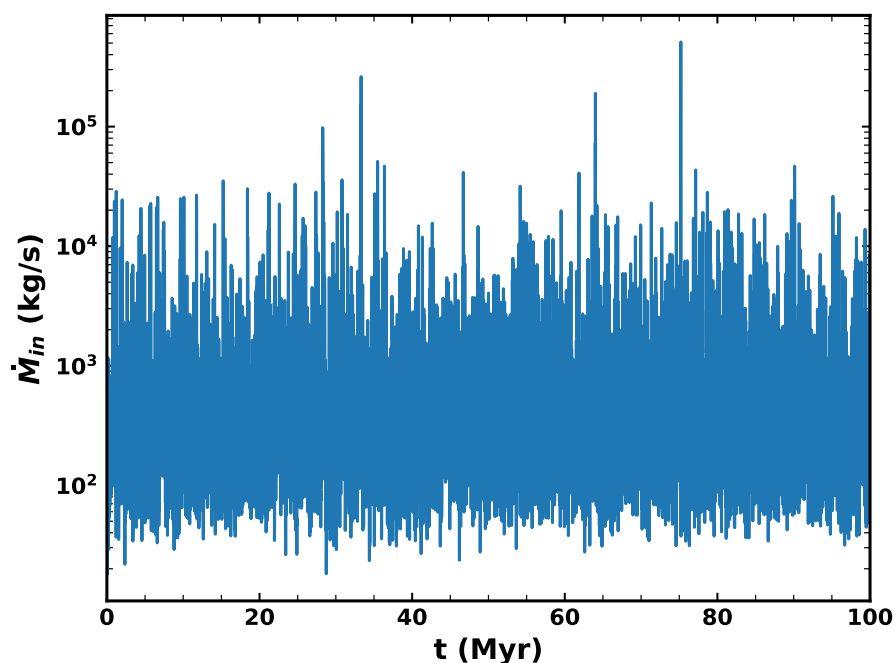


Fig. 4.13 Total mass input rate into my dust model from comet fragmentation as a function of time after removing dynamically-dominated grains and assuming a fraction $\epsilon = 5$ per cent of mass produced in a comet fragmentation becomes dust.

times my model best fits the zodiacal cloud, the mass input rate is 6,240 and 11,100 kg s^{-1} (i.e. these are epochs of higher than average mass input). Spikes of around two orders of magnitude are seen, which can be linked to the presence of very large comets, highlighting the importance of the stochastic element of my model. This can be compared to previous estimates of the amount of mass required to sustain the zodiacal cloud. Based on their model of Helios 1/2 data, Leinert et al. (1983) required a mass input of 600–1000 kg s^{-1} to sustain the zodiacal cloud in steady state, while Nesvorný et al. (2010) required a slightly higher mass input of 1000–1500 kg s^{-1} , though did not fully take into account loss of mass through collisions. However, Nesvorný et al. (2011) suggested a much higher rate of $\sim 10,000 \text{ kg s}^{-1}$ was needed due to the fact that they found grains released closer to the Sun had shorter collisional lifetimes. My mean mass input rate is thus comparable to previous estimates.

The total mass input to my dust model distributed in pericentre-eccentricity space is shown in Figure 4.14. Most mass is inputted at moderately high eccentricities due to the high eccentricities of the comets. More mass is inputted at lower pericentres due to a combination of the higher rates of splitting events closer in and the removal of grains dominated by dynamical interactions, which are more important at larger pericentres. There is a lower-bound in pericentre-eccentricity space which corresponds to an apocentre of 4 au; this is based on the orbital distribution of the parent comets (Figure 4.1).

The mass input from my fragmentation model as a function of heliocentric distance is shown in Figure 4.15, which was found by distributing the mass equally around orbits for each (q, e) bin. The mass input peaks at 4.5 au, with a sharp drop-off further from the Sun. This is due to a balance between the fact that comet fragmentation is more likely closer to the Sun, and that comets move inwards from 5.2 au, such that some may fully disrupt before getting too close to the Sun. Further, the dynamical removal of the largest grains, which dominate the mass, is much more effective further out, where drag timescales are longer, which will shift the mass input towards smaller heliocentric distances. The eccentricity of cometary orbits means that a comet on a given orbit can produce dust at a range of heliocentric distances depending where around the orbit it fragments. The comets act as a distributed source of dust, with a mass input which is concentrated inside Jupiter's orbit, but continues outside Jupiter.

In Figure 4.8 I showed which sizes of comet produced the most mass in fragmentations. However, this is slightly different from how much dust each size of comet produces which supplies the zodiacal cloud. Figure 4.16 shows the distribution of dust which is inputted into my kinetic model as a function of the initial size of the comet which produced it. This is essentially Figure 4.8, scaled by an efficiency ε of 5 per cent, and removing the dust which is assumed to stay with its parent comet. In both cases the mass input is dominated

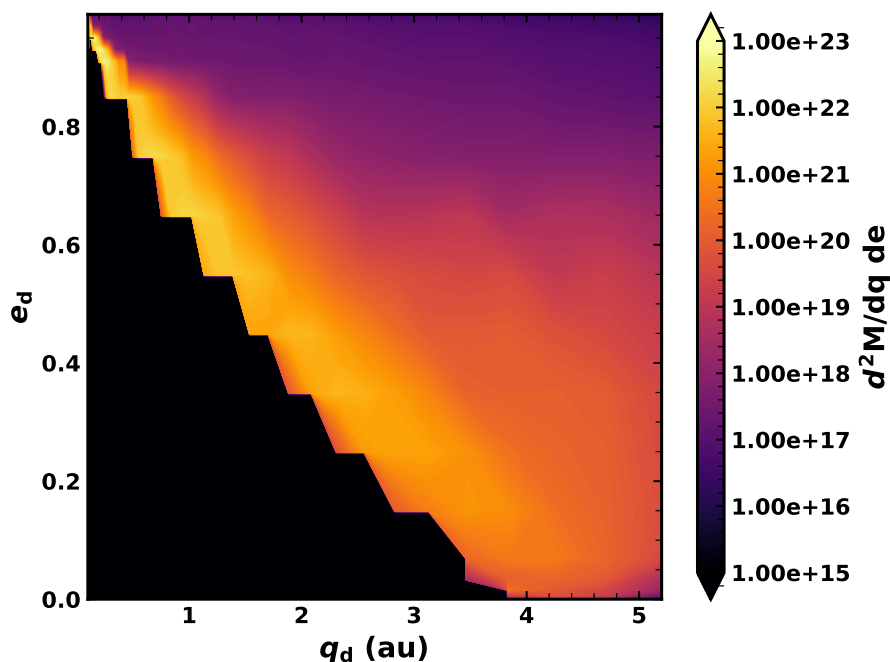


Fig. 4.14 Distribution of mass input into my dust model in terms of pericentre and eccentricity, assuming $\varepsilon = 5$ per cent of mass lost in comet fragmentations goes to dust and removing grains dominated by dynamical interactions with Jupiter, summed over the whole 100 Myr.

by comets of initial size ~ 50 km, and other than the absolute value, the distribution is very similar for $R \lesssim 50$ km. However, the contribution from $R > 200$ km comets is much more significant after the removal of dynamically-dominated grains. This is likely because these comets do not fully disrupt, such that they have longer lifetimes, and are more likely to survive to reach lower pericentres, where dust is dominated by drag and collisions. The sharp drop at $R \sim 200$ km is probably because the break in the input comet size distribution at $R = 150$ km is a minimum in terms of the mass in comets. Therefore, even including dynamical interactions, my conclusion remains that the mass input to the zodiacal cloud should be dominated by comets of initial radii ~ 50 km.

4.5.2 Dust distribution

Here I present the behaviour of dust produced by comet splittings as it evolves in my collisional evolution model, and the resulting radial and size distributions, as well as its variation in time.

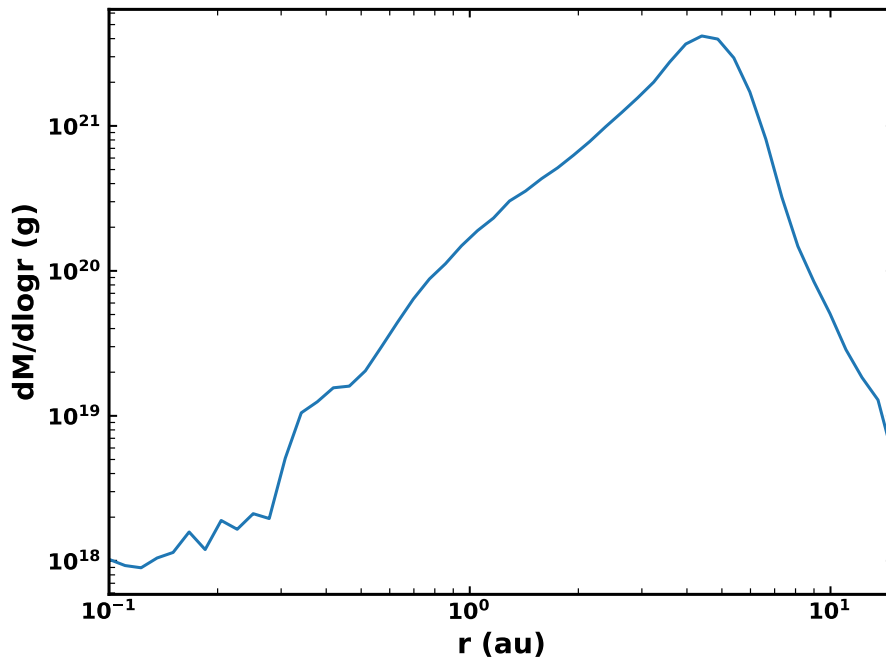


Fig. 4.15 Mass input into my dust model as a function of heliocentric distance after weighting by $\varepsilon = 5$ per cent and removing dynamically-dominated grains, summed over 100 Myr. Mass is distributed equally around the orbit in terms of mean anomaly for each combination of pericentre and eccentricity.

Optical depth

The evolution of the radial profile of geometrical optical depth with time is shown in Figure 4.17. I also show the radial profile at 66.7 Myr, when the model best fits the profile of the present-day zodiacal cloud, with a value of 7.1×10^{-8} at 1 au and a radial slope of -0.34, which both agree well with the COBE/DIRBE measurements. The radial profile is relatively flat inside of 1 au, with a shallow negative slope out to 3 au. The comets act as a distributed source, such that the radial profile continues past > 10 au, but drops off very sharply outside ~ 4 au. Such a sharp drop-off > 4 au is not seen in observations of Solar System dust (e.g. Poppe et al., 2019). However, this is due to the presence of dust from sources other than JFCs that are not included here since they contribute little to the inner few au that is the focus of this work (see also Section 4.6.6). Figure 4.17 also highlights the variations of optical depth with time: the overall level varies depending on how many comets are being scattered in and how massive they are. The shape and slope can also vary based on where comets are depositing the most mass. For example, at 60 Myr a bump is seen at ~ 1.5 au, which is likely due to a massive comet depositing a lot of mass there.

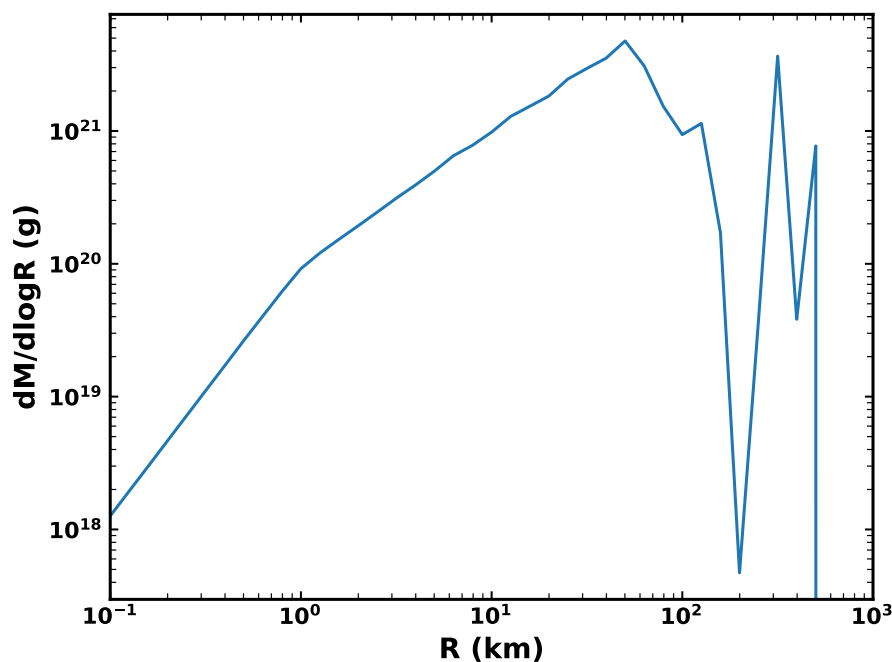


Fig. 4.16 Mass of dust produced by comets of different initial sizes over 100 Myr which supplies the zodiacal cloud (i.e. excluding the dusty fragments that are dominated by dynamical evolution). The same as Figure 4.8, but weighted by a factor of $\varepsilon = 5$ per cent, and removing dynamically-dominated dust grains.

It should be noted that the cross-sectional area and optical depth will be dominated by smaller grain sizes, while the largest grains, which dominate the mass, will not contribute significantly to the brightness. The optical depth profiles of various grain sizes are shown in Figure 4.18. Dust grains which are dominated by P-R drag should migrate inwards to give a flat optical depth profile, while grains which are being destroyed by collisions are expected to be depleted closer in, where collisions are more frequent (e.g. Wyatt, 2005; Rigley and Wyatt, 2020). The smaller grains which dominate the optical depth ($D \lesssim 100 \mu\text{m}$) have flat radial profiles due to P-R drag, causing the overall radial profile to be flat close in. The largest grains (mm- and cm-size), which supply mass to the interplanetary dust complex, are depleted by collisions closer in. The destructive collisions of these grains supply the smaller grains which dominate the zodiacal emission. This is why it is important to model the mass produced by collisions: it describes the shift of mass to smaller grain sizes, allowing me to explain the size distribution and radial profile of the dust. The importance of collisional evolution is discussed further in Section 4.7.2.

Size distribution

The size distribution of dust, expressed in terms of the distribution of cross-sectional area, is shown in Figure 4.19 at various locations. While the size distribution of dust input by comets (Figure 4.12) has two peaks and breaks in the distribution, the size distribution of my dust model has been smoothed out. The difference between the size distributions which are input to and resulting from the kinetic model suggests that the final distribution is relatively insensitive to the specifics of the input distribution, and is primarily determined by collisions and drag. At 5 au, the size distribution has a subtle peak at 0.5 mm, which is likely due to the peak there in the input size distribution (Table 4.2). Then moving inwards, the grain size dominating the cross-sectional area decreases. At 1 au the distribution of cross-sectional area peaks at $D \sim 60 \mu\text{m}$, though overall it is quite flat in the range $3 \lesssim D \lesssim 100 \mu\text{m}$.

Figure 4.20 compares the size distribution at 1 au from my model to two measurements of the flux of particles near Earth. Grun et al. (1985) developed an empirical model for the distribution of interplanetary dust at 1 au based on lunar microcraters and in situ measurements of interplanetary dust. LDEF (Love and Brownlee, 1993) measured the distribution of dust accreted to Earth over a more limited size range. The cross-sectional area distributions of

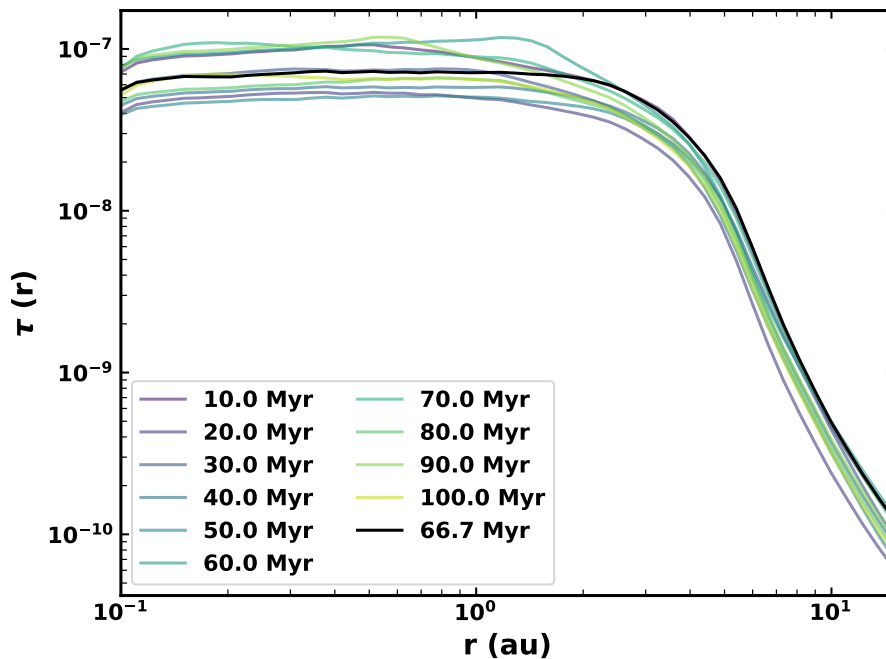


Fig. 4.17 Radial profile of geometrical optical depth at different times for my best fit model, including 66.7 Myr (black) where it best fits the present-day zodiacal cloud as measured by COBE.

Grun et al. (1985) and Love and Brownlee (1993) peak at grain diameters of 60 and 140 μm respectively, while at this time my distribution peaks at 60 μm . However, the shapes of the three distributions are slightly different: mine is relatively flat in the region of interest, whereas Grun et al. (1985) is more peaked, and LDEF has a peak at a larger grain size. At larger grain sizes my model matches Grun et al. (1985) quite well, but for $1 < D < 10 \mu\text{m}$ I predict a lot more grains than the empirical model. However, it should be noted that the in situ measurements which the empirical model was fitted to cover grain sizes $D \leq 0.9 \mu\text{m}$ and $D \geq 41 \mu\text{m}$, such that there are not direct observations of grains in the range where there is a discrepancy.

Variation of the zodiacal cloud

As mentioned previously, the distribution of dust in my model is stochastic, depending on which comets are scattered in and where they deposit dust. The variation of my three zodiacal cloud observables with time are shown in Figure 4.21: the absolute value of optical depth near Earth, $\tau(1 \text{ au})$, the slope of the radial optical depth profile between 1 and 3 au, and the grain size at which the distribution of cross-sectional area peaks. This demonstrates the

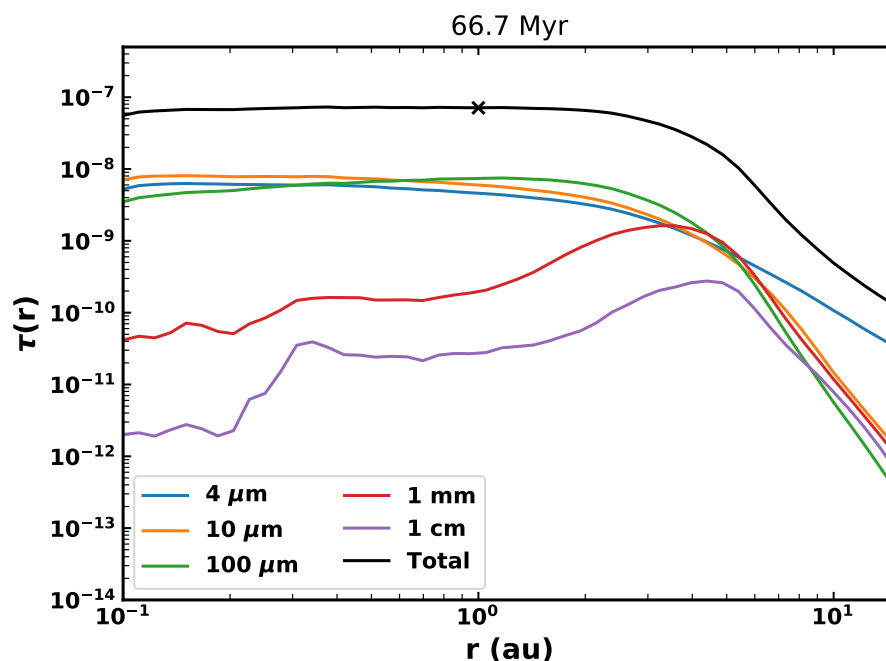


Fig. 4.18 Radial profile of geometrical optical depth from my best fit model for dust grains in size bins centred on the values shown, along with the total optical depth (black). The optical depth of the current zodiacal cloud at 1 au is marked with an x.

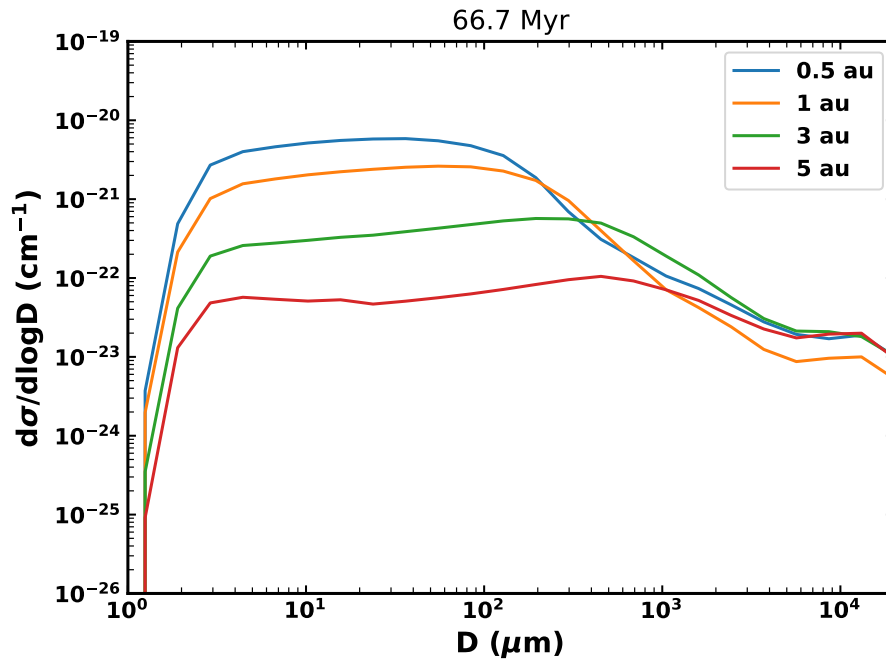


Fig. 4.19 Distribution of the volume density of cross-sectional area per size decade at different heliocentric distances as a function of grain size for my best fit model at the time when it best fits the present zodiacal cloud.

relationship between the different variables. While there is variation, the amount of dust as measured by the optical depth at 1 au is roughly constant, with a few large spikes. The radial slope fluctuates, which could be related to where mass is input by the comets: as shown in Figure 4.17, a large comet depositing a lot of mass in one particular region can cause a change in the shape of the radial profile. The dominant grain size is also highly stochastic. There are a few events where there is a large spike in optical depth, which all correspond to a sharp drop in the slope and the dominant grain size, before evolving back to the quiescent level of dust. The rapid increase in the amount of dust present during a spike likely leads to a much higher collision rate. This would cause the production of small grains and destruction of large grains, shifting the size distribution towards smaller sizes. Similarly, collisions occur more frequently closer in due to the higher relative velocities of particles. The drop in the slope of optical depth could be explained by a higher production rate of small grains by collisions closer in; since it is the smaller grains which will dominate the optical depth, this affects the overall radial slope.

While a lot of stochasticity is seen in these variables, it should be noted that the overall level of variation in the optical depth is only a factor of a few, although one spike causes a jump of an order of magnitude. However, this depends on which dynamical paths comets are

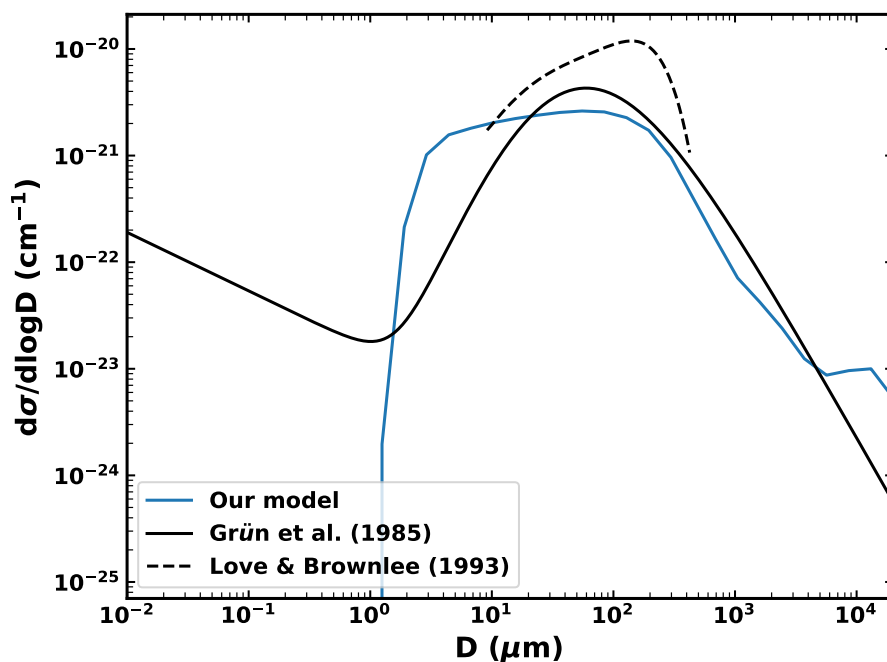


Fig. 4.20 Distribution of cross-sectional area volume density per size decade at 1 au as a function of grain size from my model at 66.7 Myr (blue), the empirical model of Grün et al. (1985, black, solid), and measurements from the LDEF satellite (Love and Brownlee, 1993, black, dashed).

placed on; when the largest comets have longer dynamical lifetimes, much larger spikes in the optical depth can be seen.

The correlation between the slope and absolute value of the optical depth can be seen more clearly in Figure 4.22, which shows the evolution of both variables against each other with time. This shows how the slope fluctuates back and forth at the quiescent level of dust depending where comets are inputting mass. Spikes in the amount of dust cause a sharp drop in the radial slope before it returns to the previous level.

The emission a distant observer would see from the zodiacal cloud will also be highly variable as a result of the stochasticity. Using realistic optical properties (see Section 4.3.1), I calculated the emission which would result from my dust model. The fractional $12\ \mu\text{m}$ excess vs. time is shown in Figure 4.23. This is stochastic and follows the same trends as the overall level of optical depth (Figure 4.21, top). The $12\ \mu\text{m}$ excess at the time the model best fits the zodiacal cloud is 4.1×10^{-5} , with a total cross-sectional area of $8.7 \times 10^{20}\ \text{cm}^2$. However, spikes in the level of dust can cause an excess as high as 6×10^{-4} , approaching levels detectable with an interferometric instrument such as the Large Binocular Telescope Interferometer (Hinz et al., 2016).

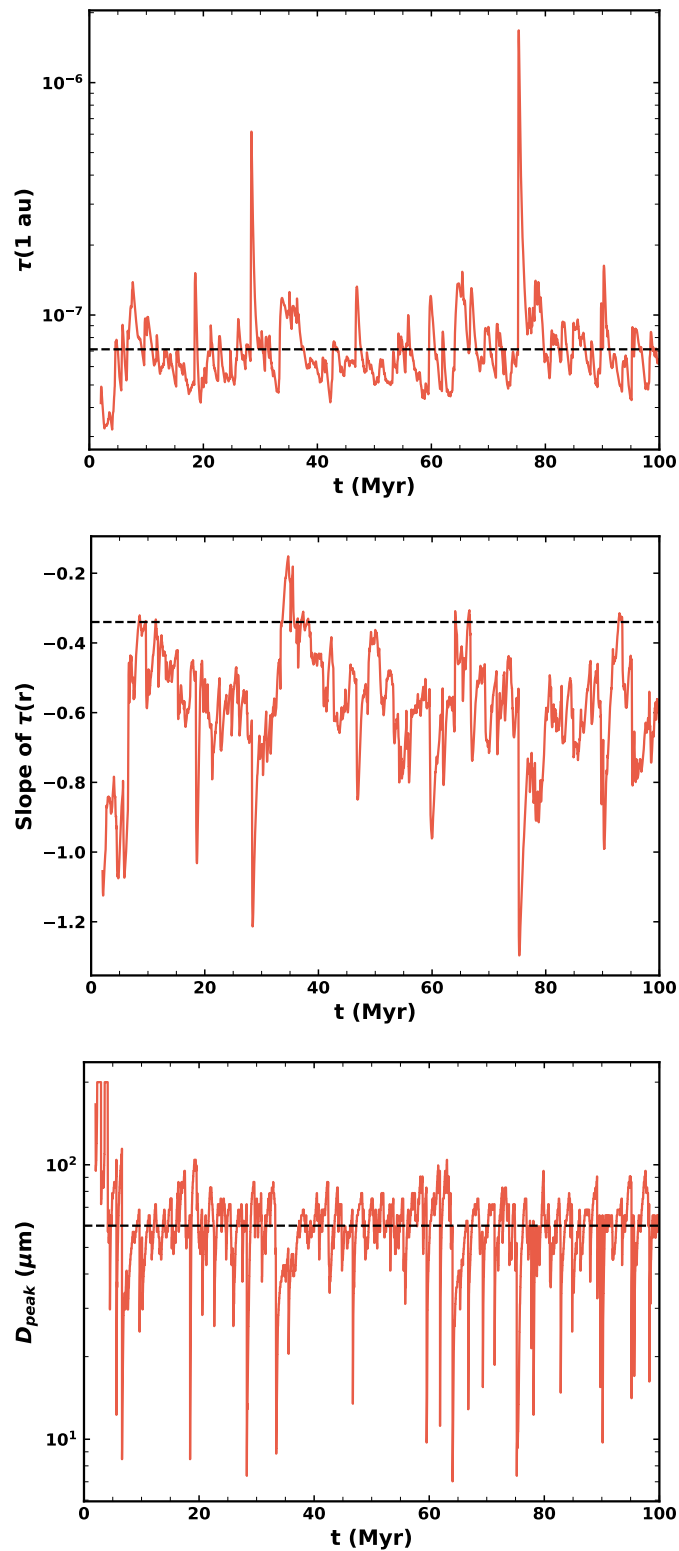


Fig. 4.21 Evolution of my three 'observables' of the zodiacal cloud as a function of time. The values of the present zodiacal cloud are shown with dashed black lines. Top: absolute value of geometrical optical depth at 1 au as a function of time. Middle: slope of the radial profile of optical depth between 1 and 3 au as a function of time. Bottom: grain size which dominates the cross-sectional area of dust grains at 1 au as a function of time.

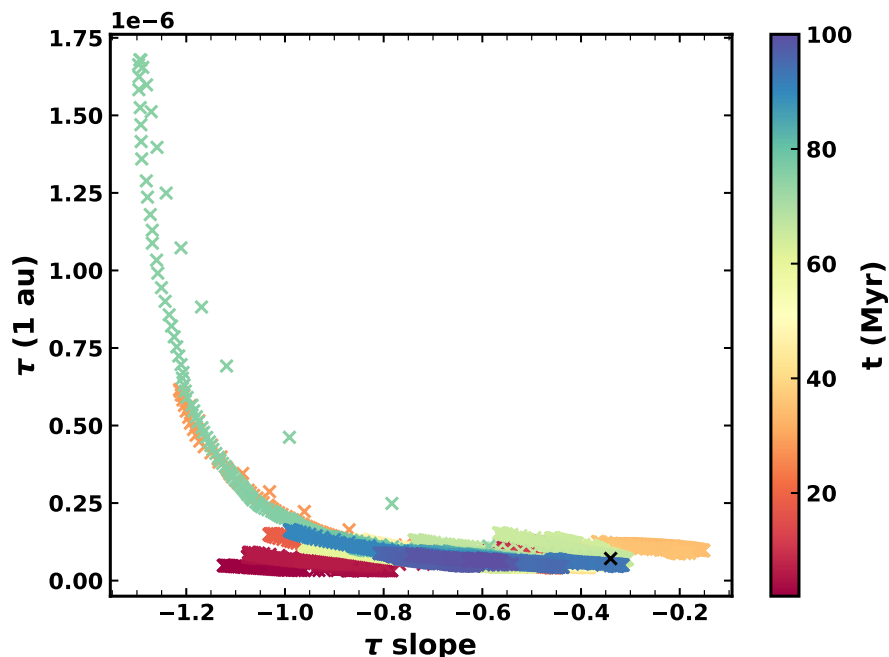


Fig. 4.22 Evolution of the absolute value and radial slope of the geometrical optical depth of my zodiacal cloud model as a function of time. The present-day zodiacal cloud is marked with an x.

Spike event

As suggested in Section 4.5.2, large comets cause occasional spikes in the level of dust, which correspond to a sharp drop in the radial slope, and a drop in the dominant grain size (see Figure 4.21). The largest spike occurs at 75.3 Myr, in which the level of dust jumps by an order of magnitude. The three observables are shown again in Figure 4.24, zoomed in on the evolution of this spike. The optical depth (Figure 4.24, top) shows that the spike in the level of dust decays after around 1.5 Myr. The slope takes a similar amount of time to return to its previous value.

By considering which large ($R \geq 100$ km) comets are scattered into the inner Solar System, this spike may be attributable to a particular comet. It might be expected that the largest spike in mass would be caused by the largest comet scattered in. However, due to the fact that $\gtrsim 100$ km comets will not lose all of their mass to fragmentations in general, the main factor determining whether large comets create massive spikes in the amounts of dust is the length of the dynamical path they are on. For example, there is one 501 km comet, and two 398 km comets scattered in during my simulation. However, these are all on dynamical paths which only spend $< 40,000$ yr in the inner Solar System. They therefore do not cause

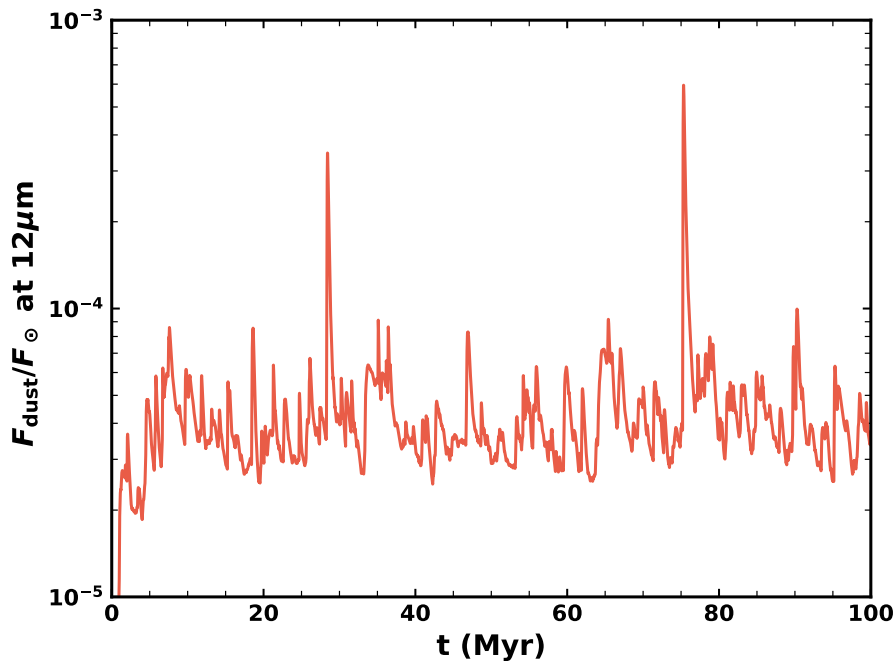


Fig. 4.23 Evolution of the fractional excess of $12 \mu\text{m}$ emission relative to the Sun which would be seen by a distant observer with time.

particularly large spikes in dust, as they are not present for long enough to lose much mass. The longest-lived large comet is a 125 km comet which is scattered in at 28.2 Myr, and has a dynamical lifetime of 284,700 yr. This seems to correspond to the peak in optical depth which occurs at 28.45 Myr, as while this comet is smaller it has a lot of time in the inner Solar System to produce mass. The effects of this particular comet last until around 29 Myr, long after it has left the inner Solar System. There is another large comet with a radius of 316 km scattered in at 74.6 Myr with a dynamical lifetime of 108,300 yr. This seems to correspond to the largest spike in optical depth at 75 Myr. Massive comets may therefore have lasting effects on the distribution of zodiacal dust if they spend long enough inside Jupiter's orbit.

This highlights that very large comets may cause huge spikes in the levels of dust, but only if their dynamical lifetimes in the inner Solar System are long enough. The highly stochastic nature of dynamical interactions means this may happen occasionally, but often large comets may have shorter lifetimes and therefore not contribute huge amounts of dust.

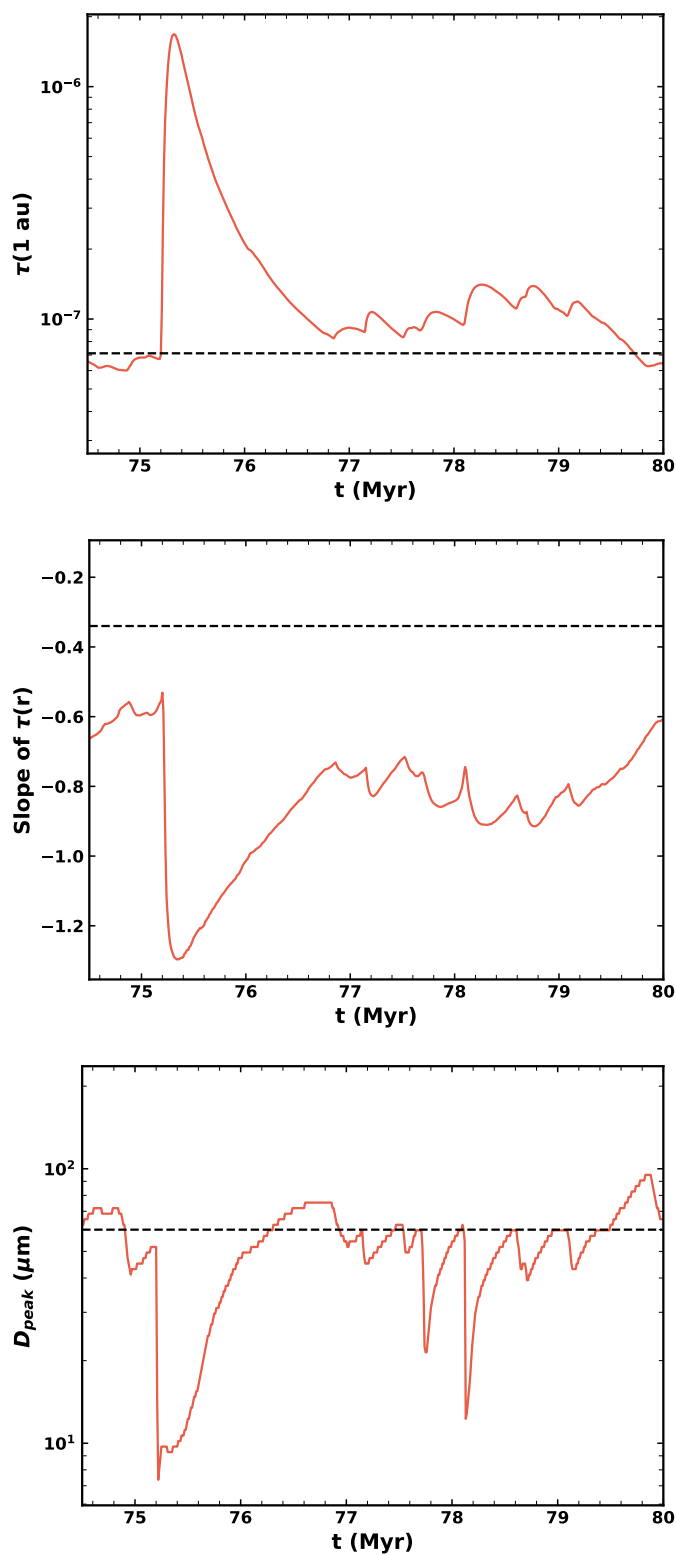


Fig. 4.24 Evolution of my three 'observables' of the zodiacal cloud as a function of time, the same as Figure 4.21, but zoomed in on a spike in the amount of dust present. The values of the present zodiacal cloud are shown with dashed black lines.

4.6 Discussion

4.6.1 Stochasticity

In Section 4.5.2 I showed that a cometary contribution to the interplanetary dust complex will be highly variable, depending on the sizes of comets which are scattered in and their dynamical lifetimes. In particular, very large comets can cause big spikes in the amount of dust if their dynamical lifetimes are long enough (Section 4.5.2).

In comparison to my model, the parameters of the present-day zodiacal cloud seem to be close to the quiescent levels of optical depth. The radial slope is at the highest end of the range of values in my model. In principle this could suggest that we have not recently had a very large comet with a long dynamical lifetime in the inner Solar System to cause a spike. Arguably it may be possible to alter the free parameters of my dust model so that the present-day is in the middle of a spike rather than close to the steady state level. However, it is very difficult to shift the parameters such that the radial slope becomes more positive. Regardless, if comets dominate the mass input to the zodiacal cloud, it is likely that the zodiacal light has been highly variable over the history of the Solar System.

4.6.2 Other free parameters

Two free parameters of the model which were not discussed in Section 4.4.2 are the maximum grain size D_{\max} and the dust density ρ . IDPs are generally assumed to have densities $\sim 2 \text{ g cm}^{-3}$, and the value I assume is 1.9 g cm^{-3} based on Rotundi et al. (2015). However, Fulle et al. (2016a) measured a density of 0.795 g cm^{-3} from Rosetta. I also tried some runs with a density of 0.795 g cm^{-3} , with the main difference being that the size distribution moved towards much larger grain sizes, giving a poorer fit to the size distribution. However, measurements of IDPs are done in terms of particle mass. Grun et al. (1985) and Love and Brownlee (1993) assume particle densities of 2.5 g cm^{-3} , such that the lower density distribution may fit observations better if I considered the size distribution in terms of particle mass, as opposed to particle size. Otherwise the density of dust grains should not affect the model too much.

I also tried varying the maximum grain size, D_{\max} , and found that 2 cm best fit the observed properties of the zodiacal cloud. This is the value used in Sections 4.4 and 4.5. With a smaller D_{\max} of 2 mm, it is possible to fit the radial profile of the zodiacal cloud with my model. However, the size distribution is a worse fit, as the cross-sectional area peaks at smaller grain sizes ($D \sim 20 - 30 \mu\text{m}$). This may be due to collisions of cm-size grains supplying smaller grain sizes. With a much larger (m-size) maximum size, the mass

accumulates in the largest particles without being destroyed in collisions or migrating inwards. The largest grain size will dominate the overall mass, so this means that the mass increases such that a quasi-steady state cannot be reached within 100 Myr. Increasing D_{\max} by a factor of three to 6 cm, the total mass reaches a steady state. However, the radial profile is always far too steep and is not able to match the observed distribution.

Observations suggest that the mass of cometary dust is dominated by grains of mm to cm-size (e.g. McDonnell et al., 1993; Green et al., 2004; Reach et al., 2007; Rotundi et al., 2015), and so ideally D_{\max} should be at least cm-size. Further, observations of splitting events suggest that large (>m-size) fragments will have a shallower size distribution (Mäkinen et al., 2001; Fuse et al., 2007; Fernández, 2009). These fragments often disappear on short timescales, such that they may undergo further fragmentations themselves. More recently, fireball observations suggest a lack of JFC material in the cm- to m-size range near Earth (Shober et al., 2021). Given that fragments \gtrsim cm-size may be able to disrupt via mechanisms other than mutual collisions, and will not contribute significantly to optical depth, I choose to set D_{\max} to 2 cm.

As discussed in Section 4.3.1, there are various size distributions I could have chosen for the dust produced by comets. I chose the size distribution found by Reach et al. (2007) when studying images of SPC debris trails, which is a broken power law with three different slopes depending on the grain size. However, I could have instead chosen to use a distribution based on fragments of comet splittings. For example, Mäkinen et al. (2001) found a distribution of fragments with a slope -2.7 fit the splitting of comet C/1999 S4 (LINEAR). By converting the magnitude of 19 fragments of comet 57P, Fernández (2009) found they had a rather shallow slope of -2.3. Meanwhile, the fragmentation of comet 73P/Schwassmann-Wachmann 3 has been widely studied (Boehnhardt et al., 2002; Sekanina, 2007). Fuse et al. (2007) measured the size distribution of a group of 54 fragments, and derived a slope of -2.1. This suggests that the large fragments of comet splitting may have a different distribution than the dust. While these size distributions are quite different, the distribution resulting from my kinetic model differs significantly from the input distribution. I therefore expect that it is relatively insensitive to the details of the input distribution, and the important part of the size distribution should be which sizes dominate the mass and cross-sectional area. The exact distribution of dust produced by fragmentations is highly uncertain, but hopefully dust trails give a good approximation.

4.6.3 Dominant comet size

I showed in Section 4.2.5 that $R \sim 50$ km comets should dominate the overall mass created by comet fragmentation (Figure 4.8). This conclusion was not changed after removing

dust grains which are dominated by dynamical interactions (Figure 4.16). While larger ($R > 100$ km) comets will dominate when they are present, they are very rare, and do not lose all of their mass to fragmentations, such that they contribute a smaller fraction of the overall mass to the interplanetary dust complex. Conversely, comets 10s of km in size are always present, and some will fully disrupt. The largest comets seen today have $R \sim 30$ km: the largest JFCs are 29P/Schwassmann-Wachmann 1 (30.2 km) and C/2011 KP36 (27.5 km) (JPL Small-Body Database¹). As $R_{\max} > 50$ km 13 per cent of the time and I clone particles every 12,000 yr, Figure 4.3 shows that I estimate comets $\gtrsim 50$ km should be scattered in on average every 100,000 yr. The dust from large comets will last for longer, such that the present-day zodiacal cloud should be dominated by the dust from these comets, despite no comets so large being seen by us in the last ~ 200 yr.

4.6.4 Historical brightness

I have assumed a constant scattering rate of comets into the inner Solar System, but this is not true over the history of the Solar System. While I have shown that stochastic variations should be important over timescales ~ 100 Myr, variations in comet input must also be taken into account. For example, the Nice model (Tsiganis et al., 2005; Gomes et al., 2005) suggests that there was a phase when many more comets were scattered into the inner Solar System at early times. Therefore, the historical brightness of the zodiacal cloud should vary both due to the stochasticity of comets which are scattered in, and also due to variations in the overall influx of comets caused by processes such as dynamical instability.

4.6.5 Model parameters

In Section 4.4.2 I fitted the free parameters of my model to match the present-day zodiacal cloud. These parameters are related to the collisional behaviour of dust grains (Q_0 , a , and α_r), and the fraction of mass lost in a comet fragmentation which becomes dust grains (ϵ).

Laboratory experiments (Fujiwara, 1986) suggest that the redistribution function of collisional fragments, α_r , has a possible range of $2.5 \lesssim \alpha_r \lesssim 4.0$. Thus my best fit value of 3.75 is reasonable. The collisional strength of dust grains, however, is poorly constrained. My final values were a normalisation of $Q_0 = 2.0 \times 10^7$ erg g⁻¹, and a slope of $a = 0.9$. In Figure 4.25 I compare my model parameters to other prescriptions for the collisional strength of particles. While the normalisation Q_0 is quite typical, the slope a is steeper than previous models in the literature. This means that I require the smallest grains (μ m-sized) to be about

¹https://ssd.jpl.nasa.gov/sbdb_query.cgi

ten times stronger than other models in the literature. However, the collisional strength is not well known for dust grains, and usually only characterised for particles > 10 cm-sized.

The final parameter I fitted was the fraction of mass lost in a fragmentation event which becomes dust, ε . My best fit value was 5 per cent. Implicit in this assumption is that fragmentation of comets will also produce m-size fragments which remain without producing dust themselves. However, the exact fraction of mass becoming dust is not well constrained. For example, photometric observations of the disruption of comet C/1999 S4 (LINEAR) (Farnham et al., 2001) suggested that most of the mass was hidden in fragments 1 mm to 50 m in size. The mass of $< \text{mm}$ dust observable was 3×10^8 kg, and the comet nucleus was estimated to be 4×10^{11} kg, suggesting only 0.1 per cent of the initial comet mass was put into dust grains $< \text{mm}$ -sized.

It should be noted that there is further uncertainty on the value of ε derived from my model due to the fact that I have assumed there are 58 visible JFCs in the range $1 \leq R \leq 10$ km, which is probably a lower limit on the number of comets in this range, as the observed sample is likely incomplete. For example, Di Sisto et al. (2009) estimated that there are 107 visible JFCs with $R > 1$ km and $q < 2.5$ au, which would increase the normalisation of the size distribution, which scales linearly with the number of visible 1–10 km comets. To

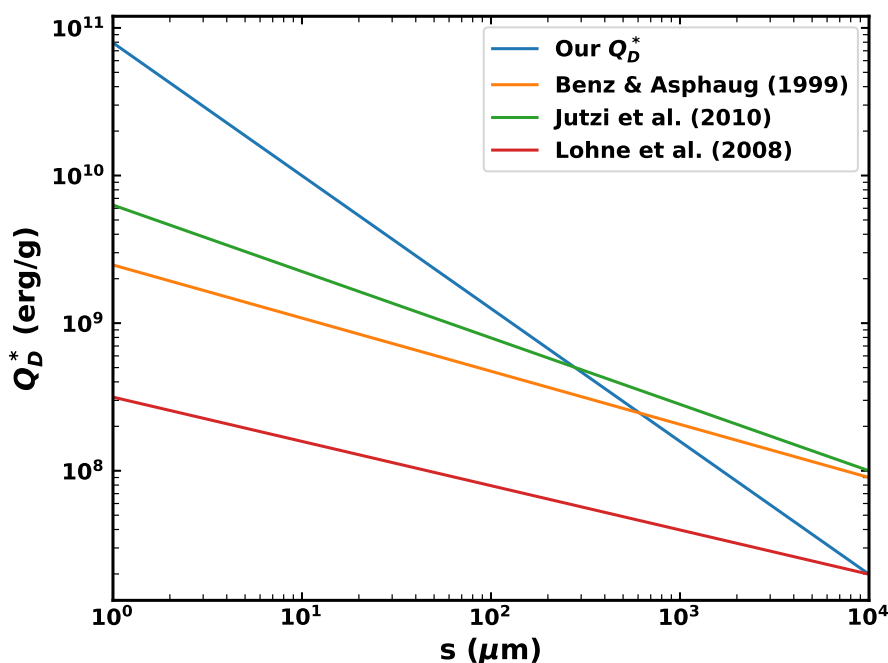


Fig. 4.25 Collisional strength, Q_D^* , of dust grains of different sizes. Four different prescriptions are compared: my best fit model, Benz and Asphaug (1999), Jutzi et al. (2010), and Löhne et al. (2008).

compensate for this I would expect the best fit model to require a value of ϵ that is decreased by a corresponding amount. There may therefore be a factor ~ 2 uncertainty in my best value of ϵ . Increasing the normalisation of the mean size distribution would also increase the probability of large (> 100 km) comets being scattered in, which may lead to an increase in how frequently large increases in dust mass occur.

4.6.6 Model limitations

Vertical distribution

One of the main limitations of my model is that because I am using a kinetic model which assumes a uniform inclination distribution, I cannot follow the evolution of particle inclinations. While this should not be too important for collisions and P-R drag, Nesvorný et al. (2010) showed that after being released from a comet, JFC particles are scattered by Jupiter, such that their inclination distribution is broader than that of JFCs. Therefore, by not modelling the dynamical interactions after dust is released from a comet, I am unable to study the inclination distribution of dust. One key metric which many models use to compare to the zodiacal cloud is the profile of thermal emission with ecliptic latitude. I am unable to compare with IRAS based on my model.

Fragmentation prescription

I have modelled comet fragmentations using the model of Di Sisto et al. (2009), who modelled comets with $q < 2.5$ au and $1 \leq R \leq 10$ km based on the need for a relatively complete sample of observations to compare to. I have extrapolated this model outside the region of parameter space it was fitted to in terms of both pericentre and comet size. I have extrapolated the pericentres fragmentation occurs at out to 5.2 au. While I would expect the probability of fragmentations to continue decreasing at larger pericentres, there could be a change in fragmentation rate e.g. at 2.5 au due to the onset of water sublimation and increased cometary activity. Fragmentations have been observed much further from the star than 2.5 au (e.g. Fernández, 2005), but their frequency is not well constrained.

Further, comets much smaller or larger than those modelled by Di Sisto et al. may fragment at different rates. According to the model, the fraction of a comet's mass lost in a fragmentation event is inversely proportional to its radius (equation 4.4). A 10 km comet loses 0.7 per cent of its mass in a fragmentation. This means that very small, sub-km comets lose most of their mass in a single event: a 0.1 km comet will lose 70 per cent of its mass in a single fragmentation, such that it will only survive two fragmentation events. Conversely, larger (> 10 km) comets require many fragmentations to lose all of their mass.

The size dependence of the Di Sisto et al. model was based on the fact that the escape velocity of a comet should be proportional to its radius, and was not considered a free parameter of the model. However, I found that the slopes of the comet size distribution resulting from the fragmentation model were too shallow compared to observations of JFCs (Section 4.2.5). Restricting the pericentres fragmentations can occur at to $q < 2.5$ au so that more comets survive long enough to reach < 2.5 au improved the comet size distribution slopes slightly, but the fit was still poor. Therefore, it is possible that a different size dependence of mass loss in fragmentations is needed. I tried a weaker dependence of the fractional mass loss on size, with $\frac{\Delta M}{M} \propto 1/\sqrt{R}$, with the resulting CSD shown in Figure 4.26. This gave a better fit to the slopes of the comet distribution for $R \lesssim 10$ km comets. Reducing the fractional mass loss per event extends the lifetime of comets, such that smaller comets had much longer lifetimes than with the $1/R$ prescription. However, the amount of mass input and the location mass was input to was not significantly changed. The main effect this has is to extend the lifetimes of comets, such that there are roughly twice as many visible comets. Such a prescription would therefore require me to halve the mass input rate of comets, and change ε accordingly to fit the zodiacal cloud. It is therefore possible that the size dependence of comet fragmentation should be further explored in order to match both the input and output size distributions of comets.

Other sources

It is important to acknowledge that while JFCs are believed to dominate, other sources will contribute to the interplanetary dust complex. Asteroids, the ISM, and other families of comets should contribute at least small amounts to our zodiacal cloud. Here I focus on the distribution of dust resulting from comet fragmentation and its variability, but a comprehensive model of the zodiacal cloud requires modelling all potential sources of dust.

Recent dynamical models place an upper limit on the asteroidal contribution of 10 per cent (Nesvorný et al., 2010; Ueda et al., 2017). In order to mimic a cometary source with an additional asteroidal contribution, I ran my best fit model again with a mass input rate which was 10 per cent lower. I then included an asteroid belt which had a constant mass input rate of 100 kg s^{-1} (10 per cent of the mean mass input), with eccentricities in the range 0.04–0.27, and pericentres in the range 1.8–3.5 au. Dust from this source was placed in a size distribution with a differential slope of -3.5, the typical value for a collisional cascade (Dohnanyi, 1969).

Including this 'asteroidal' component still allowed me to fit the observed values of the zodiacal cloud relatively well, with a best fit of 7.2×10^{-8} , -0.34, and a peak of $55 \mu\text{m}$. The radial slope becomes slightly flatter on average as dust from the asteroid belt will migrate in

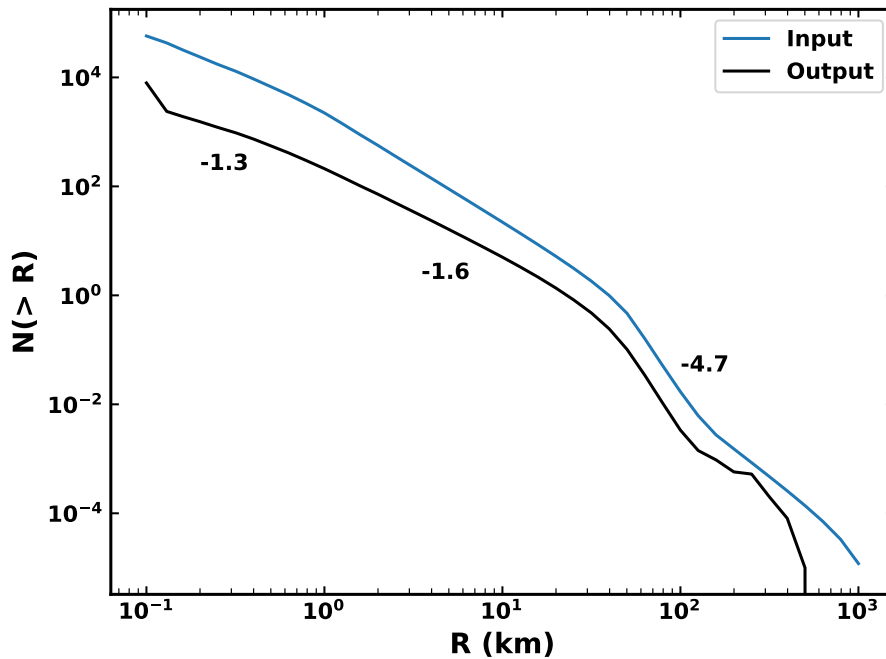


Fig. 4.26 Cumulative size distribution (CSD) of comets which is present on average in a 100 yr period (black) compared with the distribution of comets which is input (blue). The same as Figure 4.7, but an alternative prescription for the fraction of mass lost in a fragmentation event is used with a weaker dependence on comet size. The slopes of the CSD in each region are labelled by the curve.

via P-R drag. Increasing the contribution of this asteroidal source to 30 per cent, I could still obtain a reasonable fit to the zodiacal cloud, but the size distribution peaks at smaller grain sizes.

Therefore, with an 'asteroidal' contribution I could still produce a size distribution which is reasonable compared to the zodiacal cloud. However, the limitation of this approximation is that I cannot use different particle inclinations, which is the main difference between asteroidal and cometary grains, and the basis of many arguments for why comets should be the dominant source. Further, asteroidal and cometary grains will likely have different compositions, densities, and collisional strengths, rather than being homogenous.

When considering the distribution of dust further out in the Solar System, other sources become more important. For example, based on in situ measurements from the New Horizons Student Dust Counter, Poppe et al. (2019) modelled the relative contributions of different sources to interplanetary dust in the outer Solar System. They found that JFCs should be the dominant source at distances of $\lesssim 10$ au, while further out the dominant sources are the Kuiper Belt and Oort Cloud comets. My model focuses on the inner few au of the Solar

System, and so only considers the contribution of JFCs. As such, its predictions for the region > 10 au are expected to be inaccurate. Indeed, the model may also not include all of the dust expected from JFCs in this outer region, since I only considered comets when they reached within 5.2 au, whereas they could also fragment when further from the Sun.

Dynamical grains

Due to computational limitations I was unable to follow particles which are released by JFCs and dominated by dynamical interactions with Jupiter, instead assuming they are 'lost' on short timescales and therefore do not contribute significantly. These particles are typically the largest sized grains, such that they constitute a large fraction of the mass, but should not contribute significantly to the optical depth of the zodiacal cloud.

In order to estimate the contribution of these lost grains, I recorded the distribution of dust produced by fragmentations which is dominated by dynamics, weighted by the dynamical lifetime divided by the length of my simulation. This gives the 'lost' cross-sectional area, weighted by the fraction of time that the comet spends after fragmentation in the inner Solar System, to give the average distribution of dynamical grains. This is an approximation which assumes the grains stay on the orbit which the parent comet had when they were produced, when in reality they will bounce around. My best fit radial profile at 66.7 Myr is compared with the average distribution of dynamical grains in Figure 4.27 (top). The optical depth of dynamical grains is much higher further from the Sun, where P-R drag timescales are longer. The dynamical grains dominate the optical depth at $\gtrsim 8$ au. Superposing these dynamical grains on my best fit model, the slope of the radial profile for $1 \leq r \leq 3$ au goes from -0.34 to -0.27. The optical depth and size distribution at 1 au are not significantly affected. However, as mentioned above this assumes dynamical grains stay where they are produced. Therefore the actual distribution of dynamical grains may be weighted more towards smaller radii as they get scattered inwards, and so may not affect the radial slope so much. However, the exact parameters of my best fit model may be slightly different if dynamical grains could be included fully.

Figure 4.27 (bottom) compares the average radial profiles of different grain sizes. For small grains ($D < 100 \mu\text{m}$), the dynamical grains are never significant compared to those dominated by drag and collisions. For $100 \mu\text{m} < D < 1 \text{ mm}$, dynamical grains dominate the cross-sectional area at $r > 6$ au. However, for $D > 1 \text{ mm}$ grains, the dynamical grains are always comparable to those dominated by drag and collisions. This means that the main effect of not including dynamical grains in my kinetic model is that I am underestimating the number of cm-size grains. In my model cm-size grains do not contribute significantly to the cross-sectional area (see Figure 4.19), so the main effect of this is that I am underestimating

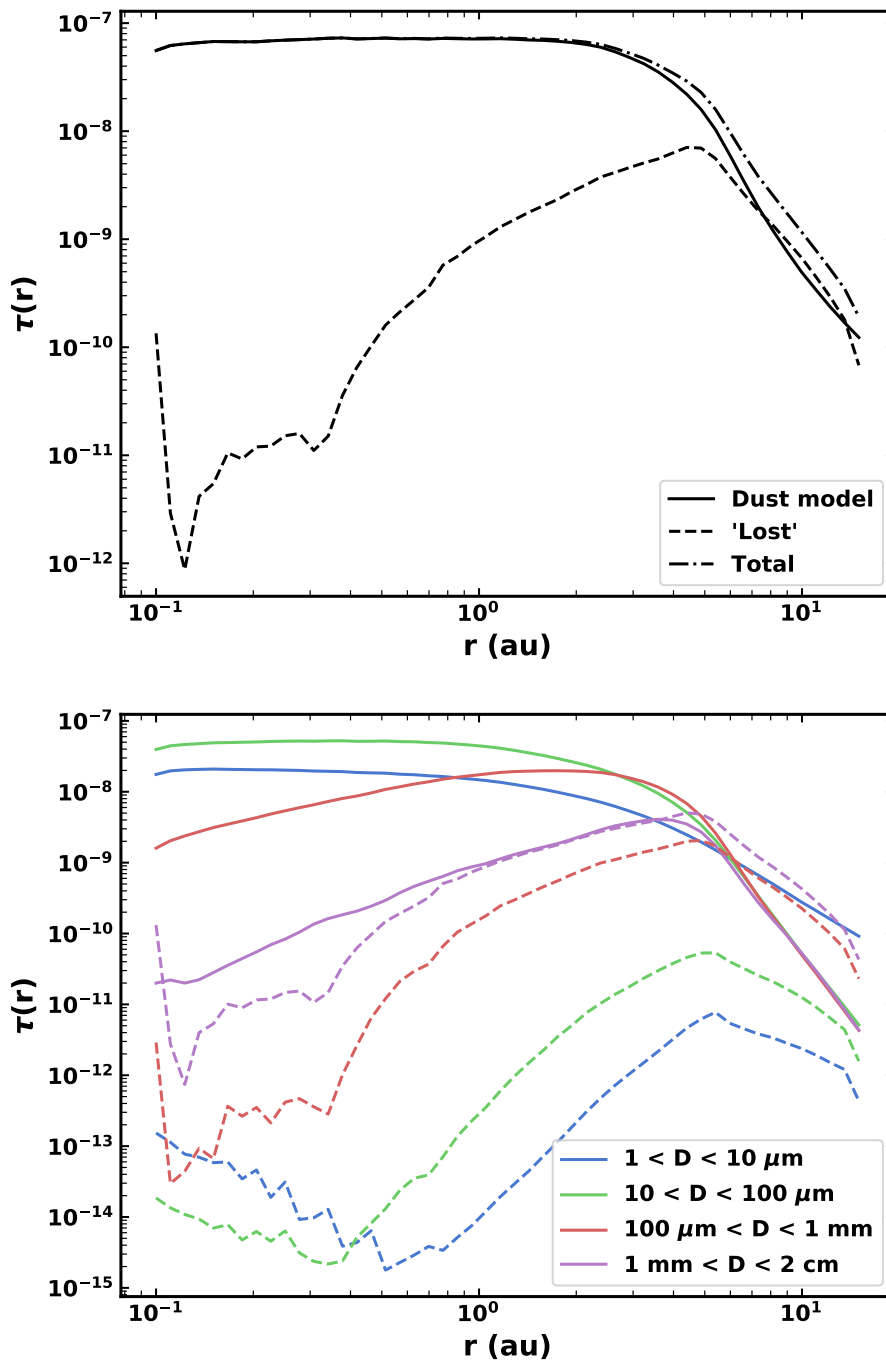


Fig. 4.27 Top: comparison of the total geometrical optical depth of my model at 66.7 Myr (solid) with the dynamically lost grains (dashed), and the overall profile summing the two contributions (dash-dotted). Bottom: Comparison of geometrical optical depth in my model (solid) with dynamically lost grains (dashed) for different grain sizes, averaged over time.

the collision rate of cm-size grains, which supplies the smaller grains. This will thus have an effect further down the size distribution. Dynamical grains will mostly affect the distribution further from the Sun, where the zodiacal cloud is more poorly characterised. Since I am underestimating the collision rate of cm-size grains, the main effect on my parameters would likely be that the collisional strength Q_D^* would not need to have such a steep slope ($a = 0.9$) if dynamical grains were included, as the collision rate of cm-size grains would be higher due to there being more grains of that size, rather than them having lower collisional strength.

My simplified treatment of dynamics also means I am unable to study fine structure in the zodiacal cloud. For example, particles may get trapped in mean-motion resonances which extend their lifetimes. Measurements with Juno showed that the radial structure of the zodiacal cloud may have fine structure (Jorgensen et al., 2021). My model instead focusses on studying the broad, overall distribution.

4.7 Comparison with other models

As discussed in the introduction, there have been many attempts to model the zodiacal cloud. Most of these models either try to fit the thermal emission (e.g. Liou et al., 1995; Nesvorný et al., 2010; Rowan-Robinson and May, 2013), usually from IRAS or COBE, or the sporadic meteoroid complex (e.g. Wiegert et al., 2009; Nesvorný et al., 2011; Pokorný et al., 2014). NASA's Meteoroid Engineering Model (MEM McNamara et al., 2004; Moorhead et al., 2020) focuses on modelling the sporadic meteoroid environment, and is tested against meteoroid impact data from the Pegasus satellites and LDEF. They adopt the Grun et al. (1985) size distribution for all sources, and follow particles with collisions and drag. ESA's Interplanetary Meteoroid Environment Model (IMEM Dikarev et al., 2004; Soja et al., 2019) is a dynamical model which is compared to the COBE latitudinal brightness profile, meteoroids, and lunar microcraters. Most of these models are dynamical, whereas I use a kinetic approach which includes the collisional evolution of dust, including fragments produced in mutual collisions.

Since collisional evolution moves mass from larger particles to smaller grains, using a kinetic model allows me to consider the origin of the size distribution in more detail. However, not including dynamical interactions with Jupiter poses its own limitations (see Section 4.6.6). In particular, dynamical models may be better suited to studying the sporadic meteoroids, for which the direction matters and axisymmetry cannot be assumed. Further, meteoroids are larger grains, for which supply by destructive collisions of bigger grains is less important. However, for smaller grains which dominate the thermal emission of the zodiacal cloud, collisions need to be taken into account (see Section 4.7.2).

4.7.1 Accretion rate onto Earth

Measurements of particle impacts onto the LDEF satellite (Love and Brownlee, 1993) gave an accretion rate of $(40 \pm 20) \times 10^6 \text{ kg yr}^{-1}$ onto Earth from dust grains in the mass range $10^{-9} < m < 10^{-4} \text{ g}$. Applying the prescription of Wyatt et al. (2010) to find the collision rates of particles on different orbits with Earth, and adding an extra factor to take into account gravitational focussing, I find an accretion rate onto Earth from grains of this size range of $7.7 \times 10^6 \text{ kg yr}^{-1}$ at the time my distribution best fits the zodiacal cloud. The range of values over the simulation are $4.4 - 57 \times 10^6 \text{ kg yr}^{-1}$, with mean value $11 \times 10^6 \text{ kg yr}^{-1}$. This is similar to the accretion rate of $15 \times 10^6 \text{ kg yr}^{-1}$ found by Nesvorný et al. (2011). While my model predicts a lower accretion rate than the one measured by LDEF, it is in agreement with previous dynamical models.

4.7.2 Collisional evolution

As mentioned above, previous models of the zodiacal cloud are primarily dynamical. If collisions are considered, they are included with a simplified prescription in which particles are removed after their collisional lifetime, ignoring the products of collisions. I argue that it is important to include the grains produced in such collisions, as these will contribute to the zodiacal light. This is important for modelling both the size distribution of dust and its radial profile.

In order to ascertain the importance of including collisional fragments in the model, I ran my best fit model again, turning off the part of the code which produces collisional fragments, such that destructive collisions only act as a loss mechanism. The resulting radial profiles are shown in Figure 4.28 (top), to compare with Figure 4.18. Overall the radial profile is much flatter than when collisional fragments are included. Small ($D \lesssim 100 \mu\text{m}$) grains still have relatively flat radial profiles. Cm-sized grains are still depleted closer in as they are lost to collisions, but mm-sized grains are much flatter. Not including the source of smaller grains from collisions has a significant effect on the size distribution, which is plotted in Figure 4.28 (bottom). With collisions only acting as a loss mechanism, the cross-sectional area is now dominated by $600 \mu\text{m}$ grains and there are significantly fewer $D < 100 \mu\text{m}$ grains, whereas with collisional fragments included the size distribution is dominated by particles 10s of μm in size. Further, the ability of my model to fit the present-day zodiacal cloud depends on the size distribution of collisional fragments α_r and the collisional strength of particles, Q_D^* . Therefore, collisional evolution is important in order to understand the size distribution, and how dust behaves outside the vicinity of Earth.

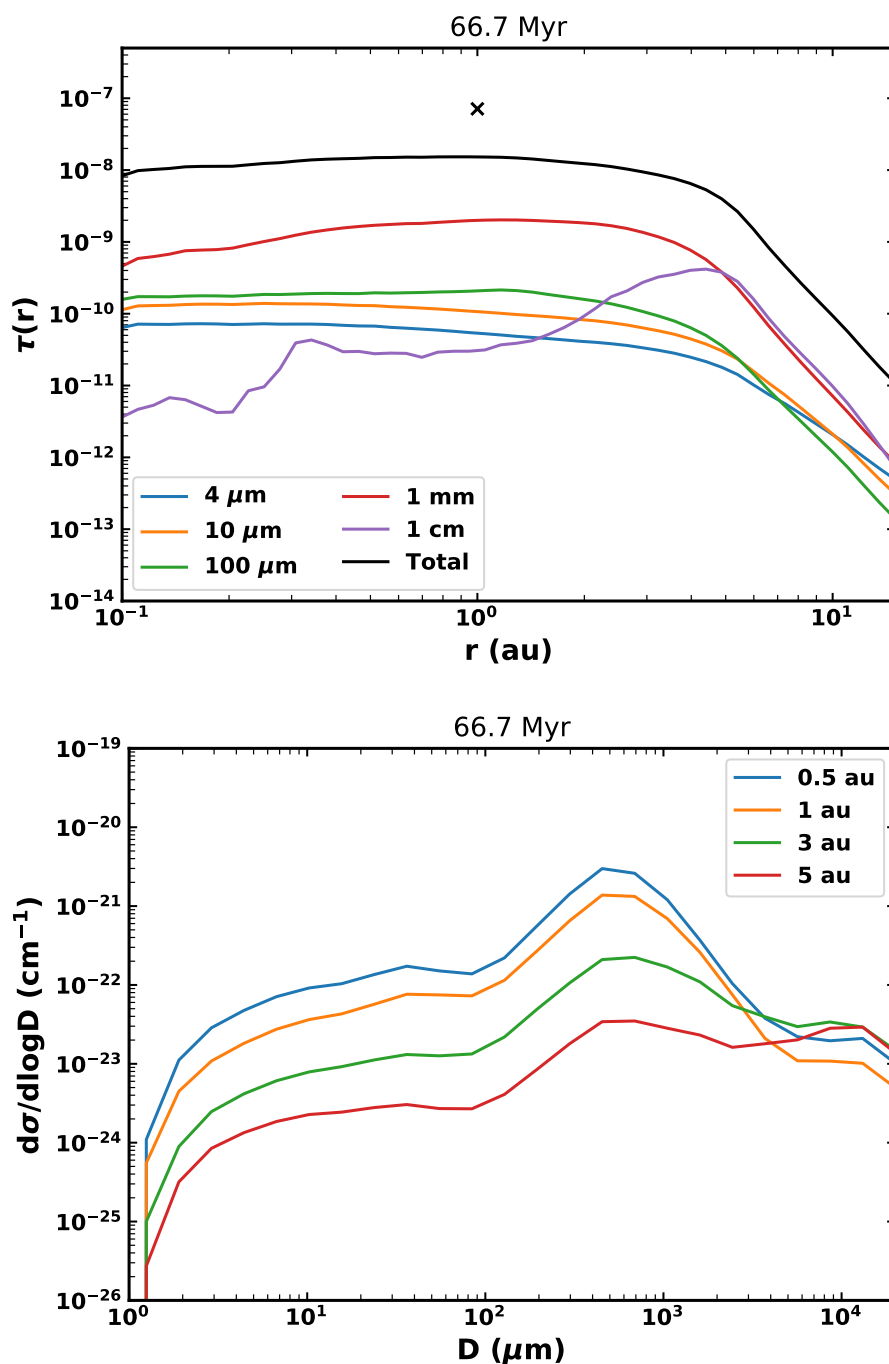


Fig. 4.28 Top: radial profile of geometrical optical depth in dust grains of different sizes in my model when collisional fragments are not included, to be compared with Figure 4.18. Bottom: size distribution of dust in terms of volume density of cross-sectional area at different heliocentric distances when collisional fragments are not included in my model, to be compared with Figure 4.19.

4.8 Conclusions

In this chapter I have developed a model for the distribution of interplanetary dust which would result from comet fragmentations. As comets from N-body simulations bounce around the inner Solar System, they undergo recurrent, spontaneous fragmentation events until they either lose all of their mass or get scattered outside Jupiter's orbit. A fraction of the mass lost in these events is converted into dust which supplies the zodiacal cloud. Such dust either stays with the parent comet due to dynamical interactions with the planets, or is input into a kinetic model which follows collisional evolution, P-R drag, and radiation pressure.

Comets are drawn from a size distribution based on the Kuiper belt, such that the resulting distribution of dust is highly stochastic, depending on the size and dynamical lifetime of comets which are scattered in. I compare my model to three observables of the present zodiacal cloud: the absolute value and slope of the radial profile of geometrical optical depth, and the grain size which dominates the cross-sectional area at 1 au. While these vary rapidly due to the stochasticity of my model, at two points in the simulation my model fits the present zodiacal cloud. I therefore suggest that comet fragmentation may be able to produce the correct size and spatial distribution of dust to supply the zodiacal cloud. Including a 10 per cent contribution of dust from the asteroid belt does not change my conclusion that the distribution can fit the zodiacal cloud. I also show that the zodiacal cloud should be highly variable over longer (Myr) timescales due to the aforementioned stochasticity. This means that the historical brightness of the zodiacal cloud may have been highly variable.

Smaller (< 10 km) comets tend to lose all of their mass in successive fragmentations, whereas larger ($\gtrsim 50$ km) comets tend to survive their dynamical lifetime without fully disrupting. Therefore for larger comets, the key factor determining how much mass they supply to the zodiacal cloud is their dynamical lifetime inside Jupiter's orbit. I predict that very large (> 100 km) comets should only be scattered into the inner Solar System rarely, such that the size of comet which should dominate the dust input to the zodiacal cloud should be ~ 50 km, as these are more common. I also show that > 100 km comets with longer dynamical lifetimes can cause spikes in the level of zodiacal dust which last for ~ 1 Myr, far longer than the dynamical lifetime of the comet itself. Large comets can therefore have a lasting effect on interplanetary dust.

My model is somewhat limited in its treatment of dynamical interactions with planets, such that more work is needed to couple the dynamical and collisional evolution of dust. However, comet fragmentation provides a promising source of interplanetary dust.

Comet disruption should also be further explored as a source of exozodiacal dust (e.g. Sezestre et al., 2019). The model presented here serves as good starting point for such an analysis, since its parameters have been tuned to ensure that it reproduces the zodiacal cloud.

Further, the stochasticity of my model suggests that if exozodiacal dust is similarly cometary in origin, it may be highly variable on long (Myr) timescales.

Chapter 5

An exocomet model for exozodiacal dust

Abstract

Warm exozodiacal dust is seen around $\sim 20\%$ of stars, often at quantities which are too high to be explainable with a P-R drag model. In this chapter, I further develop the comet fragmentation model of Chapter 4, such that it can be applied to an exoplanetary system with a different planetary system architecture to that of the Solar System. In particular, this model can be applied to η Corvi, a nearby F star which has an exceedingly bright exozodi ~ 2000 times brighter than the zodiacal cloud. This model will be able to show whether comet fragmentation can supply enough dust to its exozodiacal cloud, and produce the correct spatial distribution of dust. The model will also demonstrate the importance of considering the evolution of dust grains after they are released from a comet, and how this affects the resulting profile of exozodiacal dust.

5.1 Introduction

Many stars exhibit warm dust at levels much higher than the zodiacal cloud (Ertel et al., 2020). One star of note is η Corvi, an old (1.4 Gyr, David and Hillenbrand, 2015) F2V star at a distance of 18.3 pc (van Leeuwen, 2007). It hosts a bright, massive, cold planetesimal belt at 150 au from the star (Wyatt et al., 2005; Marino et al., 2017), and is also seen to harbour large quantities of warm dust very close to the star (< 3 au, Defrère et al., 2015; Lebreton et al., 2016). Far-infrared observations have detected no dust in between the two regions, placing upper limits on the amount of material here (Duchêne et al., 2014). Indeed, as part of the HOSTS survey η Corvi was found to have an exozodi 1950 times brighter than the zodiacal cloud (Ertel et al., 2020). This is an exceptionally bright exozodi, with far too much

exozodiacal dust in the inner planetary system to be explained by P-R drag from the outer belt (Rigley and Wyatt, 2020). Moreover, a P-R drag scenario would produce a flat radial profile of dust throughout the system, with significant emission between the cold belt and habitable zone, which has not been detected.

It has been suggested that the warm dust could be supplied by the inward scattering of exocomets (Marino et al., 2017). Comets may be able to produce dust close to the star via sublimation or fragmentation, without detectable emission in between the habitable zone and outer belt. This mechanism is supported by constraints on the dust composition from mid-infrared spectroscopy, which includes spectral features due to primitive cometary material (Lisse et al., 2012), suggesting the warm dust originates in the outer belt. Additionally, ALMA observations by Marino et al. (2017) detected CO gas at 20 au from the star, which could be explained by comets sublimating as they are scattered inwards. Previous modelling by Wyatt et al. (2007a) showed that an in-situ warm asteroid belt could not survive for the age of η Corvi, and the exozodi requires mass to be supplied at a high rate of $\sim 10^{-9} M_{\oplus} \text{ yr}^{-1}$. Marino et al. (2018) performed N-body simulations of comets being scattered inwards by a chain of 30 and 90 M_{\oplus} planets, and suggested that this scenario could supply mass to the exozodi at a high enough rate without exceeding observational upper limits on material being scattered in. However, this made some simplifying assumptions, such as that once comets reach 0.5 au, all of their mass supplies the exozodiacal cloud. In reality, comets should release mass at a range of distances from the star due to activity and fragmentation, and may not lose all of their mass via these processes. Furthermore, once dust is released from a comet, it should evolve due to the effects of mutual collisions, radiation pressure, and P-R drag. Thus, the question remains whether exocomets could produce enough dust to sustain the observed levels of exozodiacal dust, without requiring too large a mass of comets to be scattered in or producing an observable scattered disc. Another question is whether comets can produce the correct radial distribution of warm dust, with observations suggesting it should be concentrated within 2.6 au of the star (Defrère et al., 2015).

In this chapter I further develop the comet fragmentation model of Chapter 4 (Rigley and Wyatt, 2022) such that it can be applied to exoplanetary systems. This comprises two numerical models which are coupled together. The first follows individual comets from N-body simulations as their orbits evolve and they lose mass in spontaneous fragmentation events, to give the distribution of mass supplied to the exozodi by comets. The dust produced by comets is then followed by a kinetic model which accounts for evolution due to mutual collisions, radiation pressure, and P-R drag. As a first application of the model, I hope to use it to ascertain whether exocomets could deliver enough material to the exozodiacal cloud around η Corvi, and how the dust should evolve after being released from comets. This

will improve on the previous model for η Corvi by considering the behaviour of comets in terms of how often they fragment, where they fragment, and how much dust this releases, along with the subsequent evolution of dust. In Section 5.2 I describe the updated numerical model for comet fragmentation in the context of an exoplanetary system. In the Solar System (Chapter 4), the dynamics of the system is dominated by Jupiter, but in exoplanetary systems many planets can be similarly important to the dynamical evolution. Moreover, the zodiacal cloud is relatively low density, such that evolution of dust grains is dominated by dynamics and P-R drag, whereas detected exozodiacal clouds are much higher density, making collisions more important. Section 5.3 describes the necessary updates to the model for dust evolution, taking into account the interaction between destructive collisions, P-R drag, and dynamical interactions with planets. Finally, I give my conclusions in Section 5.4.

5.2 Comet scattering and fragmentation

To find the distribution of exozodiacal dust produced by comet fragmentation, I use the zodiacal cloud model of Chapter 4, which I have generalised to apply to exoplanetary systems. This assumes a population of comets whose orbits come from N-body simulations for the dynamical evolution of bodies being scattered inwards from an outer belt. Particles from the N-body simulations are cloned in time to give a continuous input of comets to the system, with each clone representing a size distribution of comets. The comet size distribution is based on numerical modelling of the population of a cold planetesimal belt. Each cloned particle is followed as it evolves through the planetary system, randomly undergoing fragmentations which produce mass and reduce the comet's size.

5.2.1 Planetary system

In order to model the dynamical evolution of comet scattering, I need to make an assumption about the underlying planetary system, as close encounters with the planets scatter comets in. While no planets have yet been detected around η Corvi, the shape of the cold outer belt can constrain the planetary system, assuming its edge is truncated by a planet. Based on sub-mm ALMA imaging of the belt, Marino et al. (2017) required a $3 - 30 M_{\oplus}$ planet with a semimajor axis of 75–100 au and an eccentricity of < 0.08 to be sculpting the outer belt. More recently, modelling by Pearce et al. (2022) required a $> 108 M_{\oplus}$ planet at < 104 au to sculpt the belt. Thus, it is likely that the outer belt is sculpted by a planet of tens of M_{\oplus} close to 100 au.

Previous studies have shown that the amount of material scattered into the inner planetary system is highly dependent on the planetary system architecture, with some systems incapable of scattering material in (Bonsor and Wyatt, 2012; Bonsor et al., 2012). These studies found that the most efficient system at scattering material in is a chain of low-mass planets. Other requirements from analytical considerations (Wyatt et al., 2017) require that there is not a massive, Jupiter-sized planet which would instead eject material; that there is an inward torque, i.e. planet masses do not significantly increase with radius; and that the cometary reservoir is replenished. Marino et al. (2018) studied the effects of varying the parameters of the planet chain, such as the planet masses and how they vary with semimajor axis, and the spacing between planets. They found that closely-spaced, equal mass planets are most efficient. For η Corvi, they suggested using a chain of equal mass planets, where the planets are either $30 M_{\oplus}$ or $90 M_{\oplus}$, starting at 100 au for the outermost planet and working inwards with spacings between planets of 12 mutual Hill radii. The mutual Hill radius between two planets is defined as

$$R_{H1,2} = \frac{1}{2}(a_1 + a_2) \left[\frac{(m_1 + m_2)}{3M_*} \right]^{1/3}, \quad (5.1)$$

where a_1 and a_2 are the semimajor axes of the planets, m_1 and m_2 are their masses, and M_* is the mass of the star (Chambers et al., 1996; Raymond et al., 2009).

I therefore ran N-body simulations using MERCURY (Chambers, 1999) and the hybrid symplectic/Bulirsch-Stoer integrator for the inward scattering of comets by a chain of planets, similar to those in Marino et al. (2018), but with higher time resolution and a smaller inner boundary. Simulations were run for chains of planets with $30 M_{\oplus}$ and $90 M_{\oplus}$ surrounding a solar-mass star, where the outermost planet has a semimajor axis of 100 au, and planets move inwards with spacings of $12 R_H$ to 1 au (see Table 5.1). These chains have ten and seven planets respectively. For simplicity, all planets are assumed to be on circular orbits. The simulations were run for 1 Gyr with a timestep of 10 days, outputting the orbital elements of comets every 1000 yr. The inner boundary was set to 0.1 au to allow comets to be scattered close to the star without being accreted onto it. For each simulation, 1000 test particles were placed in the chaotic zone of the outermost planet. The chaotic zone is defined as the range of semimajor axes in which resonances overlap, and is given by semimajor axes within a distance

$$\delta_{\text{chaos}} = 1.3a_p \left(\frac{m_p}{M_*} \right)^{2/7} \quad (5.2)$$

of the planet's semimajor axis, a_p , for a planet of mass m_p (Wisdom, 1980).

Particles are removed if they are in stable orbits which do not evolve, known as Trojans. These are defined empirically to be those particles which after 1 Myr have semimajor axes

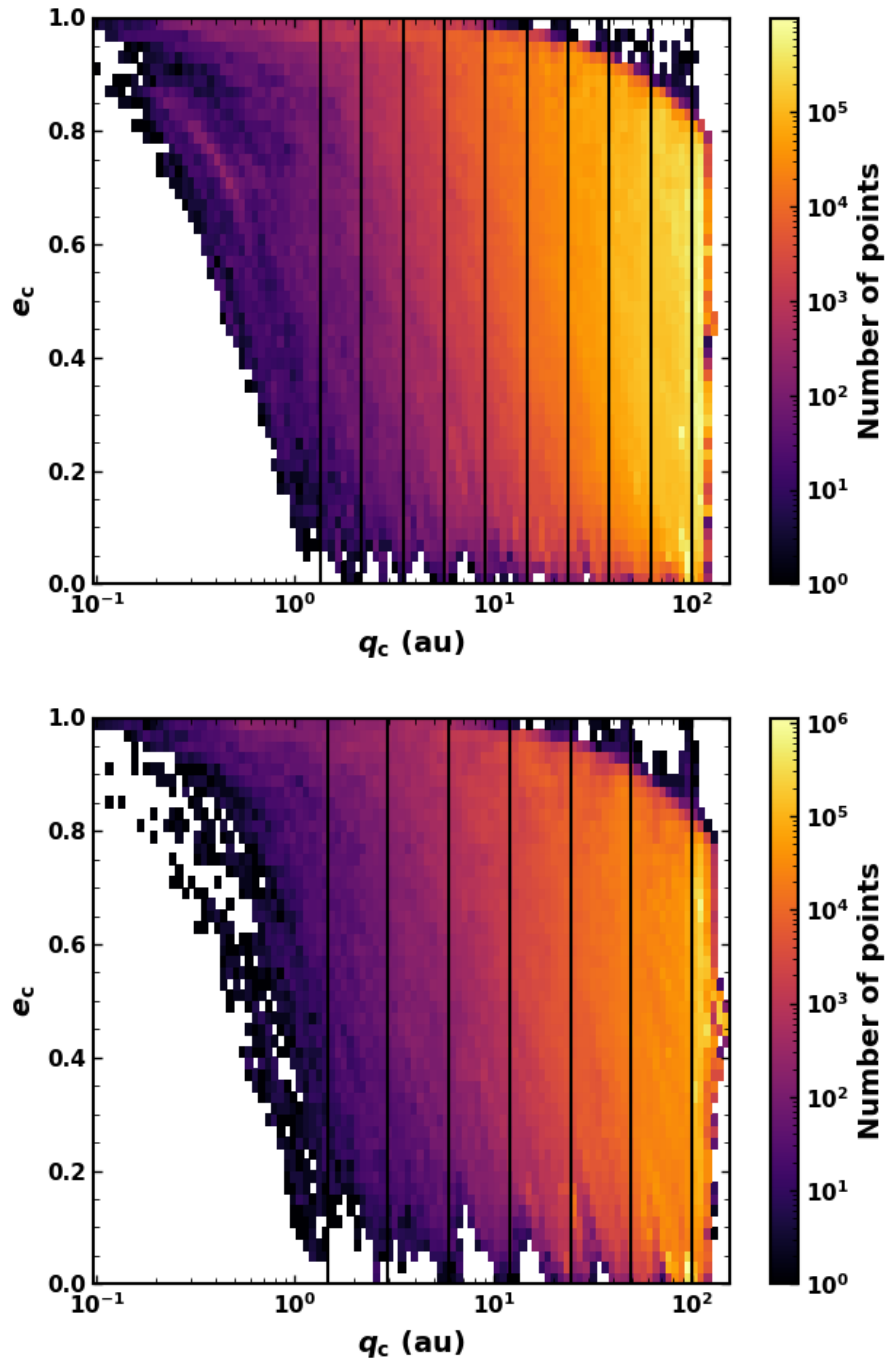


Fig. 5.1 The distribution of N-body data in terms of pericentre and eccentricity for comets scattered in from the outer belt by a chain of $30 M_{\oplus}$ planets (top) and $90 M_{\oplus}$ planets (bottom). The semimajor axes of the planets are marked with vertical lines.

within $1.2 R_H$ of the outermost planet, with an eccentricity lower than 0.03 (Marino et al., 2018). This removes around 30% of particles from the simulation, leaving a total of 694

particles for the $30 M_{\oplus}$ run, and 728 particles for the $90 M_{\oplus}$ simulation. The resulting distribution of cometary orbits in pericentre-eccentricity space is shown in Figure 5.1 for a chain of $30 M_{\oplus}$ planets (top) and $90 M_{\oplus}$ planets (bottom). In these systems comets have very long dynamical lifetimes (median of 20 Myr for $90 M_{\oplus}$ planets, and 111 Myr for $30 M_{\oplus}$ planets), and very few ever reach the habitable zone.

Table 5.1 Semimajor axes of planets for the two planetary systems considered, based on the work of Marino et al. (2018).

$m_p (M_{\oplus})$	$a_{pl} (au)$									
30	100	62.0	38.4	23.8	14.7	9.1	5.7	3.5	2.2	1.3
90	100	49.4	24.4	12.0	6.0	2.9	1.5			

5.2.2 Input of comets

One important factor when discerning the plausibility of the exocometary scenario for exozodiacal dust is whether the scattering rates of comets to the inner planetary system are so low that an unreasonably high mass of bodies is required in the outer belt. Further, the size distribution of large bodies in the outer belt is poorly constrained by observations, which trace at most mm-cm sized dust grains. These are used to infer the presence of larger bodies, but the details of the size distribution such as the slope and maximum size are not well known. I therefore chose to use a size distribution primarily based on the model of Krivov and Wyatt (2021). For the differential size distribution $n(D) \propto D^{-\alpha}$ of particles in the belt, defined such that $n(D)dD$ is the number of particles of size $D \rightarrow D + dD$, a four-slope distribution is used. Dust grains from the blowout size to mm-sized have a slope $\alpha = 3.5$, which is the standard outcome of a collisional cascade (Dohnanyi, 1969). Particles of radius 1 mm to 1 km have a slope $\alpha = 3.7$ from numerical simulations of collisional evolution. The change in slope at 1 km is because larger bodies are not yet in collisional equilibrium, as their collisional lifetime is longer than the age of the system. Assuming that planetesimals are formed via the streaming instability, which typically produces particles up to 200 km in size (e.g. Schäfer et al., 2017), bodies larger than 1 km have a primordial slope of 2.8 (Simon et al., 2016). In order to include the effect of even larger bodies such as those seen in the Solar System, I include a much steeper slope of 6 up to 1000 km bodies, similar to the steep slope found for the large objects in the Kuiper belt. The lower limit of the comet size distribution used in my model (Table 5.2) is 0.1 km, as smaller bodies may not behave like comets, and regardless will contribute little mass.

The resulting size distribution of comets assumed to lie in the outer belt is plotted in Figure 5.2. The total amount of mass is normalised using the mass input of comets in the

Table 5.2 Slopes of the differential size distribution of planetesimals in the outer belt used in my model, based on Krivov and Wyatt (2021).

Size range (km)	Slope, α
$0.1 \leq R \leq 1$	3.7
$1 \leq R \leq 200$	2.8
$200 \leq R \leq 1000$	6.0

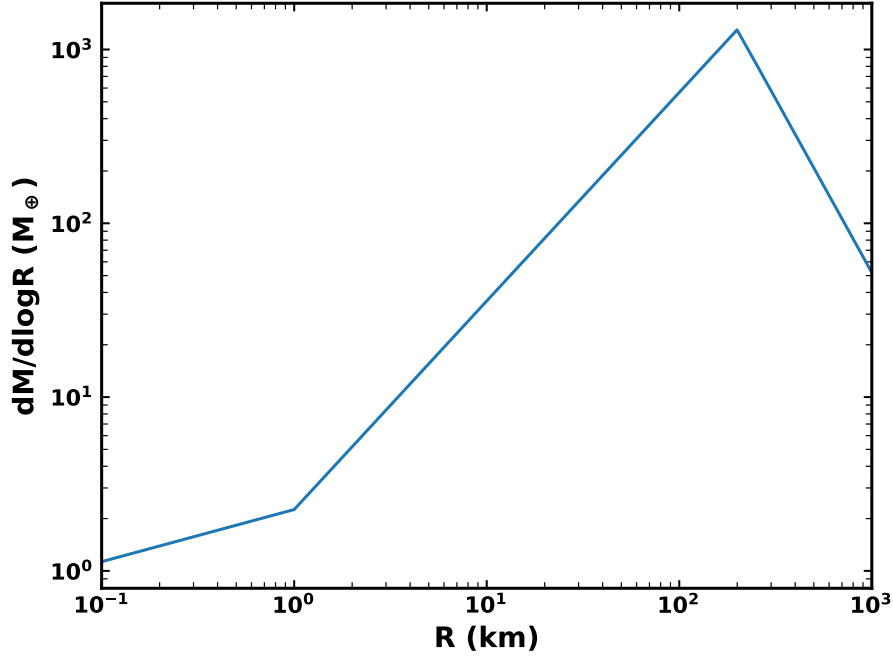


Fig. 5.2 Differential size distribution of mass per size decade in comets which is assumed to lie in the outer belt, normalised to a total mass of $470 M_{\oplus}$. In the fiducial model, it is assumed that 10% of this mass is scattered inwards over the 1.4 Gyr lifetime of the star, for a total mass input rate of comets of $3.4 \times 10^{-8} M_{\oplus} \text{ yr}^{-1}$.

size range 1–200 km. Extrapolating the observed dust mass up to 200 km-sized bodies with the size distribution of Krivov and Wyatt (2021), the mass of the belt around η Corvi should be $470 M_{\oplus}$. Assuming this is scattered in over the age of the star (1.4 Gyr), this gives an absolute upper limit on the input rate of comets of $3.4 \times 10^{-7} M_{\oplus} \text{ yr}^{-1}$. While this is higher than the rate needed to supply the exozodi, comets may not lose all of their mass through fragmentations, and only a fraction of comets will get scattered close enough to the star. While the dependence of the results on the cometary mass input rate should be explored in further work, I therefore used a mass input rate of 10% of this upper limit, i.e. an input of rate of comets of $3.4 \times 10^{-8} M_{\oplus} \text{ yr}^{-1}$.

The cumulative distribution of the largest comet size which is present every cloning step is given in Figure 5.3. Although there should be fewer comets of larger sizes, the very high mass input rate of comets used in this model means that large (> 100 km) comets are almost always present (99% of the time), and even larger comets are frequently scattered in.

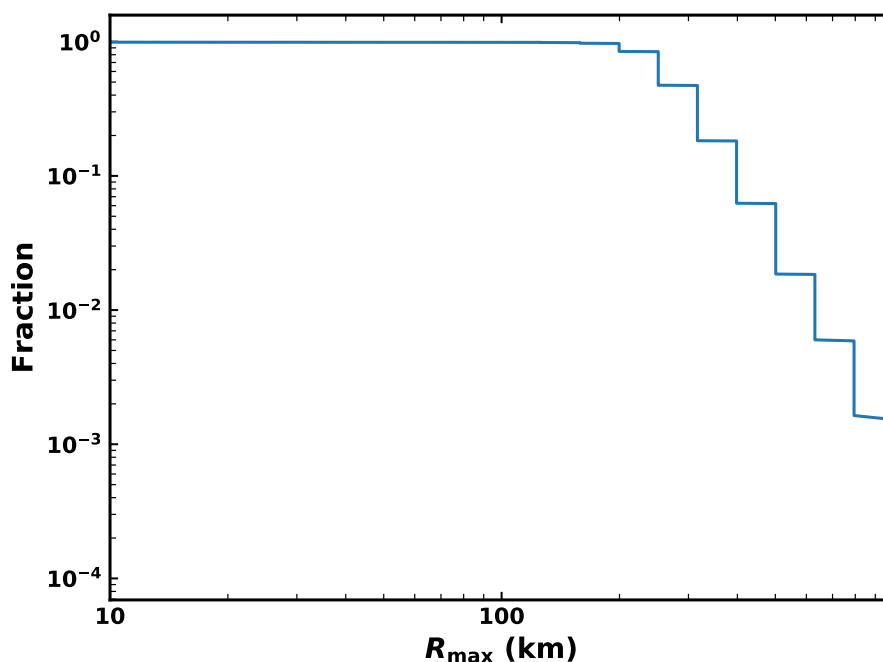


Fig. 5.3 Cumulative distribution of the largest comet present each time the size distribution is cloned with a comet mass input rate of $3.4 \times 10^{-8} M_{\oplus} \text{ yr}^{-1}$.

5.2.3 Fragmentation

In order to find the dust produced by comet fragmentation, I ran the numerical fragmentation model for 100 Myr. N-body particles are cloned in time such that they are input every 12,000 yr with the size distribution of Table 5.2. The model is not run for the stellar lifetime due to the long computation time required. Thus, an underlying assumption is that the exozodi is in a roughly "steady state", with a constant input rate of comets, and dust produced > 100 Mya does not affect the distribution seen today. Comets can take a long time to reach the inner planetary system; the time taken to reach small enough pericentres to fragment ranges from a Myr to several hundred Myr. Consequently, at a given time in the simulation, mass may be produced by comets which started being scattered inwards several Myr ago. I therefore updated the model to include the cloning of comets "backwards" in time. To better emulate a continual input of comets, comets are input from 10 Myr before the start time of

the simulation. Fragmentations which occur before the start time do not contribute to the mass input rate of dust, but this allows comets to start being scattered inwards and losing mass in fragmentations before the start time. This means that at early times, the mass input rate includes some comets which are already partway through their evolution. If backwards cloning is not included, at the start of the simulation there are no comets in the inner planetary system to produce dust, and several Myr are needed for the system to reach a steady-state regime.

Each individual comet is followed as its orbit evolves, progressively losing mass through stochastic fragmentation events. When a comet fragments, 5% of this lost mass is put into dust grains ranging from the blowout size to cm-sized on orbits which are determined by radiation pressure, as described in Section 5.3. As in Chapter 4, individual comets randomly fragment according to the prescription of Di Sisto et al. (2009). Every time it orbits the star, a comet has a probability f of fragmenting given by

$$f = \frac{1}{3} \left(\frac{q}{0.5 \text{ au}} \right)^{-1}, \quad (5.3)$$

where q is the comet's pericentre. If a comet does fragment, it loses a fraction s of its mass:

$$s = \frac{0.007}{R/(10 \text{ km})}, \quad (5.4)$$

where R is the radius of the comet. The fragmentation is assumed to occur at a random point around the orbit. While this fragmentation prescription has been fitted to observations of visible comets (with pericentres $q < 2.5$ au) in the Solar System, here I generalise it to be applicable to other stars. Assuming the underlying fragmentation mechanism is at least partially driven by sublimation of volatiles, I assume comets begin to fragment when they have pericentre distances less than a critical pericentre, which is given by

$$q_{\text{crit}} = 3 \sqrt{\frac{L_*}{L_\odot}} \text{ au}, \quad (5.5)$$

where L_* is the stellar luminosity. For η Corvi, with a luminosity of $5.1 L_\odot$, this corresponds to a critical pericentre of 6.75 au.

Only a fraction of comets from the N-body simulations (Section 5.2.1) ever get scattered close enough to the star to fragment. In both simulations, around 16% of comets have pericentres within 6.75 au at some point in their evolution. The time spent close enough to the star for fragmentation to occur ranges from 1000 yr to 10 Myr. The size dependence of the fragmentation model (equation 5.4) is such that smaller comets lose a higher fraction of

their mass in a single event. Larger comets therefore have longer lifetimes, while smaller comets should fully disrupt rapidly. The fraction of comets which survive their dynamical lifetime is plotted in Figure 5.4 for each initial comet size. Only comets which ever reach < 6.7 au and therefore have the opportunity to fragment are included. The general trend is that the survival fraction increases at larger sizes as many more fragmentation events are needed to disrupt a comet. However, a second factor is how long a comet on a given dynamical path spends in the inner planetary system. If a comet only has a few orbits $< q_{\text{crit}}$ and does not fragment, then it may survive even if it is very small; whereas if it has many orbits $< q_{\text{crit}}$ then it will inevitably disrupt regardless of its initial size. The distribution of times spent by comets with pericentres $q < q_{\text{crit}}$ is shown in Figure 5.5. A small number of dynamical paths only have a few thousand years where the comet's pericentre is low enough to fragment. The high fraction of comets which fully disrupt suggests that a large fraction of the comet mass which reaches the inner planetary system should supply the exozodi due to the generally long lifetimes $< q_{\text{crit}}$.

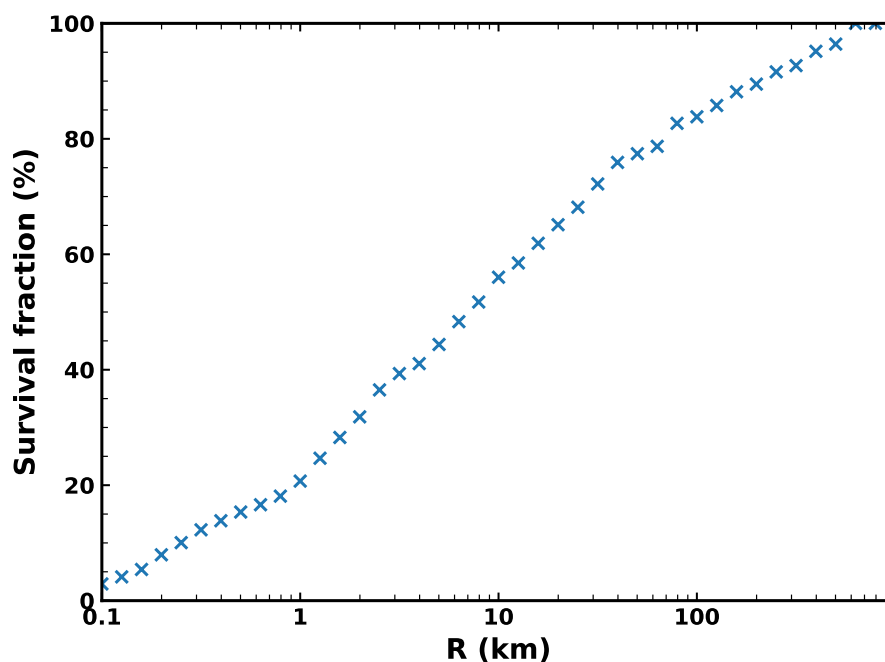


Fig. 5.4 Fraction of comets which survive their dynamical lifetime without fully disrupting, as a function of their initial size, in the presence of a chain of $90 M_{\oplus}$ planets.

The total mass produced by fragmentation of comets of each size is shown in Figure 5.6. This shows that overwhelmingly 200 km-sized comets dominate the supply of dust. Overall this matches the shape of the mass distribution of comets input (Figure 5.2), which is dominated by 200 km comets due to the change in slope there. The similarity between

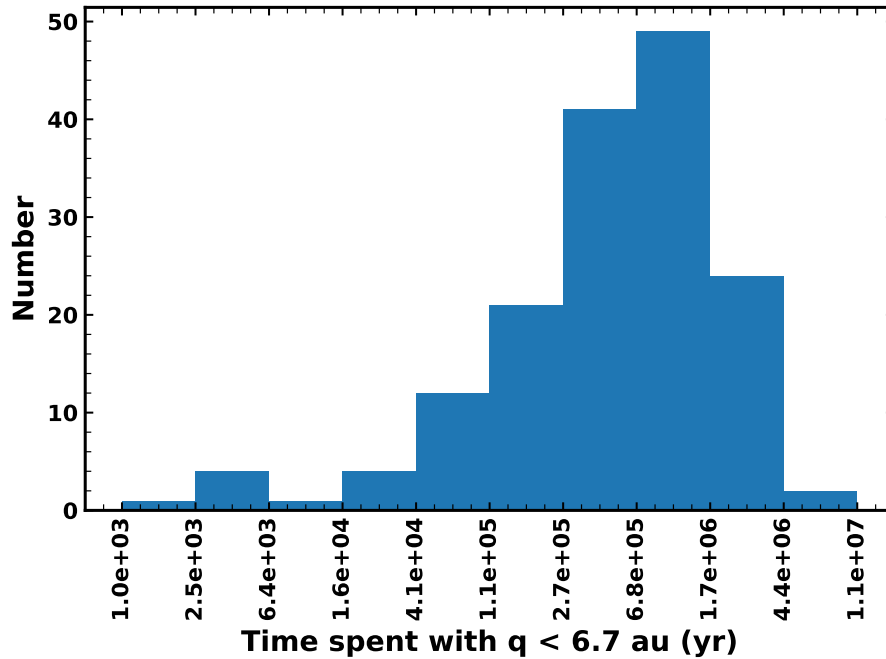


Fig. 5.5 Histogram of the time N-body particles spend with $q < q_{\text{crit}} = 6.7$ au from the N-body simulations with a chain of $90 M_{\oplus}$ planets.

the input mass distribution of comets and the distribution of dust produced by comets of different sizes suggests that a very large fraction of the input comet mass is lost to disruptions. This is because the dynamical lifetimes inside 6.7 au are generally long enough for comets to lose a high fraction of their mass, regardless of whether they completely disrupt due to fragmentation. In this regime, where the mass input rate of comets is very high such that comets of all sizes are usually present, and dynamical lifetimes are long enough for many fragmentation events to occur, the shape of the assumed comet size distribution determines which sizes of comet dominate the supply of dust.

5.3 Dust evolution

5.3.1 Grain properties and size distribution

The grain properties and size distribution used are the same as in Section 4.3.1, except that optical properties are calculated for a different stellar type. When mass is lost from a comet in a fragmentation, 5% of the mass is put into a size distribution of dust particles, from the blowout size up to grains of diameter 2 cm. This value of 5% is chosen based on fitting of the model to the zodiacal cloud and the observed number of JFCs in Chapter 4. Dust particles are

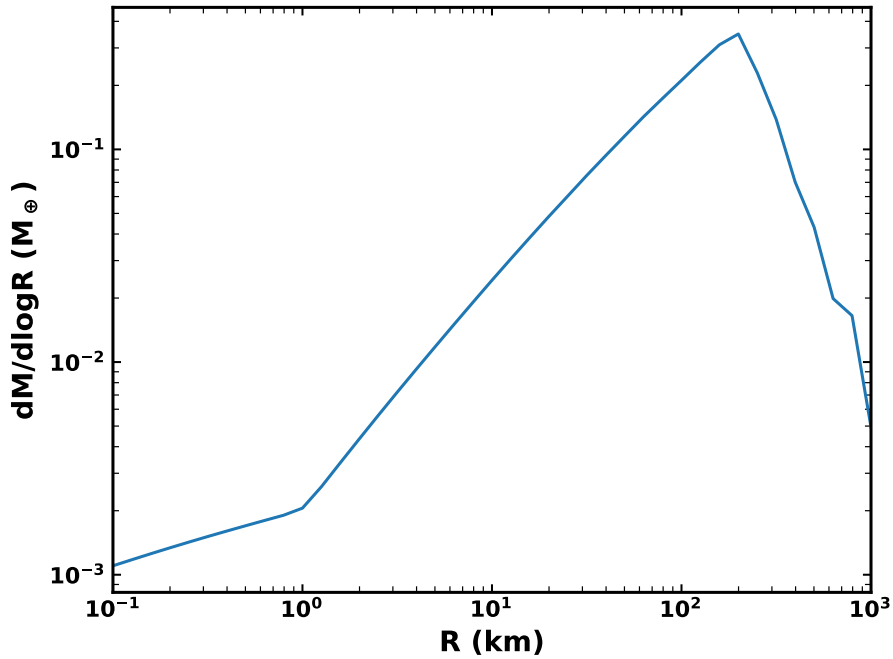


Fig. 5.6 Total mass supplied to the exozodi over 100 Myr by comets of different initial sizes. A cometary input rate of $3.4 \times 10^{-8} M_{\oplus} \text{ yr}^{-1}$ and a chain of $90 M_{\oplus}$ planets were used.

distributed in a three-slope size distribution of particles from Reach (2010) which is based on cometary dust trails. To calculate the dust optical properties, I used the method of Wyatt and Dent (2002), which is based on the core-mantle model of Li and Greenberg (1997). Particles are assumed to have a volume fraction of 1/3 silicate core to 2/3 organic refractory mantle, with a porosity of 20%. Thus the dust has a density of 1.9 g cm^{-3} . The star is assumed to have a mass of $1.4 M_{\odot}$ and luminosity of $5.1 L_{\odot}$.

Once material has been distributed in a size distribution, it is placed onto the correct orbits according to the effect of radiation pressure. This is accounted for with β , the ratio of the strength of radiation pressure to gravity acting on particles of a given size. Particles with $\beta > 1$ will rapidly be blown out of the system on hyperbolic orbits, while for grains on circular orbits, $\beta > 0.5$ is sufficient to be blown out. For the stellar mass and luminosity of η Corvi, these β values correspond to grains of diameter $3 \mu\text{m}$ and $6 \mu\text{m}$, such that there should be no grains smaller than a diameter of $3 \mu\text{m}$ present.

The dust produced in fragmentations is placed into bins depending on its orbit, in a phase space of pericentre, eccentricity, and particle size. For the phase space grid, pericentres are placed into 40 logarithmic bins from 0.05 to 30 au. Eccentricities are placed into bins from 0 to 1 which are a combination of logarithmic for low eccentricities and linear for higher eccentricities. There are nine logarithmic bins from 2×10^{-4} to 0.1, eight linear bins from 0.1

to 0.9, and five linear bins up to an eccentricity of 1. Particles are placed into 30 logarithmic size bins based on their diameter from D of $0.1 \mu\text{m}$ to 2 cm . Thus, the fragmentation model gives the amount of mass of each grain size on each orbit produced by comets as a function of time. The evolution of this dust can then be followed using a separate code.

5.3.2 Dust evolution model

It is difficult to simultaneously model the effect of dynamical interactions, P-R drag, and catastrophic collisions on the dust grains. Different models are required for the evolution of dust after it is released from a comet, depending which is the dominant effect. The evolution of dust grains evolving due to catastrophic collisions, P-R drag, and radiation pressure can be found using a kinetic model (van Lieshout et al., 2014). However, the presence of planets in the system means that in some cases close encounters with the planets may be more important than other forces acting on the dust. I therefore use the relevant timescales for these processes to determine which effect is most important in determining the evolution of dust grains of a given size which are produced on a given orbit. The calculation of these timescales must be updated from the zodiacal cloud model (Chapter 4) so that the fragmentation model may be applied to exoplanetary systems, in which the dynamics are different to the Solar System. These updates are described below, and the dynamical prescription is verified in Section 5.3.3.

Every time dust is created, the fraction of particles dominated by each force is found for every grain size. This is done using the relevant rate R_x for each process to remove a dust grain of a given size, which is the inverse of the relevant timescale, $1/t_x$. For example, the fraction of dust particles of a given size and orbit dominated by dynamical interactions is,

$$f_{\text{dyn}} = \frac{R_{\text{dyn}}}{R_{\text{dyn}} + R_{\text{PR}} + R_{\text{coll}}}, \quad (5.6)$$

where R_{dyn} , R_{PR} , and R_{coll} are the inverses of the times for a particle with the given orbital parameters and size to be lost due to dynamical interactions with planets, P-R drag, and destructive collisions respectively. A fraction $(f_{\text{PR}} + f_{\text{coll}})$ of the dust is input into the kinetic model (Section 5.3.4). This model finds the evolution of the population of particles in the phase space bins described in Section 5.3.1, taking into account the effects of destructive collisions between dust grains, P-R drag, and radiation pressure. Where dynamical interactions are more important than collisions and drag, the dust is assumed to follow the orbital evolution of its parent comet after being produced (Section 5.3.5). A fraction f_{dyn} of the dust is assumed to stick with its parent comet. Once the resulting distributions of dust from these

two populations have been found, they can be superposed to find the overall distribution of dust in the system and thus predict the thermal emission.

P-R drag

The P-R drag timescale is the time for a particle to migrate from the orbit it is produced on to an apocentre distance Q of 0.01 au, and is calculated analytically using the method of Wyatt and Whipple (1950). As in Section 4.3.2, this uses the fact that the combination of orbital elements

$$C = ae^{-4/5}(1 - e^2) = Qe^{-4/5}(1 - e) \quad (5.7)$$

is held constant throughout evolution due to P-R drag, and both Q and e decrease monotonically. The constant can be used to find the eccentricity corresponding to a desired apocentre. Then C can be used to remove semimajor axis from the equation for the evolution of eccentricity, which can be integrated to find the time taken to reach a given eccentricity and thus apocentre when a particle migrates via P-R drag.

Collisions

The collision timescale is the mean time between destructive mutual collisions per particle. This is calculated using the method of van Lieshout et al. (2014). The particle-in-a-box approach is used to find the overlap of orbits in different phase space bins (q, e, m) and thus the rate of collisions between them. However, collision rates scale with the number of particles present which are capable of destroying a given particle in a collision. The comet fragmentation model is run once to find the total distribution of dust produced in each bin of pericentre, eccentricity, and particle size as a function of time. This gives the rate of production of each particle size on each orbit with time, which can be used in calculation of collision timescales. Then the comet fragmentation model is run a second time using the same random seed, and the relevant timescales are used to determine which dust should be input to the kinetic model, and which is dominated by dynamical interactions.

To convert the rate of dust production to a population of particles, an assumption must be made about the lifetimes of particles. Previously in Chapter 4, I assumed all particles had the same lifetime when calculating collision rates. However, in reality the lifetime of particles will depend on their sizes and orbits, and the timescales for loss due to different processes. In the regime where large quantities of dust are produced, collisions will be much more significant than for the zodiacal cloud, such that the accuracy of collision timescales is more important. Thus, the model must be updated to incorporate an iterative method which is inspired by the collisional grooming algorithm (Stark and Kuchner, 2008). An iterative

process will be used to calculate the collision timescales in each bin with time. In the first iteration, the dust produced in the initial run of the fragmentation model is then assumed to survive on the orbit it is produced on for the shortest of either the relevant P-R drag or dynamical lifetime. This gives a distribution of mass as a function of time which can be used to calculate collision rates. However, by neglecting collisions this will overestimate the collision rates, as some dust should be lost to collisions such that there are fewer projectiles which can destroy a given particle. Thus, this process will then be repeated several times, but now using the shortest timescale of the estimated P-R drag, dynamical, and collisional lifetimes. Each iteration the collision rates will be updated, and should alternate between overestimating and underestimating the number of particles present and thus the collision rates. This iterative process will allow to refine the collision timescales for each bin as a function of time, to better determine which particles should be input to the kinetic model.

When mass is produced in the comet fragmentation model, the relevant collision timescale for that phase space bin at the given time can then be found. While this method does not for example include collisional fragments, it is the best approximation that can be made without running a full collisional model, which is computationally prohibitive.

Dynamics

To take into account the dynamical effects of the chain of planets on a particle, I use the cometary diffusion time (Tremaine, 1993; Brassier and Duncan, 2008). For a particle undergoing close encounters with a planet of semimajor axis a_p and mass m_p , the characteristic time for it to be ejected from the system is

$$t_{\text{diff}} \sim 1.1 \left(\frac{M_*}{M_\odot} \right)^{1.5} \left(\frac{m_p}{M_\oplus} \right)^{-2} \left(\frac{a_p}{\text{au}} \right)^{1.5} \text{Gyr}. \quad (5.8)$$

This assumes that the particle's initial semimajor axis is comparable to that of the planet, and that particles are scattered by interactions with planets in which their semimajor axes remain fixed, and pericentres are changed. The close spacing of the planet chain means that it may be possible for particles on a given orbit to be scattered by multiple planets. To take into account the effect of all planets in the chain, I sum the diffusion rates $R_{\text{diff}} = 1/t_{\text{diff}}$ for all planets which a given particle crosses the orbit of. An orbit is planet-crossing if $q < a_p < q(1+e)/(1-e)$. The regions of pericentre-eccentricity parameter space which cross each planet in the chain are shown in Figure 5.7 for the chain of 30 M_\oplus planets (top) and 90 M_\oplus planets (bottom). The planets are sufficiently closely-spaced that most of the parameter space crosses at least one planet, apart from some orbits with low eccentricity ($e \lesssim 0.2$), and those with very low pericentres ($q < 1$ au). If a given orbit (q, e) does not cross

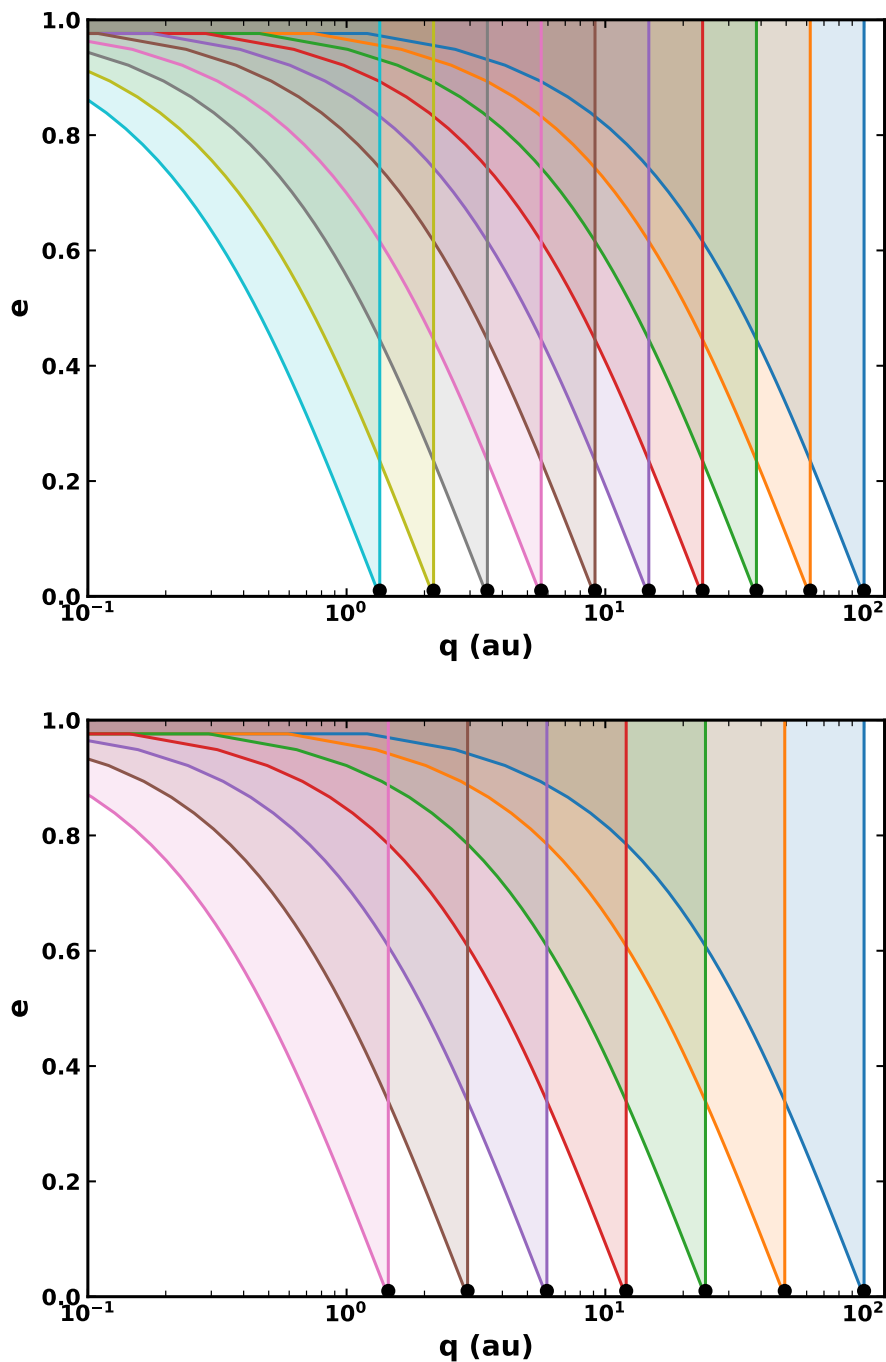


Fig. 5.7 The region of pericentre-eccentricity parameter space which crosses each planet for the chain of 30 M_{\oplus} planets (top) and 90 M_{\oplus} planets (bottom).

that of any planets, the diffusion timescale for the closest planet is used as the dynamical lifetime. It is possible that particles produced in these regions of parameter space which are not planet-crossing could be on long-lived dynamical paths, in which they do not have

close encounters with planets, allowing them to survive without being ejected for longer. However, the high eccentricity of comets which reach low pericentres and the effect of radiation pressure means that only a small fraction of dust grains are produced on orbits which are not planet-crossing.

5.3.3 Interplay between dynamics and drag

The timescales discussed in Section 5.3.2 can be used to predict which regions of parameter space are dominated by each process. While the collision rates depend on the amount of dust produced and thus cannot be calculated *a priori*, the analytical calculations for P-R drag and dynamics can be used to estimate the transition between these regimes in the absence of collisions, for example if the amount of dust produced is very low. The diffusion timescale (equation 5.8) is independent of particle size, and only depends on the orbit of a particle. The P-R drag timescale also depends on the orbit, and gets shorter for smaller particles. Thus, for particles on a given orbit, there should be some transitional grain size below which particles are dominated by drag, while larger particles evolve due to dynamical interactions. This can be found by equating the two timescales. For particles on a circular orbit, the P-R drag timescale for several grain sizes around a Sun-like star is plotted in Figure 5.8. The diffusion timescale of each planet is also shown, for 30 M_{\oplus} planets (crosses) and 90 M_{\oplus} planets (pluses). The diffusion timescales are shorter for 90 M_{\oplus} planets, as their higher mass means they can eject particles faster. While the transitional grain size should depend on the orbital elements, Figure 5.8 suggests that the transition should occur for grains of radius 100 μm to 1 mm for 30 M_{\oplus} planets, and 10–100 μm for 90 M_{\oplus} planets for particles on circular orbits. At fixed semimajor axes, the P-R drag timescale decreases for higher eccentricities, which should shift the transition size at a given semimajor axis to larger grains as eccentricity increases.

In order to ascertain whether the analytical approach described above is a good approximation for the dynamical effects, I ran N-body simulations with the effect of P-R drag included to determine what the transitional grain size should be. The N-body simulations were run using REBOUND (Rein and Liu, 2012) with the IAS15 integrator (Rein and Spiegel, 2015). The effect of P-R drag was incorporated with the radiation forces implementation of the REBOUNDX package (Tamayo et al., 2020) using β parameters calculated for particles with the composition described in Section 5.3.1 orbiting a Sun-like star. A chain of ten 30 M_{\oplus} planets (Table 5.1) were placed on circular orbits around a Sun-like star. Nine particle sizes were considered from radii of 1 μm to 1 cm, and for reference one particle size was included which is large enough to not be subject to radiation pressure (i.e. $\beta = 0$). For each grain size, 100 massless test particles were started from an initial orbit for several combinations

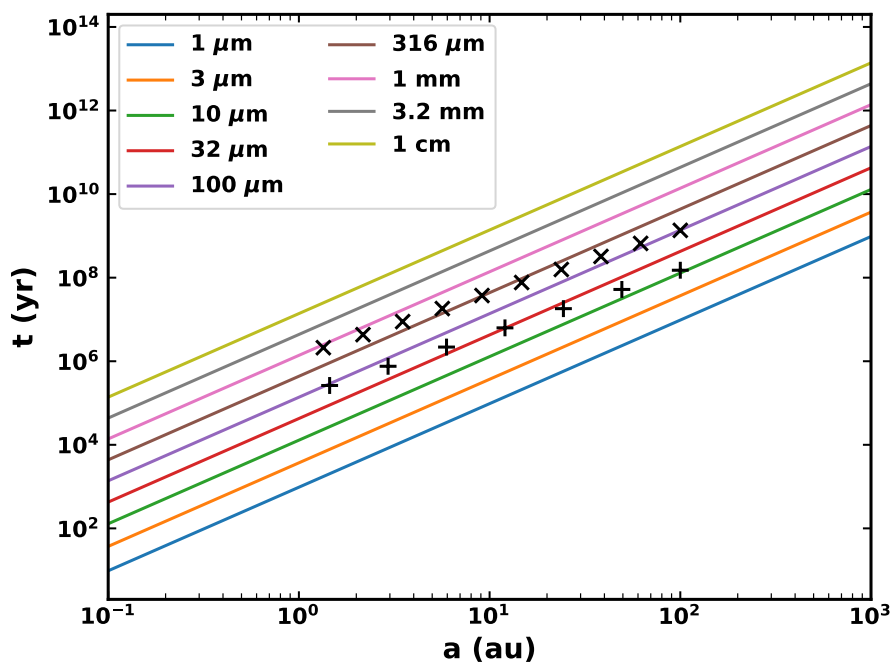


Fig. 5.8 Comparison of the analytical P-R drag and diffusion timescales for particles. The P-R drag timescales are shown for particles of radii $1 \mu\text{m}$ to 1cm with different semimajor axis on circular orbits. The diffusion timescale for each planet in the chain is shown with crosses ($30 M_{\oplus}$ planets) and pluses ($90 M_{\oplus}$ planets).

of eccentricity and pericentre with random values chosen for the longitude of ascending node, argument of pericentre, and mean anomaly. The $\beta = 0$ runs had 400 particles to better encapsulate the range of dynamical paths possible due to the stochasticity of close encounters. The initial orbits had pericentres of 2 and 6 au, and eccentricities of 0.2, 0.5, and 0.8. These values were chosen to cover the range of typical orbital elements dust grains have when produced in the comet fragmentation model. Cartesian coordinates were used for placing particles on their initial orbits in REBOUND and the simulation output to take into account the fact that the orbital elements of a particle will depend on their β parameter. Radiation pressure effectively reduces the strength of stellar gravity a particle feels, reducing the orbital velocity (e.g. Murray and Dermott, 1999). Simulations were run for either ten times the P-R drag timescale or 100 Myr, depending which was shortest.

To determine how well the analytical prescription matches the numerical simulations, I considered the number of particles of a given size remaining in the simulation as a function of time. Very different behaviour should be seen for particles dominated by P-R drag compared with dynamical scattering. In a purely P-R drag regime, the remaining number of particles with time should be a step function: all particles should drift inwards at the same rate, and all

will be accreted onto the star simultaneously. Thus, all particles should be present until the P-R drag timescale has elapsed, after which no particles should remain. On the other hand, dynamical scattering is a stochastic effect, causing particles to have a broad distribution of orbits. Thus, particles will be ejected from the system or accreted onto the star randomly. When P-R drag and dynamics are both acting, the evolution will be a mixture between the two regimes. Smaller particles may try to migrate inwards due to drag, but close encounters will cause them to be accreted onto the star either slightly earlier or later than the typical P-R drag timescale, such that the remaining number of particles is no longer a step function. Conversely, the ejection of particles by dynamical scattering may be slowed by the inward migration due to drag.

I therefore compared the numerical results for the number of particles remaining with predictions based on the analytical timescales. For each grain size and each initial orbit, I used the timescales to find the fraction of particles dominated by P-R drag, f_{PR} , and the fraction dominated by dynamics, f_{dyn} , as in equation 5.6. Then the predicted number of particles is a superposition of f_{PR} times a step function, which is centred on the P-R drag timescale and normalised to 100 particles, and f_{dyn} times the number of $\beta = 0$ particles remaining in the simulation as a function of time, normalised to 100. This prediction was then compared with the output of the simulations. An example of this is shown in Figure 5.9 for particles started on an orbit which initially had $q = 6$ au and $e = 0.8$. Results from the simulations are shown with solid lines, and the semi-analytical predictions are shown with dashed lines.

To improve the agreement between the analytical predictions and simulations, I introduced a factor k_{diff} , which multiplies the analytical diffusion rate R_{diff} to make dynamics more significant. To find the best-fit value, I tried values ranging from 0.1 to 100, and found the reduced χ^2 for the numbers of particles of each size as a function of time. The resulting χ^2 values are shown in Figure 5.10 for each initial orbit. One of the orbits ($q = 6$ au, $e = 0.2$) does not cross any planets, so as described in Section 5.3.2 the diffusion timescale for the nearest planet was used as the dynamical lifetime. The overall reduced χ^2 is shown in black for all planet-crossing orbits (solid) and all six orbits (dashed). The best-fit value for all planet-crossing orbits is $k_{\text{diff}} = 7$. Including the orbit which does not cross any planets, the best-fit value of k_{diff} is shifted to 10. This potentially suggests that even when using the nearest planet's diffusion timescale, the dynamical lifetime is slightly underestimated for particles which are not on planet-crossing orbits. Thus, in the comet fragmentation model diffusion rates are multiplied by a factor of 10 to better fit numerical results for the interplay between dynamics and P-R drag. This value of k_{diff} was used to predict the numbers of particles in Figure 5.9. While not a perfect fit, the semi-analytical model is a

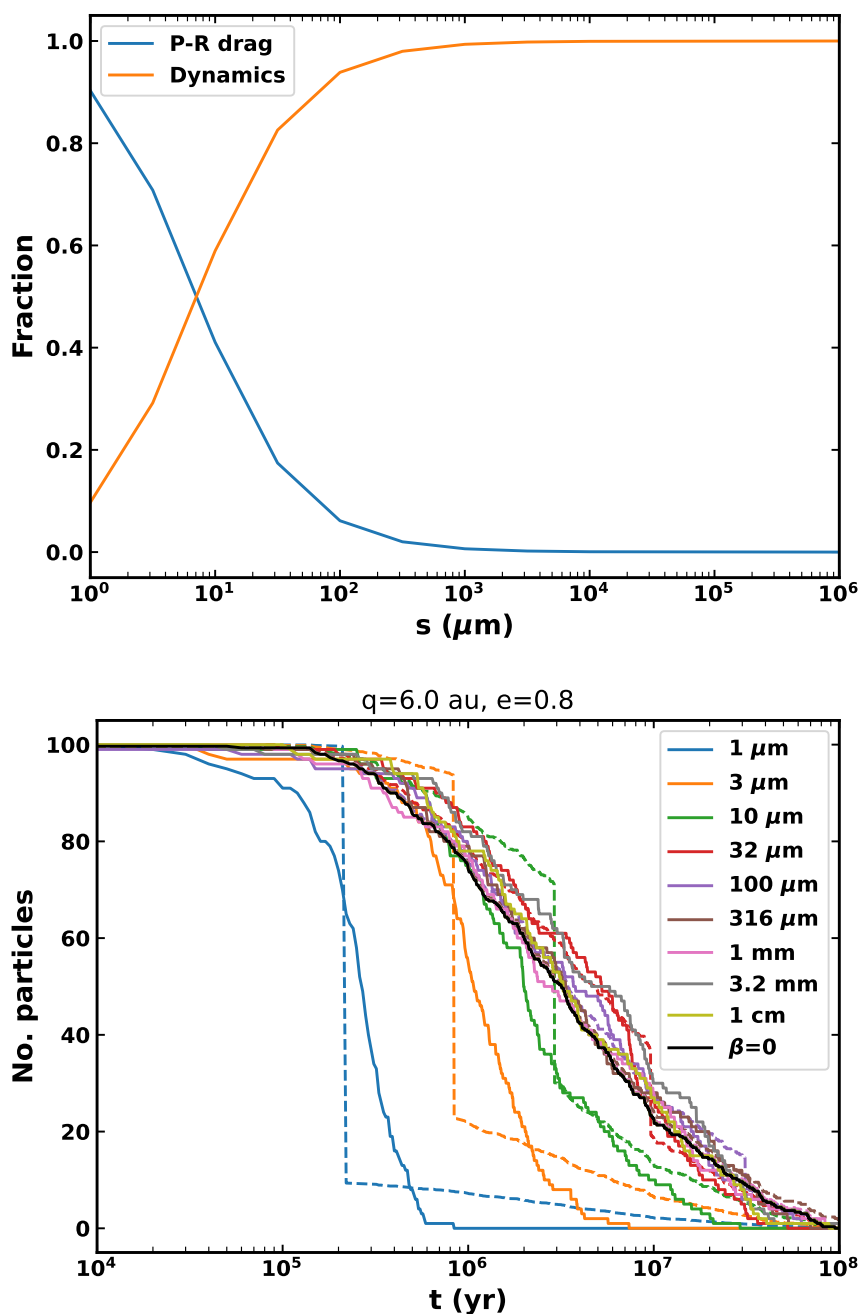


Fig. 5.9 Example of a comparison for fitting the N-body simulations with P-R drag to semi-analytical predictions for particles which are started on an initial orbit with $q = 6$ au and $e = 0.8$ in the presence of a chain of $30 M_{\oplus}$ planets. Top: the predicted fraction of particles of each size which are dominated by P-R drag (blue) and dynamics (orange). Bottom: comparison of the number of particles present as a function of time for the N-body simulations (solid lines) and the semi-analytical predictions (dashed lines). A factor of $k_{\text{diff}} = 10$ multiplies the diffusion rates to improve the match between the analytical predictions and numerical simulations.

good approximation to the number of particles, suggesting that using analytical timescales is an appropriate way to incorporate the effects of competing processes.

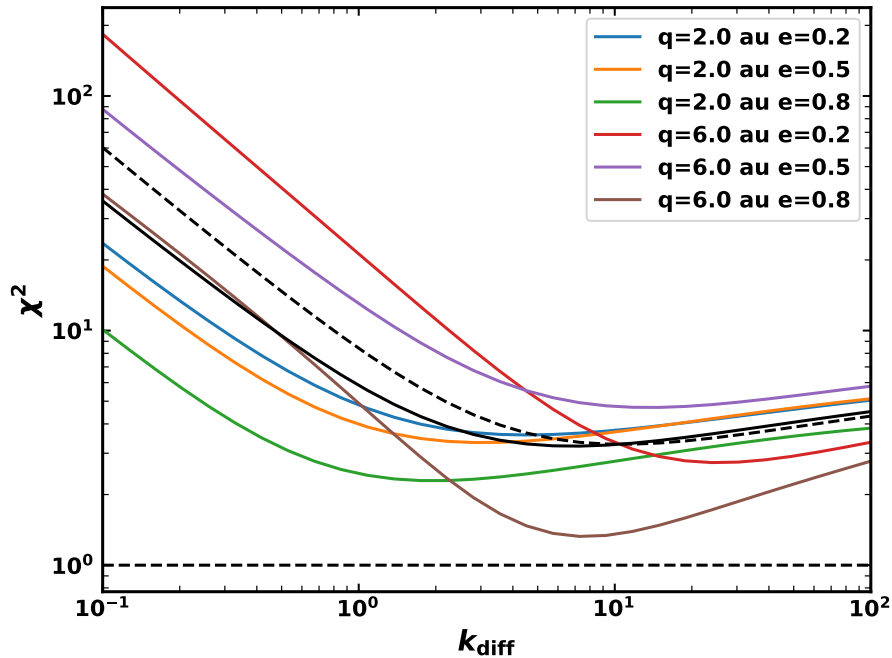


Fig. 5.10 Reduced χ^2 for the number of particles of each size as a function of time, used to fit the factor k_{diff} . Several starting orbits are shown, along with an average over all planet-crossing orbits (solid), and an average over all considered orbits (dashed).

5.3.4 Kinetic model

The evolution of dust grains dominated by drag and collisions will be followed with a kinetic model which finds the distribution of particles in terms of a grid of pericentre, eccentricity, and particle size (van Lieshout et al., 2014). Destructive collisions between particles on crossing orbits acts as a sink of those particles, and a source of smaller particles which are the collisional fragments. P-R drag acts as a diffusion term, which causes particles to migrate between adjacent orbital bins. This gives the distribution of dust present in the system as a function of time when it evolves due to catastrophic collisions, radiation pressure, and P-R drag.

Dust from the comet fragmentation model (Section 5.2) is input into the kinetic model from an empty disc if its P-R drag or collisional timescales are shorter than the dynamical lifetime. The dust grain composition and optical properties and the phase space grid which are used in the kinetic model are those described in Section 5.3.1. For the optical properties,

grains are assumed to be orbiting a star with the mass ($1.4 M_{\odot}$) and luminosity ($5.1 L_{\odot}$) of η Corvi.

The collisional grain properties are similar to those used when modelling the zodiacal cloud in Chapter 4. The collisional strength, Q_D^* , of a particle is the critical specific energy of a collision above which that particle will be destroyed, with the largest fragment at most half the mass of the original particle. For dust grains of radius s , this is parametrized by a power law as $Q_D^* = Q_0 \left(\frac{s}{\text{cm}}\right)^{-a}$. Several prescriptions have been suggested for this parametrization based on laboratory experiments and SPH simulations (e.g. Benz and Asphaug, 1999; Jutzi et al., 2010). Based on fitting of this numerical dust model to the zodiacal cloud (Rigley and Wyatt, 2022), I use $Q_0 = 2 \times 10^7 \text{ erg g}^{-1}$ and $a = 0.9$. The assumed slope of the differential size distribution of fragments which are produced in collisions, α_r , is 3.75.

5.3.5 Dynamical grains

Dust grains which are produced with a dynamical lifetime shorter than their P-R drag and collisional lifetimes are assumed to evolve primarily due to close encounters with the planets. In order to approximate this dynamical evolution after being released from a comet, dynamically-dominated grains are assumed to follow the orbital evolution of their parent comet after being produced. Although radiation pressure will modify the dust particles' orbits, and their evolution should be affected by P-R drag, this should provide a good approximation.

Every time a comet produces dust which evolves due to dynamics, the amount of mass of each grain size is recorded, along with which N-body particle the dust originated from and which step in the particle's orbital evolution the dust was produced at. This data is not recorded as a function of the time the comet was scattered in, as this creates a prohibitively large array, so instead this distribution is averaged over time. As long as variations due to stochasticity are within an order of magnitude, this should provide a reasonable approximation to the distribution of dust grains evolving dynamically. For each N-body particle, the size distribution of dust produced at each step of its evolution is evolved forwards in time to give the distribution of dust present as a function of time, which is then averaged over time.

Since comets fragment at low pericentres, dust evolving via collisions and drag should remain relatively close to the star. However, dynamical interactions can scatter particles much further from the star. Thus, the distribution of dynamical grains is important for making predictions which can be compared to observational limits on emission in the intermediate region between the exozodi and the outer belt. Conversely, the exozodi should primarily be populated by dust which is evolving due to drag and collisions due to its proximity to the star, where these forces are more important.

5.4 Conclusions

The work in this chapter is the first stage in the development of a model for the exozodiacal dust produced by fragmentation of exocomets in an exoplanetary system. Once the updated collision lifetime calculation described in Section 5.3.2 has been incorporated, this model can be used to predict the distribution of exozodiacal dust produced by exocomets in the η Corvi system. This will significantly improve upon previous cometary models, which only considered N-body simulations for the scattering of comets by planets. By including the production of dust by comets and its evolution due to various forces, I will self-consistently find the size and spatial distribution of dust.

With the model, I will be able to answer several outstanding questions, such as whether comets can supply enough mass to the exozodiacal cloud for realistic physical parameters, without exceeding observational limits on emission between the exozodi and cold outer belt. Moreover, the spatial distribution of dust can be used to predict the surface brightness profile of the exozodi, and compared with mid-infrared observations (Defrère et al., 2015).

The model will also determine what mass input rate of comets is able to supply enough exozodiacal dust, and whether this exceeds plausible limits on the outer belt's mass. At the high mass input rates which are needed for η Corvi, the cometary input of dust should be far less stochastic than in the case of the zodiacal cloud (Chapter 4). With a higher mass input rate, comets of all sizes are generally present, such that very large comets cannot cause a significant spike in emission. However, it is possible that a lower mass input rate of comets may also be plausible, with η Corvi being observed during a "spike" in its emission. With my model, I will be able to determine how frequently spikes in brightness should occur, and thus which is the more likely scenario. If a comet model is able to explain the exozodiacal dust, this may also place constraints on the parent belt. For example, bodies larger than 0.6 km should not be in collisional equilibrium, as their collisional lifetimes are too long due to how far the outer belt is from the star (Krivov and Wyatt, 2021). We therefore do not have observational evidence for the presence of bodies larger than this in the belt. However, if the comet model requires > 100 km bodies to supply the exozodiacal dust, this may imply the presence of large planetesimals in the belt.

The model will highlight the importance of the underlying planetary system on the distribution of exozodiacal dust. I will also demonstrate the effect of radiation pressure, P-R drag, and collisions on the distribution of dust produced by comets. This will improve on previous exozodi models because, for example, comets should produce more dust when they are closer to the star, giving a very different radial distribution of dust to that of comets. Depending on my results, I may be able to place constraints on the presence of planets orbiting η Corvi. A cometary scenario requires planets which cause the exocomets to be

scattered into the inner planetary system, so if I conclude the exozodi could be cometary, this provides evidence for planets interior to the outer belt.

Chapter 6

Conclusions

6.1 Summary

This thesis has studied the production and distribution of exozodiacal dust using analytical modelling and numerical simulations. In particular, I have focussed on two mechanisms for producing habitable zone dust: production in a planetesimal belt's collisional cascade and inward transport by P-R drag, or inward transport of comets which then fragment and release dust. In this chapter, I summarise the results of this thesis, then discuss future prospects for understanding the origin of exozodiacal dust.

6.1.1 Poynting-Robertson drag from an outer belt

The first mechanism for delivering dust to the habitable zone that I explored was P-R drag. In Chapter 2 I developed an analytical model for the distribution of dust grains throughout a debris disc in terms of grain size and radius from the star which was fitted to numerical results. This considers dust being produced in a planetesimal belt by a collisional cascade, and then migrating in towards the star via P-R drag while undergoing mutual collisions. This improved on previous analytical P-R drag models by simultaneously finding the size and spatial distribution of dust, allowing consideration of realistic dust optical properties when making predictions for thermal emission.

My P-R drag model was used in Chapter 3 to make predictions about the levels of dust which reach the habitable zone in this scenario. An advantage of using an analytical model is it allows for rapid parameter space exploration. By exploring the parameter space of a planetesimal belt's mass and distance from the star, I showed that there should be significant levels of exozodiacal dust in systems which are known to host cold planetesimal belts unless planets intervene. However, even belts which are too faint to currently be detected in the

far-infrared may have detectable levels of dust dragged into the habitable zone for a narrow region of parameter space, with relatively low dust masses and small radii. I then applied the model specifically to nine systems observed with LBTI as part of the HOSTS survey which are known to have outer belts, to ascertain whether P-R drag could explain the detected levels of warm dust. I showed that several of the systems have detections which agree with predictions from my P-R drag model. This includes the two systems with non-detections, which I predicted to be below their 3σ upper limits. However, three of the detected exozodi are far too high to be produced solely by P-R drag from the outer belt, and must have another origin. Moreover, I suggested that the three exozodi detections in the survey where the system is not known to host an outer belt may be produced by P-R drag if they have undetected belts lying in the region of parameter space mentioned above, with low masses and small radii.

Finally, I applied my P-R drag model more thoroughly to LBTI observations of the young A star β Leo, predicting the radial profile of warm dust. Additionally, I used the system geometry to take into account the interferometric transmission pattern of LBTI when predicting the null depth. This star is known to host an outer belt at $\sim 30 - 70$ au, along with warm dust. I showed that the level of dust dragged into the habitable zone from this outer belt is far too low, and the resultant radial profile is much flatter than the observed one. Previous modelling of the system has suggested the presence of a second, warm asteroid belt. I therefore explored the parameter space to find what warm belt would be consistent with both the stellar SED and the radial profile of warm dust. By superposing the emission from a warm belt at ~ 5 au along with dust dragged in from the outer belt, I showed a much better fit to the exozodi could be found. This suggests that either β Leo's warm dust comes from a combination of P-R drag from its outer belt and an additional warm belt, or another source is needed.

6.1.2 Inward transport and fragmentation of (exo)comets

I then considered an alternative production mechanism for warm dust, in which comets are scattered inwards from an outer belt by interactions with planets. On their way inwards, these comets spontaneously fragment, releasing dust close to the star which subsequently evolves due to collisions and P-R drag. The details of exoplanetary systems and their exocomets are poorly constrained by observations, so I started off by calibrating a model to our Solar System's zodiacal cloud. In Chapter 4 I developed a numerical model for the dust Jupiter-family comets produce in the Solar System. In this model, comets are scattered into the inner Solar System primarily by dynamical interactions with Jupiter, then randomly fragment and produce dust. I then follow the evolution of the dust produced by comets in a kinetic code which accounts for mutual collisions and P-R drag to find the resulting distribution of dust. I

showed that with plausible parameters for the model, fragmentation of JFCs can produce the correct spatial distribution of zodiacal dust, and match the size distribution of dust seen near Earth. This supports previous theories which suggested the main source of zodiacal dust should be fragmentation of comets, as cometary activity alone is unable to sustain the zodiacal cloud. My model is stochastic, such that there are large variations in the distribution of dust on long (Myr) timescales, depending on the sizes of comets which are scattered inwards and their dynamical lifetimes inside Jupiter. Thus, I showed that the zodiacal cloud should exhibit order-of-magnitude spikes in emission when large ($\gtrsim 100$ km) comets are scattered into the inner Solar System and have long dynamical lifetimes. However, the dominant contribution to the zodiacal cloud should come from ~ 50 km comets, which should be present in the inner Solar System much more frequently, and consequently dominate the quiescent level of dust.

Having calibrated the model to Solar System comets, in Chapter 5 I then developed this model further so that it may be applied to exoplanetary systems. This involved running N-body simulations for the scattering of comets by a chain of low-mass planets. It is difficult to incorporate the competing effects of dynamics, P-R drag, and collisions on the evolution of dust grains produced by comets. I therefore developed an updated dynamical prescription for the interaction of dust grains with the planetary system. The new prescription was tested using N-body simulations which include the effects of P-R drag and radiation pressure. This model can be applied to observations of η Corvi, whose exozodi is an order of magnitude too bright to be produced by P-R drag (as demonstrated in Chapter 3), such that exocomet fragmentation may be the source of dust.

6.2 Future prospects

Several current and future observatories will shed further light on the origin of exozodiacal dust. Follow-up observations of HOSTS survey (Ertel et al., 2020) detections with the LBTI will place further constraints on the radial profiles of several nearby stars. The Very Large Telescope Interferometer (VLTI) will provide multiwavelength observations, probing dust of different temperatures close to the star and providing better constraints on the dust composition through its spectral features. In particular, the VLTI/MATISSE instrument will observe stars with bright exozodis in the L and M bands (e.g. Kirchschrager et al., 2020), allowing to further study the connection between warm habitable zone dust and hot dust which lies close to the sublimation radius. A future upgrade to the VLTI known as Hi-5 (Defrère et al., 2018) will allow much higher contrast observations in the L and M bands ($3 - 5 \mu\text{m}$) which connect warm and hot exozodiacal dust. The VLTI will survey Southern

hemisphere stars, complementary to LBTI's sample. The recently launched James Webb Space Telescope's Mid-Infrared Instrument (JWST/MIRI) will resolve the habitable zones of three nearby debris disc stars (ϵ Eri, Fomalhaut, and Vega, Beichman et al., 2017). JWST will have superior resolution and sensitivity to LBTI, and be capable of constraining emission in the intermediate region between the habitable zone and outer belt. This will provide clues to the possible origin of exozodiacal dust in these systems, with different models predicting different radial profiles of dust. However, JWST will be limited to nearby stars with high luminosity, which are poor targets for exo-Earth imaging.

Several future instruments in the 2020s will provide even better observational constraints. In 2025 the Nancy Grace Roman Space Telescope (RST) will launch, including a Coronagraphic Instrument (CGI) capable of imaging at high contrasts of $\sim 10^{-9}$ in scattered light. RST/CGI will be particularly sensitive to exozodiacal dust in the outer part of the habitable zone, and should be able to observe the outer habitable zones of up to 74 nearby stars (Douglas et al., 2021). It should be able to detect exozodiacal dust in scattered light for several systems, which will complement previous observations and better constrain the dust composition and albedo. In 2027 the Extremely Large Telescope (ELT) will see first light. With a 39 m mirror, its Mid-infrared ELT Imager and Spectrograph (METIS) will be capable of searching for Earth-like planets and exozodiacal dust.

In parallel, theoretical models for the origins of habitable zone dust will continue to be developed and constrained by improved observations. With more detections, the exozodi luminosity function will be determined to lower levels of exozodiacal dust, which can be compared with the predictions of theoretical models. I plan to finish developing the model of Chapter 5 such that I am able to model the production of exozodiacal dust by disruption of exocomets and its ensuing evolution. The first system I hope to apply the model to is η Corvi, which has an exozodi 2000 times brighter than our zodiacal cloud. I will find the highest levels of exozodiacal dust that exocomets can produce for realistic model parameters, and whether this could supply the exozodi seen around η Corvi without producing a detectable scattered disc. Moreover, I will predict the surface brightness profile resulting from dust produced by comet fragmentation, and compare with previous observations.

The cometary scenario for exozodis has a vast parameter space to explore, and I plan to use my numerical model to better understand the feasibility of exocomets producing exozodiacal dust around other stars, and what the resulting radial profile of emission should look like. Additionally, I hope to link levels of exozodiacal dust to the number of comets which must be present in the habitable zone if it is supplied by exocomets. It is possible that the stochasticity I found when modelling the zodiacal cloud (Chapter 4) will mean that a given planetary system can exhibit a range of brightness levels, depending whether it is in a

quiescent stage or currently experiencing a spike in dust levels. I plan to use the model to determine whether comets scattered in from faint belts that are undetectable in the far-infrared may be able to produce exozodiacal dust levels which would impede exo-Earth missions. Given the low levels of comets produced by an undetectable outer belt, stochasticity should be important. Such systems may have detectable exozodis during the stochastic increases in brightness.

Using my models, I will be able to provide in-depth modelling of individual systems, such as that presented for β Leo in Chapter 3, and constrain their underlying planetary systems. Further, I will constrain the presence of exocomets and any resulting cometary bombardment of planets in the habitable zones of other stars. This could inform about the habitability of planets, as cometary bombardment may deliver volatiles needed for the development of life, or deplete the atmospheres of planets such that they are no longer habitable. More work also needs to be done on the planetary system architectures needed for scattering sufficient numbers of comets to the habitable zone, and the likelihood of planetary systems being capable of scattering enough comets inwards. This may require invoking additional dynamical mechanisms to prolong the lifetime of comets close to the star before they are ejected, such that they are able to supply more dust. I may be able to link the planetary system architecture to the shape of the exozodi radial profile, providing a new method of inferring the presence of planets around other stars.

References

- Absil, O., Defrère, D., Coudé du Foresto, V., Di Folco, E., Mérand, A., Augereau, J. C., Ertel, S., Hanot, C., Kervella, P., Mollier, B., Scott, N., Che, X., Monnier, J. D., Thureau, N., Tuthill, P. G., ten Brummelaar, T. A., McAlister, H. A., Sturmman, J., Sturmman, L., and Turner, N. (2013). A near-infrared interferometric survey of debris-disc stars. III. First statistics based on 42 stars observed with CHARA/FLUOR. *A&A*, 555:A104.
- Absil, O., di Folco, E., Mérand, A., Augereau, J. C., Coudé du Foresto, V., Aufdenberg, J. P., Kervella, P., Ridgway, S. T., Berger, D. H., and ten Brummelaar, T. A. (2006). Circumstellar material in the Vega inner system revealed by CHARA/FLUOR. *A&A*, 452(1):237–244.
- Absil, O., Marion, L., Ertel, S., Defrère, D., Kennedy, G. M., Romagnolo, A., Le Bouquin, J. B., Christiaens, V., Milli, J., Bonsor, A., Olofsson, J., Su, K. Y. L., and Augereau, J. C. (2021). A near-infrared interferometric survey of debris-disk stars. VII. The hot/warm dust connection. *arXiv e-prints*, page arXiv:2104.14216.
- Adams, E. R., Gulbis, A. A. S., Elliot, J. L., Benecchi, S. D., Buie, M. W., Trilling, D. E., and Wasserman, L. H. (2014). De-biased Populations of Kuiper Belt Objects from the Deep Ecliptic Survey. *AJ*, 148(3):55.
- Ansdell, M., Gaidos, E., Jacobs, T. L., Mann, A., Manara, C. F., Kennedy, G. M., Vanderburg, A., Kenworthy, M., Hirano, T., LaCourse, D. M., Hedges, C., and Frasca, A. (2019). The little dippers: transits of star-grazing exocomets? *MNRAS*, 483(3):3579–3591.
- Armitage, P. J. (2010). *Astrophysics of Planet Formation*.
- Asphaug, E. and Benz, W. (1996). Size, Density, and Structure of Comet Shoemaker-Levy 9 Inferred from the Physics of Tidal Breakup. *Icarus*, 121(2):225–248.
- Augereau, J. C. and Beust, H. (2006). On the AU Microscopii debris disk. Density profiles, grain properties, and dust dynamics. *A&A*, 455(3):987–999.
- Augereau, J. C., Lagrange, A. M., Mouillet, D., Papaloizou, J. C. B., and Grorod, P. A. (1999). On the HR 4796 A circumstellar disk. *A&A*, 348:557–569.
- Backman, D., Marengo, M., Stapelfeldt, K., Su, K., Wilner, D., Dowell, C. D., Watson, D., Stansberry, J., Rieke, G., Megeath, T., Fazio, G., and Werner, M. (2009). Epsilon Eridani’s Planetary Debris Disk: Structure and Dynamics Based on Spitzer and Caltech Submillimeter Observatory Observations. *ApJ*, 690(2):1522–1538.

- Batalha, N. M., Rowe, J. F., Bryson, S. T., Barclay, T., Burke, C. J., Caldwell, D. A., Christiansen, J. L., Mullally, F., Thompson, S. E., Brown, T. M., Dupree, A. K., Fabrycky, D. C., Ford, E. B., Fortney, J. J., Gilliland, R. L., Isaacson, H., Latham, D. W., Marcy, G. W., Quinn, S. N., Ragozzine, D., Shporer, A., Borucki, W. J., Ciardi, D. R., Gautier, Thomas N., I., Haas, M. R., Jenkins, J. M., Koch, D. G., Lissauer, J. J., Rapin, W., Basri, G. S., Boss, A. P., Buchhave, L. A., Carter, J. A., Charbonneau, D., Christensen-Dalsgaard, J., Clarke, B. D., Cochran, W. D., Demory, B.-O., Desert, J.-M., Devore, E., Doyle, L. R., Esquerdo, G. A., Everett, M., Fressin, F., Geary, J. C., Girouard, F. R., Gould, A., Hall, J. R., Holman, M. J., Howard, A. W., Howell, S. B., Ibrahim, K. A., Kinemuchi, K., Kjeldsen, H., Klaus, T. C., Li, J., Lucas, P. W., Meibom, S., Morris, R. L., Prša, A., Quintana, E., Sanderfer, D. T., Sasselov, D., Seader, S. E., Smith, J. C., Steffen, J. H., Still, M., Stumpe, M. C., Tarter, J. C., Tenenbaum, P., Torres, G., Twicken, J. D., Uddin, K., Van Cleve, J., Walkowicz, L., and Welsh, W. F. (2013). Planetary Candidates Observed by Kepler. III. Analysis of the First 16 Months of Data. *ApJS*, 204(2):24.
- Beaulieu, J. P., Bennett, D. P., Fouqué, P., Williams, A., Dominik, M., Jørgensen, U. G., Kubas, D., Cassan, A., Coutures, C., Greenhill, J., Hill, K., Menzies, J., Sackett, P. D., Albrow, M., Brilliant, S., Caldwell, J. A. R., Calitz, J. J., Cook, K. H., Corrales, E., Desert, M., Dieters, S., Dominis, D., Donatowicz, J., Hoffman, M., Kane, S., Marquette, J. B., Martin, R., Meintjes, P., Pollard, K., Sahu, K., Vinter, C., Wambsganss, J., Woller, K., Horne, K., Steele, I., Bramich, D. M., Burgdorf, M., Snodgrass, C., Bode, M., Udalski, A., Szymański, M. K., Kubiak, M., Więckowski, T., Pietrzyński, G., Soszyński, I., Szewczyk, O., Wyrzykowski, Ł., Paczyński, B., Abe, F., Bond, I. A., Britton, T. R., Gilmore, A. C., Hearnshaw, J. B., Itow, Y., Kamiya, K., Kilmartin, P. M., Korpela, A. V., Masuda, K., Matsubara, Y., Motomura, M., Muraki, Y., Nakamura, S., Okada, C., Ohnishi, K., Rattenbury, N. J., Sako, T., Sato, S., Sasaki, M., Sekiguchi, T., Sullivan, D. J., Tristram, P. J., Yock, P. C. M., and Yoshioka, T. (2006). Discovery of a cool planet of 5.5 Earth masses through gravitational microlensing. *Nature*, 439(7075):437–440.
- Beech, M. and Gauer, K. (2002). Cosmic Roulette: Comets In The Main Belt Asteroid Region. *Earth Moon and Planets*, 88(4):211–221.
- Beichman, C. A., Bryden, G., Gautier, T. N., Stapelfeldt, K. R., Werner, M. W., Misselt, K., Rieke, G., Stansberry, J., and Trilling, D. (2005). An Excess Due to Small Grains around the Nearby K0 V Star HD 69830: Asteroid or Cometary Debris? *ApJ*, 626(2):1061–1069.
- Beichman, C. A., Bryden, G., Stapelfeldt, K. R., Gautier, T. N., Grogan, K., Shao, M., Velusamy, T., Lawler, S. M., Blaylock, M., Rieke, G. H., Lunine, J. I., Fischer, D. A., Marcy, G. W., Greaves, J. S., Wyatt, M. C., Holland, W. S., and Dent, W. R. F. (2006). New Debris Disks around Nearby Main-Sequence Stars: Impact on the Direct Detection of Planets. *ApJ*, 652(2):1674–1693.
- Beichman, C. A., Rieke, G., Bouwman, J., Gaspar, A., Leisenring, J. M., Su, K. Y. L., and Ygouf, M. (2017). Coronagraphic Imaging of Young Planets and Debris Disk with NIRCcam and MIRI. JWST Proposal. Cycle 1.
- Belton, M. J. S. (2014). The size-distribution of scattered disk TNOs from that of JFCs between 0.2 and 15 km effective radius. *Icarus*, 231:168–182.
- Benz, W. and Asphaug, E. (1999). Catastrophic Disruptions Revisited. *Icarus*, 142(1):5–20.

- Bertini, I. (2011). Main Belt Comets: A new class of small bodies in the solar system. *Planet. Space Sci.*, 59(5-6):365–377.
- Beust, H., Lagrange-Henri, A. M., Vidal-Madjar, A., and Ferlet, R. (1990). The beta Pictoris circumstellar disk. X. Numerical simulations of infalling evaporating bodies. *A&A*, 236:202.
- Beust, H. and Morbidelli, A. (1996). Mean-Motion Resonances as a Source for Infalling Comets toward β Pictoris. *Icarus*, 120(2):358–370.
- Blum, J. (2018). Dust Evolution in Protoplanetary Discs and the Formation of Planetesimals. What Have We Learned from Laboratory Experiments? *Space Sci. Rev.*, 214(2):52.
- Bodman, E. H. L. and Quillen, A. (2016). KIC 8462852: Transit of a Large Comet Family. *ApJ*, 819(2):L34.
- Boehnhardt, H. (2004). in *Festou M.C., Keller H.U., Weaver H.A., eds, Comets II. University of Arizona Press, Tucson*, page 301.
- Boehnhardt, H., Holdstock, S., Hainaut, O., Tozzi, G. P., Benetti, S., and Licandro, J. (2002). 73p/Schwassmann-Wachmann 3 - One Orbit after Break-Up: Search for Fragments. *Earth Moon and Planets*, 90(1):131–139.
- Bohren, C. F. and Huffman, D. R. (1983). *Absorption and scattering of light by small particles*. Wiley.
- Boley, A. C. (2009). The Two Modes of Gas Giant Planet Formation. *ApJ*, 695(1):L53–L57.
- Boltzmann, L. (1896). *Vorlesungen über Gastheorie*. J.A. Barth, Leipzig.
- Bonsor, A., Augereau, J. C., and Thébault, P. (2012). Scattering of small bodies by planets: a potential origin for exozodiacal dust? *A&A*, 548:A104.
- Bonsor, A., Raymond, S. N., and Augereau, J.-C. (2013). The short-lived production of exozodiacal dust in the aftermath of a dynamical instability in planetary systems. *MNRAS*, 433(4):2938–2945.
- Bonsor, A., Raymond, S. N., Augereau, J.-C., and Ormel, C. W. (2014). Planetesimal-driven migration as an explanation for observations of high levels of warm, exozodiacal dust. *MNRAS*, 441(3):2380–2391.
- Bonsor, A. and Wyatt, M. C. (2012). The scattering of small bodies in planetary systems: constraints on the possible orbits of cometary material. *MNRAS*, 420(4):2990–3002.
- Bonsor, A., Wyatt, M. C., Kral, Q., Kennedy, G., Shannon, A., and Ertel, S. (2018). Using warm dust to constrain unseen planets. *MNRAS*, 480(4):5560–5579.
- Booth, M., Kennedy, G., Sibthorpe, B., Matthews, B. C., Wyatt, M. C., Duchêne, G., Kavelaars, J. J., Rodriguez, D., Greaves, J. S., Koning, A., Vican, L., Rieke, G. H., Su, K. Y. L., Moro-Martín, A., and Kalas, P. (2013). Resolved debris discs around A stars in the Herschel DEBRIS survey. *MNRAS*, 428(2):1263–1280.

- Booth, M., Wyatt, M. C., Morbidelli, A., Moro-Martín, A., and Levison, H. F. (2009). The history of the Solar system's debris disc: observable properties of the Kuiper belt. *MNRAS*, 399(1):385–398.
- Borucki, W. J., Koch, D. G., Basri, G., Batalha, N., Brown, T. M., Bryson, S. T., Caldwell, D., Christensen-Dalsgaard, J., Cochran, W. D., DeVore, E., Dunham, E. W., Gautier, Thomas N., I., Geary, J. C., Gilliland, R., Gould, A., Howell, S. B., Jenkins, J. M., Latham, D. W., Lissauer, J. J., Marcy, G. W., Rowe, J., Sasselov, D., Boss, A., Charbonneau, D., Ciardi, D., Doyle, L., Dupree, A. K., Ford, E. B., Fortney, J., Holman, M. J., Seager, S., Steffen, J. H., Tarter, J., Welsh, W. F., Allen, C., Buchhave, L. A., Christiansen, J. L., Clarke, B. D., Das, S., Désert, J.-M., Endl, M., Fabrycky, D., Fressin, F., Haas, M., Horch, E., Howard, A., Isaacson, H., Kjeldsen, H., Kolodziejczak, J., Kulesa, C., Li, J., Lucas, P. W., Machalek, P., McCarthy, D., MacQueen, P., Meibom, S., Miquel, T., Prsa, A., Quinn, S. N., Quintana, E. V., Ragozzine, D., Sherry, W., Shporer, A., Tenenbaum, P., Torres, G., Twicken, J. D., Van Cleve, J., Walkowicz, L., Witteborn, F. C., and Still, M. (2011). Characteristics of Planetary Candidates Observed by Kepler. II. Analysis of the First Four Months of Data. *ApJ*, 736(1):19.
- Boss, A. P. (2011). Formation of Giant Planets by Disk Instability on Wide Orbits Around Protostars with Varied Masses. *ApJ*, 731(1):74.
- Boyajian, T. S., LaCourse, D. M., Rappaport, S. A., Fabrycky, D., Fischer, D. A., Gandolfi, D., Kennedy, G. M., Korhonen, H., Liu, M. C., Moor, A., Olah, K., Vida, K., Wyatt, M. C., Best, W. M. J., Brewer, J., Ciesla, F., Csák, B., Deeg, H. J., Dupuy, T. J., Handler, G., Heng, K., Howell, S. B., Ishikawa, S. T., Kovács, J., Kozakis, T., Kriskovics, L., Lehtinen, J., Lintott, C., Lynn, S., Nespral, D., Nikbakhsh, S., Schawinski, K., Schmitt, J. R., Smith, A. M., Szabo, G., Szabo, R., Viuhio, J., Wang, J., Weiksnar, A., Bosch, M., Connors, J. L., Goodman, S., Green, G., Hoekstra, A. J., Jebson, T., Jek, K. J., Omohundro, M. R., Schwengeler, H. M., and Szewczyk, A. (2016). Planet Hunters IX. KIC 8462852 - where's the flux? *MNRAS*, 457(4):3988–4004.
- Bracewell, R. N. (1978). Detecting nonsolar planets by spinning infrared interferometer. *Nature*, 274(5673):780–781.
- Bracewell, R. N. and MacPhie, R. H. (1979). Searching for nonsolar planets. *Icarus*, 38(1):136–147.
- Brasser, R. and Duncan, M. J. (2008). An analytical method to compute comet cloud formation efficiency and its application. *Celestial Mechanics and Dynamical Astronomy*, 100(1):1–26.
- Brauer, F., Dullemond, C. P., and Henning, T. (2008). Coagulation, fragmentation and radial motion of solid particles in protoplanetary disks. *A&A*, 480(3):859–877.
- Brin, G. D. (1980). Three models of dust layers on cometary nuclei. *ApJ*, 237:265–279.
- Brin, G. D. and Mendis, D. A. (1979). Dust release and mantle development in comets. *ApJ*, 229:402–408.
- Bukhari Syed, M., Blum, J., Wahlberg Jansson, K., and Johansen, A. (2017). The Role of Pebble Fragmentation in Planetesimal Formation. I. Experimental Study. *ApJ*, 834(2):145.

- Burns, J. A., Lamy, P. L., and Soter, S. (1979). Radiation forces on small particles in the solar system. *Icarus*, 40(1):1–48.
- Campo Bagatin, A., Cellino, A., Davis, D. R., Farinella, P., and Paolicchi, P. (1994). Wavy size distributions for collisional systems with a small-size cutoff. *Planet. Space Sci.*, 42(12):1079–1092.
- Carrera, D., Johansen, A., and Davies, M. B. (2015). How to form planetesimals from mm-sized chondrules and chondrule aggregates. *A&A*, 579:A43.
- Cataldi, G., Brandeker, A., Olofsson, G., Larsson, B., Liseau, R., Blommaert, J., Fridlund, M., Ivison, R., Pantin, E., Sibthorpe, B., Vandenbussche, B., and Wu, Y. (2014). Herschel/HIFI observations of ionised carbon in the β Pictoris debris disk. *A&A*, 563:A66.
- Cataldi, G., Wu, Y., Brandeker, A., Ohashi, N., Moór, A., Olofsson, G., Ábrahám, P., Asensio-Torres, R., Cavallius, M., Dent, W. R. F., Grady, C., Henning, T., Higuchi, A. E., Hughes, A. M., Janson, M., Kamp, I., Kóspál, Á., Redfield, S., Roberge, A., Weinberger, A., and Welsh, B. (2020). The Surprisingly Low Carbon Mass in the Debris Disk around HD 32297. *ApJ*, 892(2):99.
- Chambers, J. E. (1999). A hybrid symplectic integrator that permits close encounters between massive bodies. *MNRAS*, 304(4):793–799.
- Chambers, J. E., Wetherill, G. W., and Boss, A. P. (1996). The Stability of Multi-Planet Systems. *Icarus*, 119(2):261–268.
- Chen, J. and Jewitt, D. (1994). On the Rate at Which Comets Split. *Icarus*, 108(2):265–271.
- Churcher, L. J., Wyatt, M. C., Duchêne, G., Sibthorpe, B., Kennedy, G., Matthews, B. C., Kalas, P., Greaves, J., Su, K., and Rieke, G. (2011). Multiwavelength modelling of the β Leo debris disc: one, two or three planetesimal populations? *MNRAS*, 417(3):1715–1734.
- Chyba, C. F., Thomas, P. J., Brookshaw, L., and Sagan, C. (1990). Cometary Delivery of Organic Molecules to the Early Earth. *Science*, 249(4967):366–373.
- Clarke, C. J., Gendrin, A., and Sotomayor, M. (2001). The dispersal of circumstellar discs: the role of the ultraviolet switch. *MNRAS*, 328(2):485–491.
- Clube, S. V. M. and Napier, W. M. (1984). The microstructure of terrestrial catastrophism. *MNRAS*, 211:953–968.
- Coker, C. T., Wang, J., and Shaklan, S. (2018). Effects of thermal and exozodiacal background on space telescope observations of exoEarths. In Lystrup, M., MacEwen, H. A., Fazio, G. G., Batalha, N., Siegler, N., and Tong, E. C., editors, *Space Telescopes and Instrumentation 2018: Optical, Infrared, and Millimeter Wave*, volume 10698 of *Society of Photo-Optical Instrumentation Engineers (SPIE) Conference Series*, page 106985G.
- Colavita, M. M., Serabyn, E., Millan-Gabet, R., Koresko, C. D., Akeson, R. L., Booth, A. J., Mennesson, B. P., Ragland, S. D., Appleby, E. C., and Berkey, B. C. (2009). Keck Interferometer Nuller Data Reduction and On-Sky Performance. *PASP*, 121(884):1120.

- Czechowski, A. and Mann, I. (2007). Collisional Vaporization of Dust and Production of Gas in the β Pictoris Dust Disk. *ApJ*, 660(2):1541–1555.
- David, T. J. and Hillenbrand, L. A. (2015). The Ages of Early-type Stars: Strömgren Photometric Methods Calibrated, Validated, Tested, and Applied to Hosts and Prospective Hosts of Directly Imaged Exoplanets. *ApJ*, 804(2):146.
- Defrère, D., Absil, O., Augereau, J. C., di Folco, E., Berger, J. P., Coudé du Foresto, V., Kervella, P., Le Bouquin, J. B., Lebreton, J., and Millan-Gabet, R. (2011). Hot exozodiacal dust resolved around Vega with IOTA/IONIC. *A&A*, 534:A5.
- Defrère, D., Absil, O., den Hartog, R., Hanot, C., and Stark, C. (2010). Nulling interferometry: impact of exozodiacal clouds on the performance of future life-finding space missions. *A&A*, 509:A9.
- Defrère, D., Hinz, P. M., Kennedy, G. M., Stone, J., Rigley, J., Ertel, S., Gaspar, A., Bailey, V. P., Hoffmann, W. F., Mennesson, B., Millan-Gabet, R., Danchi, W. C., Absil, O., Arbo, P., Beichman, C., Bonavita, M., Brusa, G., Bryden, G., Downey, E. C., Esposito, S., Grenz, P., Haniff, C., Hill, J. M., Leisenring, J. M., Males, J. R., McMahan, T. J., Montoya, M., Morzinski, K. M., Pinna, E., Puglisi, A., Rieke, G., Roberge, A., Rousseau, H., Serabyn, E., Spalding, E., Skemer, A. J., Stapelfeldt, K., Su, K., Vaz, A., Weinberger, A. J., and Wyatt, M. C. (2021). The HOSTS Survey: Evidence for an Extended Dust Disk and Constraints on the Presence of Giant Planets in the Habitable Zone of β Leo. *AJ*, 161(4):186.
- Defrère, D., Hinz, P. M., Mennesson, B., Hoffmann, W. F., Millan-Gabet, R., Skemer, A. J., Bailey, V., Danchi, W. C., Downey, E. C., and Durney, O. (2016). Nulling Data Reduction and On-sky Performance of the Large Binocular Telescope Interferometer. *ApJ*, 824(2):66.
- Defrère, D., Hinz, P. M., Skemer, A. J., Kennedy, G. M., Bailey, V. P., Hoffmann, W. F., Mennesson, B., Millan-Gabet, R., Danchi, W. C., Absil, O., Arbo, P., Beichman, C., Brusa, G., Bryden, G., Downey, E. C., Durney, O., Esposito, S., Gaspar, A., Grenz, P., Haniff, C., Hill, J. M., Lebreton, J., Leisenring, J. M., Males, J. R., Marion, L., McMahan, T. J., Montoya, M., Morzinski, K. M., Pinna, E., Puglisi, A., Rieke, G., Roberge, A., Serabyn, E., Sosa, R., Stapelfeldt, K., Su, K., Vaitheeswaran, V., Vaz, A., Weinberger, A. J., and Wyatt, M. C. (2015). First-light LBT Nulling Interferometric Observations: Warm Exozodiacal Dust Resolved within a Few AU of η Crv. *ApJ*, 799(1):42.
- Defrère, D., Ireland, M., Absil, O., Berger, J. P., Danchi, W. C., Ertel, S., Gallenne, A., Hénault, F., Hinz, P., Huby, E., Kraus, S., Labadie, L., Le Bouquin, J. B., Martin, G., Matter, A., Mennesson, B., Mérand, A., Minardi, S., Monnier, J. D., Norris, B., Orban de Xivry, G., Pedretti, E., Pott, J. U., Reggiani, M., Serabyn, E., Surdej, J., Tristram, K. R. W., and Woillez, J. (2018). Hi-5: a potential high-contrast thermal near-infrared imager for the VLTI. In Creech-Eakman, M. J., Tuthill, P. G., and Mérand, A., editors, *Optical and Infrared Interferometry and Imaging VI*, volume 10701 of *Society of Photo-Optical Instrumentation Engineers (SPIE) Conference Series*, page 107010U.
- Defrère, D., Stark, C., Cahoy, K., and Beerer, I. (2012). Direct imaging of exoEarths embedded in clumpy debris disks. In Clampin, M. C., Fazio, G. G., MacEwen, H. A., and Jr., J. M. O., editors, *Space Telescopes and Instrumentation 2012: Optical, Infrared, and Millimeter Wave*, volume 8442, pages 267 – 274. International Society for Optics and Photonics, SPIE.

- Dermott, S. F., Grogan, K., Durda, D. D., Jayaraman, S., Kehoe, T. J. J., Kortenkamp, S. J., and Wyatt, M. C. (2001). *in Grün E., Gusafson B.A.S., Dermott S., Fechtig H., eds, Interplanetary Dust. Springer, Berlin, page 569.*
- Dermott, S. F., Jayaraman, S., Xu, Y. L., Gustafson, B. Å. S., and Liou, J. C. (1994). A circumsolar ring of asteroidal dust in resonant lock with the Earth. *Nature*, 369(6483):719–723.
- Dermott, S. F., Nicholson, P. D., Burns, J. A., and Houck, J. R. (1984). Origin of the Solar System dust bands discovered by IRAS. *Nature*, 312(5994):505–509.
- Di Folco, E., Thévenin, F., Kervella, P., Domiciano de Souza, A., Coudé du Foresto, V., Ségransan, D., and Morel, P. (2004). VLTI near-IR interferometric observations of Vega-like stars. Radius and age of α PsA, β Leo, β Pic, ϵ Eri and τ Cet. *A&A*, 426:601–617.
- Di Sisto, R. P., Fernández, J. A., and Brunini, A. (2009). On the population, physical decay and orbital distribution of Jupiter family comets: Numerical simulations. *Icarus*, 203(1):140–154.
- Dikarev, V., Grün, E., Baggaley, J., Galligan, D., Landgraf, M., and Jehn, R. (2004). Modeling the Sporadic Meteoroid Background Cloud. *Earth Moon and Planets*, 95(1-4):109–122.
- Divine, N. (1993). Five populations of interplanetary meteoroids. *J. Geophys. Res.*, 98(E9):17029–17048.
- Dohnanyi, J. S. (1969). Collisional Model of Asteroids and Their Debris. *Journal of Geophysical Research*, 74:2531–2554.
- Dominik, C. and Decin, G. (2003). Age Dependence of the Vega Phenomenon: Theory. *ApJ*, 598(1):626–635.
- Dominik, C. and Tielens, A. G. G. M. (1997). The Physics of Dust Coagulation and the Structure of Dust Aggregates in Space. *ApJ*, 480(2):647–673.
- Dones, L., Brassier, R., Kaib, N., and Rickman, H. (2015). Origin and Evolution of the Cometary Reservoirs. *Space Sci. Rev.*, 197(1-4):191–269.
- Dones, L., Weissman, P. R., Levison, H. F., and Duncan, M. J. (2004). *Oort cloud formation and dynamics*, page 153.
- Douglas, E. S., Debes, J., Mennesson, B., Nemati, B., Ashcraft, J., Ren, B., Stapelfeldt, K., Savransky, D., Lewis, N. K., and Macintosh, B. (2021). Sensitivity of the Roman Coronagraph Instrument to Exozodiacal Dust. *arXiv e-prints*, page arXiv:2112.12804.
- Drazkowska, J., Bitsch, B., Lambrechts, M., Mulders, G. D., Harsono, D., Vazan, A., Liu, B., Ormel, C. W., Kretke, K., and Morbidelli, A. (2022). Planet Formation Theory in the Era of ALMA and Kepler: from Pebbles to Exoplanets. *arXiv e-prints*, page arXiv:2203.09759.
- Duchêne, G., Arriaga, P., Wyatt, M., Kennedy, G., Sibthorpe, B., Lisse, C., Holland, W., Wisniewski, J., Clampin, M., Kalas, P., Pinte, C., Wilner, D., Booth, M., Horner, J., Matthews, B., and Greaves, J. (2014). Spatially Resolved Imaging of the Two-component η Crv Debris Disk with Herschel. *ApJ*, 784(2):148.

- Duncan, M., Quinn, T., and Tremaine, S. (1987). The Formation and Extent of the Solar System Comet Cloud. *AJ*, 94:1330.
- Duncan, M. J. and Levison, H. F. (1997). A scattered comet disk and the origin of Jupiter family comets. *Science*, 276:1670–1672.
- Durda, D. D. and Dermott, S. F. (1997). The Collisional Evolution of the Asteroid Belt and Its Contribution to the Zodiacal Cloud. *Icarus*, 130(1):140–164.
- Durda, D. D., Greenberg, R., and Jedicke, R. (1998). Collisional Models and Scaling Laws: A New Interpretation of the Shape of the Main-Belt Asteroid Size Distribution. *Icarus*, 135(2):431–440.
- Economou, T. E., Green, S. F., Brownlee, D. E., and Clark, B. C. (2013). Dust Flux Monitor Instrument measurements during Stardust-NExT Flyby of Comet 9P/Tempel 1. *Icarus*, 222(2):526–539.
- Eiroa, C., Marshall, J. P., Mora, A., Montesinos, B., Absil, O., Augereau, J. C., Bayo, A., Bryden, G., Danchi, W., del Burgo, C., Ertel, S., Fridlund, M., Heras, A. M., Krivov, A. V., Launhardt, R., Liseau, R., Löhne, T., Maldonado, J., Pilbratt, G. L., Roberge, A., Rodmann, J., Sanz-Forcada, J., Solano, E., Stapelfeldt, K., Thébault, P., Wolf, S., Ardila, D., Arévalo, M., Beichmann, C., Faramaz, V., González-García, B. M., Gutiérrez, R., Lebreton, J., Martínez-Arnáiz, R., Meeus, G., Montes, D., Olofsson, G., Su, K. Y. L., White, G. J., Barrado, D., Fukagawa, M., Grün, E., Kamp, I., Lorente, R., Morbidelli, A., Müller, S., Mutschke, H., Nakagawa, T., Ribas, I., and Walker, H. (2013). DUST around NEARBY STARS. The survey observational results. *A&A*, 555:A11.
- Ercolano, B. and Pascucci, I. (2017). The dispersal of planet-forming discs: theory confronts observations. *Royal Society Open Science*, 4(4):170114.
- Ertel, S., Absil, O., Defrère, D., Le Bouquin, J. B., Augereau, J. C., Marion, L., Blind, N., Bonsor, A., Bryden, G., Lebreton, J., and Milli, J. (2014). A near-infrared interferometric survey of debris-disk stars. IV. An unbiased sample of 92 southern stars observed in H band with VLTI/PIONIER. *A&A*, 570:A128.
- Ertel, S., Defrère, D., Absil, O., Le Bouquin, J. B., Augereau, J. C., Berger, J. P., Blind, N., Bonsor, A., Lagrange, A. M., Lebreton, J., Marion, L., Milli, J., and Olofsson, J. (2016). A near-infrared interferometric survey of debris-disk stars. V. PIONIER search for variability. *A&A*, 595:A44.
- Ertel, S., Defrère, D., Hinz, P., Mennesson, B., Kennedy, G. M., Danchi, W. C., Gelino, C., Hill, J. M., Hoffmann, W. F., Rieke, G., Shannon, A., Spalding, E., Stone, J. M., Vaz, A., Weinberger, A. J., Willems, P., Absil, O., Arbo, P., Bailey, V. P., Beichman, C., Bryden, G., Downey, E. C., Durney, O., Esposito, S., Gaspar, A., Grenz, P., Haniff, C. A., Leisenring, J. M., Marion, L., McMahon, T. J., Millan-Gabet, R., Montoya, M., Morzinski, K. M., Pinna, E., Power, J., Puglisi, A., Roberge, A., Serabyn, E., Skemer, A. J., Stapelfeldt, K., Su, K. Y. L., Vaitheeswaran, V., and Wyatt, M. C. (2018a). The HOSTS Survey—Exozodiacal Dust Measurements for 30 Stars. *AJ*, 155(5):194.

- Ertel, S., Defrère, D., Hinz, P. M., Mennesson, B., Kennedy, G. M., Danchi, W. C., Gelino, C., Hill, J. M., Hoffmann, W. F., Mazoyer, J., Rieke, G., Shannon, A., Stapelfeldt, K., Spalding, E., Stone, J. M., Vaz, A., Weinberger, A. J., Willems, P., Absil, O., Arbo, P., Bailey, V. P., Beichman, C., Bryden, G., Downey, E. C., Durney, O., Esposito, S., Gaspar, A., Grenz, P., Haniff, C. A., Leisenring, J. M., Marion, L., McMahon, T. J., Millan-Gabet, R., Montoya, O. M., Morzinski, K. M., Perera, S., Pinna, E., Pott, J.-U., Power, J., Puglisi, A., Roberge, A., Serabyn, E., Skemer, A. J., Su, K. Y. L., Vaitheeswaran, V., and Wyatt, M. C. (2020). The HOSTS survey for exozodiacal dust: Observational results from the complete survey. *arXiv e-prints*, page arXiv:2003.03499.
- Ertel, S., Kennedy, G. M., Defrère, D., Hinz, P., Shannon, A. B., Mennesson, B., Danchi, W. C., Gelino, C., Hill, J. M., Hoffman, W. F., Rieke, G., Spalding, E., Stone, J. M., Vaz, A., Weinberger, A. J., Willems, P., Absil, O., Arbo, P., Bailey, V. P., Beichman, C., Bryden, G., Downey, E. C., Durney, O., Esposito, S., Gaspar, A., Grenz, P., Haniff, C. A., Leisenring, J. M., Marion, L., McMahon, T. J., Millan-Gabet, R., Montoya, M., Morzinski, K. M., Pinna, E., Power, J., Puglisi, A., Roberge, A., Serabyn, E., Skemer, A. J., Stapelfeldt, K., Su, K. Y. L., Vaitheeswaran, V., and Wyatt, M. C. (2018b). The HOSTS survey for exo-zodiacal dust: preliminary results and future prospects. In *Space Telescopes and Instrumentation 2018: Optical, Infrared, and Millimeter Wave*, volume 10698 of *Society of Photo-Optical Instrumentation Engineers (SPIE) Conference Series*, page 106981V.
- Esposito, T. M., Kalas, P., Fitzgerald, M. P., Millar-Blanchaer, M. A., Duchêne, G., Patience, J., Hom, J., Perrin, M. D., De Rosa, R. J., Chiang, E., Czekala, I., Macintosh, B., Graham, J. R., Ansdell, M., Arriaga, P., Bruzzone, S., Bulger, J., Chen, C. H., Cotten, T., Dong, R., Draper, Z. H., Follette, K. B., Hung, L.-W., Lopez, R., Matthews, B. C., Mazoyer, J., Metchev, S., Rameau, J., Ren, B., Rice, M., Song, I., Stahl, K., Wang, J., Wolff, S., Zuckerman, B., Ammons, S. M., Bailey, V. P., Barman, T., Chilcote, J., Doyon, R., Gerard, B. L., Goodsell, S. J., Greenbaum, A. Z., Hibon, P., Hinkley, S., Ingraham, P., Konopacky, Q., Maire, J., Marchis, F., Marley, M. S., Marois, C., Nielsen, E. L., Oppenheimer, R., Palmer, D., Poyneer, L., Pueyo, L., Rajan, A., Rantakyro, F. T., Ruffio, J.-B., Savransky, D., Schneider, A. C., Sivaramakrishnan, A., Soummer, R., Thomas, S., and Ward-Duong, K. (2020). Debris Disk Results from the Gemini Planet Imager Exoplanet Survey's Polarimetric Imaging Campaign. *AJ*, 160(1):24.
- Espy Kehoe, A. J., Kehoe, T. J. J., Colwell, J. E., and Dermott, S. F. (2015). Signatures of Recent Asteroid Disruptions in the Formation and Evolution of Solar System Dust Bands. *ApJ*, 811(1):66.
- Fajardo-Acosta, S. B., Beichman, C. A., and Cutri, R. M. (2000). Discovery of New Candidate Vega-type Systems from IRAS and the 2 Micron All-Sky Survey. *ApJ*, 538(2):L155–L158.
- Faramaz, V., Ertel, S., Booth, M., Cuadra, J., and Simmonds, C. (2017). Inner mean-motion resonances with eccentric planets: a possible origin for exozodiacal dust clouds. *MNRAS*, 465(2):2352–2365.
- Farnham, T. L., Kelley, M. S. P., and Bauer, J. M. (2021). Early Activity in Comet C/2014 UN271 Bernardinelli-Bernstein as Observed by TESS. , 2(6):236.

- Farnham, T. L., Schleicher, D. G., Woodney, L. M., Birch, P. V., Eberhardy, C. A., and Levy, L. (2001). Imaging and Photometry of Comet C/1999 S4 (LINEAR) Before Perihelion and After Breakup. *Science*, 292(5520):1348–1354.
- Fernández, J. A. (2005). *Comets - Nature, Dynamics, Origin and their Cosmological Relevance*. Springer, Dordrecht.
- Fernández, J. A. and Morbidelli, A. (2006). The population of faint Jupiter family comets near the Earth. *Icarus*, 185(1):211–222.
- Fernández, Y. R. (2009). That's the way the comet crumbles: Splitting Jupiter-family comets. *Planet. Space Sci.*, 57(10):1218–1227.
- Fernández, Y. R., Kelley, M. S., Lamy, P. L., Toth, I., Groussin, O., Lisse, C. M., A'Hearn, M. F., Bauer, J. M., Campins, H., Fitzsimmons, A., Licandro, J., Lowry, S. C., Meech, K. J., Pittichová, J., Reach, W. T., Snodgrass, C., and Weaver, H. A. (2013). Thermal properties, sizes, and size distribution of Jupiter-family cometary nuclei. *Icarus*, 226(1):1138–1170.
- Ferrín, I. and Orofino, V. (2021). Taurid complex smoking gun: Detection of cometary activity. *Planet. Space Sci.*, 207:105306.
- Fixsen, D. J. and Dwek, E. (2002). The Zodiacal Emission Spectrum as Determined by COBE and Its Implications. *ApJ*, 578(2):1009–1014.
- Flynn, G. J. and Durda, D. D. (2004). Chemical and mineralogical size segregation in the impact disruption of inhomogeneous, anhydrous meteorites. *Planet. Space Sci.*, 52(12):1129–1140.
- Fujiwara, A. (1986). Results obtained by laboratory simulations of catastrophic impact. *Mem. Soc. Astron. Italiana*, 57(1):47–64.
- Fulle, M., Della Corte, V., Rotundi, A., Rietmeijer, F. J. M., Green, S. F., Weissman, P., Accolla, M., Colangeli, L., Ferrari, M., Ivanovski, S., Lopez-Moreno, J. J., Epifani, E. M., Morales, R., Ortiz, J. L., Palomba, E., Palumbo, P., Rodriguez, J., Sordini, R., and Zakharov, V. (2016a). Comet 67P/Churyumov-Gerasimenko preserved the pebbles that formed planetesimals. *MNRAS*, 462:S132–S137.
- Fulle, M., Marzari, F., Della Corte, V., Fornasier, S., Sierks, H., Rotundi, A., Barbieri, C., Lamy, P. L., Rodrigo, R., Koschny, D., Rickman, H., Keller, H. U., López-Moreno, J. J., Accolla, M., Agarwal, J., A'Hearn, M. F., Altobelli, N., Barucci, M. A., Bertaux, J. L., Bertini, I., Bodewits, D., Bussoletti, E., Colangeli, L., Cosi, M., Cremonese, G., Crifo, J. F., Da Deppo, V., Davidsson, B., Debei, S., De Cecco, M., Esposito, F., Ferrari, M., Giovane, F., Gustafson, B., Green, S. F., Groussin, O., Grün, E., Gutierrez, P., Güttler, C., Herranz, M. L., Hviid, S. F., Ip, W., Ivanovski, S. L., Jerónimo, J. M., Jorda, L., Knollenberg, J., Kramm, R., Kührt, E., Küppers, M., Lara, L., Lazzarin, M., Leese, M. R., López-Jiménez, A. C., Lucarelli, F., Mazzotta Epifani, E., McDonnell, J. A. M., Mennella, V., Molina, A., Morales, R., Moreno, F., Mottola, S., Naletto, G., Oklay, N., Ortiz, J. L., Palomba, E., Palumbo, P., Perrin, J. M., Rietmeijer, F. J. M., Rodríguez, J., Sordini, R., Thomas, N., Tubiana, C., Vincent, J. B., Weissman, P., Wenzel, K. P., Zakharov, V., and Zarnecki, J. C. (2016b). Evolution of the Dust Size Distribution of Comet 67P/Churyumov-Gerasimenko from 2.2 au to Perihelion. *ApJ*, 821(1):19.

- Fuse, T., Yamamoto, N., Kinoshita, D., Furusawa, H., and Watanabe, J.-I. (2007). Observations of Fragments Split from Nucleus B of Comet 73P/Schwassmann-Wachmann 3 with Subaru Telescope. *PASJ*, 59:381–386.
- Gaidos, E. J. (1999). Observational Constraints on Late Heavy Bombardment Episodes around Young Solar Analogs. *ApJ*, 510(2):L131–L134.
- Gaudi, B. S. (2012). Microlensing Surveys for Exoplanets. *ARA&A*, 50:411–453.
- Gaudi, B. S., Seager, S., Mennesson, B., Kiessling, A., Warfield, K., Cahoy, K., Clarke, J. T., Domagal-Goldman, S., Feinberg, L., Guyon, O., Kasdin, J., Mawet, D., Plavchan, P., Robinson, T., Rogers, L., Scowen, P., Somerville, R., Stapelfeldt, K., Stark, C., Stern, D., Turnbull, M., Amini, R., Kuan, G., Martin, S., Morgan, R., Redding, D., Stahl, H. P., Webb, R., Alvarez-Salazar, O., Arnold, W. L., Arya, M., Balasubramanian, B., Baysinger, M., Bell, R., Below, C., Benson, J., Blais, L., Booth, J., Bourgeois, R., Bradford, C., Brewer, A., Brooks, T., Cady, E., Caldwell, M., Calvet, R., Carr, S., Chan, D., Cormarkovic, V., Coste, K., Cox, C., Danner, R., Davis, J., Dewell, L., Dorsett, L., Dunn, D., East, M., Effinger, M., Eng, R., Freebury, G., Garcia, J., Gaskin, J., Greene, S., Hennessy, J., Hilgemann, E., Hood, B., Holota, W., Howe, S., Huang, P., Hull, T., Hunt, R., Hurd, K., Johnson, S., Kissil, A., Knight, B., Kolenz, D., Kraus, O., Krist, J., Li, M., Lisman, D., Mandic, M., Mann, J., Marchen, L., Marrese-Reading, C., McCready, J., McGown, J., Missun, J., Miyaguchi, A., Moore, B., Nemati, B., Nikzad, S., Nissen, J., Novicki, M., Perrine, T., Pineda, C., Polanco, O., Putnam, D., Qureshi, A., Richards, M., Eldorado Riggs, A. J., Rodgers, M., Rud, M., Saini, N., Scalisi, D., Scharf, D., Schulz, K., Serabyn, G., Sigrist, N., Sikkia, G., Singleton, A., Shaklan, S., Smith, S., Southerd, B., Stahl, M., Steeves, J., Sturges, B., Sullivan, C., Tang, H., Taras, N., Tesch, J., Therrell, M., Tseng, H., Valente, M., Van Buren, D., Villalvazo, J., Warwick, S., Webb, D., Westerhoff, T., Wofford, R., Wu, G., Woo, J., Wood, M., Ziemer, J., Arney, G., Anderson, J., Maíz-Apellániz, J., Bartlett, J., Belikov, R., Bendek, E., Cenko, B., Douglas, E., Dulz, S., Evans, C., Faramaz, V., Feng, Y. K., Ferguson, H., Follette, K., Ford, S., García, M., Geha, M., Gelino, D., Götberg, Y., Hildebrandt, S., Hu, R., Jahnke, K., Kennedy, G., Kreidberg, L., Isella, A., Lopez, E., Marchis, F., Macri, L., Marley, M., Matzko, W., Mazoyer, J., McCandliss, S., Meshkat, T., Mordasini, C., Morris, P., Nielsen, E., Newman, P., Petigura, E., Postman, M., Reines, A., Roberge, A., Roederer, I., Ruane, G., Schwieterman, E., Sirbu, D., Spalding, C., Teplitz, H., Tumlinson, J., Turner, N., Werk, J., Wofford, A., Wyatt, M., Young, A., and Zellem, R. (2020). The Habitable Exoplanet Observatory (HabEx) Mission Concept Study Final Report. *arXiv e-prints*, page arXiv:2001.06683.
- Geiler, F. and Krivov, A. V. (2017). Does warm debris dust stem from asteroid belts? *MNRAS*, 468(1):959–970.
- Genda, H., Kobayashi, H., and Kokubo, E. (2015). Warm Debris Disks Produced by Giant Impacts during Terrestrial Planet Formation. *ApJ*, 810(2):136.
- Giannini, E. and Lunine, J. I. (2013). Microlensing detection of extrasolar planets. *Reports on Progress in Physics*, 76(5):056901.
- Gkotsinas, A., Guilbert-Lepoutre, A., Raymond, S. N., and Nesvorný, D. (2022). Thermal processing of Jupiter Family Comets during their chaotic orbital evolution. *arXiv e-prints*, page arXiv:2202.06685.

- Gladman, B., Marsden, B. G., and Vanlaerhoven, C. (2008). Nomenclature in the Outer Solar System. In Barucci, M. A., Boehnhardt, H., Cruikshank, D. P., Morbidelli, A., and Dotson, R., editors, *The Solar System Beyond Neptune*, page 43.
- Gomes, R., Levison, H. F., Tsiganis, K., and Morbidelli, A. (2005). Origin of the cataclysmic Late Heavy Bombardment period of the terrestrial planets. *Nature*, 435(7041):466–469.
- Greaves, J. S., Holland, W. S., Moriarty-Schieven, G., Jenness, T., Dent, W. R. F., Zuckerman, B., McCarthy, C., Webb, R. A., Butner, H. M., Gear, W. K., and Walker, H. J. (1998). A Dust Ring around ϵ Eridani: Analog to the Young Solar System. *ApJ*, 506(2):L133–L137.
- Greaves, J. S. and Wyatt, M. C. (2010). Debris discs and comet populations around Sun-like stars: the Solar system in context. *MNRAS*, 404(4):1944–1951.
- Green, S. F., McDonnell, J. A. M., McBride, N., Colwell, M. T. S. H., Tuzzolino, A. J., Economou, T. E., Tsou, P., Clark, B. C., and Brownlee, D. E. (2004). The dust mass distribution of comet 81P/Wild 2. *Journal of Geophysical Research (Planets)*, 109(E12):E12S04.
- Grigorieva, A., Artymowicz, P., and Thébault, P. (2007a). Collisional dust avalanches in debris discs. *A&A*, 461(2):537–549.
- Grigorieva, A., Thébault, P., Artymowicz, P., and Brandeker, A. (2007b). Survival of icy grains in debris discs. The role of photosputtering. *A&A*, 475(2):755–764.
- Grün, E., Krüger, H., and Srama, R. (2019). The Dawn of Dust Astronomy. *Space Sci. Rev.*, 215(7):46.
- Grun, E., Zook, H. A., Fechtig, H., and Giese, R. H. (1985). Collisional balance of the meteoritic complex. *Icarus*, 62(2):244–272.
- Gustafson, B. A. S. (1994). Physics of Zodiacal Dust. *Annual Review of Earth and Planetary Sciences*, 22:553–595.
- Güttler, C., Blum, J., Zsom, A., Ormel, C. W., and Dullemond, C. P. (2010). The outcome of protoplanetary dust growth: pebbles, boulders, or planetesimals?. I. Mapping the zoo of laboratory collision experiments. *A&A*, 513:A56.
- Hahn, J. M., Zook, H. A., Cooper, B., and Sunkara, B. (2002). Clementine Observations of the Zodiacal Light and the Dust Content of the Inner Solar System. *Icarus*, 158(2):360–378.
- Hanner, M. S., Sparrow, J. G., Weinberg, J. L., and Beeson, D. E. (1976). in *Elsaesser H., Fechtig H., eds, Proc. IAU Colloq. 31, Interplanetary Dust and Zodiacal Light. Springer, Berlin*, volume 48, page 29.
- Hanner, M. S., Weinberg, J. L., DeShields, L. M., I., Green, B. A., and Toller, G. N. (1974). Zodiacal light and the asteroid belt: The view from Pioneer 10. *J. Geophys. Res.*, 79(25):3671.
- Haug, U. (1958). Über die Häufigkeitsverteilung der Bahnelemente bei den interplanetaren Staubteilchen. Mit 9 Textabbildungen. *Zeitschrift für Astrophysik*, 44:71.

- Hauser, M. G., Gillett, F. C., Low, F. J., Gautier, T. N., Beichman, C. A., Neugebauer, G., Aumann, H. H., Baud, B., Boggess, N., and Emerson, J. P. (1984). IRAS observations of the diffuse infrared background. *ApJ*, 278:L15–L18.
- Helled, R., Bodenheimer, P., Podolak, M., Boley, A., Meru, F., Nayakshin, S., Fortney, J. J., Mayer, L., Alibert, Y., and Boss, A. P. (2014). Giant Planet Formation, Evolution, and Internal Structure. In Beuther, H., Klessen, R. S., Dullemond, C. P., and Henning, T., editors, *Protostars and Planets VI*, page 643.
- Higuchi, A. E., Saigo, K., Kobayashi, H., Iwasaki, K., Momose, M., Soon, K. L., Sakai, N., Kunitomo, M., Ishihara, D., and Yamamoto, S. (2019). First Subarcsecond Submillimeter-wave [C I] Image of 49 Ceti with ALMA. *ApJ*, 883(2):180.
- Hillenbrand, L. A., Carpenter, J. M., Kim, J. S., Meyer, M. R., Backman, D. E., Moro-Martín, A., Hollenbach, D. J., Hines, D. C., Pascucci, I., and Bouwman, J. (2008). The Complete Census of 70 μm -Bright Debris Disks within “The Formation and Evolution of Planetary Systems” Spitzer Legacy Survey of Sun-like Stars. *ApJ*, 677(1):630–656.
- Hinz, P., Bailey, V. P., Defrère, D., Downey, E., Esposito, S., Hill, J., Hoffmann, W. F., Leisenring, J., Montoya, M., and McMahon, T. (2014). Commissioning the LBTI for use as a nulling interferometer and coherent imager. In *Optical and Infrared Interferometry IV*, volume 9146 of *Society of Photo-Optical Instrumentation Engineers (SPIE) Conference Series*, page 91460T.
- Hinz, P. M., Angel, J. R. P., Hoffmann, W. F., McCarthy, D. W., McGuire, P. C., Cheselka, M., Hora, J. L., and Woolf, N. J. (1998). Imaging circumstellar environments with a nulling interferometer. *Nature*, 395(6699):251–253.
- Hinz, P. M., Angel, J. R. P., Woolf, N. J., Hoffmann, W. F., and McCarthy, D. W. (2000). BLINC: a testbed for nulling interferometry in the thermal infrared. In Léna, P. and Quirrenbach, A., editors, *Interferometry in Optical Astronomy*, volume 4006 of *Society of Photo-Optical Instrumentation Engineers (SPIE) Conference Series*, pages 349–353.
- Hinz, P. M., Defrère, D., Skemer, A., Bailey, V., Stone, J., Spalding, E., Vaz, A., Pinna, E., Puglisi, A., Esposito, S., Montoya, M., Downey, E., Leisenring, J., Durney, O., Hoffmann, W., Hill, J., Millan-Gabet, R., Mennesson, B., Danchi, W., Morzinski, K., Grenz, P., Skrutskie, M., and Ertel, S. (2016). Overview of LBTI: a multipurpose facility for high spatial resolution observations. In Malbet, F., Creech-Eakman, M. J., and Tuthill, P. G., editors, *Optical and Infrared Interferometry and Imaging V*, volume 9907 of *Proc. SPIE Conf. Ser.*, page 990704.
- Holland, W. S., Matthews, B. C., Kennedy, G. M., Greaves, J. S., Wyatt, M. C., Booth, M., Bastien, P., Bryden, G., Butner, H., Chen, C. H., Chrysostomou, A., Davies, C. L., Dent, W. R. F., Di Francesco, J., Duchêne, G., Gibb, A. G., Friberg, P., Ivison, R. J., Jenness, T., Kavelaars, J., Lawler, S., Lestrade, J.-F., Marshall, J. P., Moro-Martín, A., Panić, O., Phillips, N., Serjeant, S., Schieven, G. H., Sibthorpe, B., Vican, L., Ward-Thompson, D., van der Werf, P., White, G. J., Wilner, D., and Zuckerman, B. (2017). SONS: The JCMT legacy survey of debris discs in the submillimetre. *MNRAS*, 470(3):3606–3663.
- Holsapple, K. A. (1994). Catastrophic disruptions and cratering of solar system bodies: a review and new results. *Planet. Space Sci.*, 42(12):1067–1078.

- Hörz, F., Bastien, R., Borg, J., Bradley, J. P., Bridges, J. C., Brownlee, D. E., Burchell, M. J., Chi, M., Cintala, M. J., Dai, Z. R., Djouadi, Z., Dominguez, G., Economou, T. E., Fairey, S. A. J., Floss, C., Franchi, I. A., Graham, G. A., Green, S. F., Heck, P., Hoppe, P., Huth, J., Ishii, H., Kearsley, A. T., Kissel, J., Leitner, J., Leroux, H., Marhas, K., Messenger, K., Schwandt, C. S., See, T. H., Snead, C., Stadermann, F. J., Stephan, T., Stroud, R., Teslich, N., Trigo-Rodríguez, J. M., Tuzzolino, A. J., Troadec, D., Tsou, P., Warren, J., Westphal, A., Wozniakiewicz, P., Wright, I., and Zinner, E. (2006). Impact Features on Stardust: Implications for Comet 81P/Wild 2 Dust. *Science*, 314(5806):1716.
- Housen, K. R. and Holsapple, K. A. (1990). On the fragmentation of asteroids and planetary satellites. *Icarus*, 84(1):226–253.
- Housen, K. R. and Holsapple, K. A. (1999). Scale Effects in Strength-Dominated Collisions of Rocky Asteroids. *Icarus*, 142(1):21–33.
- Hughes, A. M., Duchêne, G., and Matthews, B. C. (2018). Debris Disks: Structure, Composition, and Variability. *ARA&A*, 56:541–591.
- Hui, M.-T., Farnocchia, D., and Micheli, M. (2019). C/2010 U3 (Boattini): A Bizarre Comet Active at Record Heliocentric Distance. *AJ*, 157(4):162.
- Hui, M.-T., Jewitt, D., and Clark, D. (2018). Pre-discovery Observations and Orbit of Comet C/2017 K2 (PANSTARRS). *AJ*, 155(1):25.
- Ishihara, D., Onaka, T., Kataza, H., Salama, A., Alfageme, C., Cassatella, A., Cox, N., García-Lario, P., Stephenson, C., Cohen, M., Fujishiro, N., Fujiwara, H., Hasegawa, S., Ita, Y., Kim, W., Matsuhara, H., Murakami, H., Müller, T. G., Nakagawa, T., Ohyama, Y., Oyabu, S., Pyo, J., Sakon, I., Shibai, H., Takita, S., Tanabé, T., Uemizu, K., Ueno, M., Usui, F., Wada, T., Watarai, H., Yamamura, I., and Yamauchi, C. (2010). The AKARI/IRC mid-infrared all-sky survey. *A&A*, 514:A1.
- Jackson, A. P. and Wyatt, M. C. (2012). Debris from terrestrial planet formation: the Moon-forming collision. *MNRAS*, 425(1):657–679.
- Jenniskens, P. (2008). Mostly Dormant Comets and their Disintegration into Meteoroid Streams: A Review. *Earth Moon and Planets*, 102(1-4):505–520.
- Jewitt, D. (2012). The Active Asteroids. *AJ*, 143(3):66.
- Jewitt, D. (2021). Systematics and Consequences of Comet Nucleus Outgassing Torques. *AJ*, 161(6):261.
- Jewitt, D., Hui, M.-T., Mutchler, M., Weaver, H., Li, J., and Agarwal, J. (2017). A Comet Active Beyond the Crystallization Zone. *ApJ*, 847(2):L19.
- Jewitt, D., Kim, Y., Mutchler, M., Agarwal, J., Li, J., and Weaver, H. (2021). Cometary Activity Begins at Kuiper Belt Distances: Evidence from C/2017 K2. *AJ*, 161(4):188.
- Jewitt, D., Mutchler, M., Weaver, H., Hui, M.-T., Agarwal, J., Ishiguro, M., Kleyna, J., Li, J., Meech, K., Micheli, M., Wainscoat, R., and Weryk, R. (2016). Fragmentation Kinematics in Comet 332P/Ikeya-Murakami. *ApJ*, 829(1):L8.

- Jewitt, D. C. and Luu, J. X. (1995). The Solar System Beyond Neptune. *AJ*, 109:1867.
- Johansen, A. and Lambrechts, M. (2017). Forming Planets via Pebble Accretion. *Annual Review of Earth and Planetary Sciences*, 45(1):359–387.
- Johansen, A., Oishi, J. S., Mac Low, M.-M., Klahr, H., Henning, T., and Youdin, A. (2007). Rapid planetesimal formation in turbulent circumstellar disks. *Nature*, 448(7157):1022–1025.
- Jones, J. and Brown, P. (1993). Sporadic meteor radiant distributions - Orbital survey results. *MNRAS*, 265:524.
- Jones, M. H., Bewsher, D., and Brown, D. S. (2013). Imaging of a Circumsolar Dust Ring Near the Orbit of Venus. *Science*, 342(6161):960–963.
- Jorgensen, J. L., Benn, M., Connerney, J. E. P., Denver, T., Jorgensen, P. S., Andersen, A. C., and Bolton, S. J. (2021). Distribution of Interplanetary Dust Detected by the Juno Spacecraft and Its Contribution to the Zodiacal Light. *Journal of Geophysical Research (Planets)*, 126(3):e06509.
- Jutzi, M., Michel, P., Benz, W., and Richardson, D. C. (2010). Fragment properties at the catastrophic disruption threshold: The effect of the parent body’s internal structure. *Icarus*, 207(1):54–65.
- Kaib, N. A. (2022). Comet Fading Begins Beyond Saturn. *arXiv e-prints*, page arXiv:2202.04126.
- Kalas, P., Graham, J. R., Fitzgerald, M. P., and Clampin, M. (2013). STIS Coronagraphic Imaging of Fomalhaut: Main Belt Structure and the Orbit of Fomalhaut b. *ApJ*, 775(1):56.
- Kelsall, T., Weiland, J. L., Franz, B. A., Reach, W. T., Arendt, R. G., Dwek, E., Freudenreich, H. T., Hauser, M. G., Moseley, S. H., and Odegard, N. P. (1998). The COBE Diffuse Infrared Background Experiment Search for the Cosmic Infrared Background. II. Model of the Interplanetary Dust Cloud. *ApJ*, 508(1):44–73.
- Kennedy, G. M. (2018). Exocomet orbit fitting: accelerating coma absorption during transits of β Pictoris. *MNRAS*, 479(2):1997–2006.
- Kennedy, G. M., Hope, G., Hodgkin, S. T., and Wyatt, M. C. (2019). An automated search for transiting exocomets. *MNRAS*, 482(4):5587–5596.
- Kennedy, G. M. and Piette, A. (2015). Warm exo-Zodi from cool exo-Kuiper belts: the significance of P-R drag and the inference of intervening planets. *MNRAS*, 449(3):2304–2311.
- Kennedy, G. M. and Wyatt, M. C. (2013). The bright end of the exo-Zodi luminosity function: disc evolution and implications for exo-Earth detectability. *MNRAS*, 433(3):2334–2356.
- Kennedy, G. M., Wyatt, M. C., Bailey, V., Bryden, G., Danchi, W. C., Defrère, D., Haniff, C., Hinz, P. M., Lebreton, J., Mennesson, B., Millan-Gabet, R., Morales, F., Panić, O., Rieke, G. H., Roberge, A., Serabyn, E., Shannon, A., Skemer, A. J., Stapelfeldt, K. R., Su, K. Y. L., and Weinberger, A. J. (2015). Exo-zodi Modeling for the Large Binocular Telescope Interferometer. *ApJS*, 216(2):23.

- Kenyon, S. J. and Bromley, B. C. (2004). Collisional Cascades in Planetesimal Disks. II. Embedded Planets. *AJ*, 127(1):513–530.
- Kenyon, S. J. and Bromley, B. C. (2006). Terrestrial Planet Formation. I. The Transition from Oligarchic Growth to Chaotic Growth. *AJ*, 131(3):1837–1850.
- Kenyon, S. J. and Bromley, B. C. (2008). Variations on Debris Disks: Icy Planet Formation at 30-150 AU for 1-3 M_{\odot} Main-Sequence Stars. *ApJS*, 179(2):451–483.
- Kenyon, S. J. and Bromley, B. C. (2010). Variations on Debris Disks. II. Icy Planet Formation as a Function of the Bulk Properties and Initial Sizes of Planetesimals. *ApJS*, 188(1):242–279.
- Kervella, P., Arenou, F., Mignard, F., and Thévenin, F. (2019). Stellar and substellar companions of nearby stars from Gaia DR2. Binarity from proper motion anomaly. *A&A*, 623:A72.
- Kiefer, F., Lecavelier des Etangs, A., Boissier, J., Vidal-Madjar, A., Beust, H., Lagrange, A. M., Hébrard, G., and Ferlet, R. (2014). Two families of exocomets in the β Pictoris system. *Nature*, 514(7523):462–464.
- Kirchschlager, F., Ertel, S., Wolf, S., Matter, A., and Krivov, A. V. (2020). First L band detection of hot exozodiacal dust with VLT/MATISSE. *MNRAS*, 499(1):L47–L52.
- Kirchschlager, F., Wolf, S., Krivov, A. e. V., Mutschke, H., and Brunngräber, R. (2017). Constraints on the structure of hot exozodiacal dust belts. *MNRAS*, 467(2):1614–1626.
- Kóspál, Á., Moór, A., Juhász, A., Ábrahám, P., Apai, D., Csengeri, T., Grady, C. A., Henning, T., Hughes, A. M., Kiss, C., Pascucci, I., and Schmalzl, M. (2013). ALMA Observations of the Molecular Gas in the Debris Disk of the 30 Myr Old Star HD 21997. *ApJ*, 776(2):77.
- Kral, Q., Krivov, A. V., Defrère, D., van Lieshout, R., Bonsor, A., Augereau, J.-C., Thébault, P., Ertel, S., Lebreton, J., and Absil, O. (2017). Exozodiacal clouds: hot and warm dust around main sequence stars. *The Astronomical Review*, 13(2):69–111.
- Kral, Q., Marino, S., Wyatt, M. C., Kama, M., and Matrà, L. (2019). Imaging [CI] around HD 131835: reinterpreting young debris discs with protoplanetary disc levels of CO gas as shielded secondary discs. *MNRAS*, 489(4):3670–3691.
- Kral, Q., Matrà, L., Kennedy, G. M., Marino, S., and Wyatt, M. C. (2020). Survey of planetesimal belts with ALMA: gas detected around the Sun-like star HD 129590. *MNRAS*, 497(3):2811–2830.
- Kral, Q., Thébault, P., Augereau, J. C., Boccaletti, A., and Charnoz, S. (2014). LIDT-DD: A new hybrid model to understand debris discs observations - The case of massive collisions. In Ballet, J., Martins, F., Bournaud, F., Monier, R., and Reylé, C., editors, *SF2A-2014: Proceedings of the Annual meeting of the French Society of Astronomy and Astrophysics*, pages 187–192.
- Kral, Q., Thébault, P., Augereau, J. C., Boccaletti, A., and Charnoz, S. (2015). Signatures of massive collisions in debris discs. A self-consistent numerical model. *A&A*, 573:A39.

- Kral, Q., Thébault, P., and Charnoz, S. (2013). LIDT-DD: A new self-consistent debris disc model that includes radiation pressure and couples dynamical and collisional evolution. *A&A*, 558:A121.
- Kral, Q., Wyatt, M., Carswell, R. F., Pringle, J. E., Matrà, L., and Juhász, A. (2016). A self-consistent model for the evolution of the gas produced in the debris disc of β Pictoris. *MNRAS*, 461(1):845–858.
- Kral, Q., Wyatt, M. C., Triaud, A. H. M. J., Marino, S., Thébault, P., and Shorttle, O. (2018). Cometary impactors on the TRAPPIST-1 planets can destroy all planetary atmospheres and rebuild secondary atmospheres on planets f, g, and h. *MNRAS*, 479(2):2649–2672.
- Krivov, A. V. (2007). Physics of Debris Disks. In Krueger, H. and Graps, A., editors, *Dust in Planetary Systems*, volume 643, pages 123–132.
- Krivov, A. V., Herrmann, F., Brandeker, A., and Thébault, P. (2009). Can gas in young debris disks be constrained by their radial brightness profiles? *A&A*, 507(3):1503–1516.
- Krivov, A. V., Löhne, T., and Sremčević, M. (2006). Dust distributions in debris disks: effects of gravity, radiation pressure and collisions. *A&A*, 455:509–519.
- Krivov, A. V., Müller, S., Löhne, T., and Mutschke, H. (2008). Collisional and Thermal Emission Models of Debris Disks: Toward Planetesimal Population Properties. *ApJ*, 687(1):608–622.
- Krivov, A. V., Sremčević, M., and Spahn, F. (2005). Evolution of a Keplerian disk of colliding and fragmenting particles: a kinetic model with application to the Edgeworth Kuiper belt. *Icarus*, 174(1):105–134.
- Krivov, A. V. and Wyatt, M. C. (2021). Solution to the debris disc mass problem: planetesimals are born small? *MNRAS*, 500(1):718–735.
- Krüger, H., Dikarev, V., Anweiler, B., Dermott, S. F., Graps, A. L., Grün, E., Gustafson, B. A., Hamilton, D. P., Hanner, M. S., Horányi, M., Kissel, J., Linkert, D., Linkert, G., Mann, I., McDonnell, J. A. M., Morfill, G. E., Polanskey, C., Schwehm, G., and Srama, R. (2010). Three years of Ulysses dust data: 2005 to 2007. *Planet. Space Sci.*, 58(7-8):951–964.
- Kuchynka, P. and Folkner, W. M. (2013). A new approach to determining asteroid masses from planetary range measurements. *Icarus*, 222(1):243–253.
- Lagrange, A. M., Backman, D. E., and Artymowicz, P. (2000). Planetary Material around Main-Sequence Stars. In Mannings, V., Boss, A. P., and Russell, S. S., editors, *Protostars and Planets IV*, page 639.
- Lagrange, A. M., Bonnefoy, M., Chauvin, G., Apai, D., Ehrenreich, D., Boccaletti, A., Gratadour, D., Rouan, D., Mouillet, D., Lacour, S., and Kasper, M. (2010). A Giant Planet Imaged in the Disk of the Young Star β Pictoris. *Science*, 329(5987):57.
- Lambrechts, M. and Johansen, A. (2012). Rapid growth of gas-giant cores by pebble accretion. *A&A*, 544:A32.

- Lamy, P. L., Toth, I., Fernandez, Y. R., and Weaver, H. A. (2004). *in Festou M.C., Keller H.U., Weaver H.A., eds, Comets II. University of Arizona Press, Tucson*, page 223.
- Landgraf, M., Baggaley, W. J., Grün, E., Krüger, H., and Linkert, G. (2000). Aspects of the mass distribution of interstellar dust grains in the solar system from in situ measurements. *J. Geophys. Res.*, 105(A5):10343–10352.
- Laor, A. and Draine, B. T. (1993). Spectroscopic Constraints on the Properties of Dust in Active Galactic Nuclei. *ApJ*, 402:441.
- Lasue, J., Lévassieur-Regourd, A.-C., and Renard, J.-B. (2020). Zodiacal light observations and its link with cosmic dust: A review. *Planet. Space Sci.*, 190:104973.
- Laureijs, R. J., Jourdain de Muizon, M., Leech, K., Siebenmorgen, R., Dominik, C., Habing, H. J., Trams, N., and Kessler, M. F. (2002). A 25 micron search for Vega-like disks around main-sequence stars with ISO. *A&A*, 387:285–293.
- Lawler, S. M., Beichman, C. A., Bryden, G., Ciardi, D. R., Tanner, A. M., Su, K. Y. L., Stapelfeldt, K. R., Lisse, C. M., and Harker, D. E. (2009). Explorations Beyond the Snow Line: Spitzer/IRS Spectra of Debris Disks Around Solar-type Stars. *ApJ*, 705(1):89–111.
- Lebreton, J., Beichman, C., Bryden, G., Defrère, D., Mennesson, B., Millan-Gabet, R., and Boccaletti, A. (2016). Models of the η Corvi Debris Disk from the Keck Interferometer, Spitzer, and Herschel. *ApJ*, 817(2):165.
- Lebreton, J., van Lieshout, R., Augereau, J. C., Absil, O., Mennesson, B., Kama, M., Dominik, C., Bonsor, A., Vandeportal, J., Beust, H., Defrère, D., Ertel, S., Faramaz, V., Hinz, P., Kral, Q., Lagrange, A. M., Liu, W., and Thébault, P. (2013). An interferometric study of the Fomalhaut inner debris disk. III. Detailed models of the exozodiacal disk and its origin. *A&A*, 555:A146.
- Lecavelier Des Etangs, A. (1999). A library of stellar light variations due to extra-solar comets. *A&AS*, 140:15–20.
- Lecavelier des Etangs, A., Scholl, H., Roques, F., Sicardy, B., and Vidal-Madjar, A. (1996). Perturbations of a Planet on the β Pictoris Circumstellar Dust Disk. 3. Time Scale of Collisional Destruction versus Resonance Time Scale. *Icarus*, 123(1):168–179.
- Lee, E. J. and Chiang, E. (2016). A Primer on Unifying Debris Disk Morphologies. *ApJ*, 827(2):125.
- Leinert, C. and Moster, B. (2007). Evidence for dust accumulation just outside the orbit of Venus. *A&A*, 472(1):335–340.
- Leinert, C., Richter, I., Pitz, E., and Planck, B. (1981). The zodiacal light from 1.0 to 0.3 A.U. as observed by the HELIOS space probes. *A&A*, 103(1):177–188.
- Leinert, C., Roser, S., and Buitrago, J. (1983). How to maintain the spatial distribution of interplanetary dust. *A&A*, 118(2):345–357.
- Levison, H. F. (1996). Comet Taxonomy. In Rettig, T. and Hahn, J. M., editors, *Completing the Inventory of the Solar System*, volume 107 of *Astronomical Society of the Pacific Conference Series*, pages 173–191.

- Levison, H. F., Dones, L., and Duncan, M. J. (2001). The Origin of Halley-Type Comets: Probing the Inner Oort Cloud. *AJ*, 121(4):2253–2267.
- Levison, H. F. and Duncan, M. J. (1997). From the Kuiper Belt to Jupiter-Family Comets: The Spatial Distribution of Ecliptic Comets. *Icarus*, 127(1):13–32.
- Levison, H. F., Duncan, M. J., Dones, L., and Gladman, B. J. (2006). The scattered disk as a source of Halley-type comets. *Icarus*, 184(2):619–633.
- Li, A. and Greenberg, J. M. (1997). A unified model of interstellar dust. *A&A*, 323:566–584.
- Li, A. and Greenberg, J. M. (1998). A comet dust model for the beta Pictoris disk. *A&A*, 331:291–313.
- Li, R. and Youdin, A. N. (2021). Thresholds for Particle Clumping by the Streaming Instability. *ApJ*, 919(2):107.
- Lieman-Sifry, J., Hughes, A. M., Carpenter, J. M., Gorti, U., Hales, A., and Flaherty, K. M. (2016). Debris Disks in the Scorpius-Centaurus OB Association Resolved by ALMA. *ApJ*, 828(1):25.
- Liou, J. C., Dermott, S. F., and Xu, Y. L. (1995). The contribution of cometary dust to the zodiacal cloud. *Planet. Space Sci.*, 43(6):717–722.
- Lissauer, J. J., Hubickyj, O., D’Angelo, G., and Bodenheimer, P. (2009). Models of Jupiter’s growth incorporating thermal and hydrodynamic constraints. *Icarus*, 199(2):338–350.
- Lisse, C. M., Wyatt, M. C., Chen, C. H., Morlok, A., Watson, D. M., Manoj, P., Sheehan, P., Currie, T. M., Thebault, P., and Sitko, M. L. (2012). Spitzer Evidence for a Late-heavy Bombardment and the Formation of Ureilites in η Corvi at ~ 1 Gyr. *ApJ*, 747(2):93.
- Löhne, T., Augereau, J. C., Ertel, S., Marshall, J. P., Eiroa, C., Mora, A., Absil, O., Stapelfeldt, K., Thébault, P., Bayo, A., Del Burgo, C., Danchi, W., Krivov, A. V., Lebreton, J., Letawe, G., Magain, P., Maldonado, J., Montesinos, B., Pilbratt, G. L., White, G. J., and Wolf, S. (2012). Modelling the huge, Herschel-resolved debris ring around HD 207129. *A&A*, 537:A110.
- Löhne, T., Krivov, A. V., Kirchschrager, F., Sende, J. A., and Wolf, S. (2017). Collisions and drag in debris discs with eccentric parent belts. *A&A*, 605:A7.
- Löhne, T., Krivov, A. V., and Rodmann, J. (2008). Long-Term Collisional Evolution of Debris Disks. *ApJ*, 673(2):1123–1137.
- Love, S. G. and Brownlee, D. E. (1993). A Direct Measurement of the Terrestrial Mass Accretion Rate of Cosmic Dust. *Science*, 262(5133):550–553.
- MacGregor, M. A., Lawler, S. M., Wilner, D. J., Matthews, B. C., Kennedy, G. M., Booth, M., and Di Francesco, J. (2016). ALMA Observations of the Debris Disk of Solar Analog τ Ceti. *ApJ*, 828(2):113.
- MacGregor, M. A., Matrà, L., Kalas, P., Wilner, D. J., Pan, M., Kennedy, G. M., Wyatt, M. C., Duchene, G., Hughes, A. M., and Rieke, G. H. (2017). A Complete ALMA Map of the Fomalhaut Debris Disk. *ApJ*, 842(1):8.

- Mäkinen, J. T. T., Bertaux, J.-L., Combi, M. R., and Quémerais, E. (2001). Water Production of Comet C/1999 S4 (LINEAR) Observed with the SWAN Instrument. *Science*, 292(5520):1326–1329.
- Mannings, V. and Barlow, M. J. (1998). Candidate Main-Sequence Stars with Debris Disks: A New Sample of Vega-like Sources. *ApJ*, 497(1):330–341.
- Marboeuf, U., Bonsor, A., and Augereau, J. C. (2016). Extrasolar comets: The origin of dust in exozodiacal disks? *Planet. Space Sci.*, 133:47–62.
- Marino, S., Bonsor, A., Wyatt, M. C., and Kral, Q. (2018). Scattering of exocomets by a planet chain: exozodi levels and the delivery of cometary material to inner planets. *MNRAS*, 479(2):1651–1671.
- Marino, S., Matrà, L., Stark, C., Wyatt, M. C., Casassus, S., Kennedy, G., Rodriguez, D., Zuckerman, B., Perez, S., Dent, W. R. F., Kuchner, M., Hughes, A. M., Schneider, G., Steele, A., Roberge, A., Donaldson, J., and Nesvold, E. (2016). Exocometary gas in the HD 181327 debris ring. *MNRAS*, 460(3):2933–2944.
- Marino, S., Wyatt, M. C., Panić, O., Matrà, L., Kennedy, G. M., Bonsor, A., Kral, Q., Dent, W. R. F., Duchene, G., and Wilner, D. (2017). ALMA observations of the η Corvi debris disc: inward scattering of CO-rich exocomets by a chain of 3–30 M_{\oplus} planets? *MNRAS*, 465(3):2595–2615.
- Marois, C., Macintosh, B., Barman, T., Zuckerman, B., Song, I., Patience, J., Lafrenière, D., and Doyon, R. (2008). Direct Imaging of Multiple Planets Orbiting the Star HR 8799. *Science*, 322(5906):1348.
- Marois, C., Zuckerman, B., Konopacky, Q. M., Macintosh, B., and Barman, T. (2010). Images of a fourth planet orbiting HR 8799. *Nature*, 468(7327):1080–1083.
- Marshall, J. P., Krivov, A. V., del Burgo, C., Eiroa, C., Mora, A., Montesinos, B., Ertel, S., Bryden, G., Liseau, R., Augereau, J. C., Bayo, A., Danchi, W., Löhne, T., Maldonado, J., Pilbratt, G. L., Stapelfeldt, K., Thebault, P., White, G. J., and Wolf, S. (2013). Herschel observations of the debris disc around HIP 92043. *A&A*, 557:A58.
- Matrà, L., MacGregor, M. A., Kalas, P., Wyatt, M. C., Kennedy, G. M., Wilner, D. J., Duchene, G., Hughes, A. M., Pan, M., and Shannon, A. (2017). Detection of Exocometary CO within the 440 Myr Old Fomalhaut Belt: A Similar CO+CO₂ Ice Abundance in Exocomets and Solar System Comets. *ApJ*, 842(1):9.
- Matthews, B. C., Krivov, A. V., Wyatt, M. C., Bryden, G., and Eiroa, C. (2014). Observations, Modeling, and Theory of Debris Disks. In Beuther, H., Klessen, R. S., Dullemond, C. P., and Henning, T., editors, *Protostars and Planets VI*, page 521.
- Matthews, B. C., Sibthorpe, B., Kennedy, G., Phillips, N., Churcher, L., Duchêne, G., Greaves, J. S., Lestrade, J. F., Moro-Martin, A., Wyatt, M. C., Bastien, P., Biggs, A., Bouvier, J., Butner, H. M., Dent, W. R. F., di Francesco, J., Eisloffel, J., Graham, J., Harvey, P., Hauschildt, P., Holland, W. S., Horner, J., Ibar, E., Ivison, R. J., Johnstone, D., Kalas, P., Kavelaars, J., Rodriguez, D., Udry, S., van der Werf, P., Wilner, D., and Zuckerman, B. (2010). Resolving debris discs in the far-infrared: Early highlights from the DEBRIS survey. *A&A*, 518:L135.

- Mayor, M., Marmier, M., Lovis, C., Udry, S., Ségransan, D., Pepe, F., Benz, W., Bertaux, J. L., Bouchy, F., Dumusque, X., Lo Curto, G., Mordasini, C., Queloz, D., and Santos, N. C. (2011). The HARPS search for southern extra-solar planets XXXIV. Occurrence, mass distribution and orbital properties of super-Earths and Neptune-mass planets. *arXiv e-prints*, page arXiv:1109.2497.
- Mayor, M. and Queloz, D. (1995). A Jupiter-mass companion to a solar-type star. *Nature*, 378(6555):355–359.
- McDonnell, J. A. M., McBride, N., Beard, R., Bussoletti, E., Colangeli, L., Eberhardt, P., Firth, J. G., Grard, R., Green, S. F., and Greenberg, J. M. (1993). Dust particle impacts during the Giotto encounter with comet Grigg-Skjellerup. *Nature*, 362(6422):732–734.
- McNamara, H., Jones, J., Kauffman, B., Suggs, R., Cooke, W., and Smith, S. (2004). Meteoroid Engineering Model (MEM): A Meteoroid Model For The Inner Solar System. *Earth Moon and Planets*, 95(1-4):123–139.
- Meech, K. J., Hainaut, O. R., and Marsden, B. G. (2004). Comet nucleus size distributions from HST and Keck telescopes. *Icarus*, 170(2):463–491.
- Meech, K. J., Kleyna, J. T., Hainaut, O., Micheli, M., Bauer, J., Denneau, L., Keane, J. V., Stephens, H., Jedicke, R., Wainscoat, R., Weryk, R., Flewelling, H., Schunová-Lilly, E., Magnier, E., and Chambers, K. C. (2017). CO-driven Activity in Comet C/2017 K2 (PANSTARRS). *ApJ*, 849(1):L8.
- Mennesson, B., Millan-Gabet, R., Serabyn, E., Colavita, M. M., Absil, O., Bryden, G., Wyatt, M., Danchi, W., Defrère, D., Doré, O., Hinz, P., Kuchner, M., Ragland, S., Scott, N., Stapelfeldt, K., Traub, W., and Woillez, J. (2014). Constraining the Exozodiacal Luminosity Function of Main-sequence Stars: Complete Results from the Keck Nuller Mid-infrared Surveys. *ApJ*, 797(2):119.
- Meunier, N. and Lagrange, A. M. (2022). A new estimation of astrometric exoplanet detection limits in the habitable zone around nearby stars. *A&A*, 659:A104.
- Meyer, M. R., Hillenbrand, L. A., Backman, D., Beckwith, S., Bouwman, J., Brooke, T., Carpenter, J., Cohen, M., Cortes, S., Crockett, N., Gorti, U., Henning, T., Hines, D., Hollenbach, D., Kim, J. S., Lunine, J., Malhotra, R., Mamajek, E., Metchev, S., Moro-Martin, A., Morris, P., Najita, J., Padgett, D., Pascucci, I., Rodmann, J., Schlingman, W., Silverstone, M., Soderblom, D., Stauffer, J., Stobie, E., Strom, S., Watson, D., Weidenschilling, S., Wolf, S., and Young, E. (2006). The Formation and Evolution of Planetary Systems: Placing Our Solar System in Context with Spitzer. *PASP*, 118(850):1690–1710.
- Millan-Gabet, R., Serabyn, E., Mennesson, B., Traub, W. A., Barry, R. K., Danchi, W. C., Kuchner, M., Stark, C. C., Ragland, S., Hrynevych, M., Woillez, J., Stapelfeldt, K., Bryden, G., Colavita, M. M., and Booth, A. J. (2011). Exozodiacal Dust Levels for Nearby Main-sequence Stars: A Survey with the Keck Interferometer Nuller. *ApJ*, 734(1):67.
- Minato, T., Köhler, M., Kimura, H., Mann, I., and Yamamoto, T. (2006). Momentum transfer to fluffy dust aggregates from stellar winds. *A&A*, 452(2):701–707.
- Moerchen, M. M., Telesco, C. M., Packham, C., and Kehoe, T. J. J. (2007). Mid-Infrared Resolution of a 3 AU Radius Debris Disk around ζ Leporis. *ApJ*, 655(2):L109–L112.

- Moór, A., Curé, M., Kóspál, Á., Ábrahám, P., Csengeri, T., Eiroa, C., Gunawan, D., Henning, T., Hughes, A. M., Juhász, A., Pawellek, N., and Wyatt, M. (2017). Molecular Gas in Debris Disks around Young A-type Stars. *ApJ*, 849(2):123.
- Moorhead, A. V., Kingery, A., and Ehlert, S. (2020). NASA's Meteoroid Engineering Model 3 and its ability to replicate spacecraft impact rates. *Journal of Spacecraft and Rockets*, 57:160–176.
- Morbidelli, A. and Nesvorný, D. (2020). Kuiper belt: formation and evolution. In Prialnik, D., Barucci, M. A., and Young, L., editors, *The Trans-Neptunian Solar System*, pages 25–59.
- Morbidelli, A., Nesvorný, D., Bottke, W. F., and Marchi, S. (2021). A re-assessment of the Kuiper belt size distribution for sub-kilometer objects, revealing collisional equilibrium at small sizes. *Icarus*, 356:114256.
- Moreno, F., Snodgrass, C., Hainaut, O., Tubiana, C., Sierks, H., Barbieri, C., Lamy, P. L., Rodrigo, R., Koschny, D., Rickman, H., Keller, H. U., Agarwal, J., A'Hearn, M. F., Barucci, M. A., Bertaux, J. L., Bertini, I., Besse, S., Bodewits, D., Cremonese, G., Da Deppo, V., Davidsson, B., Debei, S., De Cecco, M., Ferri, F., Fornasier, S., Fulle, M., Groussin, O., Gutiérrez, P. J., Gutiérrez-Marques, P., Güttler, C., Hviid, S. F., Ip, W. H., Jorda, L., Knollenberg, J., Kovacs, G., Kramm, J. R., Kührt, E., Küppers, M., Lara, L. M., Lazzarin, M., López-Moreno, J. J., Marzari, F., Mottola, S., Naletto, G., Oklay, N., Pajola, M., Thomas, N., Vincent, J. B., Della Corte, V., Fitzsimmons, A., Faggi, S., Jehin, E., Opitom, C., and Tozzi, G. P. (2016). The dust environment of comet 67P/Churyumov-Gerasimenko from Rosetta OSIRIS and VLT observations in the 4.5 to 2.9 AU heliocentric distance range inbound. *A&A*, 587:A155.
- Moro-Martín, A. and Malhotra, R. (2003). Dynamical Models of Kuiper Belt Dust in the Inner and Outer Solar System. *AJ*, 125(4):2255–2265.
- Murray, C. D. and Dermott, S. F. (1999). *Solar system dynamics*.
- Mustill, A. J. and Wyatt, M. C. (2009). Debris disc stirring by secular perturbations from giant planets. *MNRAS*, 399(3):1403–1414.
- Mustill, A. J. and Wyatt, M. C. (2011). A general model of resonance capture in planetary systems: first- and second-order resonances. *MNRAS*, 413(1):554–572.
- Napier, W. M. (2001). Temporal variation of the zodiacal dust cloud. *MNRAS*, 321(3):463–470.
- Napier, W. M. (2019). The hazard from fragmenting comets. *MNRAS*, 488(2):1822–1827.
- Nesvold, E. and Kuchner, M. J. (2015). Modeling Collisions in Circumstellar Debris Disks with SMACK. In *American Astronomical Society Meeting Abstracts #225*, volume 225 of *American Astronomical Society Meeting Abstracts*, page 330.06.
- Nesvold, E. R., Kuchner, M. J., Rein, H., and Pan, M. (2013). SMACK: A New Algorithm for Modeling Collisions and Dynamics of Planetesimals in Debris Disks. *ApJ*, 777(2):144.

- Nesvold, E. R., Naoz, S., and Fitzgerald, M. P. (2017). HD 106906: A Case Study for External Perturbations of a Debris Disk. *ApJ*, 837(1):L6.
- Nesvorný, D., Bottke, W. F., Levison, H. F., and Dones, L. (2003). Recent Origin of the Solar System Dust Bands. *ApJ*, 591(1):486–497.
- Nesvorný, D., Bottke, W. F., Vokrouhlický, D., Sykes, M., Lien, D. J., and Stansberry, J. (2008). Origin of the Near-Ecliptic Circumsolar Dust Band. *ApJ*, 679(2):L143.
- Nesvorný, D., Janches, D., Vokrouhlický, D., Pokorný, P., Bottke, W. F., and Jenniskens, P. (2011). Dynamical Model for the Zodiacal Cloud and Sporadic Meteors. *ApJ*, 743(2):129.
- Nesvorný, D., Jenniskens, P., Levison, H. F., Bottke, W. F., Vokrouhlický, D., and Gounelle, M. (2010). Cometary Origin of the Zodiacal Cloud and Carbonaceous Micrometeorites. Implications for Hot Debris Disks. *ApJ*, 713(2):816–836.
- Nesvorný, D., Sykes, M., Lien, D. J., Stansberry, J., Reach, W. T., Vokrouhlický, D., Bottke, W. F., Durda, D. D., Jayaraman, S., and Walker, R. G. (2006). Candidates for Asteroid Dust Trails. *AJ*, 132(2):582–595.
- Nesvorný, D. and Vokrouhlický, D. (2016). Neptune’s Orbital Migration Was Grainy, Not Smooth. *ApJ*, 825(2):94.
- Nesvorný, D., Vokrouhlický, D., Dones, L., Levison, H. F., Kaib, N., and Morbidelli, A. (2017). Origin and Evolution of Short-period Comets. *ApJ*, 845(1):27.
- Núñez, P. D., Scott, N. J., Mennesson, B., Absil, O., Augereau, J. C., Bryden, G., ten Brummelaar, T., Ertel, S., Coudé du Foresto, V., Ridgway, S. T., Sturmman, J., Sturmman, L., Turner, N. J., and Turner, N. H. (2017). A near-infrared interferometric survey of debris-disc stars. VI. Extending the exozodiacal light survey with CHARA/JouFLU. *A&A*, 608:A113.
- O’Brien, D. P., Walsh, K. J., Morbidelli, A., Raymond, S. N., and Mandell, A. M. (2014). Water delivery and giant impacts in the ‘Grand Tack’ scenario. *Icarus*, 239:74–84.
- Olofsson, J., Thébault, P., Kral, Q., Bayo, A., Boccaletti, A., Godoy, N., Henning, T., van Holstein, R. G., Maucó, K., Milli, J., Montesinos, M., Rein, H., and Sefilian, A. A. (2022). The vertical structure of debris disks and the impact of gas. *arXiv e-prints*, page arXiv:2202.08313.
- Oort, J. H. (1950). The structure of the cloud of comets surrounding the Solar System and a hypothesis concerning its origin. *Bull. Astron. Inst. Netherlands*, 11:91–110.
- Ormel, C. W. (2017). The Emerging Paradigm of Pebble Accretion. In Pessah, M. and Gressel, O., editors, *Formation, Evolution, and Dynamics of Young Solar Systems*, volume 445 of *Astrophysics and Space Science Library*, page 197.
- Ormel, C. W., Dullemond, C. P., and Spaans, M. (2010). A New Condition for the Transition from Runaway to Oligarchic Growth. *ApJ*, 714(1):L103–L107.
- Pavlenko, Y., Kulyk, I., Shubina, O., Vasylenko, M., Dobrycheva, D., and Korsun, P. (2022). New exocomets of β Pic. *arXiv e-prints*, page arXiv:2202.13373.

- Pawellek, N. and Krivov, A. V. (2015). The dust grain size-stellar luminosity trend in debris discs. *MNRAS*, 454(3):3207–3221.
- Pawellek, N., Krivov, A. V., Marshall, J. P., Montesinos, B., Ábrahám, P., Moór, A., Bryden, G., and Eiroa, C. (2014). Disk Radii and Grain Sizes in Herschel-resolved Debris Disks. *ApJ*, 792(1):65.
- Pearce, T. D., Krivov, A. V., and Booth, M. (2020). Gas trapping of hot dust around main-sequence stars. *MNRAS*, 498(2):2798–2813.
- Pearce, T. D., Launhardt, R., Ostermann, R., Kennedy, G. M., Gennaro, M., Booth, M., Krivov, A. V., Cugno, G., Henning, T. K., Quirrenbach, A., Musso Barucci, A., Matthews, E. C., Ruh, H. L., and Stone, J. M. (2022). Planet populations inferred from debris discs: insights from 178 debris systems in the ISPY, LEECH and LStEN planet-hunting surveys. *arXiv e-prints*, page arXiv:2201.08369.
- Pearce, T. D. and Wyatt, M. C. (2014). Dynamical evolution of an eccentric planet and a less massive debris disc. *MNRAS*, 443(3):2541–2560.
- Pepe, F., Lovis, C., Ségransan, D., Benz, W., Bouchy, F., Dumusque, X., Mayor, M., Queloz, D., Santos, N. C., and Udry, S. (2011). The HARPS search for Earth-like planets in the habitable zone. I. Very low-mass planets around <ASTROBJ>HD 20794</ASTROBJ>, <ASTROBJ>HD 85512</ASTROBJ>, and <ASTROBJ>HD 192310</ASTROBJ>. *A&A*, 534:A58.
- Pitjeva, E. V. and Pitjev, N. P. (2018). Masses of the Main Asteroid Belt and the Kuiper Belt from the Motions of Planets and Spacecraft. *Astronomy Letters*, 44(8-9):554–566.
- Plavchan, P., Jura, M., and Lipsky, S. J. (2005). Where Are the M Dwarf Disks Older Than 10 Million Years? *ApJ*, 631(2):1161–1169.
- Pokorný, P., Vokrouhlický, D., Nesvorný, D., Campbell-Brown, M., and Brown, P. (2014). Dynamical Model for the Toroidal Sporadic Meteors. *ApJ*, 789(1):25.
- Poppe, A. R. (2016). An improved model for interplanetary dust fluxes in the outer Solar System. *Icarus*, 264:369–386.
- Poppe, A. R., Lisse, C. M., Piquette, M., Zemcov, M., Horányi, M., James, D., Szalay, J. R., Bernardoni, E., and Stern, S. A. (2019). Constraining the Solar System’s Debris Disk with In Situ New Horizons Measurements from the Edgeworth-Kuiper Belt. *ApJ*, 881(1):L12.
- Prialnik, D. and Bar-Nun, A. (1990). Gas Release in Comet Nuclei. *ApJ*, 363:274.
- Quanz, S. P., Absil, O., Benz, W., Bonfils, X., Berger, J.-P., Defrère, D., van Dishoeck, E., Ehrenreich, D., Fortney, J., Glauser, A., Grenfell, J. L., Janson, M., Kraus, S., Krause, O., Labadie, L., Lacour, S., Line, M., Linz, H., Loicq, J., Miguel, Y., Pallé, E., Queloz, D., Rauer, H., Ribas, I., Rugheimer, S., Selsis, F., Snellen, I., Sozzetti, A., Stapelfeldt, K. R., Udry, S., and Wyatt, M. (2021a). Atmospheric characterization of terrestrial exoplanets in the mid-infrared: biosignatures, habitability, and diversity. *Experimental Astronomy*.

- Quanz, S. P., Ottiger, M., Fontanet, E., Kammerer, J., Menti, F., Dannert, F., Gheorghe, A., Absil, O., Airapetian, V. S., Alei, E., Allart, R., Angerhausen, D., Blumenthal, S., Buchhave, L. A., Cabrera, J., Carrión-González, Ó., Chauvin, G., Danchi, W. C., Dandumont, C., Defrère, D., Dorn, C., Ehrenreich, D., Ertel, S., Fridlund, M., García Muñoz, A., Gascón, C., Girard, J. H., Glauser, A., Grenfell, J. L., Guidi, G., Hagelberg, J., Helled, R., Ireland, M. J., Kopparapu, R. K., Korth, J., Kozakis, T., Kraus, S., Léger, A., Leedjårv, L., Lichtenberg, T., Lillo-Box, J., Linz, H., Liseau, R., Loicq, J., Mahendra, V., Malbet, F., Mathew, J., Mennesson, B., Meyer, M. R., Mishra, L., Molaverdikhani, K., Noack, L., Oza, A. V., Pallé, E., Parviainen, H., Quirrenbach, A., Rauer, H., Ribas, I., Rice, M., Romagnolo, A., Rugheimer, S., Schwieterman, E. W., Serabyn, E., Sharma, S., Stassun, K. G., Szulágyi, J., Wang, H. S., Wunderlich, F., Wyatt, M. C., and the LIFE collaboration (2021b). Large Interferometer For Exoplanets (LIFE): I. Improved exoplanet detection yield estimates for a large mid-infrared space-interferometer mission. *arXiv e-prints*, page arXiv:2101.07500.
- Rappaport, S., Vanderburg, A., Jacobs, T., LaCourse, D., Jenkins, J., Kraus, A., Rizzuto, A., Latham, D. W., Bieryla, A., Lazarevic, M., and Schmitt, A. (2018). Likely transiting exocomets detected by Kepler. *MNRAS*, 474(2):1453–1468.
- Raymond, S. N. and Nesvorny, D. (2020). Origin and dynamical evolution of the asteroid belt. *arXiv e-prints*, page arXiv:2012.07932.
- Raymond, S. N., O’Brien, D. P., Morbidelli, A., and Kaib, N. A. (2009). Building the terrestrial planets: Constrained accretion in the inner Solar System. *Icarus*, 203(2):644–662.
- Reach, W. T. (2010). Structure of the Earth’s circumsolar dust ring. *Icarus*, 209(2):848–850.
- Reach, W. T., Franz, B. A., Weiland, J. L., Hauser, M. G., Kelsall, T. N., Wright, E. L., Rawley, G., Stemwedel, S. W., and Spiesman, W. J. (1995). Observational confirmation of a circumsolar dust ring by the COBE satellite. *Nature*, 374(6522):521–523.
- Reach, W. T., Kelley, M. S., and Sykes, M. V. (2007). A survey of debris trails from short-period comets. *Icarus*, 191(1):298–322.
- Rebollido, I., Eiroa, C., Montesinos, B., Maldonado, J., Villaver, E., Absil, O., Bayo, A., Canovas, H., Carmona, A., Chen, C., Ertel, S., Garufi, A., Henning, T., Iglesias, D. P., Launhardt, R., Liseau, R., Meeus, G., Moór, A., Mora, A., Olofsson, J., Rauw, G., and Riviere-Marichalar, P. (2018). The co-existence of hot and cold gas in debris discs. *A&A*, 614:A3.
- Rebollido, I., Eiroa, C., Montesinos, B., Maldonado, J., Villaver, E., Absil, O., Bayo, A., Canovas, H., Carmona, A., Chen, C., Ertel, S., Henning, T., Iglesias, D. P., Launhardt, R., Liseau, R., Meeus, G., Moór, A., Mora, A., Olofsson, J., Rauw, G., and Riviere-Marichalar, P. (2020). Exocomets: A spectroscopic survey. *A&A*, 639:A11.
- Reidemeister, M., Krivov, A. V., Stark, C. C., Augereau, J. C., Löhne, T., and Müller, S. (2011). The cold origin of the warm dust around ϵ Eridani. *A&A*, 527:A57.
- Rein, H., Hernandez, D. M., Tamayo, D., Brown, G., Eckels, E., Holmes, E., Lau, M., Leblanc, R., and Silburt, A. (2019). Hybrid symplectic integrators for planetary dynamics. *MNRAS*, 485(4):5490–5497.

- Rein, H. and Liu, S. F. (2012). REBOUND: an open-source multi-purpose N-body code for collisional dynamics. *A&A*, 537:A128.
- Rein, H. and Spiegel, D. S. (2015). IAS15: a fast, adaptive, high-order integrator for gravitational dynamics, accurate to machine precision over a billion orbits. *MNRAS*, 446(2):1424–1437.
- Rein, H. and Tamayo, D. (2015). WHFAST: a fast and unbiased implementation of a symplectic Wisdom-Holman integrator for long-term gravitational simulations. *MNRAS*, 452(1):376–388.
- Rein, H. and Tamayo, D. (2016). Second-order variational equations for N-body simulations. *MNRAS*, 459(3):2275–2285.
- Rein, H. and Tamayo, D. (2017). A new paradigm for reproducing and analyzing N-body simulations of planetary systems. *MNRAS*, 467(2):2377–2383.
- Rieke, G. H., Su, K. Y. L., Stansberry, J. A., Trilling, D., Bryden, G., Muzerolle, J., White, B., Gorlova, N., Young, E. T., Beichman, C. A., Stapelfeldt, K. R., and Hines, D. C. (2005). Decay of Planetary Debris Disks. *ApJ*, 620(2):1010–1026.
- Rigley, J. K. and Wyatt, M. C. (2020). Dust size and spatial distributions in debris discs: predictions for exozodiacal dust dragged in from an exo-Kuiper belt. *MNRAS*, 497(1):1143–1165.
- Rigley, J. K. and Wyatt, M. C. (2022). Comet fragmentation as a source of the zodiacal cloud. *MNRAS*, 510(1):834–857.
- Ritson, D. J., Mojzsis, S. J., and Sutherland, J. D. (2020). Supply of phosphate to early Earth by photogeochemistry after meteoritic weathering. *Nature Geoscience*, 13(5):344–348.
- Roberge, A., Chen, C. H., Millan-Gabet, R., Weinberger, A. J., Hinz, P. M., Stapelfeldt, K. R., Absil, O., Kuchner, M. J., and Bryden, G. (2012). The Exozodiacal Dust Problem for Direct Observations of Exo-Earths. *PASP*, 124(918):799.
- Rodigas, T. J., Stark, C. C., Weinberger, A., Debes, J. H., Hinz, P. M., Close, L., Chen, C., Smith, P. S., Males, J. R., Skemer, A. J., Puglisi, A., Follette, K. B., Morzinski, K., Wu, Y.-L., Briguglio, R., Esposito, S., Pinna, E., Riccardi, A., Schneider, G., and Xompero, M. (2015). On the Morphology and Chemical Composition of the HR 4796A Debris Disk. *ApJ*, 798(2):96.
- Rotelli, L., Trigo-Rodríguez, J. M., Moyano-Camero, C. E., Carota, E., Botta, L., di Mauro, E., and Saladino, R. (2016). The key role of meteorites in the formation of relevant prebiotic molecules in a formamide/water environment. *Scientific Reports*, 6:38888.
- Rotundi, A., Sierks, H., Della Corte, V., Fulle, M., Gutierrez, P. J., Lara, L., Barbieri, C., Lamy, P. L., Rodrigo, R., Koschny, D., Rickman, H., Keller, H. U., López-Moreno, J. J., Accolla, M., Agarwal, J., A'Hearn, M. F., Altobelli, N., Angrilli, F., Barucci, M. A., Bertaux, J.-L., Bertini, I., Bodewits, D., Bussoletti, E., Colangeli, L., Cosi, M., Cremonese, G., Crifo, J.-F., Da Deppo, V., Davidsson, B., Debei, S., De Cecco, M., Esposito, F., Ferrari, M., Fornasier, S., Giovane, F., Gustafson, B., Green, S. F., Groussin, O., Grün,

- E., Güttler, C., Herranz, M. L., Hviid, S. F., Ip, W., Ivanovski, S., Jerónimo, J. M., Jorda, L., Knollenberg, J., Kramm, R., Kührt, E., Küppers, M., Lazzarin, M., Leese, M. R., López-Jiménez, A. C., Lucarelli, F., Lowry, S. C., Marzari, F., Epifani, E. M., McDonnell, J. A. M., Mennella, V., Michalik, H., Molina, A., Morales, R., Moreno, F., Mottola, S., Naletto, G., Oklay, N., Ortiz, J. L., Palomba, E., Palumbo, P., Perrin, J.-M., Rodríguez, J., Sabau, L., Snodgrass, C., Sordini, R., Thomas, N., Tubiana, C., Vincent, J.-B., Weissman, P., Wenzel, K.-P., Zakharov, V., and Zarnecki, J. C. (2015). Dust measurements in the coma of comet 67P/Churyumov-Gerasimenko inbound to the Sun. *Science*, 347(6220):aaa3905.
- Rowan-Robinson, M. and May, B. (2013). An improved model for the infrared emission from the zodiacal dust cloud: cometary, asteroidal and interstellar dust. *MNRAS*, 429(4):2894–2902.
- Samarasinha, N. H. (2001). NOTE: A Model for the Breakup of Comet LINEAR (C/1999 S4). *Icarus*, 154(2):540–544.
- Samarasinha, N. H. (2007). Rotation and activity of comets. *Advances in Space Research*, 39(3):421–427.
- Schäfer, U., Yang, C.-C., and Johansen, A. (2017). Initial mass function of planetesimals formed by the streaming instability. *A&A*, 597:A69.
- Schräpler, R., Blum, J., Krijt, S., and Raabe, J.-H. (2018). The Physics of Protoplanetary Dust Agglomerates. X. High-velocity Collisions between Small and Large Dust Agglomerates as a Growth Barrier. *ApJ*, 853(1):74.
- Schwamb, M. E. (2014). Solar System: Stranded in no-man’s-land. *Nature*, 507(7493):435–436.
- Scotti, J. V. and Melosh, H. J. (1993). Estimate of the size of comet Shoemaker-Levy 9 from a tidal breakup model. *Nature*, 365(6448):733–735.
- Sekanina, Z. (1982). The problem of split comets in review. In Wilkening, L. L., editor, *IAU Colloq. 61: Comet Discoveries, Statistics, and Observational Selection*, pages 251–287.
- Sekanina, Z. (1997). The problem of split comets revisited. *A&A*, 318:L5–L8.
- Sekanina, Z. (1999). Multiple fragmentation of comet Machholz 2 (P/1994 P1). *A&A*, 342:285–299.
- Sekanina, Z. (2007). Earth’s 2006 encounter with comet 73P/Schwassmann-Wachmann: Products of nucleus fragmentation seen in closeup. In Valsecchi, G. B., Vokrouhlický, D., and Milani, A., editors, *Near Earth Objects, our Celestial Neighbors: Opportunity and Risk*, volume 236, pages 211–220.
- Sekanina, Z. (2021). New Model for the Kreutz Sungrazer System: Contact-Binary Parent and Upgraded Classification of Discrete Fragment Populations. *arXiv e-prints*, page arXiv:2109.01297.
- Sekanina, Z. and Chodas, P. W. (2002). Fragmentation Origin of Major Sungrazing Comets C/1970 K1, C/1880 C1, and C/1843 D1. *ApJ*, 581(2):1389–1398.

- Serabyn, E., Mennesson, B., Colavita, M. M., Koresko, C., and Kuchner, M. J. (2012). The Keck Interferometer Nuller. *ApJ*, 748(1):55.
- Sezestre, É., Augereau, J. C., and Thébault, P. (2019). Hot exozodiacal dust: an exocometary origin? *A&A*, 626:A2.
- Shannon, A., Bonsor, A., Kral, Q., and Matthews, E. (2016). The unseen planets of double belt debris disc systems. *MNRAS*, 462(1):L116–L120.
- Shannon, A., Mustill, A. J., and Wyatt, M. (2015). Capture and evolution of dust in planetary mean-motion resonances: a fast, semi-analytic method for generating resonantly trapped disc images. *MNRAS*, 448(1):684–702.
- Sheret, I., Dent, W. R. F., and Wyatt, M. C. (2004). Submillimetre observations and modelling of Vega-type stars. *MNRAS*, 348(4):1282–1294.
- Shestakova, L. I. and Tambovtseva, L. V. (1997). The Thermal Destruction of Solids Near the Sun. *Earth Moon and Planets*, 76:19–45.
- Shober, P. M., Sansom, E. K., Bland, P. A., Devillepoix, H. A. R., Towner, M. C., Cupák, M., Howie, R. M., Hartig, B. A. D., and Anderson, S. L. (2021). The Main Asteroid Belt: The Primary Source of Debris on Comet-like Orbits. *Planet. Sci. J.*, 2(3):98.
- Sibthorpe, B., Kennedy, G. M., Wyatt, M. C., Lestrade, J. F., Greaves, J. S., Matthews, B. C., and Duchêne, G. (2018). Analysis of the Herschel DEBRIS Sun-like star sample. *MNRAS*, 475(3):3046–3064.
- Sibthorpe, B., Vandenbussche, B., Greaves, J. S., Pantin, E., Olofsson, G., Acke, B., Barlow, M. J., Blommaert, J. A. D. L., Bouwman, J., Brandeker, A., Cohen, M., De Meester, W., Dent, W. R. F., di Francesco, J., Dominik, C., Fridlund, M., Gear, W. K., Glauser, A. M., Gomez, H. L., Hargrave, P. C., Harvey, P. M., Henning, T., Heras, A. M., Hogerheijde, M. R., Holland, W. S., Ivison, R. J., Leeks, S. J., Lim, T. L., Liseau, R., Matthews, B. C., Naylor, D. A., Pilbratt, G. L., Polehampton, E. T., Regibo, S., Royer, P., Sicilia-Aguilar, A., Swinyard, B. M., Waelkens, C., Walker, H. J., and Wesson, R. (2010). The Vega debris disc: A view from Herschel. *A&A*, 518:L130.
- Simon, J. B., Armitage, P. J., Li, R., and Youdin, A. N. (2016). The Mass and Size Distribution of Planetesimals Formed by the Streaming Instability. I. The Role of Self-gravity. *ApJ*, 822(1):55.
- Simon, J. B., Armitage, P. J., Youdin, A. N., and Li, R. (2017). Evidence for Universality in the Initial Planetesimal Mass Function. *ApJ*, 847(2):L12.
- Smoluchowski, M. V. (1916). Drei Vorträge über Diffusion, Brownsche Bewegung und Koagulation von Kolloidteilchen. *Zeitschrift für Physik*, 17:557–585.
- Snodgrass, C., Fitzsimmons, A., Lowry, S. C., and Weissman, P. (2011). The size distribution of Jupiter Family comet nuclei. *MNRAS*, 414(1):458–469.
- Soja, R. H., Grün, E., Strub, P., Sommer, M., Millinger, M., Vaubaillon, J., Alius, W., Camodeca, G., Hein, F., Laskar, J., Gastineau, M., Fienga, A., Schwarzkopf, G. J., Herzog, J., Gutsche, K., Skuppin, N., and Srama, R. (2019). IMEM2: a meteoroid environment model for the inner solar system. *A&A*, 628:A109.

- Soja, R. H., Sommer, M., Herzog, J., Agarwal, J., Rodmann, J., Srama, R., Vaubaillon, J., Strub, P., Hornig, A., Bausch, L., and Grün, E. (2015). Characteristics of the dust trail of 67P/Churyumov-Gerasimenko: an application of the IMEX model. *A&A*, 583:A18.
- Stark, C. C., Belikov, R., Bolcar, M. R., Cady, E., Crill, B. P., Ertel, S., Groff, T., Hildebrandt, S., Krist, J., Lisman, P. D., Mazoyer, J., Mennesson, B., Nemati, B., Pueyo, L., Rauscher, B. J., Riggs, A. J., Ruane, G., Shaklan, S. B., Sirbu, D., Soummer, R., Laurent, K. S., and Zimmerman, N. (2019). ExoEarth yield landscape for future direct imaging space telescopes. *Journal of Astronomical Telescopes, Instruments, and Systems*, 5:024009.
- Stark, C. C. and Kuchner, M. J. (2008). The Detectability of Exo-Earths and Super-Earths Via Resonant Signatures in Exozodiacal Clouds. *ApJ*, 686(1):637–648.
- Stark, C. C. and Kuchner, M. J. (2009). A New Algorithm for Self-consistent Three-dimensional Modeling of Collisions in Dusty Debris Disks. *ApJ*, 707(1):543–553.
- Stark, C. C., Roberge, A., Mandell, A., Clampin, M., Domagal-Goldman, S. D., McElwain, M. W., and Stapelfeldt, K. R. (2015). Lower Limits on Aperture Size for an ExoEarth Detecting Coronagraphic Mission. *ApJ*, 808(2):149.
- Stock, N. D., Su, K. Y. L., Liu, W., Hinz, P. M., Rieke, G. H., Marengo, M., Stapelfeldt, K. R., Hines, D. C., and Trilling, D. E. (2010). The Structure of the β Leonis Debris Disk. *ApJ*, 724(2):1238–1255.
- Stone, J. M., Skemer, A. J., Hinz, P. M., Bonavita, M., Kratter, K. M., Maire, A.-L., Defrere, D., Bailey, V. P., Spalding, E., Leisenring, J. M., Desidera, S., Bonnefoy, M., Biller, B., Woodward, C. E., Henning, T., Skrutskie, M. F., Eisner, J. A., Crepp, J. R., Patience, J., Weigelt, G., De Rosa, R. J., Schlieder, J., Brandner, W., Apai, D., Su, K., Ertel, S., Ward-Duong, K., Morzinski, K. M., Schertl, D., Hofmann, K.-H., Close, L. M., Brems, S. S., Fortney, J. J., Oza, A., Buenzli, E., and Bass, B. (2018). The LEECH Exoplanet Imaging Survey: Limits on Planet Occurrence Rates under Conservative Assumptions. *AJ*, 156(6):286.
- Su, K. Y. L., De Buizer, J. M., Rieke, G. H., Krivov, A. V., Löhne, T., Marengo, M., Stapelfeldt, K. R., Ballering, N. P., and Vacca, W. D. (2017). The Inner 25 au Debris Distribution in the ϵ Eri System. *AJ*, 153(5):226.
- Su, K. Y. L., Rieke, G. H., Malhotra, R., Stapelfeldt, K. R., Hughes, A. M., Bonsor, A., Wilner, D. J., Balog, Z., Watson, D. M., Werner, M. W., and Misselt, K. A. (2013). Asteroid Belts in Debris Disk Twins: Vega and Fomalhaut. *ApJ*, 763(2):118.
- Su, K. Y. L., Rieke, G. H., Stansberry, J. A., Bryden, G., Stapelfeldt, K. R., Trilling, D. E., Muzerolle, J., Beichman, C. A., Moro-Martin, A., Hines, D. C., and Werner, M. W. (2006). Debris Disk Evolution around A Stars. *ApJ*, 653(1):675–689.
- Sykes, M. V. (1988). IRAS Observations of Extended Zodiacal Structure. *ApJ*, 334:L55.
- Sykes, M. V., Grün, E., Reach, W. T., and Jenniskens, P. (2004). *The interplanetary dust complex and comets*, page 677.
- Sykes, M. V., Lebofsky, L. A., Hunten, D. M., and Low, F. (1986). The Discovery of Dust Trails in the Orbits of Periodic Comets. *Science*, 232(4754):1115–1117.

- Sykes, M. V. and Walker, R. G. (1992). Cometary dust trails I. Survey. *Icarus*, 95(2):180–210.
- Tamayo, D., Rein, H., Shi, P., and Hernandez, D. M. (2020). REBOUNDx: a library for adding conservative and dissipative forces to otherwise symplectic N-body integrations. *MNRAS*, 491(2):2885–2901.
- Tambovtseva, L. V. and Shestakova, L. i. (1999). Cometary splitting due to thermal stresses. *Planet. Space Sci.*, 47(3-4):319–326.
- Tanaka, H., Inaba, S., and Nakazawa, K. (1996). Steady-State Size Distribution for the Self-Similar Collision Cascade. *Icarus*, 123(2):450–455.
- Tancredi, G., Fernández, J. A., Rickman, H., and Licandro, J. (2000). A catalog of observed nuclear magnitudes of Jupiter family comets. *A&AS*, 146:73–90.
- Tancredi, G., Fernández, J. A., Rickman, H., and Licandro, J. (2006). Nuclear magnitudes and the size distribution of Jupiter family comets. *Icarus*, 182(2):527–549.
- The LUVOIR Team (2019). The LUVOIR Mission Concept Study Final Report. *arXiv e-prints*, page arXiv:1912.06219.
- Thébault, P. (2009). Vertical structure of debris discs. *A&A*, 505(3):1269–1276.
- Thébault, P. (2012). A new code to study structures in collisionally active, perturbed debris discs: application to binaries. *A&A*, 537:A65.
- Thébault, P. and Augereau, J. C. (2007). Collisional processes and size distribution in spatially extended debris discs. *A&A*, 472(1):169–185.
- Thébault, P., Augereau, J. C., and Beust, H. (2003). Dust production from collisions in extrasolar planetary systems. The inner beta Pictoris disc. *A&A*, 408:775–788.
- Thebault, P. and Kral, Q. (2019). Is there more than meets the eye? Presence and role of sub-micron grains in debris discs. *A&A*, 626:A24.
- Thebault, P., Kral, Q., and Ertel, S. (2012). Planet signatures in collisionally active debris discs: scattered light images. *A&A*, 547:A92.
- Thébault, P. and Wu, Y. (2008). Outer edges of debris discs. How sharp is sharp? *A&A*, 481(3):713–724.
- Thureau, N. D., Greaves, J. S., Matthews, B. C., Kennedy, G., Phillips, N., Booth, M., Duchêne, G., Horner, J., Rodriguez, D. R., Sibthorpe, B., and Wyatt, M. C. (2014). An unbiased study of debris discs around A-type stars with Herschel. *MNRAS*, 445(3):2558–2573.
- Tremaine, S. (1993). The distribution of comets around stars. In Phillips, J. A., Thorsett, S. E., and Kulkarni, S. R., editors, *Planets Around Pulsars*, volume 36 of *Astronomical Society of the Pacific Conference Series*, pages 335–344.
- Trilling, D. E., Bryden, G., Beichman, C. A., Rieke, G. H., Su, K. Y. L., Stansberry, J. A., Blaylock, M., Stapelfeldt, K. R., Beeman, J. W., and Haller, E. E. (2008). Debris Disks around Sun-like Stars. *ApJ*, 674(2):1086–1105.

- Tsiganis, K., Gomes, R., Morbidelli, A., and Levison, H. F. (2005). Origin of the orbital architecture of the giant planets of the Solar System. *Nature*, 435(7041):459–461.
- Ueda, T., Kobayashi, H., Takeuchi, T., Ishihara, D., Kondo, T., and Kaneda, H. (2017). Size Dependence of Dust Distribution around the Earth Orbit. *AJ*, 153(5):232.
- van Leeuwen, F. (2007). Validation of the new Hipparcos reduction. *A&A*, 474(2):653–664.
- van Lieshout, R., Dominik, C., Kama, M., and Min, M. (2014). Near-infrared emission from sublimating dust in collisionally active debris disks. *A&A*, 571:A51.
- Vitense, C., Krivov, A. V., Kobayashi, H., and Löhne, T. (2012). An improved model of the Edgeworth-Kuiper debris disk. *A&A*, 540:A30.
- Wang, J. H. and Brassier, R. (2014). An Oort Cloud origin of the Halley-type comets. *A&A*, 563:A122.
- Weidenschilling, S. J. (1977). Aerodynamics of solid bodies in the solar nebula. *MNRAS*, 180:57–70.
- Weidenschilling, S. J. and Cuzzi, J. N. (1993). Formation of Planetesimals in the Solar Nebula. In Levy, E. H. and Lunine, J. I., editors, *Protostars and Planets III*, page 1031.
- Weissman, P. R. and Lowry, S. C. (2003). The Size Distribution of Jupiter-Family Cometary Nuclei. In Mackwell, S. and Stansbery, E., editors, *Lunar and Planetary Science Conference*, volume 34 of *Lunar and Planetary Science Conference*, page 2003.
- Weissman, P. R. and Lowry, S. C. (2008). Structure and density of cometary nuclei. *Meteoritics and Planetary Science*, 43(6):1033–1047.
- Whipple, F. L. (1978). Cometary Brightness Variation and Nucleus Structure (Paper dedicated to Professor Hannes Alfvén on the occasion of his 70th birthday, 30 May 1978.). *Moon and Planets*, 18(3):343–359.
- Wiegert, P., Vaubaillon, J., and Campbell-Brown, M. (2009). A dynamical model of the sporadic meteoroid complex. *Icarus*, 201(1):295–310.
- Wisdom, J. (1980). The resonance overlap criterion and the onset of stochastic behavior in the restricted three-body problem. *AJ*, 85:1122–1133.
- Womack, M., Sarid, G., and Wierzchos, K. (2017). CO in Distantly Active Comets. *PASP*, 129(973):031001.
- Wright, E. L., Eisenhardt, P. R. M., Mainzer, A. K., Ressler, M. E., Cutri, R. M., Jarrett, T., Kirkpatrick, J. D., Padgett, D., McMillan, R. S., Skrutskie, M., Stanford, S. A., Cohen, M., Walker, R. G., Mather, J. C., Leisawitz, D., Gautier, Thomas N., I., McLean, I., Benford, D., Lonsdale, C. J., Blain, A., Mendez, B., Irace, W. R., Duval, V., Liu, F., Royer, D., Heinrichsen, I., Howard, J., Shannon, M., Kendall, M., Walsh, A. L., Larsen, M., Cardon, J. G., Schick, S., Schwalm, M., Abid, M., Fabinsky, B., Naes, L., and Tsai, C.-W. (2010). The Wide-field Infrared Survey Explorer (WISE): Mission Description and Initial On-orbit Performance. *AJ*, 140(6):1868–1881.

- Wyatt, M. C. (2003). Resonant Trapping of Planetesimals by Planet Migration: Debris Disk Clumps and Vega's Similarity to the Solar System. *ApJ*, 598(2):1321–1340.
- Wyatt, M. C. (2005). The insignificance of P-R drag in detectable extrasolar planetesimal belts. *A&A*, 433:1007–1012.
- Wyatt, M. C. (2006). Dust in Resonant Extrasolar Kuiper Belts: Grain Size and Wavelength Dependence of Disk Structure. *ApJ*, 639(2):1153–1165.
- Wyatt, M. C. (2008). Evolution of debris disks. *ARA&A*, 46:339–383.
- Wyatt, M. C. (2018). *Debris Disks: Probing Planet Formation*, page 146.
- Wyatt, M. C., Bonsor, A., Jackson, A. P., Marino, S., and Shannon, A. (2017). How to design a planetary system for different scattering outcomes: giant impact sweet spot, maximizing exocomets, scattered discs. *MNRAS*, 464(3):3385–3407.
- Wyatt, M. C., Booth, M., Payne, M. J., and Churcher, L. J. (2010). Collisional evolution of eccentric planetesimal swarms. *MNRAS*, 402(1):657–672.
- Wyatt, M. C., Clarke, C. J., and Booth, M. (2011). Debris disk size distributions: steady state collisional evolution with Poynting-Robertson drag and other loss processes. *Celestial Mechanics and Dynamical Astronomy*, 111:1–28.
- Wyatt, M. C. and Dent, W. R. F. (2002). Collisional processes in extrasolar planetesimal discs - dust clumps in Fomalhaut's debris disc. *MNRAS*, 334(3):589–607.
- Wyatt, M. C., Dermott, S. F., Grogan, K., and Jayaraman, S. (1999). A Unique View Through the Earth's Resonant Ring. In Bica, M. D., Cutri, R. M., and Madore, B. F., editors, *Astrophysics with Infrared Surveys: A Prelude to SIRTf*, volume 177 of *Astronomical Society of the Pacific Conference Series*, page 374.
- Wyatt, M. C., Greaves, J. S., Dent, W. R. F., and Coulson, I. M. (2005). Submillimeter Images of a Dusty Kuiper Belt around η Corvi. *ApJ*, 620(1):492–500.
- Wyatt, M. C., Kral, Q., and Sinclair, C. A. (2020). Susceptibility of planetary atmospheres to mass-loss and growth by planetesimal impacts: the impact shoreline. *MNRAS*, 491(1):782–802.
- Wyatt, M. C., Smith, R., Greaves, J. S., Beichman, C. A., Bryden, G., and Lisse, C. M. (2007a). Transience of Hot Dust around Sun-like Stars. *ApJ*, 658(1):569–583.
- Wyatt, M. C., Smith, R., Su, K. Y. L., Rieke, G. H., Greaves, J. S., Beichman, C. A., and Bryden, G. (2007b). Steady State Evolution of Debris Disks around A Stars. *ApJ*, 663(1):365–382.
- Wyatt, M. C., van Lieshout, R., Kennedy, G. M., and Boyajian, T. S. (2018). Modelling the KIC8462852 light curves: compatibility of the dips and secular dimming with an exocomet interpretation. *MNRAS*, 473(4):5286–5307.
- Wyatt, S. P. and Whipple, F. L. (1950). The Poynting-Robertson effect on meteor orbits. *ApJ*, 111:134–141.

- Yang, B., Jewitt, D., Zhao, Y., Jiang, X., Ye, Q., and Chen, Y.-T. (2021). Discovery of Carbon Monoxide in Distant Comet C/2017 K2 (PANSTARRS). *ApJ*, 914(1):L17.
- Yang, H. and Ishiguro, M. (2015). Origin of Interplanetary Dust through Optical Properties of Zodiacal Light. *ApJ*, 813(2):87.
- Yelverton, B., Kennedy, G. M., and Su, K. Y. L. (2020). No significant correlation between radial velocity planet presence and debris disc properties. *MNRAS*, 495(2):1943–1957.
- Yelverton, B., Kennedy, G. M., Su, K. Y. L., and Wyatt, M. C. (2019). A statistically significant lack of debris discs in medium separation binary systems. *MNRAS*, 488(3):3588–3606.
- Yoshida, F. and Terai, T. (2017). Small Jupiter Trojans Survey with the Subaru/Hyper Suprime-Cam. *AJ*, 154(2):71.
- Youdin, A. N. and Goodman, J. (2005). Streaming Instabilities in Protoplanetary Disks. *ApJ*, 620(1):459–469.
- Zieba, S., Zwintz, K., Kenworthy, M. A., and Kennedy, G. M. (2019). Transiting exocomets detected in broadband light by TESS in the β Pictoris system. *A&A*, 625:L13.
- Zsom, A., Ormel, C. W., Güttler, C., Blum, J., and Dullemond, C. P. (2010). The outcome of protoplanetary dust growth: pebbles, boulders, or planetesimals? II. Introducing the bouncing barrier. *A&A*, 513:A57.
- Zuckerman, B. (2019). The Nearby, Young, Argus Association: Membership, Age, and Dusty Debris Disks. *ApJ*, 870(1):27.
- Zuckerman, B. and Song, I. (2012). A 40 Myr Old Gaseous Circumstellar Disk at 49 Ceti: Massive CO-rich Comet Clouds at Young A-type Stars. *ApJ*, 758(2):77.